

**Mechanisms and Kinetics of Proton-Coupled
Electron-Transfer Oxidation of Phenols**

by

Na Song

A dissertation submitted to the Graduate Faculty of
Auburn University
in partial fulfillment of the
requirements for the Degree of
Doctor of Philosophy

Auburn, Alabama
December 12, 2011

Keywords: Proton-coupled electron-transfer, phenol oxidation, outer-sphere,
kinetics and mechanisms, transition metal complexes, stopped-flow.

Copyright 2011 by Na Song

Approved by

David Stanbury, Chair, Professor of Chemistry and Biochemistry
Holly Ellis, Associate Professor of Chemistry and Biochemistry
Christian Goldsmith, Assistant Professor of Chemistry and Biochemistry
German Mills, Associate Professor of Chemistry and Biochemistry

Abstract

The kinetics of the aqueous oxidation of phenol by a deficiency of $[\text{IrCl}_6]^{2-}$ has been investigated. The reaction initially produces $[\text{IrCl}_6]^{3-}$ and phenoxy radicals. The inhibition caused by $[\text{IrCl}_6]^{3-}$ can be prevented by use of dibromonitroso-benzenesulfonate (DBNBS) as a phenoxy radical scavenger. The phenoxy radicals primarily couple to form 4,4'-biphenol, 2,2'-biphenol, 2,4'-biphenol, and 4-phenoxyphenol. Further oxidation of these coupling products leads to a rather complex mixture of final products. The rate laws for the oxidation of the four coupling products by $[\text{IrCl}_6]^{2-}$ have the same form as those for the oxidation of phenol itself:

$$-\frac{d[\text{Ir}^{\text{IV}}]}{dt} = \frac{(k_{\text{ArOH}} + k_{\text{ArO}^-}K_a/[\text{H}^+])}{1 + K_a/[\text{H}^+]} [\text{ArOH}]_{\text{tot}}[\text{Ir}^{\text{IV}}].$$
 Values for k_{ArOH} and k_{ArO^-} have been

determined at 25 °C and are assigned to H_2O -CPET (water associated concerted proton coupled electron transfer) and electron-transfer mechanisms respectively. Kinetic simulations of a combined mechanism that includes the oxidation of phenol as well as the subsequent reactions show that the degree of overoxidation is rather limited at high pH but quite extensive at low pH. This pH-dependent overoxidation leads to a pH-dependent stoichiometric factor in the rate law for oxidation of phenol, and causes some minor deviations in the rate law for oxidation of phenol. Empirically, these minor deviations can be accommodated by introduction of a third term in the rate law that includes a "pH-dependent rate constant", but this approach masks the mechanistic origins of the effect.

One-electron oxidation of alkyl- and alkoxy-substituted phenols (2-methylphenol, 2,6-dimethylphenol, 2,4,6-trimethylphenol, 4-*tert*-butylphenol and 4-methoxyphenol) has been studied. pH-dependent stoichiometric factors corresponding to overoxidation are found with all substituted phenols except for 2,4,6-trimethylphenol and 4-methoxyphenol. In the 2,4,6-trimethylphenol reaction, the identification of product, 4-hydroxymethyl-2,6-dimethylphenol, rules out the overoxidation steps and there is no need to include an “overoxidation pH-dependent” rate constant. The solvent H/D KIE’s for the phenols pathway provide further evidence for a H₂O-CPET mechanism of oxidation of phenols by [IrCl₆]²⁻.

Overoxidation is also observed in the reaction between *N*-acetyl-*L*-tyrosinamide (a protected tyrosine derivative) and [IrCl₆]²⁻. Fitting the data to a two-term rate law yields second-order rate constants of $k_{\text{ArOH}} = 5.4 \pm 0.6 \text{ M}^{-1} \text{ s}^{-1}$ and $k_{\text{ArO}^-} = (4.5 \pm 0.3) \times 10^7 \text{ M}^{-1} \text{ s}^{-1}$.

Analysis of the kinetic data of the oxidation of phenol by [Os(phen)₃]³⁺ yields the rate law: $-\frac{d[\text{Os}^{\text{III}}]}{dt} = 2k_{\text{dim}} \frac{[\text{Os}^{\text{III}}]^2 [\text{ArOH}]_{\text{tot}}^2}{[\text{Os}^{\text{II}}]^2} \left(\frac{K_{\text{ArOH}}}{K_{\text{a}} + [\text{H}^+]} \right)^2$ where the reaction rate is second-order in both [Os(phen)₃]³⁺ and phenol. $K_{\text{ArOH}} = 1.1 \times 10^{-10} \text{ M}$ and $K_{\text{ArO}^-} = 7.0$ are obtained from thermodynamics. k_{ArO^-} is calculated to be $2.1 \times 10^9 \text{ M}^{-1} \text{ s}^{-1}$ according to Marcus theory and this value is also supported by kinetic simulations.

Acknowledgments

The first person I would like to thank is my advisor, Dr. David Stanbury, for his kindness and patience to guide my PhD journey, for his generosity to teach me not only the knowledge but also the attitude to be a scientist, and for all his help to navigate my academic way. I am very grateful to my committee members, Dr. German Mills, Dr. Christian Goldsmith and Dr. Holly Ellis, for their advice with respect to my research, career and writing. I also want to thank Dr. Thomas Albrecht-Schmitt who helped me at the beginning of this work. Many thanks to Dr. John Gorden for helping me to synthesize a complex, Dr. Douglas Goodwin for allowing me to use his stopped-flow instrument, Dr. Yonnie Wu for collecting mass spectroscopic data and Dr. Michael Meadows for helping me acquire NMR data. I also would like to thank my previous and current lab colleagues: Dr. Xiaoguang Wang who helped me a lot when I started this research, Dr. Thanasekaran Pounraj who gave me some useful advice and Mr. Nootan Bhattarai who discusses the research with me. I thank all my friends and colleagues at Auburn for their supports and encouragement.

Finally, I would like to thank my family, without their love and support I never could have gotten this far. I especially thank my husband, Jie Wu, for always being on my side and helping me keep my faith.

Table of Contents

Abstract.....	ii
Acknowledgments.....	iv
List of Tables	ix
List of Schemes.....	xiii
List of Figures.....	xiv
Chapter 1 Literature Review.....	1
1.1 Outer-Sphere Electron Transfer	1
1.2 Proton-Coupled Electron-Transfer (PCET)	7
1.3 Oxidation of Phenols.....	9
Chapter 2 Proton-Coupled Electron-Transfer Oxidation of Phenol by Hexachloroiridate(IV).....	14
2.1 Introduction.....	14
2.2 Experimental Section.....	15
2.2.1 Reagents and Solutions	15
2.2.2 Methods.....	18
2.3 Results.....	22
2.3.1 Oxidation of Phenol	22
2.3.1.1 Hexachloroiridate(III) Effects	22
2.3.1.2 General Base Catalytic Test.	25

2.3.1.3 Spin Trapping Effect	26
2.3.1.4 Phenol Dependence	29
2.3.1.5 Dependence on $p[H^+]$	30
2.3.1.6 Inclusion of the k^o Term	32
2.3.1.7 Kinetic Isotope Effect (KIE)	35
2.3.2 Overoxidation of Phenol	36
2.3.2.1 Coupling Products	36
2.3.2.2 pK_a values of 4,4'-Biphenol and 2,4'-Biphenol .	39
2.3.2.3 Overoxidation of Phenol.....	41
2.4 Discussion and Conclusion	56
Chapter 3 Oxidation of alkyl- and alkoxy-substituted phenols by Hexachloroiridate(IV)	75
3.1 Introduction	75
3.2 Experimental Section	76
3.2.1 Reagents and Solutions	76
3.2.2 Methods	78
3.3 Results	78
3.3.1 The Oxidation of 2-Methylphenol.....	78
3.3.2 The Oxidation of 2,6-Dimethylphenol	88
3.3.3 The Oxidation of 2,4,6-Trimethylphenol (TMP)	95
3.3.4 The Oxidation of 4-Methoxyphenol.....	102
3.3.5 The oxidation of 4- <i>tert</i> -Butylphenol	107
3.4 Discussion and Conclusion	111
3.4.1 Mechanism	111

3.4.2 Mechanism of k_{ArO^-} Term.....	113
3.4.3 Mechanism of k_{ArOH} Term.....	118
Chapter 4 Oxidation of Ac-Y-NH ₂ by Hexachloroiridate(IV).....	132
4.1 Introduction.....	132
4.2 Experimental Section.....	132
4.2.1 Reagents and Solutions.....	132
4.2.2 Methods.....	133
4.3 Results.....	134
4.3.1 Hexachloroiridate(III) Inhibition.....	134
4.3.2 Spin Trapping Effect.....	137
4.3.3 Ac-Y-NH ₂ Dependence.....	138
4.3.4 Dependence on p[H ⁺].....	138
4.3.5 Stoichiometry and Overoxidation.....	142
4.3.6 Control Experiments.....	145
4.4 Discussion and Conclusion.....	145
Chapter 5 Oxidation of phenol by tris-(1,10-phenanthroline)osmium(III).....	149
5.1 Introduction.....	149
5.2 Experimental Section.....	149
5.2.1 Reagents and Solutions.....	149
5.2.2 Methods.....	151
5.3 Results.....	152
5.3.1 Characterization of the Osmium Complexes.....	152
5.3.2 Kinetics.....	153

5.4 Discussion and Conclusion	167
References.....	173
Appendix A Experimental Details in Chapters 2–5.....	180

List of Tables

Table 2-1. Kinetic Dependence on Concentration of Buffer	25
Table 2-2. Kinetic Data for the Reaction of Phenol with Ir ^{IV} in the Presence of PBN, DMPO, POBN, MNP, DMNBS and DBNBS.....	28
Table 2-3. Kinetic Data for the Reaction of Phenol with Ir ^{IV} in the Presence of DBNBS	29
Table 2-4. Kinetic Dependence of Phenol Oxidation on DBNBS at High p[H ⁺].....	30
Table 2-5. Kinetics Data for the Reactions of Ir ^{IV} with the Phenol Coupling Products ...	43
Table 2-6. Comparison of the Experimental Data of 4,4'- and 2,4'-Biphenol Oxidation at Different p[H ⁺]	47
Table 2-7. The Mechanism of Phenol Reaction and the Simulation Model.....	64
Table 2-8. The Overoxidation Rate Constants at Different p[H ⁺]	65
Table 2-9. Comparison of the Experimental Data with Overoxidation and No Overoxidation Simulation Results of the Phenol Reaction at Different p[H ⁺] in Absence of DBNBS.....	67
Table 2-10. Simulation Product Concentrations of the Phenol Reaction at Different p[H ⁺] Without DBNBS.....	69
Table 2-11. Comparison of the Experimental Data with Overoxidation Simulation Results of the Phenol Reaction in the Presence of Ir ^{III} or Various DBNBS Concentration.....	71
Table 3-1. Kinetic Data for the Reaction Between Cresol and Ir ^{IV} with Added Ir ^{III} in the Presence of Spin Trapping Agents PBN, DMPO, POBN, MNP, DMNBS and DBNBS.....	82
Table 3-2. Kinetic Effect of Cu ²⁺ and Dipic for Xylenol Oxidation	91
Table 3-3. Kinetic Data for the Reaction of Phenols with Ir ^{IV}	114

Table 3-4. Calculated Data for Phenols and the Reactions with Ir ^{IV}	115
Table 3-5. Thermodynamic Parameters for CPET and ET/PT Mechanisms.....	122
Table 3-6. Kinetic data for Phenols Oxidation by ClO ₂	124
Table 3-7. Thermodynamic and Kinetic Parameters for Phenol Oxidation by Different Oxidants.....	127
Table 3-8. Activation Parameters for Cresol and MOP Oxidation by Ir ^{IV}	131
Table 4-1. Kinetic Data for the Reaction of Ac-Y-NH ₂ with Ir ^{IV} in the Presence of DBNBS.....	137
Table 5-1. UV-Visible Absorbance of Os Complexes in 0.01 M HCl Solution.....	156
Table 5-2. Kinetic Data for the Reaction of Phenol with Os ^{III} in the Presence of Dipic or DBNBS.....	165
Table 5-3. The Mechanism of Phenol Reaction and the Simulation Model.....	170
Table 5-4. Comparison of the Experimental Data with the Simulation Results at different p[H ⁺].....	171
Table 5-5. Comparison of the Experimental Data to the Simulation Results in the Presence of Various Concentration of DBNBS	171
Table A-1. Kinetic Dependence of Phenol Oxidation on [Phenol] _{tot}	180
Table A-2. Kinetic Dependence of Phenol Oxidation on p[H ⁺] Without DBNBS.....	181
Table A-3. Kinetic Dependence of Phenol Oxidation on p[H ⁺] with DBNBS.....	182
Table A-4. Nonlinear-Least-Squares Regression Results of the $k_{\text{obs}}/[\text{phenol}]_{\text{tot}}$ vs p[H ⁺] Plot with 2-Term and 3-Term Rate Law Models in the Absence of DBNBS	183
Table A-5. Nonlinear-Least-Squares Regression Results of the $k_{\text{obs}}/[\text{phenol}]_{\text{tot}}$ vs p[H ⁺] Plot with 2-Term and 3-Term Rate Law Models in the Presence of DBNBS	184
Table A-6. Comparison of k_{obs} in H ₂ O and in D ₂ O.....	185
Table A-7. Kinetic Dependence on [Cresol] _{tot}	185

Table A-8. Kinetic Dependence of Biphenols and 4-Phenoxyphenol Oxidation on $p[H^+]$	186
Table A-9. Kinetic Dependence of Cresol Oxidation on $p[H^+]$ with DNBBS	187
Table A-10. Nonlinear-Least-Squares Regression Results of the $k_{obs}/[cresol]_{tot}$ vs $p[H^+]$ Plot with 2-Term and 3-Term Rate Law Models in the Presence of DNBBS	188
Table A-11. Kinetic Dependence of Cresol Oxidation on Temperature	189
Table A-12. Kinetic Isotope Effect for Oxidation of Cresol	189
Table A-13. Kinetic Dependence on $[Xylenol]_{tot}$	190
Table A-14. Kinetic Dependence of Xylenol Oxidation on $p[H^+]$	191
Table A-15. Nonlinear-Least-Squares Regression Results of the $k_{obs}/[xylenol]_{tot}$ vs $p[H^+]$ Plot with 2-Term and 3-Term Rate Law Models	192
Table A-16. Kinetic Isotope Effect for Oxidation of Xylenol	193
Table A-17. Kinetic Dependence on $[TMP]_{tot}$	193
Table A-18. $p[H^+]$ Dependence of TMP Oxidation	194
Table A-19. Kinetic Isotope Effect for Oxidation of TMP	195
Table A-20. Kinetic Isotope Effect for Oxidation of MOP	195
Table A-21. Kinetic Dependence of MOP Oxidation on $p[H^+]$	196
Table A-22. Kinetic Dependence of MOP Oxidation on Temperature	197
Table A-23. Kinetic Dependence of TBP Oxidation on $p[H^+]$	198
Table A-24. Nonlinear-Least-Squares Regression Results of the $k_{obs}/[TBP]_{tot}$ vs $p[H^+]$ Plot with 2-Term and 3-Term Rate Law Models in the Presence of DNBBS	199
Table A-25. Kinetic Dependence on $[Ac-Y-NH_2]_{tot}$	200
Table A-26. Kinetic Dependence of Ac-Y-NH ₂ Oxidation on $p[H^+]$	201

Table A-27. Nonlinear-Least-Squares Regression Results of the $k_{\text{obs}}/[\text{Ac-Y-NH}_2]_{\text{tot}}$ vs $\text{p}[\text{H}^+]$ Plot with 2-Term and 3-Term Rate Law Models in the Presence of DBNBS.....	202
Table A-28. Kinetic Dependence on $[\text{Os}^{\text{III}}]_0$	203
Table A-29. Kinetic data for the oxidation with various $[\text{phenol}]_{\text{tot}}$	203
Table A-30. Kinetic Dependence on $[\text{Os}^{\text{II}}]_0$	204
Table A-31. Kinetic Dependence on $\text{p}[\text{H}^+]$	204

List of Schemes

Scheme 1-1. Electron Transfer Process	2
Scheme 1-2. PCET pathways.....	8
Scheme 1-3. The electron and proton flow in Photosystem II.....	10
Scheme 1-4. The electron and proton flow in Class I RNRs.....	11
Scheme 2-1. Structure of spin trapping agents tested.....	26
Scheme 2-2. Expected dimerization products of phenoxy radical and their composition according to literature	37
Scheme 3-1. Structures of reductants.....	77
Scheme 4-1. The structures of Ac-Y-NH ₂ and Ac-Phe-NH ₂	133
Scheme 5-1. Structure of [Os(phen) ₃] ²⁺	150

List of Figures

Figure 1-1. Potential energy surfaces for an outer-sphere electron transfer reaction	5
Figure 2-1. ¹ H NMR spectrum of 2,4'-biphenol in CDCl ₃	19
Figure 2-2. UV-vis spectra of (NH ₄) ₂ [IrCl ₆] and (NH ₄) ₃ [IrCl ₆] in aqueous solution	21
Figure 2-3. Kinetic traces of oxidation of phenol by Ir ^{IV} at different p[H ⁺]	23
Figure 2-4. Comparative traces of the phenol reaction with added Ir ^{III} and no added Ir ^{III}	24
Figure 2-5. Trace of the phenol reaction with added DBNBS	27
Figure 2-6. Plot of <i>k</i> _{obs} vs [phenol] _{tot}	31
Figure 2-7. Plot of <i>k</i> _{obs} /[phenol] _{tot} vs p[H ⁺] in the absence of DBNBS	33
Figure 2-8. Plot of <i>k</i> _{obs} /[phenol] _{tot} vs p[H ⁺] with DBNBS	34
Figure 2-9. The UV-vis spectra of four coupling isomers	38
Figure 2-10. Titration of 3.0 × 10 ⁻⁵ M 4,4'-biphenol	40
Figure 2-11. Titration of 5.0 × 10 ⁻⁵ M 2,4'-biphenol	42
Figure 2-12. UV-Vis spectra of products of 4,4'-/2,2'-/2,4'-biphenol oxidation	45
Figure 2-13. The kinetic trace of 4,4'-biphenol reacting with Ir ^{IV} at 398 nm	46
Figure 2-14. Titration of 1.5 mL 4,4'-biphenol by Ir ^{IV}	48
Figure 2-15. Kinetic trace of 4,4'-biphenol oxidation at 488 nm	50
Figure 2-16. Plot of <i>k</i> _{obs} /[substrate] _{tot} vs p[H ⁺]	51
Figure 2-17. The kinetic trace of 2,2'-biphenol reacting with Ir ^{IV} at 406 nm	52
Figure 2-18. UV-Vis spectra during the reaction between 2,4'-biphenol and Ir ^{IV}	54

Figure 2-19. The kinetic trace of 2,4'-biphenol reacting with Ir ^{IV} at 398 nm	55
Figure 2-20. UV-Vis spectra during the reaction between phenol and Ir ^{IV}	57
Figure 2-21. The kinetic trace and curve fit of the reaction between phenol and Ir ^{IV}	58
Figure 2-22. Comparative pH dependence of the phenol reaction experimental data and simulation results	66
Figure 3-1. Kinetic trace of the Ir ^{IV} consumption in the cresol oxidation	80
Figure 3-2. Comparative traces of the cresol reaction with Ir ^{IV} and in the presence of added Ir ^{III} in H ₂ O	81
Figure 3-3. Kinetic traces of the cresol reaction with added DBNBS and first order fit..	83
Figure 3-4. Plot of k_{obs} vs $[\text{cresol}]_{\text{tot}}$	85
Figure 3-5. Plot of $k_{\text{obs}}/[\text{cresol}]_{\text{tot}}$ vs $\text{p}[\text{H}^+]$ with DBNBS	86
Figure 3-6. Plot of $\log(k_{\text{obs}}/T)$ vs $1/T$	87
Figure 3-7. Trace of the xylenol reaction and first-order fit	89
Figure 3-8. Comparative traces of the xylenol reaction with added 5×10^{-4} M Ir ^{III} and 2.5×10^{-3} M Ir ^{III}	90
Figure 3-9. Plot of k_{obs} vs $[\text{xylenol}]_{\text{tot}}$	93
Figure 3-10. Plot of $k_{\text{obs}}/[\text{xylenol}]_{\text{tot}}$ vs $\text{p}[\text{H}^+]$	94
Figure 3-11. Kinetic trace of the Ir ^{IV} consumption in the TMP oxidation	96
Figure 3-12. Comparative traces of the TMP reaction with added Ir ^{III}	97
Figure 3-13. Plot of k_{obs} vs $[\text{TMP}]_{\text{tot}}$	99
Figure 3-14. Plot of $k_{\text{obs}}/[\text{TMP}]_{\text{tot}}$ vs $\text{p}[\text{H}^+]$	100
Figure 3-15. ¹ H NMR identification of TMP oxidation Products	101
Figure 3-16. Kinetic trace of the Ir ^{IV} consumption in the MOP oxidation	104
Figure 3-17. Plot of $k_{\text{obs}}/[\text{MOP}]_{\text{tot}}$ vs $\text{p}[\text{H}^+]$	105
Figure 3-18. Plots of $\ln(k_{\text{obs}}/T)$ vs $1/T$	106

Figure 3-19. Kinetic trace of the Ir ^{IV} consumption in the TBP oxidation	108
Figure 3-20. Kinetic trace of the Ir ^{IV} consumption in the TBP oxidation with DNBNS	109
Figure 3-21. Plot of $k_{\text{obs}}/[\text{TBP}]_{\text{tot}}$ vs $\text{p}[\text{H}^+]$	110
Figure 3-22. Plot of $(\Delta G^\ddagger - w_{12})$ versus ΔG°	117
Figure 3-23. Correlations between the second-order rate constants for reaction of phenols (k_{ArOH}) and phenoxide anions (k_{ArO^-}) with Ir ^{IV} versus substituent constants σ^+	119
Figure 3-24. Plot of $\text{p}K_{\text{a}}$ versus substituent constants σ^+	120
Figure 3-25. Plot of kinetic isotopic effect versus substituent constants σ^+	123
Figure 3-26. Plot of $\ln k(\text{ClO}_2)$ versus $\ln k(\text{Ir}^{\text{IV}})$	125
Figure 3-27. Plot of $\ln k_{\text{ArOH}}$ versus $\Delta G^\ddagger_{\text{CPET}}$ for phenol oxidation by different oxidants	129
Figure 3-28. Plot of $\ln k_{\text{ArOH}}$ versus $\Delta G^\ddagger_{\text{CPET}}$ for the Ir ^{IV} reduction by different phenols	130
Figure 4-1. Trace of the Ac-Y-NH ₂ reaction and first-order fit.....	135
Figure 4-2. Comparative traces of the Ac-Y-NH ₂ reaction with added Ir ^{III}	136
Figure 4-3. Trace of the Ac-Y-NH ₂ reaction with DNBNS and first-order fit	139
Figure 4-4. Plot of k_{obs} vs $[\text{Ac-Y-NH}_2]_{\text{tot}}$	140
Figure 4-5. Plot of $k_{\text{obs}}/[\text{Ac-Y-NH}_2]_{\text{tot}}$ vs $\text{p}[\text{H}^+]$	141
Figure 4-6. Titration of Ac-Y-NH ₂ with Ir ^{IV} at $\text{p}[\text{H}^+] = 5.5$ and 25 °C	143
Figure 4-7. The titration curve of Ac-Y-NH ₂ solution by Ir ^{IV} solution at $\text{p}[\text{H}^+] = 5.5$...	144
Figure 5-1. ¹ H NMR spectrum of [Os(phen) ₃]Cl ₂ in D ₂ O (aromatic region)	154
Figure 5-2. UV-vis Spectra of [Os(phen) ₃]Cl ₂ and [Os(phen) ₃]Cl ₃	155
Figure 5-3. Kinetic traces of the phenol oxidation by Os ^{III}	157
Figure 5-4. Plot of $t_{1/2}$ vs $1/[\text{Os}^{\text{III}}]_0$	158
Figure 5-5. Kinetic trace of phenol oxidation by Os ^{III} at 550 nm.....	160

Figure 5-6. Plot of k_{obs} vs $[\text{phenol}]_{\text{tot}}^2$	161
Figure 5-7. Plot of $k_{\text{obs}}/[\text{phenol}]_{\text{tot}}^2$ vs $1/[\text{Os}^{\text{II}}]_0^2$	162
Figure 5-8. Plot of $[\text{Os}^{\text{II}}]_0^2 k_{\text{obs}}/[\text{phenol}]_{\text{tot}}^2$ versus $\text{p}[\text{H}^+]$	164
Figure 5-9. Kinetic trace of phenol oxidation by Os^{III} with DBNBS at 480 nm	166

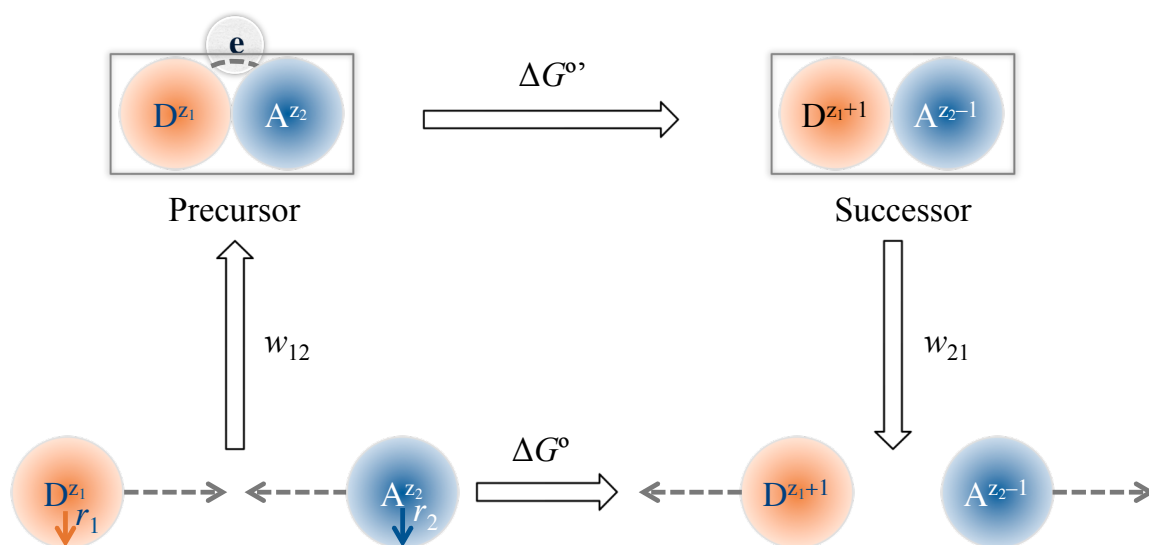
Chapter 1

LITERATURE REVIEW

1.1 Outer-Sphere Electron Transfer

Electron transfer is a fundamental step of many chemical and biological processes, such as photosynthesis, nitrogen fixation and phosphorylation.¹⁻³ The study of electron transfer has been facilitated by technological advances in stopped-flow kinetics, electrochemistry and pulse radiolysis. Electron transfer can be classified as either inner-sphere or outer-sphere. In an inner-sphere electron transfer reaction, the oxidant and reductant connect with each other through a covalent chemical bond, whereas, in an outer-sphere electron transfer reaction, the reactants associate through more indirect interactions. One motivation for the study of outer-sphere electron transfer is that most biological redox is done through this mechanism. Furthermore, the combination of theoretical works of Collision theory and Marcus theory is applied successfully to describe the outer-sphere electron transfer reaction, through which the prediction of the actual rate constants can be achieved. A detailed electron transfer process between D (donor) and A (acceptor) is described in Scheme 1-1.

Collision Theory. The first step in Scheme 1-1 is the diffusion-controlled collision between D and A. In Debye's colliding sphere model, D and A are both treated as spheres with radii r_1 and r_2 , and charges of z_1 and z_2 , respectively. The energy needed to bring the



Scheme 1-1. Electron Transfer Process.

two separated reactants (spheres from an infinite distance) to the closest approach distance (the center-to-center separation distance), $r_{12} = r_1 + r_2$, is known as the electrostatic energy or Coulombic work (w_{12}) as shown in eq 1-1.⁴ This term depends on dielectric medium (dielectric constant D) and the total ionic strength (μ) of the solution.

$$w_{12} = \frac{z_1 z_2 e^2}{D r_{12} (1 + \beta r_{12} \sqrt{\mu})} \quad (1-1)$$

Here, the constant β is the reciprocal Debye radius and e is the electron charge (4.803×10^{-10} esu). Since all of the reactions in this thesis are aqueous, D is set to 78.4. If the distance r is in angstroms and μ in molar, $\beta = 0.328 \text{ \AA}^{1/2}/\text{mol}^{1/2}$ and w_{12} can be simplified to eq 1-2 in kilojoules per mole.

$$w_{12} = \frac{17.7 z_1 z_2}{r_{12}(1 + 0.328 r_{12} \sqrt{\mu})} \quad (1-2)$$

The collision results in the transient formation of “precursor” complex, $[D^{z_1}, A^{z_2}]$, subsequent electron transfer forms the short-lived “successor” complex, $[D^{z_1+1}, A^{z_2-1}]$. The electron transfer details will be explained by Marcus theory in the next part. We define the corrected Gibbs free energy, $\Delta G^{o'}$, as the free energy difference between the successor and precursor. This differs from the standard Gibbs free energy, ΔG^o , which is the energy difference between separated reactants and separated products. This is important because Marcus theory correlates rate constants to $\Delta G^{o'}$ rather than ΔG^o .

The successor complex dissociates to give the final products of the electron transfer, D^{z_1+1} and A^{z_2-1} . The energy associated with this process ($-w_{21}$) is electrostatic energy

$$w_{21} = \frac{17.7 (z_1+1) (z_2-1)}{r_{12}(1 + 0.328 r_{12} \sqrt{\mu})} \quad (1-3)$$

The corrected Gibbs free energy $\Delta G^{o'}$ is related to ΔG^o by eq 1-4.

$$\Delta G^{o'} = \Delta G^o - w_{12} + w_{21} \quad (1-4)$$

The Gibbs free energy, ΔG^o , in eq 1-4 can be calculated according to eq 1-5 using the standard reduction potentials of the oxidant and reductant.

$$\Delta G^\circ = -Z (E_{\text{oxidant}} - E_{\text{reductant}}) F \quad (1-5)$$

Marcus Theory for Electron Transfer. Rudolph A. Marcus was recognized with a Nobel Prize in Chemistry in 1992 for his theoretical description of the outer-sphere electron transfer mechanism. Over the past few decades, Marcus theory has been increasingly applied in the study of chemistry and biology.⁵⁻¹¹ In Marcus theory, the free energy of activation, ΔG^\ddagger , is related to the corrected Gibbs free energy of the reaction, ΔG° , by the quadratic equation 1-6:²

$$\Delta G^\ddagger = w_{12} + \frac{\lambda}{4} \left(1 + \frac{\Delta G^\circ}{\lambda}\right)^2 \quad (1-6)$$

The w_{12} term is the same as that described by eqs 1-1 and 1-2. λ is the energy associated with the outer- and inner-sphere reorganization that accompanies the transition from the precursor to the successor states. For an outer-sphere reaction, the energy barrier is determined by the changes in bond lengths and angles of the donor and acceptor molecules, which is quite small in most cases. However, the energy barrier for reorientation of solvent molecules is a major component due to the different electronic properties and charge distribution between the successor and precursor. ΔG^\ddagger , λ and ΔG° are represented schematically in Figure 1-1.

The potential energy surfaces of electron transfer between the reactants and products are depicted in Figure 1-1. The horizontal axis is the reaction coordinate, which corresponds to the motions of all atomic nuclei. The left parabolic curve R represents the

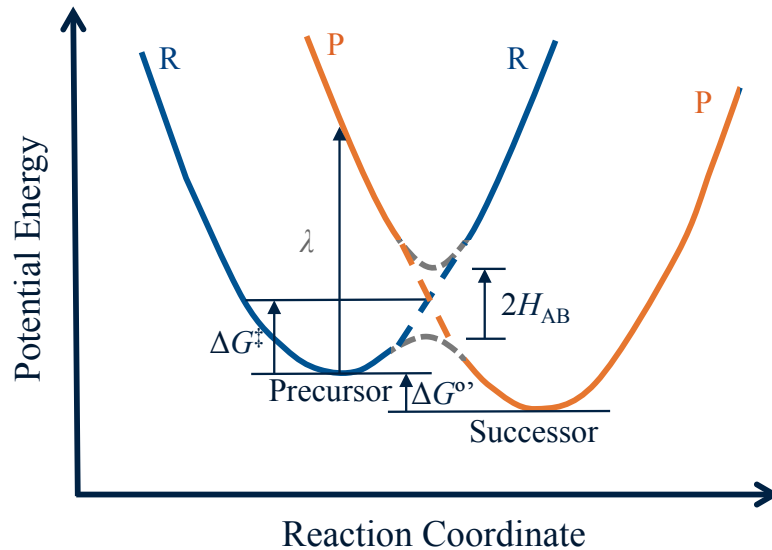


Figure 1-1. Potential energy surfaces for an outer-sphere electron transfer reaction.

potential surface of reactants plus the surrounding medium with the minimum point indicating the nuclear coordinate for an equilibrium configuration of precursor complexes. Whereas, the curve P represents the potential surface of products plus the surrounding medium with the minima denoting the equilibrium nuclear coordinates of successor complexes. The intersection of the two parabolas, the transition state, is the only place where electron transfer can occur while complying with both Franck-Condon principle (that is, electron transfer occurs so rapidly that no change in nuclear coordinates can occur during the transfer) and the first law of thermodynamics (conservation of energy). However, weak electronic interaction between D and A splits the potential energy surfaces, and the orbital mixing generates the resonance energy, which produces the electronic coupling. This can be described by the electronic matrix element, H_{AB} . The energy difference between two minima is the corrected Gibbs free energy of the reaction,

ΔG° . The energy difference between the precursor and the intersection is the free energy of activation, ΔG^\ddagger , which is related to electron transfer rate constant, k_{et} , through the Eyring equation 1-7.

$$k_{et} = \kappa Z \exp(-\Delta G^\ddagger/RT) \quad (1-7)$$

Here, Z is the collision frequency and reported to be $10^{11} \text{ M}^{-1} \text{ s}^{-1}$. κ is the transmission coefficient, which represents the probability of electron transfer per passage. κ is large (= 1) for an adiabatic reaction where the change of nuclear coordinates is sufficiently slow when passing the intersection and the system stays at equilibrium. However, when the jumping occurs with a high passing velocity through the intersection, or when the splitting of the potential surface is small due to weak electronic interaction, the probability κ of going from the precursor to the successor surface is very small ($\kappa \ll 1$), and this process is defined as nonadiabatic.

Marcus Cross Relation (MCR). The reorganization energy, λ , can be obtained from the two relative self-exchange reactions 1-8 and 1-9.



k_{11} and λ_{11} correspond to the reaction between oxidized and reduced forms of the electron donor D and k_{22} and λ_{22} belong to the reaction between oxidized and reduced forms of

electron acceptor A. For both reactions 1-9 and 1-10, $\Delta G^{\circ} = 0$ and according to eq 1-6, $\Delta G^{\ddagger} = w + \lambda/4$. An assumption (eq 1-11)¹² used to derive the MCR (eqs 1-12 to 1-15)² is that the reorganization energy for the cross-reaction (eq 1-10), λ_{12} , is equal to the average of λ_{11} and λ_{22} .

$$\lambda_{12} = \frac{\lambda_{11} + \lambda_{22}}{2} \quad (1-11)$$

$$k_{12} = (k_{11}k_{22}K_{12}f_{12})^{1/2}W_{12} \quad (1-12)$$

$$\ln f_{12} = \frac{[\ln K_{12} + (w_{12} - w_{21}) / RT]^2}{4[\ln(k_{11}k_{22} / Z^2) + (w_{11} + w_{22}) / RT]} \quad (1-13)$$

$$W_{12} = \exp[(-w_{12} - w_{21} + w_{11} + w_{22})/2RT] \quad (1-14)$$

$$w_{ij} = \frac{17.7 z_i z_j}{r_{ij}(1 + 0.328r_{ij}\sqrt{\mu})} \quad (1-15)$$

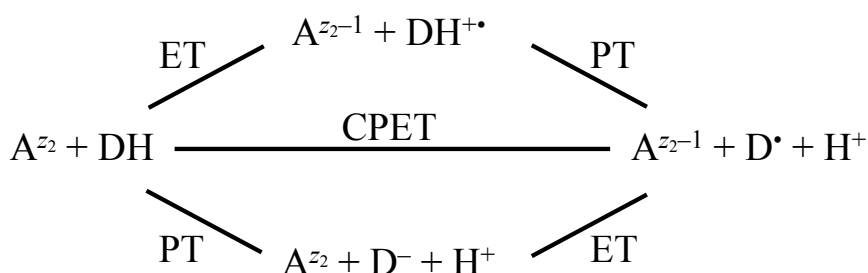
As noted above, Z is the collision frequency ($10^{11} \text{ M}^{-1} \text{ s}^{-1}$), w_{11} , w_{22} , w_{12} and w_{21} correspond to Coulombic works. K_{12} is the equilibrium constant. W_{12} and f_{12} are adjustable factors that depend on the ionic strength, reaction media, radii and charges of reactants.

1.2 Proton-Coupled Electron-Transfer (PCET)

In 1959 Halpern proposed that the oxidation of formate by permanganate in acidic solutions might undergo electron transfer coupled with proton transfer.¹³ The coupling of electron and proton through in phosphorylation was recognized two years later by

Mitchell.¹⁴ PCET has subsequently been studied extensively through theoretical and experimental means.¹⁵⁻²⁴

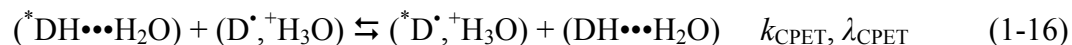
In redox reactions involving weak acids and bases, deprotonation can occur with electron transfer. When one or more protons and electrons are transferred, two fundamental mechanisms are most frequently proposed: sequential and concerted PCET. Three possible pathways are considered for transferring one electron and one proton, as shown in Scheme 1-2: Electron transfer followed by proton transfer (ET/PT), proton transfer prior to electron transfer (PT/ET) and concerted PCET (CPET) mechanism (protons and electrons are transferred simultaneously).



Scheme 1-2. PCET pathways.

Here, DH is the electron and proton donor and A is the electron acceptor. CPET may occur in acidic media where high H^+ concentrations limit the deprotonation of DH, and consequently PT/ET pathway.

Marcus Theory for H₂O-CPET. In aqueous solution, the solvent water serves as the proton acceptor in CPET.²⁵⁻²⁷ The self-exchange CPET reaction is described in eq 1-16, with λ_{CPET} as the self-exchange reorganization energy.



Here, “ \cdots ” represents hydrogen bonds between DH (for example, phenol) and H_2O .²⁸

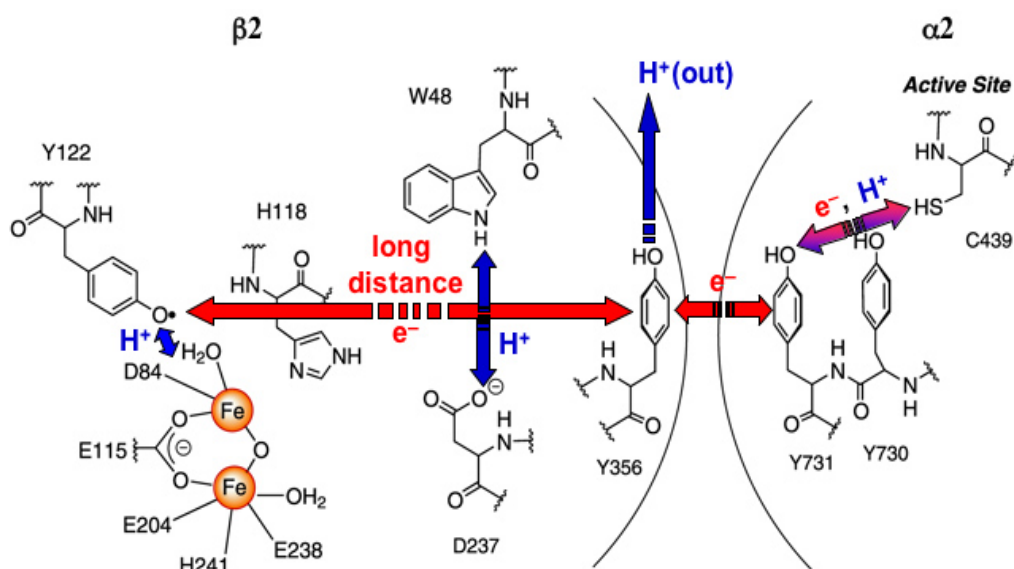
Combined with the self-exchange reaction of the oxidant (1-9), the total reorganization energy can be calculated by $\lambda = (\lambda_{\text{CPET}} + \lambda_{22})/2$.²⁶

1.3 Oxidation of Phenols

Since they were first isolated from coal tar by Runge in 1834,²⁹ phenol and its derivatives have been widely found in nature, for example, serving as components in many antibiotics, colorants, flavonoids, neurotransmitters and hormones.³⁰⁻³⁴ Other phenols are medicinally and industrially vital.³⁵⁻³⁷ Tyrosine, one of the 22 proteinogenic amino acids, contains a phenol side chain which is essential for its biological functions; In a phosphorylation process, for example, tyrosine residues are tagged with phosphate groups and act as receptors in signal transduction.³⁸ Tyrosine sulfation is another process where a sulfate group is added to tyrosine residues, through which the protein-protein interactions are strengthened.³⁹

One important function of tyrosine is that it serves as an electron donor in photosystem II, reducing the oxidized chlorophyll.^{40,41} In photosynthesis, the photons of sunlight are absorbed by chlorophyll A in photosystem II and excite P_{680} to the excited state, P_{680}^+ . During the excitation process, electrons are released and passed through a redox reaction to pheophytin, then subsequently to plastoquinone, where protons are transferred to the corresponding quinol. Eventually electrons are transferred to photosystem I where NADP is reduced to NADPH. The excited P_{680}^+ is a strong

orthogonal PCET through which the electron and proton are transferred to different acceptors.^{18,44-46} Scheme 1-4 shows the PCET in Class I RNRs.



Scheme 1-4. The electron and proton flow in Class I RNRs. Obtained from <http://web.mit.edu/biochemistry/research.htm> on September 2011.

One-electron oxidation of phenols in aqueous media is currently of intense interest due to the abovementioned biochemical systems. The structural constraints of these systems enforce long-distance electron transfer and outer-sphere mechanisms. The current consensus is that these reactions are subject to general base catalysis.^{47, 48} However, the pH dependence when water is the proton acceptor remains enigmatic: there is general agreement that the reactions are pH-independent at high acidity, increase in rate with increasing pH, and reach a limiting rate at high pH, but some reports indicate an approximate inverse half-order dependence on $[H^+]$ in the intermediate pH region,^{49, 50} while others support an inverse first-order dependence.^{51, 52} The half-order dependence

has led to the controversial proposal of a pH-dependent driving force.^{49, 50} The question of whether the reactions in acidic media (pH 1–3) operate through a sequential or concerted PCET mechanism is unresolved.

One approach to gaining insight into PCET is to study reactions in which one of the reactants is a typical inorganic outer-sphere electron-transfer reagent with no acid/base properties: this constraint confines much of the electron-proton coupling considerations to the other reaction partner. The transition metal complexes, such as $[\text{IrCl}_6]^{2-}$ and $[\text{Os}(\text{phen})_3]^{3+}$, have proven to be valuable outer-sphere electron-transfer oxidants.⁵³⁻⁶⁰

In Chapter 2, we present kinetic data on the oxidation of phenol and the four coupling products (4,4'-/2,2'-/2,4'-biphenol and 4-phenoxyphenol) by $[\text{IrCl}_6]^{2-}$, obtained under conditions where buffer catalysis is insignificant. These data support an inverse first-order dependence on $[\text{H}^+]$ near neutral pH, a concerted PCET mechanism at low pH, and a degree of overoxidation that is pH-dependent. The oxidation of phenol by Ir^{IV} was the subject of a classic study by Cecil and Littler 40 years ago.⁵¹ That paper showed that the reaction yields Ir^{III} and a variety of phenolic oxidation products and that it has a simple two-term rate law (described in the following chapter). Limitations of the study by Cecil and Littler included the inability to exclude completely the effects of Ir^{III} , the instrumental restriction to measuring relatively slow rates, the unknown driving forces for the rate-limiting steps, the unknown rate of self-reaction of the phenoxy radicals, the unknown $\text{p}K_{\text{a}}$ of ArOH^{*+} , and uncertainty as to whether the acid pathway (k_{ArOH}) was a sequential process of electron transfer to form ArOH^{*+} followed by its deprotonation or whether it was a concerted PCET process. Here we use DNBNS as a phenoxy radical scavenger to eliminate the kinetic effects of Ir^{III} , we use stopped-flow methods to obtain

kinetic data under conditions where the rates are much faster, we use numerical modeling and the now-known properties of the phenoxy radicals to confirm the basic mechanism, and we use kinetic isotope effects (KIEs) to probe the concertedness of the ArOH oxidation pathway.

Chapter 3 extends the studies of oxidation by Ir^{IV} to alkyl- and alkoxy-substituted phenols (2-methylphenol, 2,6-dimethylphenol, 2,4,6-trimethylphenol, 4-*tert*-butylphenol and 4-methoxyphenol). The reaction of 2,4,6-trimethylphenol yields 4-hydroxymethyl-2,6-dimethylphenol rather than the coupling products obtained from phenol. Apparently the 2,4,6-trimethylphenoxy radical disproportionates with oxidation at the 4-methyl position, which eliminates the overoxidation process and gives an excellent inverse first-order dependence on [H⁺] near neutral pH. Marcus theory is applied to explain both electron transfer and H₂O-CPET processes.

Chapter 4 describes the oxidation of one of the tyrosine derivatives, *N*-acetyl-tyrosine amide, by Ir^{IV}. Overoxidation is observed and the values of k_{ArOH} and k_{ArO^-} are obtained by fitting the data to a two-term rate law.

The oxidation of phenol by tris-(1,10-phenanthroline)osmium(III) is presented in Chapter 5. Analysis of the kinetic data yields a second-order dependence on [Os(phen)₃]³⁺ and phenol, and an inverse second-order dependence on [Os(phen)₃]²⁺ and H⁺.

Chapter 2

PROTON-COUPLED ELECTRON-TRANSFER OXIDATION OF PHENOL BY HEXACHLOROIRIDATE(IV)

This Chapter is based on the following papers and reprints were made with permission from America Chemical Society.

(a) Song, N.; Stanbury, D. M. *Inorg. Chem.* **2008**, *47*, 11458.

(b) Song, N.; Stanbury, D. M. *Inorg. Chem.*, DOI: 10.1021/ic201897m.

2.1 Introduction

Redox reactions in aqueous solution are often accompanied by changes in protonation. When the reactions proceed via one-electron steps the phenomenon of proton-coupled electron transfer (PCET) is often involved. The breadth of importance of PCET is immense, and PCET is of great significance because it is often an absolute criterion of reactivity.²³ One approach to gaining insight into PCET is to study reactions where one of the reactants is a typical inorganic outer-sphere electron-transfer reagent with no acid/base properties: this constraint confines much of the electron-proton coupling considerations to the other reaction partner. Oxidation of phenols has become central in developing the concepts of PCET, in part because of its importance in revealing the function of tyrosine in redox proteins, but also because these reactions are quite amenable to study. Accordingly, the oxidation of phenol by $[\text{IrCl}_6]^{2-}$ has been the focus of a classic publication,⁵¹ and it is now of interest as a model for reactions where electron

transfer occurs in concert with proton transfer to the solvent: H₂O-CPET.²⁵⁻²⁷

Despite its importance, the oxidation of phenol by [IrCl₆]²⁻ presents certain difficulties. One of these is that the phenolic products are a complex mixture,⁵¹ and it is unclear how the post-rate-limiting steps lead to this mixture. It is also unclear whether these latter stages in the reaction have any influence on the measurements of the putative rate-limiting steps. Of further concern is the pH dependence of the rates, which displays deviations from the classic two-term rate law for such reactions²⁷ and might provide additional evidence in support of a pH-dependent rate constant as has been reported previously for the oxidation of phenol by [Ru(bpy)₃]³⁺.⁵⁰ Herein is reported a study on the [IrCl₆]²⁻ oxidations of the four major products derived from coupling of the phenoxy radical. These rates are then incorporated into an overall mechanism for the oxidation of phenol, which shows that overoxidation is responsible for many of the reaction products. Moreover, it is shown that the degree of overoxidation is pH-dependent and that this can account for the observed deviations from the classical two-term rate law.

2.2 Experimental Section

2.2.1 Reagents and Solutions

All commercial chemical reagents were used as received except as noted. Ammonium hexachloroiridate(III) monohydrate (Ir^{III}), 2,6-dimethylacetanilide, chlorosulfonic acid, 3-chloroperoxybenzoic acid, disodium, *N-tert*-butyl-phenyl-nitrone (PBN), α -(4-pyridyl-*N*-oxide)-*N-tert*-butylnitrone (POBN), 2-methyl-2-nitrosopropane (MNP), 5,5-dimethyl-1-pyrroline *N*-oxide (DMPO), deuterium oxide, 3,5-dibromosulfanilic acid sodium salt, 2-iodophenol, 4-hydroxyphenylboronic acid,

palladium(II) acetate, 1,1'-bis(diphenylphosphino)-ferrocene (dppf), potassium carbonate, sodium acetate anhydrous, cacodylic acid and sodium hydroxide were purchased from Sigma-Aldrich Chemicals Co. Perchloric acid, ammonium perchlorate, sodium chloride, ammonium chloride, copper(II) nitrate trihydrate, acetic acid, monochloroacetic acid, ethanol, diethyl ether, 1,4-dioxane, petroleum ether, ethyl acetate, acetonitrile, hydrochloric acid and hydrogen peroxide were from Fisher Scientific Co. 2,2'-Biphenol, 4,4'-biphenol and 4-phenoxyphenol are commercially available from Acros Organics. Ammonium hexachloroiridate(IV) (Ir^{IV}) was purchased from Alfa or prepared according to the literature⁶¹ by the addition of ammonium chloride (Fisher) to a solution of sodium hexachloroiridate(IV) hexahydrate. Phenol (Fluka) was recrystallized from a 75% weight/weight water solution as described in the literature.⁶²

All solutions were freshly prepared with deionized water provided by a Barnstead NANO Pure Infinity ultrapure water system, and purged with argon gas prior to the reactions to prevent potential complications caused by O_2 . In order to increase the concentration of the solution, 4,4'-biphenol or 2,4'-biphenol was first dissolved in CH_3CN or ethanol and then diluted with water to make a reaction solution where less than 1% w/w organic solvent was present. The ionic strength was adjusted by lithium perchlorate trihydrate (GFS) and was approximately equal in both oxidants and reductants solutions to prevent Schlieren effects (or refractive index effect⁶³). Selected buffer solutions (acetate, monochloroacetate, and cacodylate buffers) were applied to control the pH if necessary.

Preparation of Sodium 3,5-Dibromo-4-nitrosobenzenesulfonate (DBNBS). This compound was synthesized from 3,5-dibromosulfanilic acid sodium salt according to the

method of Kaur et al.⁶⁴ and further purified using procedure type C of Hamilton et al..⁶⁵ A mixture of 3,5-dibromosulfanilic acid (10 mmol), anhydrous sodium acetate (10 mmol), 7.9 mL of a 30% aqueous hydrogen peroxide solution and 30 mL of glacial acetic acid was warmed gently to dissolve the solid. The solution was stored at room temperature for 14 days. Then the crude yellow solid product was collected and washed with glacial acetic acid, cold ethanol, diethyl ether/1,4-dioxane (1:1), and cold ethanol again. A pale-yellow powder was obtained after drying. Yield: 30%. Mp: > 300 °C. ¹H NMR (D₂O): δ 8.30 (s, 2H). ¹³C NMR (D₂O): δ 119.10 (aryl-CBr), 131.03 (aryl-CH), 141.00 (aryl-CSO₃Na), 147.61 (aryl-CNO).

Preparation of Sodium 2,4-Dimethyl-3-nitrosobenzene Sulfonate (DMNBS).

This compound was prepared according to the literature.^{66,67} The 2,6-dimethylacetanilide (18 mmol) was added into 10 mL of cold ClSO₃H with stirring. After reacting for 15 min at 5 °C, 1h at 25 °C and 10 min at 40 °C, the mixture was poured onto cracked ice to form a white solid of sulfonyl chloride. Then this compound was treated with concentrated HCl under reflux for 1 h before neutralization by NaOH to produce sodium 2,6-dimethylaniline-3-sulfonate. Sodium sulfonate (10 mmol) was dissolved in 30 mL of methanol and oxidized by *m*-chloroperoxybenzoic acid (10 mmol) with stirring for 1 h at room temperature. Then ether was added to precipitate the final product. Yield: 80%. ¹H NMR (D₂O): δ 2.56 (s, 3H), 2.75 (s, 3H), 7.54 (d, 1H), 8.13 (d, 1H).

Preparation of 2,4'-Biphenol. 2,4'-Biphenol was prepared through a previously described Pd-catalyzed Suzuki-Miyaura coupling reaction.⁶⁸ Under dry nitrogen, 4-hydroxyphenylboronic acid (1.4 mmol), Pd(OAc)₂ (0.14 mmol), bis(diphenylphosphino)-ferrocene (dppf) (0.14 mmol), and K₂CO₃ (3 mmol) were added to a solution of 2-

iodophenol (1 mmol) in 10 mL THF. The reaction was stirred under reflux for 1 day and monitored by thin-layer chromatography. After the reaction was completed, the crude product was purified by column chromatography on silica gel (eluent PE/EtOAc = 3.5/1). Then, sublimation was performed under vacuum at 160 °C to remove the non-volatile metal residue impurities, and resublimation was carried out at 110 °C to remove the volatile impurities. Yield: 50%. Mp: 161.2–162.8 °C. ¹H NMR (CDCl₃) (Figure 2-1): δ 4.89 (s, 1H), 5.14 (s, 1H), 6.94–6.99 (m, 4H), 7.20–7.24 (m, 2H), 7.34–7.36 (m, 2H).

2.2.2 Methods

A Corning 450 pH/ion meter was used with a Mettler Toledo InLab 421 or InLab Semi-Micro-L combination pH electrode. The reference electrode electrolyte was replaced with 3 M NaCl to prevent the precipitate of KClO₄. Electrode calibrations at $\mu = 0.1$ M (LiClO₄) were carried out with 0.01–0.1 M perchloric acid. With the known H⁺ concentration and pH reading, the activity coefficient $\gamma (= 0.839 \pm 0.04)$ was obtained from equation $p[H^+] = \text{pH} + \log \gamma$, where $p[H^+]$ is equal to $-\log [H^+]$. When the pK_a of 4,4'/2,4'-biphenol is measured, an alkaline error may occur with a pH value higher than 11. Thus, we calibrated the electrode with 1×10^{-3} M NaOH at $\mu = 0.1$ M (LiClO₄) and found that the true pH is equal to the apparent pH plus 0.3.

All measurements were performed at 25.0 ± 0.1 °C. The kinetics experiments were carried out on a Hi-Tech SF-51 stopped-flow spectrophotometer with OLIS 4300 data acquisition and analysis software. UV-vis spectra were monitored on a HP-8453 diode-array spectrophotometer equipped with a Brinkman Lauda RM6 thermostatted water bath to maintain the temperature at 25 °C, and the solutions were prepared in a 1.0 cm quartz cells. Because (NH₄)₂[IrCl₆] has strong absorbance around 488 nm while the

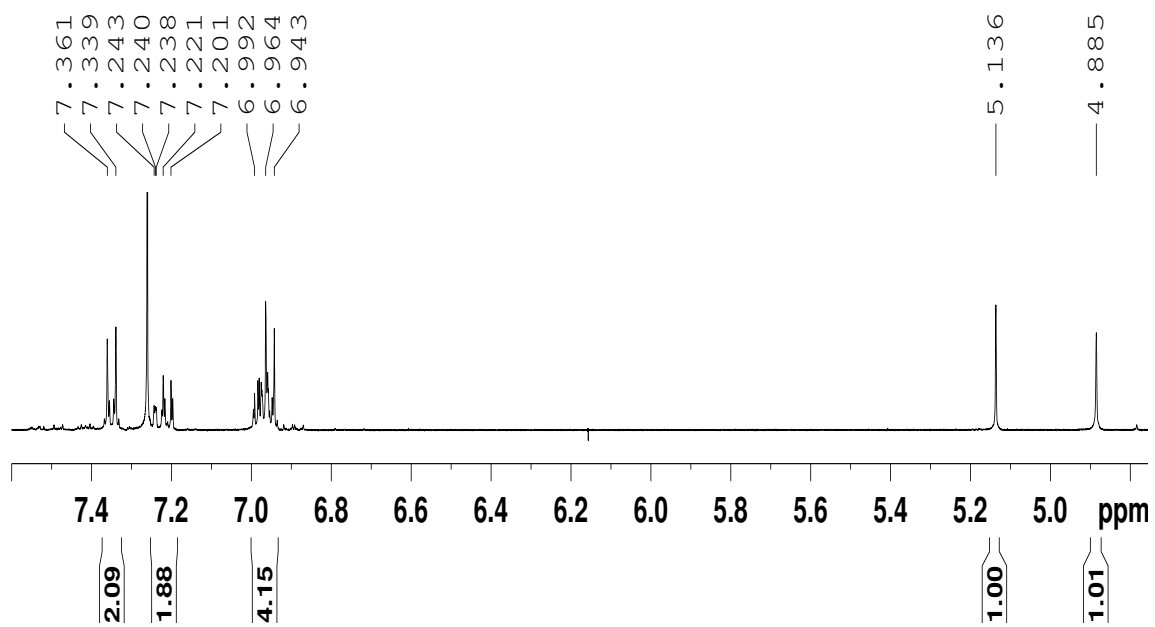


Figure 2-1. ^1H NMR spectrum of 2,4'-biphenol in CDCl_3 . This spectrum matches the previously reported results.⁶⁹

corresponding product $(\text{NH}_4)_3[\text{IrCl}_6]$ does not, as shown in Figure 2-2, all kinetics data were obtained by monitoring the absorbance of Ir^{IV} at λ_{max} (488 nm) with $\epsilon_{488} = (3.9 \pm 0.1) \times 10^3 \text{ M}^{-1} \text{ cm}^{-1}$.⁵⁵ In order to detect the DBNBS influence on the reactions of phenol, we also observed the absorbance change over the wavelength 400–525 nm at intervals of 25 nm. For the phenol and 4-phenoxyphenol reactions, the observed pseudo-first-order rate constants were obtained from the fitting of kinetic traces over 5 half-lives to first-order exponential functions. For 4,4'-biphenol and 2,2'-biphenol the observed initial rate constants were determined from the slope of the linear regression of logarithm of absorbance at 488 nm within the first half-life, while for 2,4'-biphenol the rate constants were obtained from double-exponential fits. The *Specfit/32* version 3.0.15 global analysis system was applied to simulate the reaction traces, and the *GraphPad Prism 4 or 5* software was used to analyze the rate law with $1/Y^2$ weighting. Each reported observed rate constant k_{obs} is the average of at least five individual shots. The average k_{obs} values are fit to rate law in *Prism*, and therefore, the reported uncertainties reflect the scatter of k_{obs} .

^1H and ^{13}C NMR spectra were acquired on a Bruker AV 400 MHz spectrometer; chemical shifts in CDCl_3 are relative to TMS and in D_2O are relative to DSS. The melting points were obtained using an Electrothermal IA 9100 digital melting point apparatus. Cyclic voltammograms (CV) and Osteryoung square-wave voltammograms (OSWV) were performed on a BAS 100B electrochemical analyzer equipped with a BAS C3 cell stand and a purging and stirring system; a glassy carbon electrode acts as the working electrode, Ag/AgCl (3.0 M NaCl) is the reference electrode ($E^\circ = 0.205 \text{ V}$ vs NHE),⁵⁵ and a Pt wire is used as the auxiliary electrode.

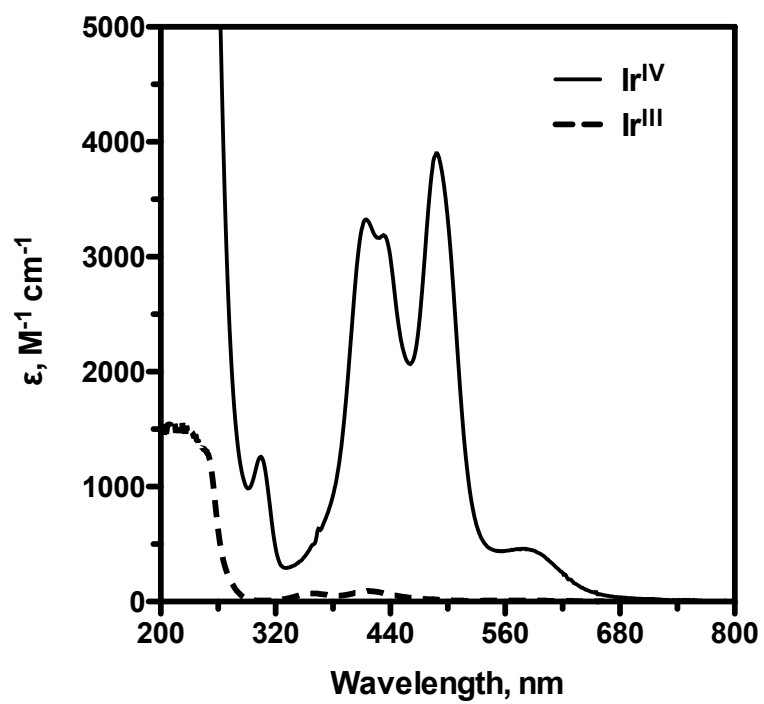


Figure 2-2. UV-vis spectra of $(\text{NH}_4)_2[\text{IrCl}_6]$ (solid line) and $(\text{NH}_4)_3[\text{IrCl}_6]$ (dashed line) in aqueous solution. $T = 25^\circ \text{C}$.

Quantum calculations of electronic spectra were performed with the *Spartan 08* software package.⁷⁰

2.3 Results

The kinetics traces for the consumption of 1×10^{-4} M Ir^{IV} in its reaction with a large excess of phenol were obtained at various p[H⁺] at 488 nm. Figure 2-3a exhibits a typical kinetic trace for a reaction with 0.44 M phenol in 0.05 M HClO₄ (p[H⁺] = 1.3). Such kinetic traces do not give good fits with either first- or second-order rate laws. As the p[H⁺] increases, good-quality pseudo-first-order fits are obtained at both p[H⁺] = 2.9 and 4.8 with 0.044 M phenol (Figure 2-3b and Figure 2-3c). At high p[H⁺] (= 7.1), the reaction with 1.8×10^{-3} M phenol is much faster and becomes non-pseudo-first-order again (Figure 2-3d). These results show a strong p[H⁺] effect on phenol oxidation by Ir^{IV}. As shown below, the deviations at low pH arise from inhibition by Ir^{III}, while the deviations at high pH are due to the absorbance of phenolic products.

2.3.1 Oxidation of Phenol

2.3.1.1 Hexachloroiridate(III) Effects

Kinetic Inhibition by Ir^{III}. At p[H⁺] = 1.3, Figure 2-4a shows the effects of adding 5-fold excess of Ir^{III} under conditions otherwise identical with those in Figure 2-3a. The retarding effect of Ir^{III} at this pH is seen to be quite strong and clearly can be expected to cause deviations from pseudo-first-order kinetics of the type shown in Figure 2-3a. On the other hand, at p[H⁺] = 7.1, no Ir^{III} inhibition is observed with the addition of 5- and 10-fold excess of Ir^{III} (Figure 2-4b, c), and so the deviations from pseudo-first order

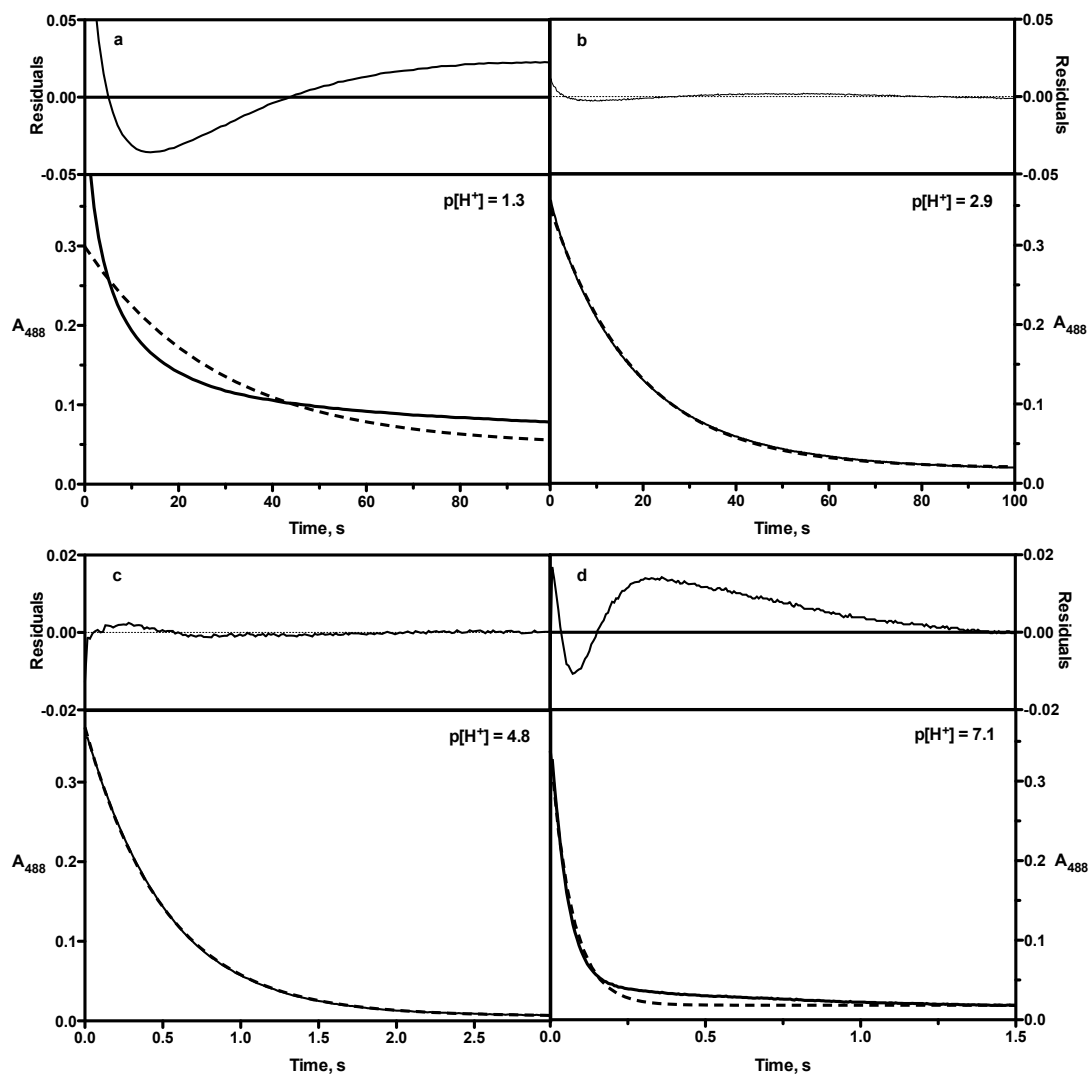


Figure 2-3. Kinetic traces of oxidation of phenol by 1×10^{-4} M of Ir^{IV} at different $\text{p}[\text{H}^+]$. Lower boxes show the experimental traces (solid lines) and the pseudo-first-order fits (dashed lines). Upper boxes show the residuals in the fits. $\mu = 0.1$ M (LiClO_4); $T = 25$ °C. (a) $[\text{Phenol}]_{\text{tot}} = 0.44$ M; $[\text{HClO}_4] = 0.05$ M. (b) $[\text{Phenol}]_{\text{tot}} = 0.044$ M; $\text{p}[\text{H}^+] = 2.9$ (0.02 M monochloroacetate buffer). (c) $[\text{Phenol}]_{\text{tot}} = 0.044$ M; $\text{p}[\text{H}^+] = 4.8$ (0.02 M acetate buffer). (d) $[\text{Phenol}]_{\text{tot}} = 1.8 \times 10^{-3}$ M; $\text{p}[\text{H}^+] = 7.1$ (0.02 M cacodylate buffer).

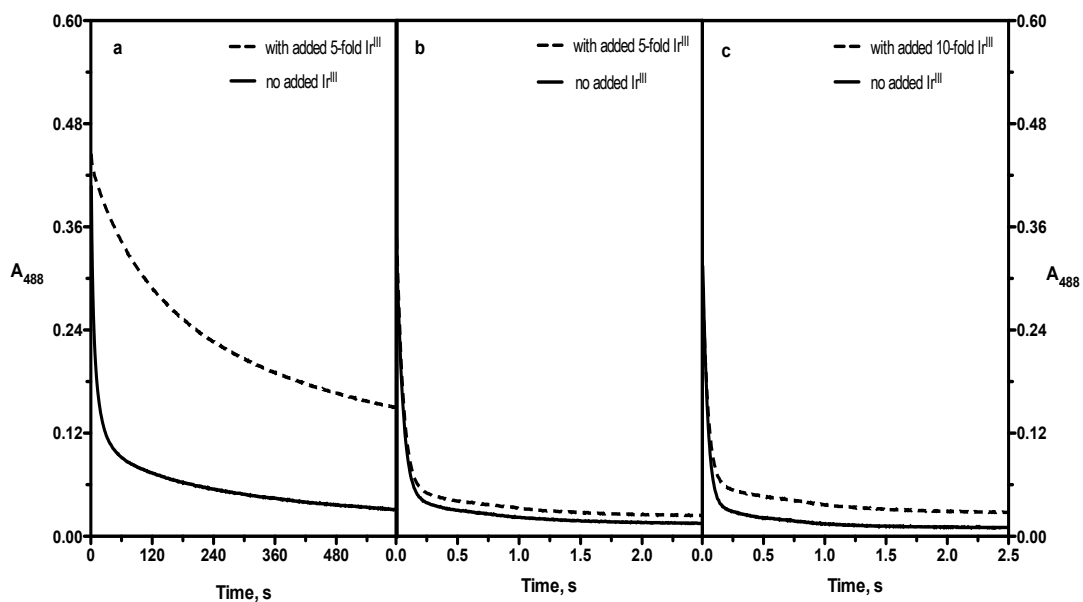


Figure 2-4. Comparative traces of the phenol reaction with added Ir^{III} (dashed line) and no added Ir^{III} (solid line) in H_2O . $[\text{Ir}^{\text{IV}}]_0 = 1 \times 10^{-4} \text{ M}$; $\mu = 0.1 \text{ M}$ (LiClO_4); $T = 25 \text{ }^\circ\text{C}$. (a) $[\text{Phenol}]_{\text{tot}} = 0.44 \text{ M}$; $[\text{Ir}^{\text{III}}] = 5 \times 10^{-4} \text{ M}$; $[\text{HClO}_4] = 0.05 \text{ M}$. (b) $[\text{Phenol}]_{\text{tot}} = 1.8 \times 10^{-3} \text{ M}$; $[\text{Ir}^{\text{III}}] = 5 \times 10^{-4} \text{ M}$; $\text{p}[\text{H}^+] = 7.1$ (0.02 M cacodylate buffer). (c) $[\text{Phenol}]_{\text{tot}} = 1.8 \times 10^{-3} \text{ M}$; $[\text{Ir}^{\text{III}}] = 1 \times 10^{-3} \text{ M}$; $\text{p}[\text{H}^+] = 7.1$ (0.02 M cacodylate buffer).

kinetics at this pH (Figure 2-3d) are due to factors other than inhibition by Ir^{III}.

Basicity of Ir^{III}. The basicity of Ir^{III} was probed by measuring the pH dependency of the cyclic voltammetry of 1×10^{-3} M of Ir^{IV} in the p[H⁺] range of 0–2 at 1 M ionic strength (LiClO₄). p[H⁺] values were adjusted by HClO₄ according to $p[H^+] = -\log [HClO_4]$. Reversible CVs ($E_{1/2} = 0.717 \pm 0.007$ V vs Ag/AgCl) were obtained over this pH range. No pH dependence of $E_{1/2}$ was observed under all of these conditions, which implies that Ir^{III} is not significantly basic even in 1 M H⁺. Bruhn et al. observed a small but significant dependence of $E_{1/2}$ over this same pH range in H⁺/Na⁺ media;⁷¹ we attribute this effect to the differing specific interaction coefficients of these two ions.

2.3.1.2 General Base Catalytic Test.

Tests for general base catalysis were performed as follows:

First, for the phenol reaction at p[H⁺] = 6.5 (shown in Table 2-1), the cacodylate buffer concentration was varied from 2 to 20 mM, and after correction for pH fluctuations, no significant corresponding rate variation was detected.

Table 2-1. Kinetic Dependence on Concentration of Buffer. ^a

[buffer] × 10 ⁻³ , M	($k_{\text{obs}}/[\text{phenol}]_{\text{tot}} \times 10^{-3}$, M ⁻¹ s ⁻¹)	p[H ⁺]
2.0	2.31	6.44
4.0	2.72	6.49
20	3.12	6.57

^a All the reactions were run under pseudo-first-order conditions. $[Ir^{IV}]_0 = 1 \times 10^{-4}$ M; $[\text{phenol}]_{\text{tot}} = 4.4 \times 10^{-3}$ M; $\mu = 0.1$ M (LiClO₄); The p[H⁺] values were maintained using cacodylate buffers; $T = 25$ °C.

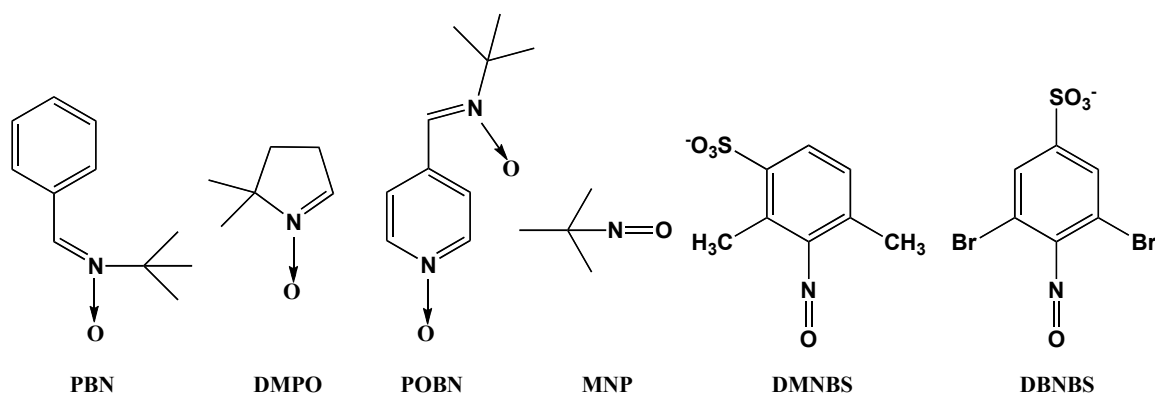
Second, tests were also performed on the reaction between 1.8×10^{-3} M of phenol and 1×10^{-4} M of $(\text{NH}_4)_2\text{IrCl}_6$ at $\text{p}[\text{H}^+] = 7$ (0.02 M cacodylate buffer) at 0.1 M ionic strength (LiClO_4). The concentration of ammonium was varied from 0.2 to 0.7 mM because the oxidant used was $(\text{NH}_4)_2[\text{IrCl}_6]$; no kinetic effect was detected.

Third, if phenol itself were a catalyst, then a second-order dependence on $[\text{phenol}]$ would be expected, contrary to our observations as described below.

In summary, these results show that the kinetic data presented herein on phenol oxidation by Ir^{IV} are free of complications arising from general base catalysis. This conclusion is in agreement with the recent report from Irebo et al. and Bonin et al. that general base catalysis in outer-sphere phenol oxidation can be insignificant under certain conditions.^{26,48,72}

2.3.1.3 Spin Trapping Effect

Several conventional spin traps^{67,73-79} (illustrated in Scheme 2-1) were investigated for their effects on the kinetics of the phenol/ Ir^{IV} reaction in 0.05 M H^+ .



Scheme 2-1. Structure of spin trapping agents tested.

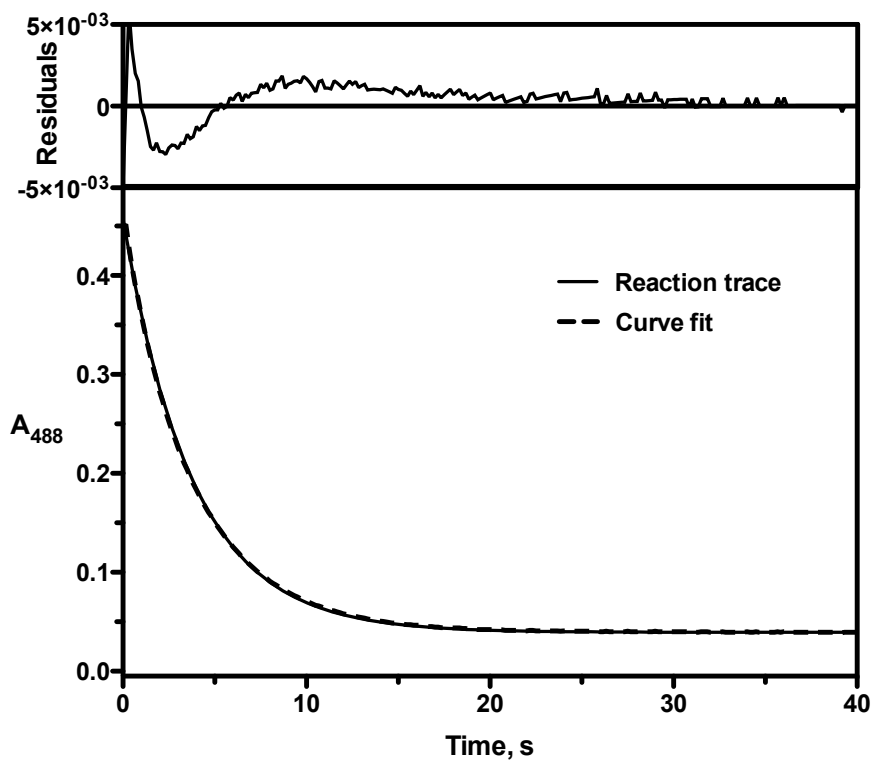


Figure 2-5. Trace of the phenol reaction with added DNBBS. Lower box shows the experimental trace (solid line) and the pseudo-first-order fit (dashed line). Upper box shows the residuals in the fit. $[\text{Ir}^{\text{IV}}]_0 = 1 \times 10^{-4} \text{ M}$; $[\text{phenol}]_{\text{tot}} = 0.44 \text{ M}$; $[\text{DNBNS}] = 10 \text{ mM}$; $[\text{HClO}_4] = 0.05 \text{ M}$; $\mu = 0.1 \text{ M (LiClO}_4)$; $T = 25 \text{ }^\circ\text{C}$.

We found DNBNS is quite effective in this regard. Figure 2-5 illustrates the dramatically improved fit to a first-order rate law achieved with only 10 mM DNBNS. The other spin traps PBN, DMPO, POBN, and MNP barely affect the reaction, and DMNBS is only partially effective (Table 2-2).

Table 2-2. Kinetic Data for the Reaction of Phenol with Ir^{IV} in the Presence of PBN, DMPO, POBN, MNP, DMNBS and DNBNS.^a

Spin Trapping Agent	t _{1/2} , s	SD ^b
No Spin Trapping Agent	8.0	0.016 ^c
1 mM PBN	8.0	0.011 ^c
1 mM DMPO	8.0	0.016 ^c
2 mM POBN	8.0	0.012 ^c
4 mM MNP	8.0	0.006 ^c
2 mM DMNBS	6.0	0.011 ^c
1 mM DNBNS	4.4	0.004

^a [Ir^{IV}]₀ = 1 × 10⁻⁴ M; [phenol]_{tot} = 0.44 M; [HClO₄] = 0.05 M; μ = 0.1 M (LiClO₄); T =

25 °C. ^b SD = standard deviation of curve fit residuals over the first 4 half lives. ^c

Successive half lives increase progressively.

These results are not unexpected, given the known specificity of DNBNS for phenoxy radicals.⁷⁹ Tests in 0.05 M H⁺ with concentrations of DNBNS ranging from 0.1 to 15 mM (Table 2-3) show that the effects saturate at about 5 mM DNBNS. A standard DNBNS concentration of 10 mM is used in the experiments described below. The approach to

Table 2-3. Kinetic Data for the Reaction of Phenol with Ir^{IV} in the Presence of DBNBS.^a

[DBNBS] × 10 ³ , M	t _{1/2} , s	Residuals ^b
0	8.0	0.05
0.10	6.7	0.03
1.0	4.4	0.02
5.0	2.7	0.008
10	2.7	0.006
15	2.5	0.006

^a [Ir^{IV}]₀ = 1 × 10⁻⁴ M; [phenol]_{tot} = 0.443 M; [HClO₄] = 0.05 M; μ = 0.1 M (LiClO₄); T = 25 °C. ^b Maximum residuals of the first-order fits over the first five half-lives.

saturation is expected to be dependent on both the efficiency of phenoxy radical scavenging and the DBNBS dimerization equilibrium ($K = 1.3 \times 10^{-3}$ M).⁸⁰

The effects of DBNBS are also significant at p[H⁺] 7. The results (Table 2-4) show that DBNBS removes the deviations from pseudo-first-order kinetics that are otherwise seen at this pH. The effect is attributed to DBNBS interception of phenoxy radicals, the dimerization of which would lead to absorbing intermediates (biphenoxinones), as shown below.

2.3.1.4 Phenol Dependence

In the presence of 10 mM DBNBS, the oxidations of phenol by Ir^{IV} in 0.05 M HClO₄ were carried out with phenol concentration (22.2–443) × 10⁻³ M under pseudo-first-order conditions. Another set of experiments was also performed at p[H⁺] = 5.1 in

Table 2-4. Kinetic Dependence of Phenol Oxidation on DBNBS at High p[H⁺].^a

p[H ⁺]	[DBNBS] × 10 ³ , M	k _{obs} , s ⁻¹	STDV ^b
7.11	0	22.4	6.73 × 10 ⁻³
7.09	5.0	23.2	1.23 × 10 ⁻³
6.94	10	17.3	5.49 × 10 ⁻⁴

^a [Ir^{IV}]₀ = 1 × 10⁻⁴ M; [phenol]_{tot} = 1.8 × 10⁻³ M; μ = 0.1 M (LiClO₄); The p[H⁺] values were maintained using 0.02 M cacodylate buffers; T = 25 °C. ^b Standard deviation of first-order curve fit residuals over 1 s.

the absence of DBNBS with phenol concentration (1.77–44.3) × 10⁻³ M. The kinetic data are collected in Table A-1 (in appendix A). The linear plots of k_{obs} versus [phenol] shown in Figure 2-6a-b show that the conditional rate constants are 0.612 ± 0.001 M⁻¹ s⁻¹ at p[H⁺] = 1.3 and 106 ± 4 M⁻¹ s⁻¹ at p[H⁺] = 5.1. These results demonstrate that the rate law is first-order with respect to [phenol]_{tot} and the kinetics are sensitive to p[H⁺].

2.3.1.5 Dependence on p[H⁺]

A simple two-term rate law arises from the assumption that both phenol and the phenolate anion can react with Ir^{IV}, as shown by eqs 2-1 and 2-2:

$$-\frac{d[\text{Ir}^{\text{IV}}]}{dt} = \frac{(k_{\text{ArOH}} + k_{\text{ArO}} - K_a/[\text{H}^+])}{1 + K_a/[\text{H}^+]} [\text{ArOH}]_{\text{tot}} [\text{Ir}^{\text{IV}}] \quad (2-1)$$

$$\frac{k_{\text{obs}}}{[\text{ArOH}]_{\text{tot}}} = \frac{(k_{\text{ArOH}} + k_{\text{ArO}} - K_a/[\text{H}^+])}{1 + K_a/[\text{H}^+]} \quad (2-2)$$

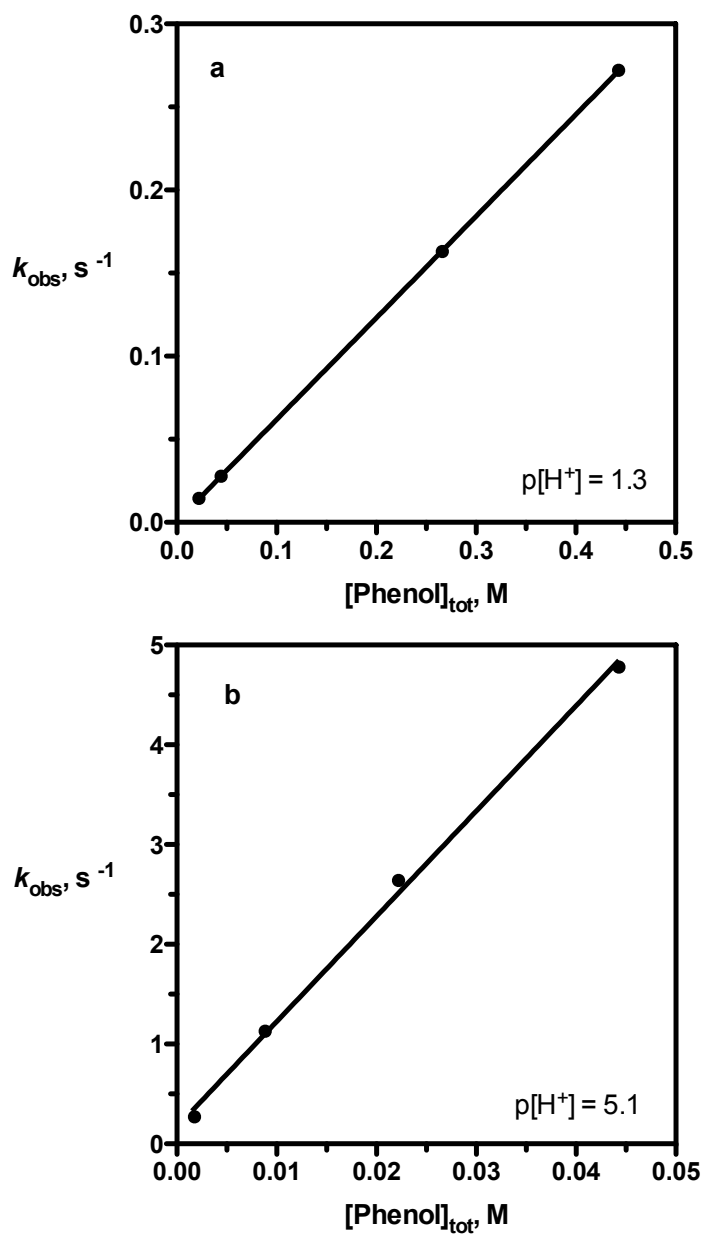


Figure 2-6. Plot of k_{obs} vs $[\text{phenol}]_{\text{tot}}$. $[\text{Ir}^{\text{IV}}]_0 = 1 \times 10^{-4}$ M; $\mu = 0.1$ M (LiClO_4); $T = 25$ °C. (a) $[\text{HClO}_4] = 0.05$ M; $[\text{phenol}]_{\text{tot}} = (22.2\text{--}443) \times 10^{-3}$ M; $[\text{DBNBS}] = 10$ mM. (b) $\text{p}[\text{H}^+] = 5.1$ (0.02 M acetate buffer); $[\text{phenol}]_{\text{tot}} = (1.77\text{--}44.3) \times 10^{-3}$ M. Solid lines are linear fits. Data from Table A-1.

Here, K_a is the acid dissociation constant of phenol, $pK_{a,ArOH} = 9.79$ at $\mu = 0.1 \text{ M}^{81}$. k_{ArOH} and k_{ArO^-} represent the reactivities of phenol and phenolate anion.

Between $p[H^+] = 2.4$ and 6.8 , the oxidation of phenol by Ir^{IV} in the absence of DBNBS gives good-quality pseudo-first-order fits, as shown in Figure 2-3b and Figure 2-3c. This feature enables us to study the $p[H^+]$ effect on the rate constants from $p[H^+] = 2.46$ to 6.74 with $1 \times 10^{-4} \text{ M } Ir^{IV}$ and $(4.43\text{--}44.3) \times 10^{-3} \text{ M}$ phenol. Selected buffers were employed to maintain the $p[H^+]$ values. The data are summarized in Table A-2 and the plot of $k_{obs}/[phenol]_{tot}$ versus $p[H^+]$ is shown in Figure 2-7. A nonlinear least-squares fit of the data to eq 2-2 shows that the rates conform to this two-term rate law with $k_{ArOH} = 0.54 \pm 0.02 \text{ M}^{-1} \text{ s}^{-1}$ and $k_{ArO^-} = (5.0 \pm 0.1) \times 10^6 \text{ M}^{-1} \text{ s}^{-1}$.

As described above, in the presence of 10 mM DBNBS, the kinetic traces of reactions between $1 \times 10^{-4} \text{ M}$ of Ir^{IV} and $(1.77\text{--}44.3) \times 10^{-3} \text{ M}$ of phenol obey pseudo-first-order kinetics over the wider $p[H^+]$ range of $1\text{--}7$. Experiments above $pH = 7$ were not performed because of the known instability of Ir^{IV} at high pH .⁸² The details of these experiments are summarized in Table A-3, and they show that the reaction obeys eq 2-2 (Figure 2-8) with the rate constants about 50% greater than those without the addition of DBNBS: $k_{ArOH} = 0.77 \pm 0.03 \text{ M}^{-1} \text{ s}^{-1}$ and $k_{ArO^-} = (8.0 \pm 0.2) \times 10^6 \text{ M}^{-1} \text{ s}^{-1}$. As discussed below, this rate increase induced by DBNBS is attributed to differing stoichiometric factors.

2.3.1.6 Inclusion of the k^o Term

It has been reported that eq 2-2 is inadequate to describe the reaction of phenol with $[Ru(bpy)_3]^{3+}$, and a “pH-dependent rate constant” (the k^o term) was introduced as in eq 2-3 to fit the data.⁵⁰

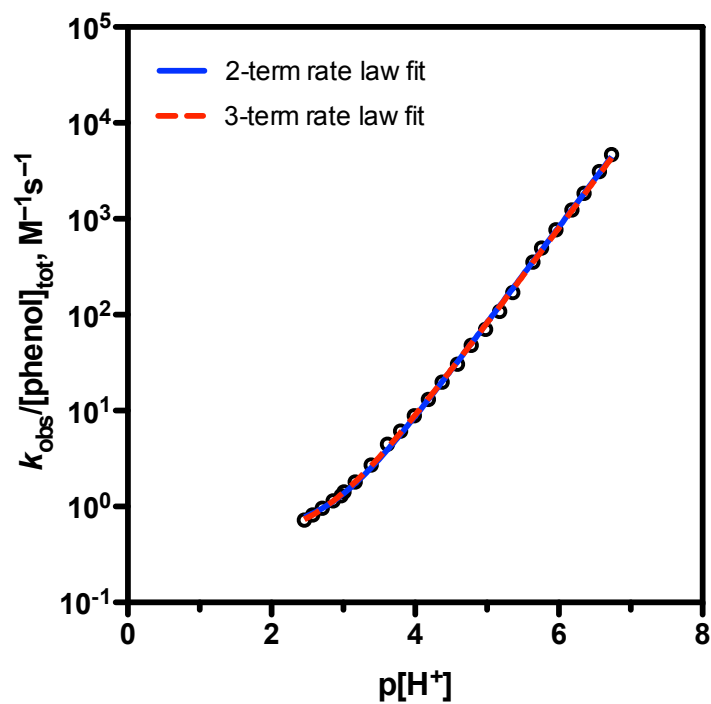


Figure 2-7. Plot of $k_{\text{obs}}/[\text{phenol}]_{\text{tot}}$ vs $\text{p}[\text{H}^+]$ in the absence of DNBNS. $[\text{Ir}^{\text{IV}}]_0 = 1 \times 10^{-4} \text{ M}$; $\mu = 0.1 \text{ M}$ (LiClO_4); $T = 25 \text{ }^\circ\text{C}$. The following buffers (0.02 M) were employed to maintain constant $\text{p}[\text{H}^+]$ values: monochloroacetate buffer for $2.4 < \text{p}[\text{H}^+] < 3.4$, acetate buffer for $3.6 < \text{p}[\text{H}^+] < 5.4$, and cacodylate buffer for $5.6 < \text{p}[\text{H}^+] < 7.0$. Solid line is the fit to eq 2-2 and the dashed line is the fit to eq 2-3. Data from Table A-2.

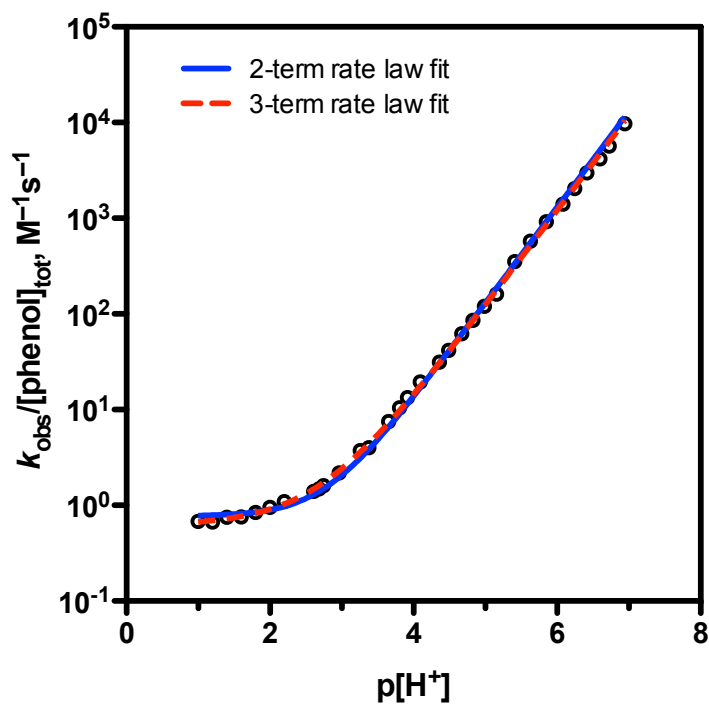


Figure 2-8. Plot of $k_{\text{obs}}/[\text{phenol}]_{\text{tot}}$ vs $\text{p}[\text{H}^+]$ with DBNBS. $[\text{Ir}^{\text{IV}}]_0 = 1 \times 10^{-4} \text{ M}$; $[\text{DBNBS}] = 10 \text{ mM}$; $\mu = 0.1 \text{ M (LiClO}_4)$; $T = 25 \text{ }^\circ\text{C}$. $\text{p}[\text{H}^+] = -\log [\text{HClO}_4]$ in the $\text{p}[\text{H}^+]$ range of 1.0–2.2. The following buffers (0.02 M) were employed to maintain constant $\text{p}[\text{H}^+]$ values: monochloroacetate buffer for $2.4 < \text{p}[\text{H}^+] < 3.4$, acetate buffer for $3.6 < \text{p}[\text{H}^+] < 5.4$, and cacodylate buffer for $5.4 < \text{p}[\text{H}^+] < 7.0$. Solid line is the fit to eq 2-2 and the dashed line is the fit to eq 2-3. Data from Table A-3.

$$\frac{k_{\text{obs}}}{[\text{ArOH}]_{\text{tot}}} = \frac{k_{\text{ArOH}} + k^{\circ} 10^{0.5\text{p}[\text{H}^+]} + k_{\text{ArO}^-} 10^{(\text{p}[\text{H}^+] - \text{p}K_{\text{a}})}}{1 + 10^{(\text{p}[\text{H}^+] - \text{p}K_{\text{a}})}} \quad (2-3)$$

When the pH-dependent data for the oxidation by Ir^{IV} with no added DBNBS are fit with eq 2-3, the optimized values are $k_{\text{ArOH}} = 0.40 \pm 0.06 \text{ M}^{-1} \text{ s}^{-1}$, $k_{\text{ArO}^-} = (4.9 \pm 0.1) \times 10^6 \text{ M}^{-1}$, and $k^{\circ} = (6.5 \pm 3) \times 10^{-3} \text{ M}^{-1} \text{ s}^{-1}$ (Table A-4). This fit yields slightly improved residuals, but the values of k_{ArOH} and k_{ArO^-} are virtually unchanged. Over the $\text{p}[\text{H}^+]$ range of 1–7, the maximum contribution of the k° term to the total rate is 16% and occurs around $\text{p}[\text{H}^+] = 2.7$. Although this k° term has only marginal statistical significance, we show below that it is a consequence of pH-dependent stoichiometric factors.

In the presence of DBNBS, fitting the data to eq 2-3 yields slightly improved residuals relative to eq 2-2 (Table A-5). The fitted values for k_{ArOH} and k_{ArO^-} are only slightly changed: $k_{\text{ArOH}} = 0.59 \pm 0.03 \text{ M}^{-1} \text{ s}^{-1}$, $k_{\text{ArO}^-} = (7.3 \pm 0.1) \times 10^6 \text{ M}^{-1}$ and $k^{\circ} = (2.0 \pm 0.3) \times 10^{-2} \text{ M}^{-1} \text{ s}^{-1}$. The maximum contribution from the k° term is 28% and appears at the same $\text{p}[\text{H}^+]$ as in the result without DBNBS. The origin of the k° term in the presence of DBNBS is currently unknown but is speculated to arise from a pH-dependent overoxidation of the DBNBS/phenoxy adduct.

2.3.1.7 Kinetic Isotope Effect (KIE)

The deuterium KIE in the reaction between phenol and Ir^{IV} was measured by comparing the rates in a D_2O solution to those in normal H_2O . The experiments were performed at $[\text{H}^+] = 0.09 \text{ M}$ in the presence of 10 mM DBNBS, and thus the KIE refers to k_{ArOH} . The rates are independent of the pH under these conditions, so the equilibrium

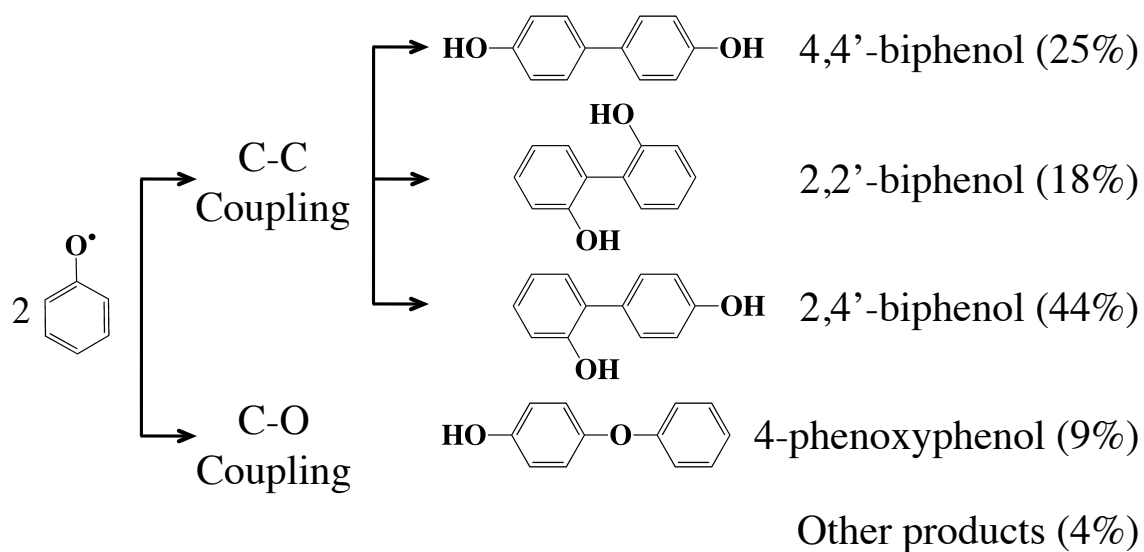
isotope effect on K_a is not an issue. All data are shown in Table A-6. The KIE value is 3.5 ± 0.3 , which clearly indicates a primary KIE and implies cleavage of the O-H bond in the rate-limiting step. Although this result is taken as evidence of a concerted PCET mechanism (see below), the measured KIE is not extremely large, so it is conceivable that the measured k_{ArOH} value includes a small contribution from a parallel sequential PCET mechanism. Focusing on the (major) concerted PCET component, the solvent (water) must be acting as the proton acceptor because Ir^{III} is not appreciably basic and no other bases appear in the rate law. A similar KIE and mechanism were recently reported for the oxidation of phenol by three $Ru^{III}(bpy)_3$ -type complexes²⁵ and for the oxidation of hydroxylamine by Ir^{IV} .⁶⁰

2.3.2 Overoxidation of Phenol

2.3.2.1 Coupling Products

As we have described elsewhere,²⁷ the second step of the reaction between phenol and Ir^{IV} is the self-reaction of the phenoxy radicals. This self-reaction is currently believed to occur through C-C and C-O coupling to generate the four major expected product isomers in Scheme 2-2. According to the pulse irradiation experiments,⁸³ the yields of these products are 25% for 4,4'-biphenol, 18% for 2,2'-biphenol, 44% for 2,4'-biphenol and 9% for 4-phenoxyphenol. The remaining 4% corresponds to unidentified products.

The UV-vis spectra of the four coupling isomers in H_2O or a 0.2% ethanol/water mixture are shown in Figure 2-9. 4,4'-Biphenol has strong absorption at 263 nm with molar absorptivity (ϵ_{263}) of $2.1 \times 10^4 M^{-1} cm^{-1}$. The maximum absorption wavelength is red-shifted to 279 nm when the structure changes to 2,2'-biphenol and its ϵ_{279} value is 5.9



Scheme 2-2. Expected dimerization products of phenoxy radical and their composition according to literature.⁸³

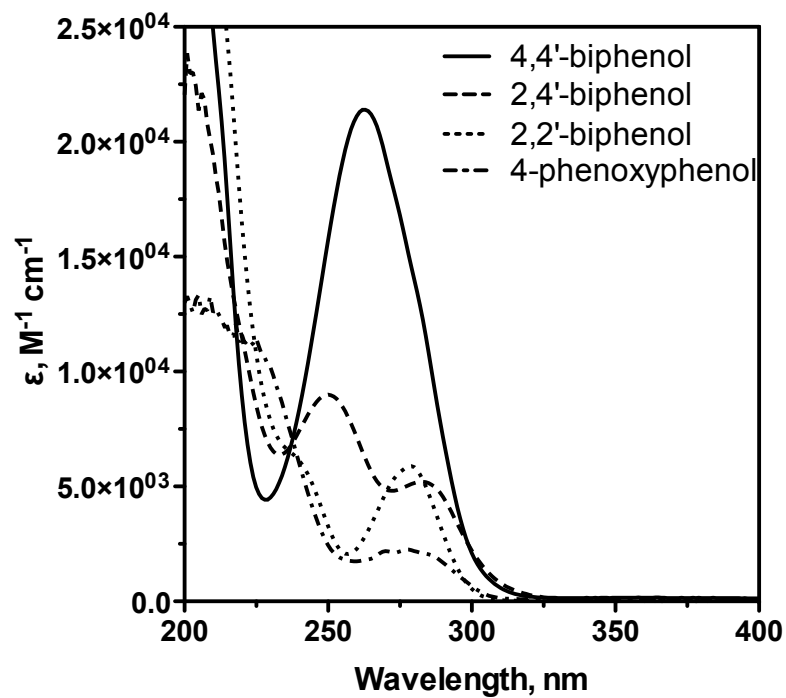


Figure 2-9. The UV-vis spectra of four coupling isomers. The spectra of 2,2'-biphenol and 4-phenoxyphenol were recorded in water, and those of 4,4'- and 2,4'-biphenol were obtained in 0.2% ethanol-water solution. $T = 25$ °C.

$\times 10^3 \text{ M}^{-1} \text{ cm}^{-1}$. Two absorption bands are observed for 2,4'-biphenol: 250 nm and 283 nm ($\epsilon_{250} = 9.0 \times 10^3 \text{ M}^{-1} \text{ cm}^{-1}$ and $\epsilon_{283} = 5.2 \times 10^3 \text{ M}^{-1} \text{ cm}^{-1}$). The spectrum of 4-phenoxyphenol exhibits a weaker and broader absorption at 278 nm with $\epsilon_{278} = 2.2 \times 10^3 \text{ M}^{-1} \text{ cm}^{-1}$.

2.3.2.2 pK_a values of 4,4'-Biphenol and 2,4'-Biphenol

Spectrometric titration with NaOH was used to determine the two pK_a values for 4,4'-biphenol because controversial results were found previously.⁸⁴⁻⁸⁶ At 0.1 M ionic strength (LiClO_4), $3 \times 10^{-5} \text{ M}$ 4,4'-biphenol was titrated from pH = 6.5 to 12.6 with various concentrations of NaOH. The titration was repeated three times and the results are reproducible. UV-vis spectra of one of the titrations are shown in Figure 2-10a. These spectra exhibit a loss of absorbance at 260 nm due to consumption of the biphenol and a gain of absorbance at 288 nm. The titration curve at 288 nm, after volume corrections, is sigmoidal, as shown in Figure 2-10b. Satisfactory fits of this curve to a model involving a single ionizable proton could not be obtained. On the other hand, an excellent fit was obtained with a model that included two ionizable protons, as in eq 2-4:

$$A = \frac{\epsilon_{\text{HOArArO-C}}}{1 + 10^{(\text{pH}-\text{p}K_{a2})} + 10^{(\text{p}K_{a1}-\text{pH})}} + \frac{\epsilon_{\text{-OArArO-C}}}{1 + 10^{(\text{p}K_{a2}-\text{pH})} + 10^{(\text{p}K_{a1}+\text{p}K_{a2}-2\text{pH})}} + \frac{\epsilon_{\text{HOArArOHC}}}{1 + 10^{(\text{pH}-\text{p}K_{a1})} + 10^{(2\text{pH}-\text{p}K_{a1}-\text{p}K_{a2})}} \quad (2-4)$$

Equation 2-4 expresses for the total absorption (A) as a function of the pH, pK_{a1} , and pK_{a2} , the total biphenol concentration (c), and the molar absorptivities (ϵ) for all three protonated and deprotonated forms. The result of the fit to eq 2-4 is shown in Figure 2-10b, and the derived values are $pK_{a1} = 9.66 \pm 0.05$ and $pK_{a2} = 10.92 \pm 0.4$, $\epsilon_{\text{HOArArO}^-} =$

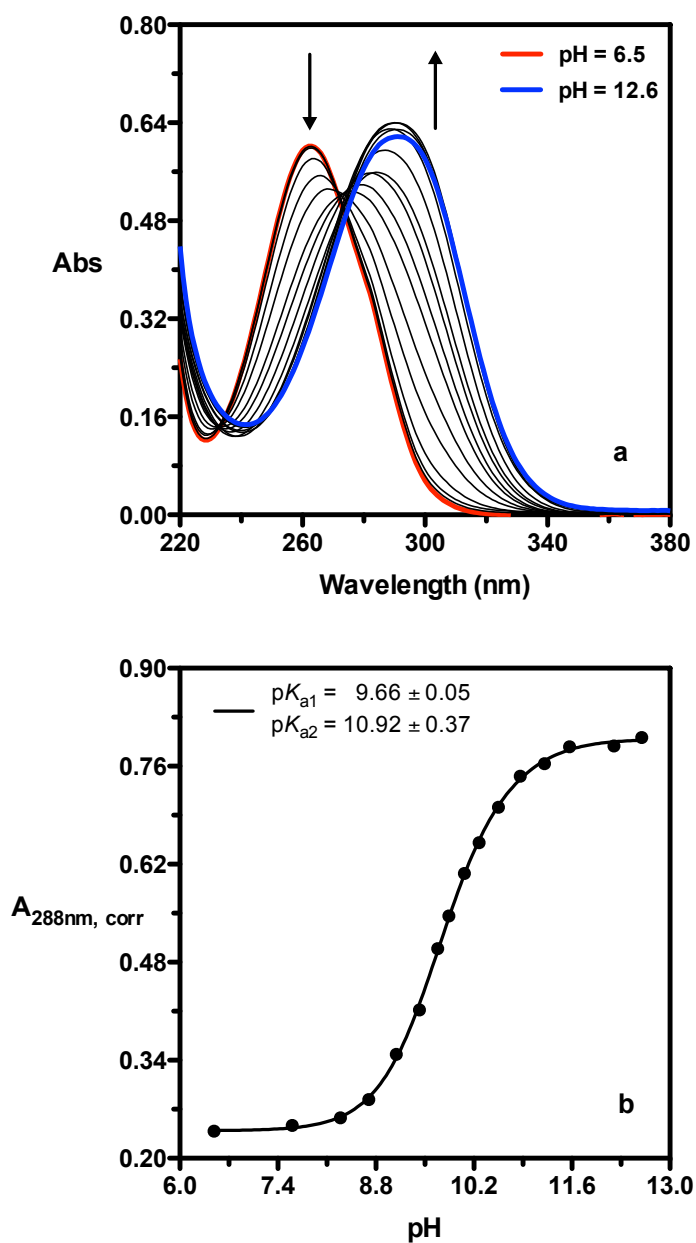


Figure 2-10. Titration of 3.0×10^{-5} M 4,4'-biphenol. $\mu = 0.1$ M (LiClO_4); $T = 25$ °C. (a) Absorbance spectra of 4,4'-biphenol during titration with various concentrations of NaOH in aqueous solution. pH between 6.5 and 12.6. (b) Titration curve at 288 nm after volume correction. Solid line is the fit to eq 2-4.

$2.4 \times 10^4 \text{ M}^{-1} \text{ cm}^{-1}$, $\varepsilon_{\text{-OArArO}^-} = 2.7 \times 10^4 \text{ M}^{-1} \text{ cm}^{-1}$ and $\varepsilon_{\text{HOArArOH}} = 8.0 \times 10^3 \text{ M}^{-1} \text{ cm}^{-1}$.

This $\text{p}K_{\text{a}1}$ value is very close to that reported by Jonsson et al.,⁸⁵ and the $\text{p}K_{\text{a}2}$ value is as expected for successive $\text{p}K_{\text{a}}$ s.

A similar titration of 2,4'-biphenol was performed three times and the results are reproducible. Figure 2-11a shows a complex series of UV-vis spectra of one of the titrations. The curve at 310 nm (Figure 2-11b) is sigmoidal, but the curve at 285 clearly shows that three species are involved. A fit of the absorbance data at 285 nm to eq 2-4 yields the following values: $\text{p}K_{\text{a}1} = 9.65 \pm 0.04$, $\text{p}K_{\text{a}2} = 10.96 \pm 0.06$, $\varepsilon_{\text{HOArArO}^-} = 8.5 \times 10^3 \text{ M}^{-1} \text{ cm}^{-1}$, $\varepsilon_{\text{-OArArO}^-} = 6.1 \times 10^3 \text{ M}^{-1} \text{ cm}^{-1}$ and $\varepsilon_{\text{HOArArOH}} = 5.2 \times 10^3 \text{ M}^{-1} \text{ cm}^{-1}$. A fit at 310 nm yields $\text{p}K_{\text{a}1} = 9.68 \pm 0.04$, $\text{p}K_{\text{a}2} = 10.89 \pm 0.05$, $\varepsilon_{\text{HOArArO}^-} = 4.8 \times 10^3 \text{ M}^{-1} \text{ cm}^{-1}$, $\varepsilon_{\text{-OArArO}^-} = 8.8 \times 10^3 \text{ M}^{-1} \text{ cm}^{-1}$ and $\varepsilon_{\text{HOArArOH}} = 4.9 \times 10^2 \text{ M}^{-1} \text{ cm}^{-1}$. The agreement between the $\text{p}K_{\text{a}}$ values at these two wavelengths is excellent.

The two $\text{p}K_{\text{a}}$ values for 2,2'-biphenol are quite different from those of the 4,4' and 2,4' isomers.⁸⁵ This difference is attributed to hydrogen bonding between the two O atoms, which is only possible for the 2,2'-isomer. The $\text{p}K_{\text{a}1}$ values for all four coupling isomers are summarized in Table 2-5.

2.3.2.3 Overoxidation of Phenol

As shown below, Ir^{IV} oxidizes all four of these coupling isomers rapidly, which leads to overoxidation in the phenol reaction. A full account of the phenol reaction is thus dependent on the details of each of these overoxidation pathways.

The Oxidation of 4,4'-Biphenol. Qualitatively, the reaction of Ir^{IV} with 4,4'-biphenol is signaled by the rapid loss of absorbance at 488 nm, which is characteristic of Ir^{IV} . A concurrent absorbance increase occurs at 398 nm, and this absorbance decays at

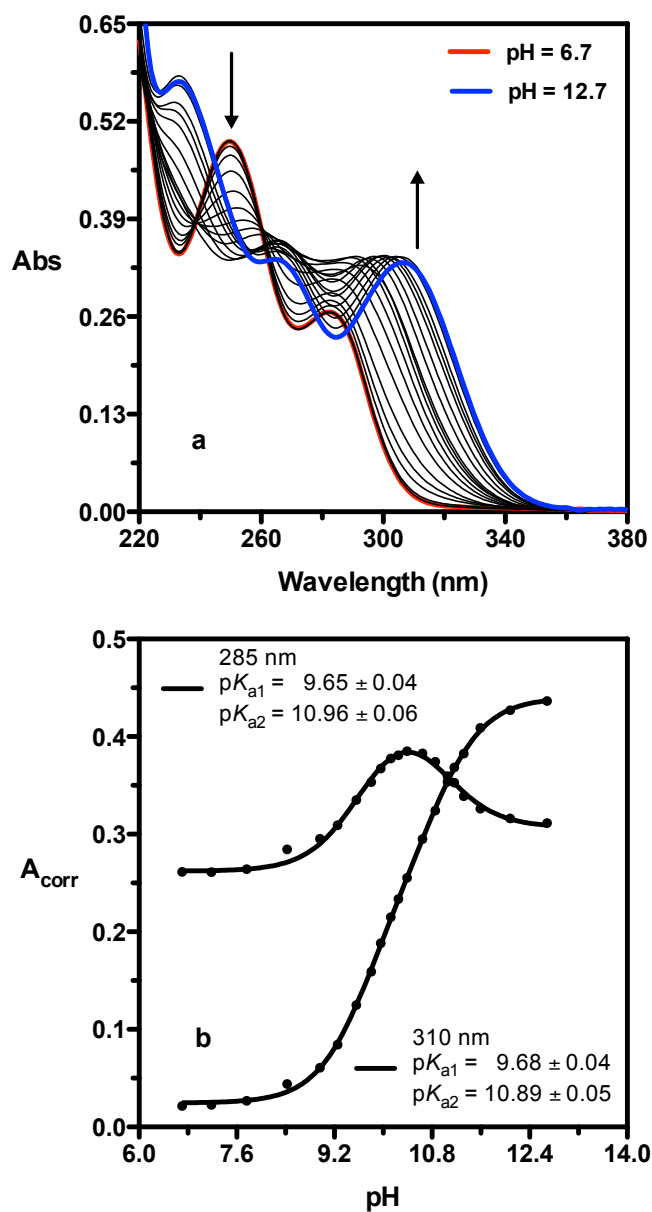


Figure 2-11. Titration of 5.0×10^{-5} M 2,4'-biphenol. $\mu = 0.1$ M (LiClO_4); $T = 25$ °C. (a) Absorbance spectra of 2,4'-biphenol during titration with various concentrations of NaOH in aqueous solution. pH between 6.7 and 12.7 (b) Titration curves at 285 nm and 310 nm after volume correction. Solid lines are the fits to eq 2-4.

Table 2-5. Kinetics Data for the Reactions of Ir^{IV} with the Phenol Coupling Products.^a

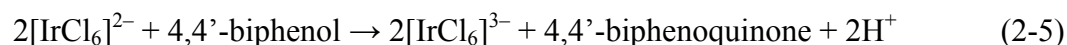
Substrate	k_{ArOH}	k_{ArO^-}	$\text{p}K_{\text{a1}}$	E_{f} , V	E_{f} , V
	$\text{M}^{-1} \text{s}^{-1}$	$\text{M}^{-1} \text{s}^{-1}$		$\text{ArO}^\bullet/\text{ArO}^-$	$\text{ArO}^\bullet, \text{H}^+$ /ArOH
phenol	0.77 ± 0.03	$(8.0 \pm 0.2) \times 10^6$	9.79^b	0.80^f	1.38
4,4'-biphenol	$(4.6 \pm 0.4) \times 10^4$	$(6.5 \pm 0.7) \times 10^8$	9.66^c	0.64^d	1.21
2,2'-biphenol	6.6 ± 2.6	$(4.0 \pm 0.7) \times 10^6$	7.60^d	1.00^d	1.45
2,4'-biphenol	$(4.0 \pm 0.6) \times 10^3$	$(1.3 \pm 0.3) \times 10^8$	9.67^c		
4-phenoxy phenol	$(1.2 \pm 0.1) \times 10^3$	$(1.1 \pm 0.2) \times 10^8$	9.90^e		

^a Ar = 4,4'-/2,2'-/2,4'-HOC₆H₄C₆H₄, 4-C₆H₅OC₆H₄. Rate constants obtained by fitting the k_{obs} results in Table A-8 to eq 2-2 and with the K_{a} 's constrained to the values given above. ^b Reference 81. ^c This work. ^d Reference 85. ^e The reported $\text{p}K_{\text{a1}} = 9.81$ at $\mu = 0.25$ M in reference 87 is converted to $\text{p}K_{\text{a1}} = 9.90$ at $\mu = 0.1$ M using Davies equation. ^f E_{f} corrected in this work from E° in reference 88.

longer time scales. A UV-vis spectrum of the 398 nm intermediate generated from the reaction of 2.5×10^{-5} M 4,4'-biphenol with 2.5×10^{-5} M Ir^{IV} at $\text{p}[\text{H}^+] = 5.5$ is shown in Figure 2-12. This absorbance decays with an initial rate of $1.7 \times 10^{-4} \text{ s}^{-1}$ as shown in Figure 2-13. When the same experiment is performed at $\text{p}[\text{H}^+] = 2.5$, the maximum absorbance at 398 nm and its initial decay rate are close to those obtained at $\text{p}[\text{H}^+] = 5.5$, as shown in Table 2-6. The species absorbing at 398 nm is assigned as 4,4'-biphenoquinone, which was claimed to be observed at 400 nm in the oxidation of phenol by other metal complexes.⁸⁹⁻⁹⁰ Our results imply that the decomposition of 4,4'-biphenoquinone is almost pH-independent. The initial (maximum) absorbance of 4,4'-biphenoquinone at 398 nm yields a molar absorptivity $5.2 \times 10^4 \text{ M}^{-1} \text{ cm}^{-1}$ in aqueous solution, based on the assumption that 1 mol is produced per 2 mol of Ir^{IV} ; this value for ϵ_{398} is consistent with the reported value ($\approx 5 \times 10^4 \text{ M}^{-1} \text{ cm}^{-1}$).⁹¹

In a spectrophotometric titration at $\text{p}[\text{H}^+] = 5.5$, 4.8×10^{-5} M Ir^{IV} was added to 1.5 mL of 4.8×10^{-5} M 4,4'-biphenol, generating the titration curves in Figure 2-14. At 398 nm, the absorbance (after correction for dilution) rises linearly to an abrupt end point, and after the end point, the absorbance is stable. The end point corresponds to a consumption ratio of $n_{\text{Ir}^{\text{IV}}}/n_{4,4'\text{-biphenol}}$ of 2.5:1. Apparently, the 4,4'-biphenoquinone product undergoes further oxidation in the presence of 4,4'-biphenol. The absorbance at 488 nm (due to Ir^{IV}) remains essentially zero (Figure 2-14b) prior to the same abrupt end point observed at 398 nm, implying that Ir^{IV} is fully consumed up to the end point.

The principal reaction is thus



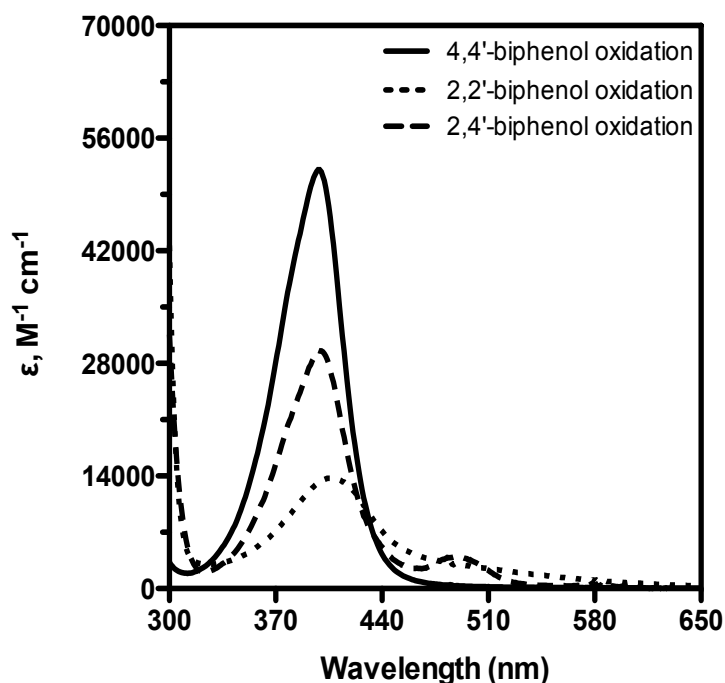


Figure 2-12. UV-Vis spectra of products of 4,4'-/2,2'-/2,4'-biphenol oxidation. $[\text{Ir}^{\text{IV}}]_0 = 2.5 \times 10^{-5} \text{ M}$; $\mu = 0.1 \text{ M}$ (LiClO_4); $T = 25 \text{ }^\circ\text{C}$. The solid line is the 4,4'-biphenol oxidation: $[\text{4,4'-biphenol}]_0 = 2.5 \times 10^{-5} \text{ M}$; $\text{p}[\text{H}^+] = 5.5$ (0.02 M acetate buffer). The short dashed line was obtained from the 2,2'-biphenol oxidation: $[\text{2,2'-biphenol}]_0 = 1 \times 10^{-3} \text{ M}$; $\text{p}[\text{H}^+] = 4.0$ (0.02 M acetate buffer). The long dashed line results from the 2,4'-biphenol reaction: $[\text{2,4'-biphenol}]_0 = 2 \times 10^{-4} \text{ M}$; $[\text{HClO}_4] = 0.05 \text{ M}$. The absorption with a maximum peak at approximately 400 nm is assumed to be the spectrum from a product of the oxidation reaction. The molar absorptivity, ϵ , was calculated based on the stoichiometry that one equivalent of biphenquinone product is obtained from two equivalents of Ir^{IV} .

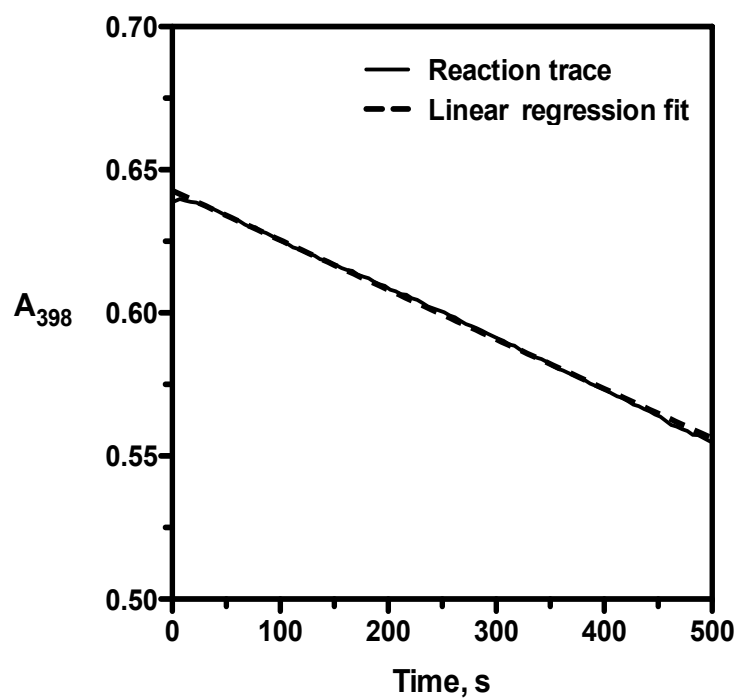


Figure 2-13. The kinetic trace of 2.5×10^{-5} M 4,4'-biphenol reacting with 2.5×10^{-5} M Ir^{IV} at 398 nm (solid line). $\text{p}[\text{H}^+] = 5.5$ (0.02 M acetate buffer); $\mu = 0.1$ M (LiClO_4); $T = 25$ °C. Slope = $-1.7 \times 10^{-4} \text{ s}^{-1}$. Solid line is the experimental trace, and dashed line shows the zero-order fit.

Table 2-6. Comparison of the Experimental Data of 4,4'- and 2,4'-Biphenol Oxidation at Different p[H⁺].^a

	p[H ⁺] ^b	[biphenol] _{tot} × 10 ⁴ , M	A _{398, max}	Decay rate, ^c s ⁻¹
4,4'-biphenol	2.52	0.25	0.640	(1.70 ± 0.02) × 10 ⁻⁴
	5.49	0.25	0.653	(1.57 ± 0.01) × 10 ⁻⁴
2,4'-biphenol	1.30	2.0		(7.00 ± 0.12) × 10 ⁻³
	2.52	0.25		(3.90 ± 0.27) × 10 ⁻³
	2.51	2.5		(3.55 ± 0.60) × 10 ⁻³
	5.47	0.25	0.146	(7.35 ± 0.12) × 10 ⁻³
	5.81	2.5	0.146	(1.19 ± 0.02) × 10 ⁻²
	6.85	2.0	0.204 ^d	(1.74 ± 0.25) × 10 ^{-2d}
	7.00	0.50	0.113	(1.22 ± 0.04) × 10 ⁻²

^a [Ir^{IV}]₀ = 2.5 × 10⁻⁵ M; μ = 0.1 M (LiClO₄). ^b p[H⁺] = 1.3 is obtained with 0.05 M of HClO₄. The following buffers (0.02 M) were employed to maintain constant p[H⁺] values: monochloroacetate buffer for p[H⁺] = 2.5, acetate buffer for p[H⁺] = 5.5 and 5.8, and cacodylate buffer for p[H⁺] = 6.8–7.0. ^c Initial rates were calculated for 4,4'-biphenol, while first-order rate constants were obtained for 2,4'-biphenol. ^d Obtained from stopped-flow measurements.

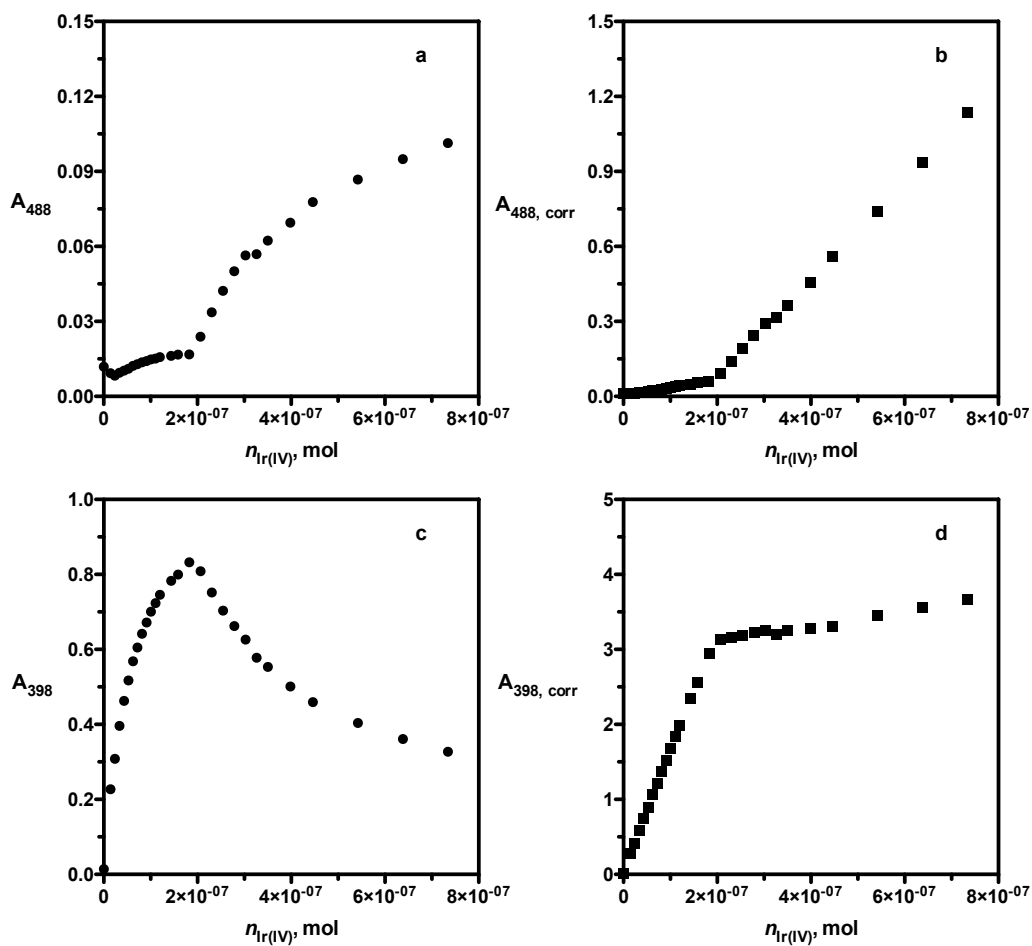


Figure 2-14. Titration of 1.5 mL 4,4'-biphenol by Ir^{IV} . $[\text{4,4}'\text{-biphenol}]_0 = 4.8 \times 10^{-5}$ M; $[\text{Ir}^{\text{IV}}]_0 = 4.8 \times 10^{-5}$ M; $\text{p}[\text{H}^+] = 5.5$ (0.02 M acetate buffer); $\mu = 0.1$ M (LiClO_4); $T = 25$ °C.

(a) Monitored at 488 nm. (b) Absorbance at 488 nm corrected using $A_{\text{corr}} =$

$A_{\text{obs}} * V_{\text{total}} / V_{\text{initial}}$. (c) Monitored at 398 nm. (d) Absorbance at 398 nm corrected using $A_{\text{corr}} =$

$= A_{\text{obs}} * V_{\text{total}} / V_{\text{initial}}$.

Kinetic studies were performed with an excess of 4,4'-biphenol over Ir^{IV}, but because of its low solubility, the initial concentrations of 4,4'-biphenol were not high enough to ensure strictly pseudo-first-order conditions. Thus, values of k_{obs} were obtained from the slope of the linear regression of the logarithm of absorbance at 488 nm within the first half-life (Figure 2-15). Rates were determined at p[H⁺] 1–7, and the data are shown in Table A-8. These pH-dependent data conform to eq 2-2 (Figure 2-16), and they yield the following rate constants: $k_{\text{ArOH}} = (4.6 \pm 0.4) \times 10^4 \text{ M}^{-1} \text{ s}^{-1}$ and $k_{\text{ArO}^-} = (6.5 \pm 0.7) \times 10^8 \text{ M}^{-1} \text{ s}^{-1}$ (Table 2-5).

The Oxidation of 2,2'-Biphenol. UV-vis spectroscopy was used to detect the products of the reaction between $1 \times 10^{-3} \text{ M}$ 2,2'-biphenol and $2.5 \times 10^{-5} \text{ M}$ Ir^{IV} at p[H⁺] = 4.0. As shown in Figure 2-12, a weak absorbance peak appears at 406 nm with a broad shoulder observed in the range of 450–600 nm. This spectrum is attributed to the absorption of 2,2'-biphenone, with $\epsilon_{406} = 1.4 \times 10^4 \text{ M}^{-1} \text{ cm}^{-1}$ in an aqueous solution. It decomposes slowly as is shown in Figure 2-17.

The kinetic experiments on the oxidation of 2,2'-biphenol by Ir^{IV} were performed by using stopped-flow spectroscopy to monitor the loss of Ir^{IV} at 488 nm at p[H⁺] 1–7 with at least a 10-fold molar excess of biphenol over Ir^{IV}. However, because of the absorbance of products at 488 nm and their subsequent decay, deviations from pseudo-first-order kinetics were observed at some p[H⁺]. Therefore, the initial rate constants were calculated from the slopes of semilog plots of $(A - A_{\infty})$ vs t . The reaction rates increase dramatically as the p[H⁺] increases, although the oxidation is extremely slow at low p[H⁺], as shown in Figure 2-16. Values for k_{ArOH} and k_{ArO^-} obtained by fitting the data in Table A-8 to eq 2-2 are $6.6 \pm 3 \text{ M}^{-1} \text{ s}^{-1}$ and $(4.0 \pm 0.7) \times 10^6 \text{ M}^{-1} \text{ s}^{-1}$, respectively.

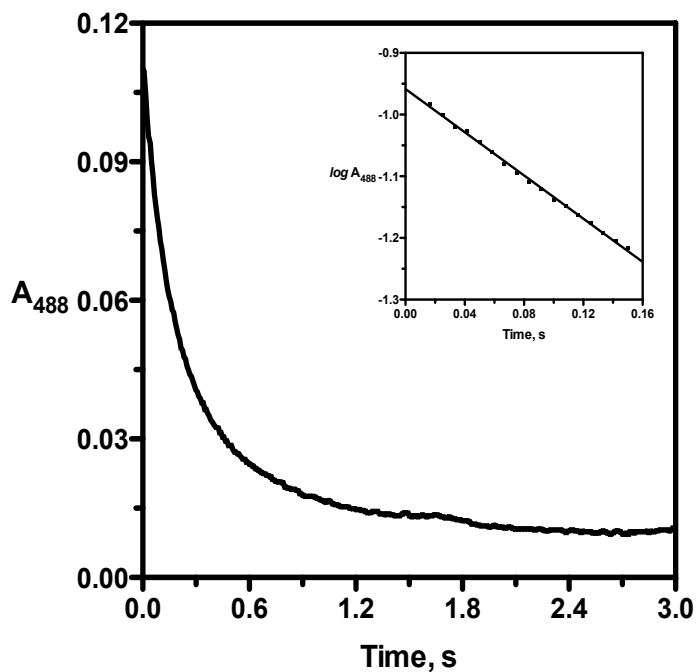


Figure 2-15. Kinetic trace of 4,4'-biphenol oxidation at 488 nm. $[\text{Ir}^{\text{IV}}]_0 = 2.5 \times 10^{-5} \text{ M}$; $[\text{4,4'-biphenol}] = 1 \times 10^{-4} \text{ M}$; $[\text{HClO}_4] = 0.05 \text{ M}$; $\mu = 0.1 \text{ M}$ (LiClO_4); $T = 25 \text{ }^\circ\text{C}$. The insert is the linear regression of $\log A$ in the first half time. Slope = $-1.764 \pm 0.021 \text{ s}^{-1}$ ($R = 0.9978$) and the observed initial rate constant ($k_{\text{obs}} = -\ln(10) \times \text{slope}$) is calculated to be 4.06 s^{-1} .

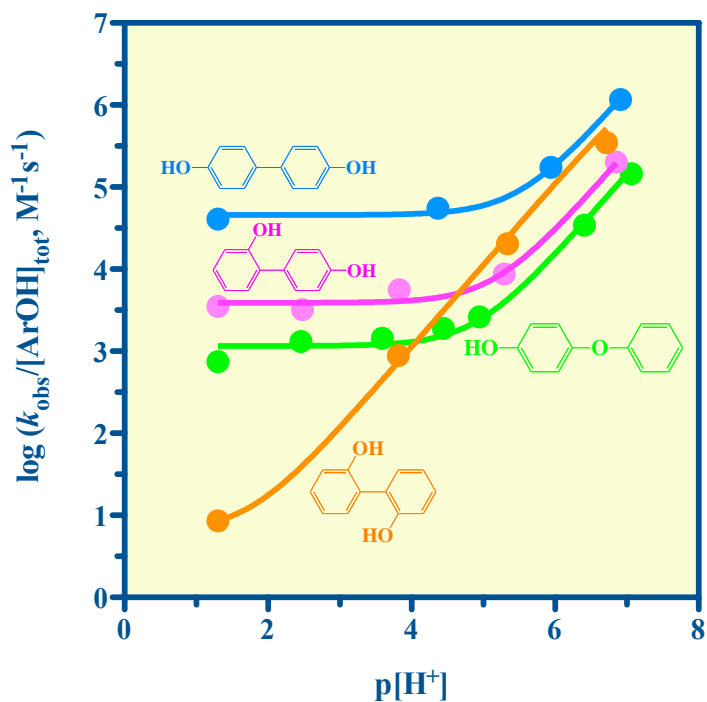


Figure 2-16. Plot of $k_{\text{obs}}/[\text{substrate}]_{\text{tot}}$ vs $\text{p}[\text{H}^+]$. $[\text{Ir}^{\text{IV}}]_0 = 2.5 \times 10^{-5} \text{ M}$; $\mu = 0.1 \text{ M}$ (LiClO_4); $T = 25 \text{ }^\circ\text{C}$. $\text{p}[\text{H}^+] = -\log [\text{HClO}_4]$ in the $\text{p}[\text{H}^+]$ range of 1.0–2.2. The following buffers (0.02 M) were employed to maintain constant $\text{p}[\text{H}^+]$ values: monochloroacetate buffer for $2.4 < \text{p}[\text{H}^+] < 3.6$, acetate buffer for $3.7 < \text{p}[\text{H}^+] < 5.4$, and cacodylate buffer for $5.5 < \text{p}[\text{H}^+] < 7.1$. Solid lines are fits to eq 2-2. Data from Table A-8.

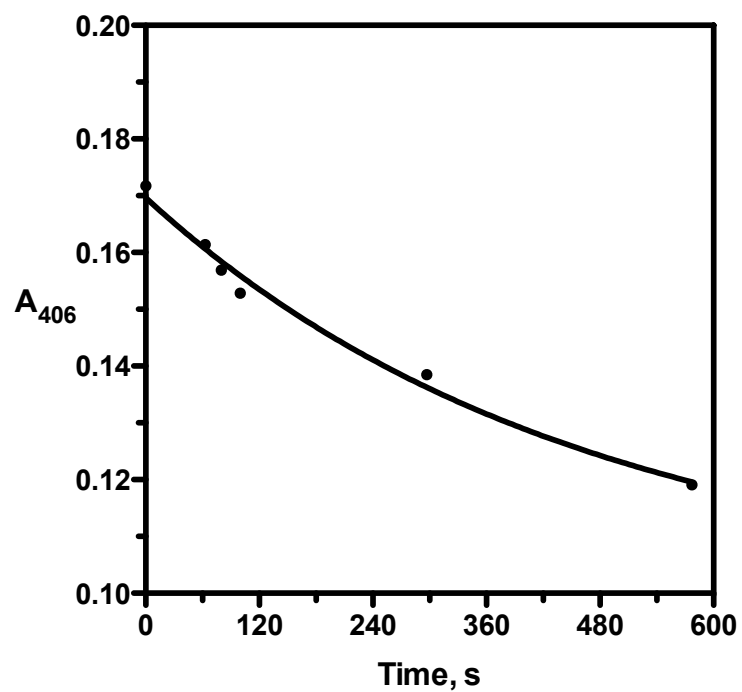


Figure 2-17. The kinetic trace of 1×10^{-3} M 2,2'-biphenol reacting with 2.5×10^{-5} M Ir^{IV} at 406 nm. $\text{p}[\text{H}^+] = 4.0$ (0.02 M acetate buffer); $\mu = 0.1$ M (LiClO_4); $T = 25$ °C. Solid line is the first-order fit.

The Oxidation of 2,4'-Biphenol. The products of the reaction between 2×10^{-4} M 2,4'-biphenol and 2.5×10^{-5} M Ir^{IV} at $[\text{HClO}_4] = 0.05$ M were investigated by UV-vis spectroscopy. As is shown in Figure 2-18, an intermediate that has an absorbance maximum at 398 nm is produced rapidly, and then it undergoes decomposition with a first-order rate constant of $7.2 \times 10^{-3} \text{ s}^{-1}$ ($3.5 \times 10^{-2} \text{ s}^{-1}$ was obtained by the stopped-flow instrument at 488 nm, as shown in Table A-8). The first UV-vis spectrum obtained after mixing (~ 10 s) is shown in Figure 2-12; it has a main peak at 398 nm and a minor peak at 488 nm (overlapping with that of Ir^{IV}). Assignment of this spectrum to 2,4'-biphenoquinone is supported by density functional theory calculations at B3LYP/6-31G* level that produce an electronic spectrum with a major peak at ~ 320 nm and a secondary peak at 460 nm. With the assumption of a 2:1 Ir^{IV} /2,4'-biphenoquinone stoichiometry, the experimental spectrum yields $\epsilon_{398} = 3.0 \times 10^4 \text{ M}^{-1} \text{ cm}^{-1}$ and $\epsilon_{488} = 4.0 \times 10^3 \text{ M}^{-1} \text{ cm}^{-1}$.

At $\text{p}[\text{H}^+] = 6.9$ and 398 nm, the kinetic traces are triphasic, showing a rapid rise in absorbance, a slower small-amplitude fall, and then an even slower large-amplitude fall (Figure 2-19). The first phase occurs on the same time frame as the initial absorbance loss at 488 nm (see below). This triphasic behavior is thus attributed to the rapid production of 2,4'-biphenoquinone in the first phase, followed by its biphasic decay. Because of the relatively rapid decay in the second phase, it was not possible to obtain an accurate value for ϵ_{398} at this pH, a value of only $1.6 \times 10^4 \text{ M}^{-1} \text{ cm}^{-1}$ corresponding to the maximum absorbance.

At 488 nm the kinetic traces exhibit biphasic decay. Double-exponential fits were used to obtain the fast pseudo-first-order rate constants for the consumption of Ir^{IV} (k_{obs}) as well as the slower first-order rate constant for the decay of 2,4'-biphenoquinone ($k_{\text{obs},2}$)

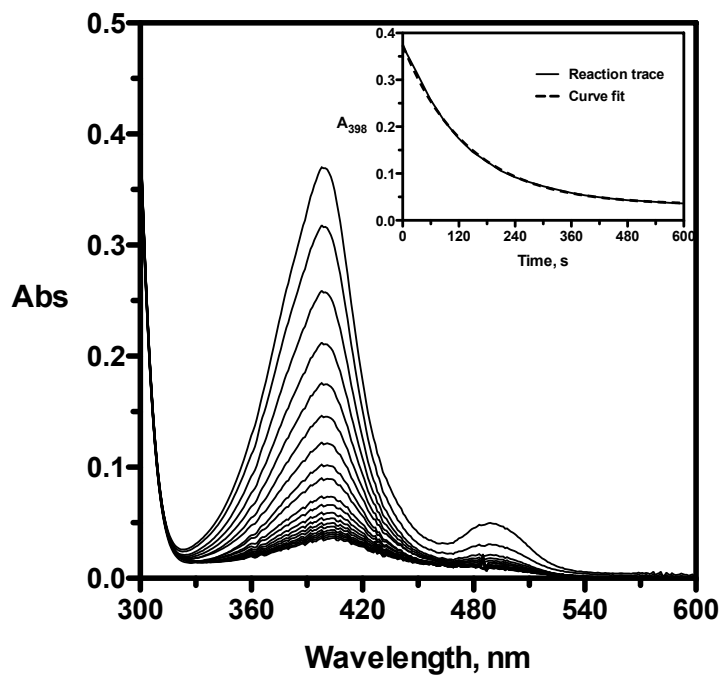


Figure 2-18. UV-Vis spectra during the reaction between 2×10^{-4} M of 2,4'-biphenol and 2.5×10^{-5} M of Ir^{IV} . $[\text{HClO}_4] = 0.05$ M; $\mu = 0.1$ M (LiClO_4); $T = 25$ °C; 30 s interval between spectra. The inset shows the kinetic trace at 398 nm. $k_{\text{obs}} = 7.18 \times 10^{-3} \text{ s}^{-1}$.

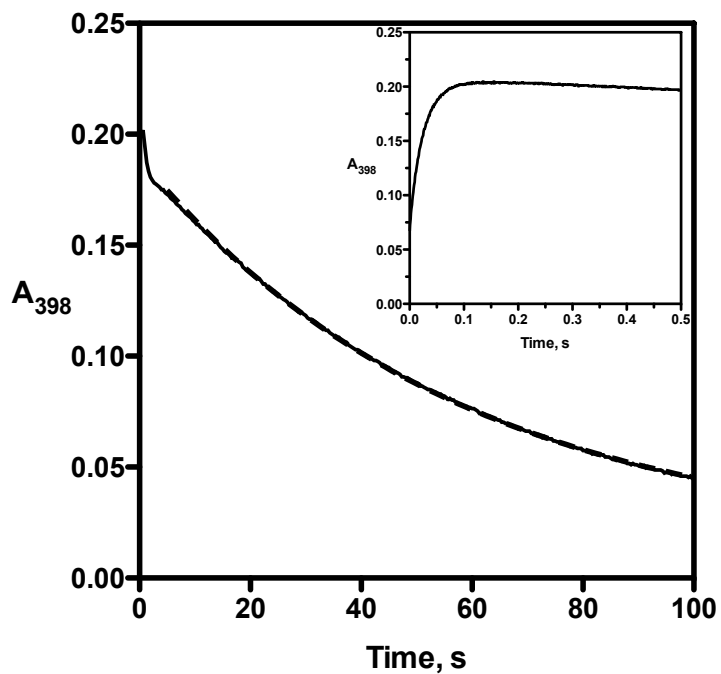


Figure 2-19. The kinetic trace of 2×10^{-4} M 2,4'-biphenol reacting with 2.5×10^{-5} M Ir^{IV} at 398 nm. $\text{p}[\text{H}^+] = 6.9$ (0.02 M cacodylate buffer); $\mu = 0.1$ M (LiClO_4); $T = 25$ °C. Solid line is the experimental trace the dashed line shows the pseudo-first-order fit for the decomposition part. The insert shows the enlarged reaction trace at the beginning 0.5 s.

(shown in Table A-8). The $p[H^+]$ dependence of the Ir^{IV} reduction was studied at $p[H^+]$ 1–7. A fit of the values of k_{obs} to eq 2-2 generated $k_{ArOH} = (4.0 \pm 0.6) \times 10^3 M^{-1} s^{-1}$ and $k_{ArO^-} = (1.3 \pm 0.3) \times 10^8 M^{-1} s^{-1}$ (Table 2-5).

The Oxidation of 4-Phenoxyphenol. Kinetic studies of the reaction of 0.3 mM 4-phenoxyphenol with $2.5 \times 10^{-5} M Ir^{IV}$ were carried out in the $p[H^+]$ range of 1–7. The decay traces of Ir^{IV} at 488 nm display excellent pseudo-first-order behavior under these conditions (Table A-8). A fit of the data to rate law (2-2) led to the following parameters: $k_{ArOH} = (1.2 \pm 0.1) \times 10^3 M^{-1} s^{-1}$ and $k_{ArO^-} = (1.1 \pm 0.2) \times 10^8 M^{-1} s^{-1}$ (Table 2-5).

Evidence of Overoxidation of Phenol. As is shown in Figure 2-20, the reaction between 0.0443 M phenol and $1 \times 10^{-4} M Ir^{IV}$ at $p[H^+] = 2.5$ displays a loss of absorbance at 488 nm, signaling the consumption of Ir^{IV} , and there is a concurrent rise in absorbance at 398 nm that is assigned to the formation of biphenoquinones arising from oxidation of the biphenol coupling products. Figure 2-21 displays the absorbance at 398 nm on a longer time scale to demonstrate the rise-fall character of the signal. A double-exponential nonlinear regression fit generates two observed rate constants: the one related to the fast step is equal to $3.6 \times 10^{-2} s^{-1}$ and it corresponds to the consumption of Ir^{IV} at 488 nm, while the one related to the slow step is equal to $3.7 \times 10^{-3} s^{-1}$ which corresponds to the decay of 2,4'-biphenoquinone (Table 2-6).

2.4 Discussion and Conclusion

The initial steps in the oxidation of phenol by Ir^{IV} are now well established.^{27,51} First, depending on the pH either phenol itself or its conjugate base undergoes reversible one-electron oxidation to produce the phenoxyl radical and $[IrCl_6]^{3-}$. Second, the phenoxyl

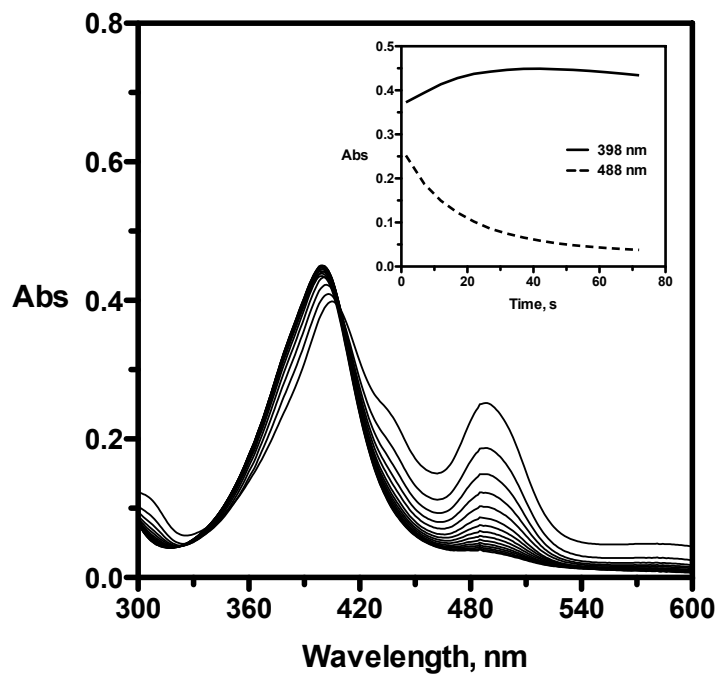


Figure 2-20. UV-Vis spectra during the reaction between 4.43×10^{-2} M of phenol and 1×10^{-4} M of Ir^{IV} . $\text{p}[\text{H}^+] = 2.5$ (0.02 M monochloroacetate buffer); $\mu = 0.1$ M (LiClO_4); $T = 25$ °C; 5 s interval between spectra. The inset shows the kinetic traces at 398 nm (solid line) and 488 nm (dashed line).

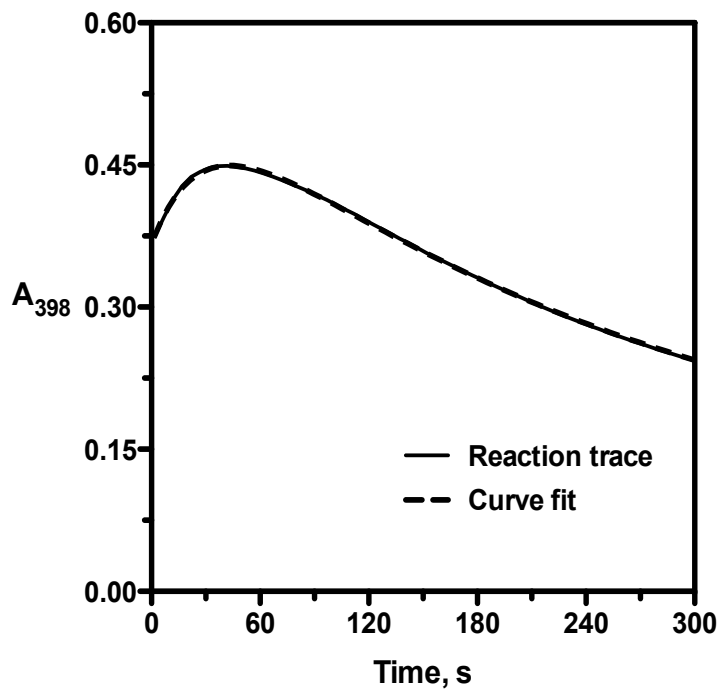


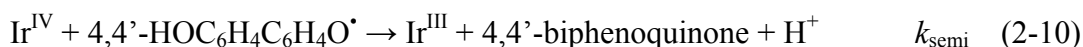
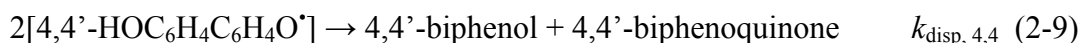
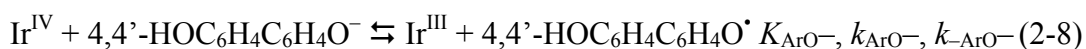
Figure 2-21. The kinetic trace and curve fit of the reaction between 4.43×10^{-2} M phenol and 1×10^{-4} M Ir^{IV} at 398 nm. $\text{p}[\text{H}^+] = 2.5$ (0.02 M monochloroacetate buffer); $\mu = 0.1$ M (LiClO_4); $T = 25$ °C. $k_{\text{obs, fast}} = 3.55 \times 10^{-2} \text{ s}^{-1}$ and $k_{\text{obs, slow}} = 3.73 \times 10^{-3} \text{ s}^{-1}$. Solid line is the experimental trace; dashed line shows the two-exponential fit.

radicals undergo bimolecular C–C coupling to produce biphenols and C–O coupling to produce phenoxyphenol. Crucial evidence for this mechanism includes the pH dependence of the rates, the kinetic inhibition by Ir^{III} and its removal by the spin-trap DBNBS, and the simulation of these effects with a kinetic model employing realistic values for the four redox rate constants and the radical coupling overall rate constant. Early on, Cecil and Littler recognized that this model is incomplete because it fails to account for the observed production of diphenoquinone;⁵¹ they proposed that the initial diphenol coupling products were oxidized further, generating diphenoquinone. Our in-situ UV-vis data provide further evidence for this overoxidation mechanism. Our current studies of the direct oxidations of the four principal phenoxy coupling products allow quantitative tests of the overoxidation mechanism and provide an explanation of the apparent pH-dependent rate constant (k^o in eq 2-3).

As shown in Figure 2-16, all four coupling products are oxidized by Ir^{IV} with rates that are highly sensitive to the pH. Moreover, they all (and phenol itself) exhibit two-term rate laws, as given by eq 2-2. A notable difference between the oxidations of the biphenols and phenol is that the biphenols undergo net two-electron oxidation to yield quinones, while phenol undergoes a net one-electron oxidation to yield radical coupling products. Evidently, the biphenols achieve their two-electron oxidations through one-electron oxidation and their conjugate bases to form semiquinones, followed by the rapid one-electron conversion of the semiquinones to the quinones. Radical coupling occurs in the case of phenol because the phenoxy radical is not easily oxidized to its cation.

The overall oxidation of 4,4'-biphenol by Ir^{IV} as in eq 2-5 is close to thermoneutral at pH = 1 because $E^o(4,4'\text{-biphenoquinone}, 2\text{H}^+/4,4'\text{-biphenol}) = 0.94 \text{ V vs NHE}^{92}$ while

$E^\circ(\text{Ir}^{\text{IV}}/\text{Ir}^{\text{III}}) = 0.893 \text{ V}$).⁹³ This reaction becomes more favorable as the pH increases. In view of the overall stoichiometry (eq 2-5) and the two-term rate law (eq 2-2), a reasonable reaction mechanism is



Here, direct oxidation of the biphenol generates the biphenosemiquinone through a concerted electron-proton-transfer mechanism. This step is uphill and, hence, is shown as reversible because $E^\circ(4,4'\text{-HOC}_6\text{H}_4\text{C}_6\text{H}_4\text{O}^\bullet, \text{H}^+/4,4'\text{-HOC}_6\text{H}_4\text{C}_6\text{H}_4\text{OH}) = 1.21 \text{ V}$ [calculated from $E^\circ(\text{ArO}^\bullet, \text{H}^+/\text{ArOH}) = E^\circ(\text{ArO}^\bullet/\text{ArO}^-) + 0.059 \text{ p}K_a$ with $E^\circ(\text{ArO}^\bullet/\text{ArO}^-) = 0.64 \text{ V vs NHE}^{85}$]. Oxidation of the conjugate base of biphenol occurs through simple electron transfer; both of these are in direct analogy with the oxidation of phenol. The fate of the semiquinone could be either disproportionation as in eq 2-9, or further oxidation, as in eq 2-10. Disproportionation was reported previously for the semiquinone in the absence of good oxidants;⁸⁹ although the disproportionation rate constant was not determined, it can be expected to be large because the reaction has a large driving force: $E^\circ(4,4'\text{-biphenoquinone}, 2\text{H}^+/4,4'\text{-biphenol}) = 0.94 \text{ V vs NHE}^{92}$ and $E^\circ(4,4'\text{-HOC}_6\text{H}_4\text{C}_6\text{H}_4\text{O}^\bullet, \text{H}^+/4,4'\text{-HOC}_6\text{H}_4\text{C}_6\text{H}_4\text{OH}) = 1.21 \text{ V vs NHE}$. On the other hand,

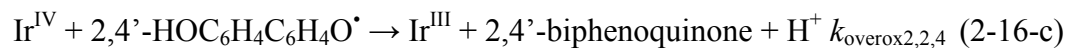
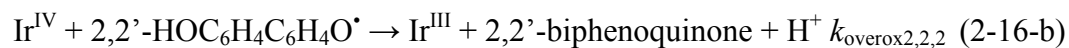
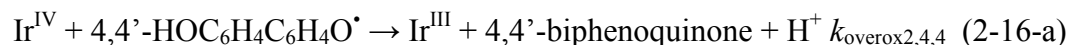
semiquinones are easily oxidized,⁹⁴ and the oxidation of 4,4'-biphenosemiquinone is quite favorable: $E^\circ(4,4'\text{-biphenoquinone}, \text{H}^+ / 4,4'\text{-biphenosemiquinone}) = 0.67 \text{ V}$ (as calculated from the above data). Moreover, the semiquinone is relatively acidic with a $\text{p}K_{\text{a}}$ of 6.3 for $4,4'\text{-HOC}_6\text{H}_4\text{C}_6\text{H}_4\text{O}^\cdot$.⁸⁵ Clearly, a large rate constant can be anticipated for k_{semi} . The low steady-state concentration of the semiquinone ensures that its reaction with Ir^{IV} will be dominant.

2,2'-biphenol is more acidic than 4,4'-biphenol by about 2 $\text{p}K$ units. This difference is attributed to the formation of an internal hydrogen bond between the two O atoms oxygens in the 2,2'-biphenolate monoanion. The value of k_{ArO^-} is about a factor of 100 less for 2,2'-biphenol than for 4,4'-biphenol (for reasons discussed below). The result of these two effects is that the rates of oxidation of the two biphenol isomers are quite similar at $\text{pH} = 7$. On the other hand, the value for k_{ArOH} is 10000-fold less for 2,2'-biphenol, so the pH -independent region of the rate law is limited to only quite acidic conditions (Figure 2-16). Despite these quantitative differences, we infer the same qualitative mechanism for oxidation of the two substrates.

Unlike 2,2'-biphenol, 2,4'-biphenol is incapable of internal hydrogen bonding and thus resembles 4,4'-biphenol quite closely in its oxidation by Ir^{IV} .

4-Phenoxyphenol has a $\text{p}K_{\text{a}}$ value and values for k_{ArOH} and k_{ArO^-} that are similar to those of 4,4'-biphenol, and hence its rate- pH profile is similar. Upon oxidation, it yields the 4-phenoxyphenoxy radical rather than a semiquinone, and hence the ultimate product is due to radical coupling.

The above considerations lead to the following mechanism for the overall oxidation of phenol:



The first step in this mechanism corresponds to the reversible concerted proton-electron-transfer oxidation of neutral phenol, and the second step is the reversible outer-sphere electron-transfer from the phenolate anion. The acid/base reaction relating phenol and phenolate (eq 2-13) is assumed to be at equilibrium because of rapid proton transfer. Values for k_{ArOH} and k_{ArO^-} are directly measured as described above, while values for K_{ArOH} and K_{ArO^-} are calculated from the forward rate constants and the E_f values at $\mu =$

0.1 M: $E_f(\text{Ir}^{\text{IV}}/\text{Ir}^{\text{III}}) = 0.893 \text{ V}$,⁹³ $E_f(\text{C}_6\text{H}_5\text{O}^\bullet/\text{C}_6\text{H}_5\text{O}^-) = 0.80 \text{ V}$, corrected from 0.79 V at $\mu = 0.0 \text{ M}$ ⁸⁸ by $\log \gamma = -Az_i^2\mu^{1/2}/(1 + \mu^{1/2})$, and $E_f(\text{C}_6\text{H}_5\text{O}^\bullet, \text{H}^+/\text{C}_6\text{H}_5\text{OH}) = 1.38 \text{ V}$ [calculated from $E_f(\text{ArO}^\bullet, \text{H}^+/\text{ArOH}) = E_f(\text{ArO}^\bullet/\text{ArO}^-) + 0.059\text{p}K_a$]. Dimerization of the phenoxy radical, which can be partially rate-limiting under certain conditions, forms the four major coupling isomers: 4,4'-, 2,2'-, and 2,4'-biphenol and 4-phenoxyphenol. Under the assumption that the dimerization rate constant producing each species is proportional to its yield, $k_{\text{dim},4,4}$, $k_{\text{dim},2,2}$, $k_{\text{dim},2,4}$ and $k_{\text{dim},\text{pop}}$ in eqs 2-14 a-d are $2.88 \times 10^8 \text{ M}^{-1} \text{ s}^{-1}$, $2.07 \times 10^8 \text{ M}^{-1} \text{ s}^{-1}$, $5.06 \times 10^8 \text{ M}^{-1} \text{ s}^{-1}$, and $1.04 \times 10^8 \text{ M}^{-1} \text{ s}^{-1}$, respectively, according to the reported overall $2k_{\text{dim}}$ value⁹⁵ and yield of each isomer.⁸³

Further one-electron oxidations of the phenol coupling products are shown in eqs 2-15 a-d without reference to the pH dependence evident in Figure 2-16. In our simulations described below, the rate constants for these steps, $k_{\text{overox}1,4,4}$, $k_{\text{overox}1,2,2}$, $k_{\text{overox}1,2,4}$ and $k_{\text{overox}1,\text{pop}}$, are conditional on the pH and are derived from the parameters in Table 2-5. Eqs 2-16 a-c depict the semiquinones as undergoing oxidation by Ir^{IV} ; in the simulations, we assign rapid rate constants for these oxidations, but the results are insensitive to the exact values used. Eq 2-16-d depicts a rapid second-order decay through dimerization for the phenoxyphenoxy radical based on analogy with other phenoxy radicals.

Kinetic simulations of the oxidation of phenol based on the above mechanism were performed by the use of the *Specfit/32* computer program,⁹⁶ with the exact model specified in Table 2-7. These simulations yielded decays of $[\text{Ir}^{\text{IV}}]$, the half-lives of which were then used to generate simulated pseudo-first-order rate constants, $k_{\text{obs},\text{sim}}$. Figure 2-22a (data from Table 2-9) shows that these results give an excellent fit to the experimental pH dependence of the reaction. Figure 2-22b compares the simulated results

Table 2-7. The Mechanism of Phenol Reaction and the Simulation Model.

Equations	Kinetic Parameter ^a	Reactions in the model	Species
eq 2-11	$k_{\text{ArOH}} = 0.31$	$A + B \rightarrow C + D + E$	k_1 A = Ir ^{IV}
	$k_{-\text{ArOH}} = 5.0 \times 10^7$	$C + D + E \rightarrow A + B$	k_{-1} B = C ₆ H ₅ OH
eq 2-12	$k_{\text{ArO}^-} = 4.0 \times 10^6$	$A + F \rightarrow C + D$	k_2 C = Ir ^{III}
	$k_{-\text{ArO}^-} = 1.0 \times 10^5$	$C + D \rightarrow A + F$	k_{-2} D = C ₆ H ₅ O [•]
eq 2-13	$K_a = 1.6 \times 10^{-10}$	$B \rightarrow E + F$	k_3 E = H ⁺
		$E + F \rightarrow B$	k_{-3} F = C ₆ H ₅ O ⁻
		$B + G \rightarrow F + H$	k_4 G = OH ⁻
		$F + H \rightarrow B + G$	k_{-4} H = H ₂ O
Buffer	$K = K_a/K_w$	$I \rightarrow J + E$	k_5 I = Buffer
		$J + E \rightarrow I$	k_{-5} J = Conjugate Base
		$I + G \rightarrow J + H$	k_6
		$J + H \rightarrow I + G$	k_{-6}
eq 2-14-a	$k_{\text{dim}, 4,4} = 2.9 \times 10^8$	$2 * D \rightarrow K$	k_7 K = 4,4'-biphenol
eq 2-14-b	$k_{\text{dim}, 2,3} = 2.1 \times 10^8$	$2 * D \rightarrow L$	k_8 L = 2,2'-biphenol
eq 2-14-c	$k_{\text{dim}, 2,4} = 5.1 \times 10^8$	$2 * D \rightarrow M$	k_9 M = 2,4'-biphenol
eq 2-14-d	$k_{\text{dim}, \text{pop}} = 1.0 \times 10^8$	$2 * D \rightarrow N$	k_{10} N = 4-phenoxyphenol
eq 2-15-a	$k_{\text{overox}1, 4,4}: \text{known}^b$	$A + K \rightarrow C + O + E$	k_{11} O = 4,4'-HOArArO [•]
eq 2-15-b	$k_{\text{overox}1, 2,2}: \text{known}^b$	$A + L \rightarrow C + P + E$	k_{12} P = 2,2'-HOArArO [•]
eq 2-15-c	$k_{\text{overox}1, 2,4}: \text{known}^b$	$A + M \rightarrow C + Q + E$	k_{13} Q = 2,4'-HOArArO [•]
eq 2-15-d	$k_{\text{overox}1, \text{pop}}: \text{known}^b$	$A + N \rightarrow C + R + E$	k_{14} R = 4-C ₆ H ₅ OC ₆ H ₄ O [•]
eq 2-16-a	$k_{\text{overox}2, 4,4} = 1.0 \times 10^9$	$A + O \rightarrow C + S + E$	k_{15} S = 4,4'-BPQ
eq 2-16-b	$k_{\text{overox}2, 2,2} = 1.0 \times 10^9$	$A + P \rightarrow C + T + E$	k_{16} T = 2,2'-BPQ
eq 2-16-c	$k_{\text{overox}2, 2,4} = 1.0 \times 10^9$	$A + Q \rightarrow C + U + E$	k_{17} U = 2,4'-BPQ
eq 2-16-d	$k_{\text{dec}, \text{pop}} = 1.0 \times 10^9$	$2 * R \rightarrow V$	k_{18} V = 4-P
eq 2-18	$k_{\text{DBNBS}} = 2.0 \times 10^5$	$D + W \rightarrow X$	k_{19} W = DBNBS
eq 2-19	$k_{\text{adduct}} = 1.0 \times 10^7$	$A + X \rightarrow C + Y$	k_{20} X = Adduct [•]
eq 2-17	$k_{\text{dim}, \text{DBS}} = 1.3 \times 10^6$	$Z \rightarrow 2 * W$	k_{21} Y = Adduct ⁺
	$k_{-\text{dim}, \text{DBS}} = 1.0 \times 10^9$	$2 * W \rightarrow Z$	k_{-21} Z = DBNBS dimer

^a Rate constants k (M⁻¹ s⁻¹), acid dissociation constant K_a and water dissociation constant $K_w = 1.0 \times 10^{-14}$. ^b See Table 2-8.

Table 2-8. The Overoxidation Rate Constants at Different $p[H^+]$ Obtained from the Curve Fit of Figure 2-16.

$p[H^+]$	$k_{\text{overox1, 4,4}}, M^{-1} s^{-1}$	$k_{\text{overox1, 2,2}}, M^{-1} s^{-1}$	$k_{\text{overox1, 2,4}}, M^{-1} s^{-1}$	$k_{\text{overox1, pop}}, M^{-1} s^{-1}$
1.30	4.6×10^4	8.6	4.0×10^3	1.2×10^3
2.46	4.6×10^4	36	4.0×10^3	1.2×10^3
2.86	4.6×10^4	80	4.0×10^3	1.2×10^3
3.39	4.6×10^4	2.4×10^1	4.0×10^3	1.2×10^3
3.99	4.8×10^4	1.0×10^3	4.2×10^3	1.4×10^3
4.59	5.2×10^4	4.0×10^3	5.1×10^3	1.7×10^3
5.36	7.9×10^4	2.4×10^4	1.0×10^4	4.3×10^3
6.18	2.6×10^5	1.4×10^5	4.5×10^4	2.1×10^4
6.74	8.2×10^5	4.9×10^5	1.5×10^5	7.5×10^4

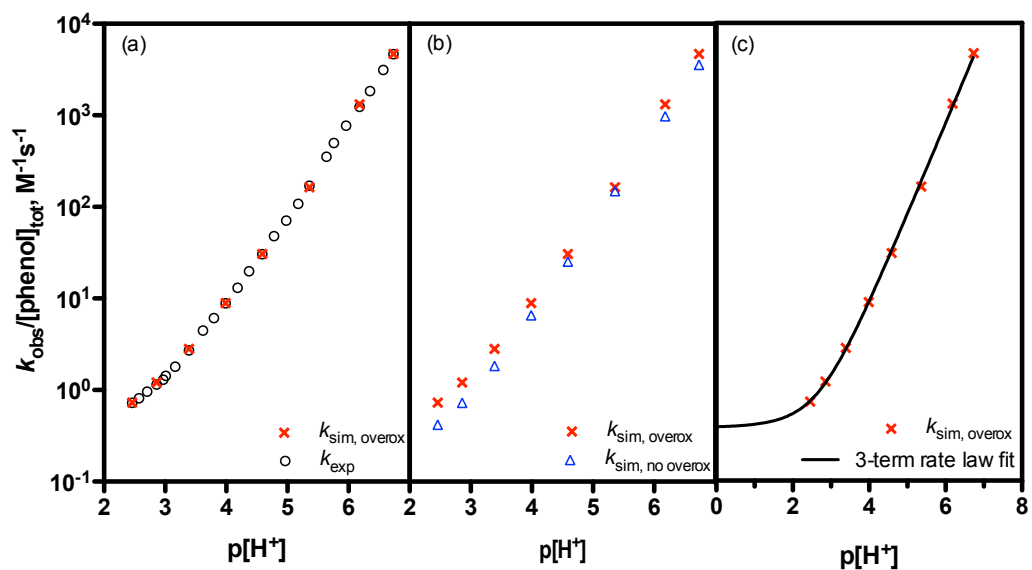


Figure 2-22. Comparative pH dependence of the phenol reaction experimental data and simulation results. (a) The experimental data and simulated results with overoxidation. (b) The simulated results with and without overoxidation. (c) The simulated result with overoxidation and its 3-term rate law curve fit.

Table 2-9. Comparison of the Experimental Data with Overoxidation and No Overoxidation Simulation Results of the Phenol Reaction at Different p[H⁺] in Absence of DBNBS.^a

p[H ⁺]	[phenol] _{tot} × 10 ³ , M	<i>k</i> _{exp} ^b M ⁻¹ s ⁻¹	<i>k</i> _{sim, overox} ^c M ⁻¹ s ⁻¹	<i>k</i> _{sim, no overox} ^d M ⁻¹ s ⁻¹	Stoich. factor ^e
2.46	44.3	7.26 × 10 ⁻¹	7.30 × 10 ⁻¹	4.18 × 10 ⁻¹	1.75
2.86	44.3	1.15	1.21	7.26 × 10 ⁻¹	1.67
3.39	44.3	2.71	2.82	1.84	1.54
3.99	44.3	8.87	8.92	6.55	1.36
4.59	44.3	30.4	30.7	25.2	1.22
5.36	44.3	170	164	149	1.10
6.18	4.43	1.24 × 10 ³	1.32 × 10 ³	978	1.35
6.74	4.43	4.67 × 10 ³	4.67 × 10 ³	3.56 × 10 ³	1.31

^a [Ir^{IV}]₀ = 1 × 10⁻⁴ M; The following buffers (0.02 M) were employed to maintain constant p[H⁺] values: monochloroacetate buffer for 2.4 < p[H⁺] < 3.4, acetate buffer for 3.9 < p[H⁺] < 5.4, and cacodylate buffer for 6.1 < p[H⁺] < 6.8. ^b From Table A-2. ^c Calculated from the half live of overoxidation simulation model with *k*_{overox1} and *k*_{overox2}; The series of rate constants *k*_{overox1} at different p[H⁺] are generated from each curve in Figure 2-16. ^d Calculated from the half live of no overoxidation simulation model (*k*_{overox} = 0 and *k*_{disp} = 0). ^e pH-dependent stoichiometric factor = *k*_{sim, overox}/*k*_{sim, no overox}.

from the full mechanism with those obtained when overoxidation (eqs 2-15 a-d and 2-16 a-d) is excluded from the mechanism, and it shows that overoxidation increases the net rates at low pH but less so at higher pH. As a result, overoxidation leads to a pH dependence that deviates systematically from the simple two-term rate law in eq 2-2. Figure 2-22c shows that the simulations with overoxidation included give an excellent fit to the three-term rate law (eq 2-3), with fitted values of $k_{ArOH} = 0.38 \pm 0.14 \text{ M}^{-1} \text{ s}^{-1}$, $k_{ArO^-} = (4.9 \pm 0.2) \times 10^6 \text{ M}^{-1} \text{ s}^{-1}$ and $k^o = (8.2 \pm 7) \times 10^{-3} \text{ M}^{-1} \text{ s}^{-1}$. Although the statistical uncertainty in k^o is large, the value of k^o is in good agreement with the value derived from the experimental data. Evidently, the origin of the k^o term in the fit of empirical rate law (2-3) to the experimental results is the pH-dependent influence of overoxidation on the rate of consumption of Ir^{IV} .

If overoxidation were not occurring, the rate constants in eq 2-2 would agree exactly with those in the mechanism, corresponding to a stoichiometric factor of unity in the rate law. An effect of overoxidation is that the rate constants derived from eq 2-2 are somewhat larger than the rate constants for the elementary steps, which means that overoxidation introduces stoichiometric factors greater than unity. These stoichiometric factors, calculated as the ratio $k_{\text{sim}}(\text{with overoxidation})/k_{\text{sim}}(\text{without overoxidation})$, decrease systematically from 1.75 at pH 2.46 to 1.10 at pH 5.36 (Table 2-9). They also depend somewhat on the phenol concentration. It is the pH dependence of the stoichiometric factor that leads to the k^o term in rate law (2-3).

Another consequence of the pH-dependent stoichiometric factor is that the yields of the reaction products are also pH-dependent. As shown in Table 2-10, at pH 2.46 the simulated yield of the initial coupling products per 1 mol of Ir^{IV} (corrected for the 1:2

Table 2-10. Simulation Product Concentrations of the Phenol Reaction at Different p[H⁺]
Without DBNBS.^a

Species	p[H ⁺] = 2.46		p[H ⁺] = 5.36	
	[Product] × 10 ⁶ , M	% of Ir ^{IVb}	[Product] × 10 ⁶ , M	% of Ir ^{IVb}
4,4'-BP	1.15 × 10 ⁻³		6.98	
2,2'-BP	4.67		6.98	
2,4'-BP	6.46 × 10 ⁻²	9.6%	18.6	72.9%
4-POP	0.138		3.95	
4,4'-BPQ	7.28		4.27	
2,2'-BPQ	0.582		1.16	
2,4'-BPQ	12.8	90.4%	1.25	27.1%
4-P	1.26		0.059	

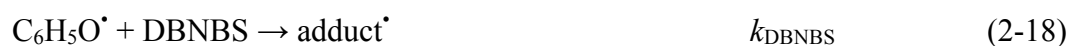
^a [Ir^{IV}]₀ = 1 × 10⁻⁴ M; p[H⁺] = 2.46 was maintained by means of a 0.02 M

monochloroacetate buffer; p[H⁺] = 5.36 was maintained using a 0.02 M acetate buffer. ^b

Percentage of Ir^{IV} was converted for four products. One equivalent of biphenol product was formed from the reaction of phenol with two equivalents of Ir^{IV}, and one equivalent of biphenoquinone product was obtained from four equivalents of Ir^{IV}.

stoichiometric ratio) is 9.6% and the yield of the overoxidation products (corrected for the 1:4 stoichiometric ratio) is 90.4%. However, at pH 5.36 these yields cross over to 72.9% and 27.1%, respectively.

In the presence of the spin-trap DBNBS, three more steps are added to the above mechanism:



As mentioned above, only the monomer of DBNBS can scavenge the phenoxy radical. Therefore, the dimerization step of DBNBS with equilibrium constant $K_{\text{dim,DBNBS}}$ of $1.3 \times 10^{-3} \text{ M}$ should be included in our mechanism.⁸⁰ The phenoxy radical is scavenged by DBNBS to form an adduct which undergoes a rapid oxidation by Ir^{IV} , as in eqs 2-18 and 2-19. Competition between the scavenging of the phenoxy radical by DBNBS and its dimerization is evident in the kinetic saturation dependence on $[\text{DBNBS}]$, as shown in Table 2-3. Simulations of this saturation effect at $\text{p}[\text{H}^+] = 1.3$, performed with the mechanism in Table 2-7, are sensitive to the value of k_{DBNBS} . As shown in Table 2-11, a good fit is obtained when the rate constant of $\text{C}_6\text{H}_5\text{O}^\bullet/\text{DBNBS}$ adduct formation, k_{DBNBS} , is $2.0 \times 10^5 \text{ M}^{-1} \text{ s}^{-1}$. This rate constant is large enough to enable 10 mM concentrations of DBNBS to scavenge the phenoxy radicals completely, preventing their backreaction with Ir^{III} and ensuring that the rate-limiting step in the oxidation by Ir^{IV} is the initial oxidation of phenol.

Table 2-11. Comparison of the Experimental Data with Overoxidation Simulation Results of the Phenol Reaction in the Presence of Ir^{III} or Various DBNBS Concentration.^a

[Ir ^{III}] ₀ , M	[DBNBS], mM	<i>t</i> _{1/2, exp} , ^b S	<i>t</i> _{1/2, sim} , ^c S
0	0	8.0	5.4
0	0.1	6.7	5.0
0	1.0	4.4	3.8
0	5.0	2.7	3.0
0	10	2.7	2.8
0	15	2.5	2.8
5 × 10 ⁻⁴	0	255	271

^a [Ir^{IV}]₀ = 1 × 10⁻⁴ M; [phenol] = 0.443 M; [HClO₄] = 0.05 M. ^b From Table 2-2. ^c From overoxidation simulation model with *k*_{overox1}, *k*_{overox2}, *k*_{DBNBS}, *k*_{adduct}, *k*_{dim,DBS} and *k*_{-dim,DBS}; the series of rate constants *k*_{overox1} at p[H⁺] = 1.3 is from Table 2-8.

A remaining question is the origin of the pH dependence of the $[\text{Ru}(\text{bpy})_3]^{3+}$ /phenol reaction reported by Sjodin et al., which required the three-term eq 2-3.⁵⁰ First, we note that Bonin et al. were unable to reproduce the effect and found the two-term eq 2-2 to be adequate.²⁵ Second, the degree of overoxidation to be expected depends on the phenol concentration, and this concentration was not disclosed in the original report. Third, the degree of overoxidation should also depend on the rate constants for $[\text{Ru}(\text{bpy})_3]^{3+}$ oxidation of the phenolic coupling products, and these rate constants are unknown. However, it can be shown that a significant degree of overoxidation should occur in acidic media if favorable choices are made for the reactant concentrations and rate constants.

Rate Constant Trends. Table 2-5 shows that the values for k_{ArO^-} range from 4.0×10^6 to $6.5 \times 10^8 \text{ M}^{-1} \text{ s}^{-1}$ for the five phenolate ions considered in this study. These rate constants correspond to electron-transfer reactions, and hence it is reasonable to use the cross-relationship of Marcus theory, as given in eqs 1-12 to 1-15 to rationalize their variations.⁹⁷

In these equations, k_{12} is the cross-electron-transfer rate constant ($k_{\text{ArO}^-} = 8.0 \times 10^6 \text{ M}^{-1} \text{ s}^{-1}$ for phenoxide), and k_{11} and k_{22} are the self-exchange rate constants of the $\text{C}_6\text{H}_5\text{O}^\bullet/\text{C}_6\text{H}_5\text{O}^-$ and $\text{Ir}^{\text{IV}}/\text{Ir}^{\text{III}}$ redox couples, respectively. A value for k_{22} of $2 \times 10^5 \text{ M}^{-1} \text{ s}^{-1}$ is used in the calculation,⁹⁸ and $1 \times 10^{11} \text{ M}^{-1} \text{ s}^{-1}$ is used for Z , the collision frequency.⁹⁹ Z_i , Z_j are ionic charges of the reactants, R is the ideal gas constant, and r is the center to center distance between two reactants when they are approaching to each other. The radii of $[\text{IrCl}_6]^{2-}$ and $\text{C}_6\text{H}_5\text{O}^-$ are 4.1 \AA ⁵⁸ and 2.5 \AA , respectively, estimated from Corey–Pauling–Koltun atomic models. μ is the ionic strength. w_{ij} is the electrostatic energy

between reactants i and j . If the distance r is in angstroms and μ in molar, then w_{12} can be calculated according to eq 1-15 in kilojoules per mole. With all of these parameters and the experimental values of k_{12} and K_{12} , k_{11} is calculated from the above equations as $2.3 \times 10^6 \text{ M}^{-1} \text{ s}^{-1}$. The phenoxide anion and the phenoxyl radical are predicted to have quite similar structures, with the largest difference being a 0.015 \AA change in the C–O bond length.¹⁰⁰ Such a small structural change should not contribute significantly to the self-exchange barrier. Estimates of the solvation contribution to the self-exchange barrier ($\Delta G_{\text{os}}^\ddagger$) are difficult to make because the phenolate charge is highly localized on the oxygen end of the anion; however, this charge localization should cause $\Delta G_{\text{os}}^\ddagger$ to be larger than that for a spherical anion of comparable size. As a result, the significant overall self-exchange barrier implied by the k_{11} above value is attributed principally to the solvent barrier. A significantly greater value for k_{11} of $1.9 \times 10^8 \text{ M}^{-1} \text{ s}^{-1}$ was previously measured directly by electron spin resonance line broadening.¹⁰¹ Apparently, the solvent barrier is reduced in the actual self-exchange process, possibly through a weak association between the radical and the phenoxide anion.

In the case of the 4,4'-biphenoxide anion [$E^\circ(\text{ArO}^\bullet/\text{ArO}^-) = 0.64 \text{ V}$],⁸⁵ k_{ArO^-} is considerably larger than that for phenoxide itself. Most of this increase can be ascribed to the greater driving force for the reaction, but there is also some contribution from a greater self-exchange rate constant ($k_{11} = 4 \times 10^7 \text{ M}^{-1} \text{ s}^{-1}$). A reduced self-exchange barrier can be attributed to the delocalized electronic structure of the semiquinone radical.

The 2,2'-biphenoxide anion is considerably more difficult to oxidize [$E^\circ(\text{ArO}^\bullet/\text{ArO}^-) = 1.00 \text{ V}$]⁸⁵ than phenoxide, but the two substrates have quite similar k_{ArO^-} values. A large self-exchange rate constant of $3 \times 10^8 \text{ M}^{-1} \text{ s}^{-1}$ is required by these data. It is

conceivable that the internal hydrogen bonding in the 2,2' isomer reduces the degree of hydrogen bonding with the solvent and thus leads to a greater k_{11} value. Corresponding discussions of the 2,4'-biphenoxide and 4-phenoxyphenoxide rates will require determination of the relevant E° values.

We have previously argued that the direct oxidation of phenol by Ir^{IV} (eq 2-11, k_{ArOH}) involves proton transfer to the solvent in concert with electron transfer (H_2O -CPET).²⁷ This mechanistic assignment was based largely on the significant solvent deuterium KIE, the high acidity of the $\text{ArOH}^{+\bullet}$ radical cation, and the low basicity of Ir^{III} . This conclusion is strengthened by the CV measurements described above, which show that Ir^{III} is not significantly protonated in 1 M H^+ . Further support for this H_2O -CPET mechanism is provided by a linear free-energy relationship that relates the rates of oxidation of phenol to the E° values for Ir^{IV} and a set of three Ru^{III} oxidants.²⁵ It seems reasonable to assign a H_2O -CPET mechanism to all of the phenol reactions in Table 2-5. Recently, Bonin et al. have developed a theoretical treatment of CPET reactions with water (and other bases) as the proton acceptor;²⁶ this theory predicts, in the absence of other effects, that these reactions should display a typically Marcusian dependence of the rates on the driving forces. Qualitatively, Table 2-5 shows that this expectation is met in comparing phenol with 4,4'-biphenol and in comparing 4,4'-biphenol with 2,2'-biphenol. However, 2,2'-biphenol reacts 9 times faster than phenol, even though it is 0.07 V more difficult to oxidize. This apparent contradiction may signal the importance of several other variables in the theory of H_2O -CPET.

Chapter 3

OXIDATION OF ALKYL- AND ALKOXY-SUBSTITUTED PHENOLS BY HEXACHLOROIRIDATE(IV)

3.1 Introduction

Substituted phenols have been widely found in nature and have important pharmaceutical, medicinal and chemical applications.³⁰⁻³⁷ The mono- or poly-substituents alter the properties of phenol such as electronic effects, steric hindrance, hydrophobicity, hydrophilicity and hydrogen-bonding effect.¹⁰² Among those substituents, the methyl, *t*-butyl and methoxy groups are the simplest ones that have been involved in research over one century and their properties are well investigated. The diversities in pK_a values and reduction potentials of these phenols generate a wide range of driving forces for their oxidation, and in conjunction with the kinetic data obtained from experiments can elucidate the mechanism of the oxidations.

The oxidation of four alkyl-substituted phenols (2-methylphenol, 2,6-dimethylphenol, 2,4,6-trimethylphenol and 4-*tert*-butylphenol) and one alkoxy-substituted phenol (4-methoxyphenol) by $[\text{IrCl}_6]^{2-}$ are investigated in this chapter. 4-Hydroxymethyl-2,6-dimethylphenol is identified to be one of the products of 2,4,6-trimethylphenol oxidation, which rules out the overoxidation process. Overoxidation could not occur in the reaction between Ir^{IV} and 4-methoxyphenol due to the rapid

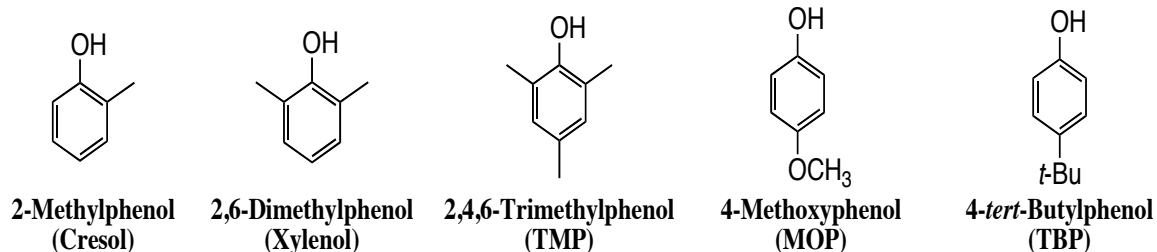
reaction rate. Two-term and three-term rate laws (applied if overoxidation are observed) are used to obtain the rate constants of oxidation of phenols (k_{ArOH}), phenolates (k_{ArO^-}), and overoxidations (k^o). Mechanisms are proposed for these reactions, and Marcus theory is applied to explain both electron transfer and H₂O-CPET processes.

3.2 Experimental Section

3.2.1 Reagents and Solutions

All commercial chemical reagents were used as received except as noted. 2-Methylphenol (cresol), 2,6-dimethylphenol (xylenol), 2,4,6-trimethylphenol (abbreviated as TMP), 4-methoxyphenol (abbreviated as MOP), methoxybenzene (anisole), ammonium hexachloroiridate(III) monohydrate (abbreviated as Ir^{III}), disodium 2,6-pyridinedicarboxylate (abbreviated as dipic), deuterium oxide, sodium acetate anhydrous, cacodylic acid and sodium hydroxide were purchased from Sigma–Aldrich Chemicals Co. 4-*tert*-Butylphenol (abbreviated as TBP) was received from Fluka. Perchloric acid, ammonium perchlorate, sodium chloride, ammonium chloride, copper(II) nitrate trihydrate, acetic acid, monochloroacetic acid, formaldehyde solution, toluene, and ethyl acetate were obtained from Fisher Scientific Co. Ammonium hexachloroiridate(IV) (abbreviated as Ir^{IV}) was purchased from Alfa or prepared according to the literature⁶¹ by addition of ammonium chloride (Fisher) to a solution of sodium hexachloroiridate(IV) hexahydrate. All spin trapping agents utilized in this study were as described in Chapter 2. The structures of reductants used in this work are shown in Scheme 3-1.

Efforts to study the oxidation of 4-methylphenol were stymied by our inability to obtain this reagent in sufficient purity. All attempts yielded a significant contamination



Scheme 3-1. Structures of reductants.

by 2-methylphenol.

All solutions were freshly prepared with deionized water provided by a Barnstead NANO Pure Infinity ultrapure water system, and purged with argon gas prior to the reactions to prevent potential complications caused by O₂. The ionic strength was adjusted by lithium perchlorate trihydrate (GFS) and was approximately equal in both oxidants and resultants solutions to prevent Schlieren effects (or refractive index effect⁶³). Selected buffer solutions (acetate, monochloroacetate, and cacodylate buffers) were applied to control the pH if necessary.

Preparation of 4-Hydroxymethyl-2,6-dimethylphenol. This compound was prepared as described previously.¹⁰³ A 37% formaldehyde solution (0.818 g) was added to a 1 mL toluene solution of 2,6-dimethylphenol (10 mmol). Then, A 48% NaOH solution (0.833 g) was slowly added into the above solution at 10 °C with stirring. After reacting 20 h at 25 °C, the solution was poured into 15 mL water and neutralized by acetic acid. The precipitate was collected and recrystallized from ethyl acetate to yield the final product. Yield: 60%. Mp: 104–105 °C. ¹H NMR (D₂O): δ 2.22 (s, 6H), 4.48 (s, 2H), 7.04 (s, 2H).

3.2.2 Methods

A Corning 450 pH/ion meter was used with a Mettler Toledo InLab 421 or InLab Semi-Micro-L combination pH electrode. The reference electrode electrolyte was replaced with 3 M NaCl to prevent the formation of KClO_4 precipitate. With the known H^+ concentration and pH reading, the activity coefficient γ ($= 0.839 \pm 0.04$) was obtained from equation $\text{p}[\text{H}^+] = \text{pH} + \log \gamma$, where $\text{p}[\text{H}^+]$ is equal to $-\log [\text{H}^+]$.

All measurements were performed at 25.0 ± 0.1 °C. The kinetics experiments were carried out on a Hi-Tech SF-51 stopped-flow spectrophotometer with OLIS 4300 data acquisition and analysis software. UV-vis spectra were monitored on a HP-8453 diode array spectrophotometer equipped with a Brinkman Lauda RM6 thermostated water bath to maintain the temperature at 25 °C. All kinetics data were obtained by monitoring the absorbance of Ir^{IV} at 488 nm. The observed pseudo-first-order rate constants were obtained from fitting kinetic traces over five half lives to first-order exponential functions and each reported observed rate constant is the average of at least 5 shots. The Specfit/32 version 3.0.15 global analysis system was applied to simulate the reaction traces, and the GraphPad Prism 4 or 5 software was used to analyze the rate law with $1/Y^2$ weighting. ^1H NMR spectra were acquired on a Bruker AV 400 MHz spectrometer; chemical shifts in D_2O are relative to DSS. The melting points were obtained using an Electrothermal IA 9100 digital melting point apparatus.

3.3 Results

3.3.1 The Oxidation of 2-Methylphenol

A kinetic trace for the consumption of 1×10^{-4} M Ir^{IV} in its reaction with 0.01 M cresol under acidic conditions ($[\text{HClO}_4] = 0.05$ M), as shown in Figure 3-1, does not yield a good fit to a first-order rate law.

Hexachloroiridate(III) Inhibition. We tested the Ir^{III} inhibition effect on the cresol oxidation at different $\text{p}[\text{H}^+]$ (= 1.3, 2.52 and 4.24) with a 5-fold excess of Ir^{III} . A strong inhibiting effect was observed when the reaction was run in 0.05 M HClO_4 with 0.02 M cresol (Figure 3-2a). This inhibition implies an outer-sphere electron transfer mechanism for the oxidation of cresol by Ir^{IV} . As the $\text{p}[\text{H}^+]$ increased to 2.52, the reaction became faster and the additional Ir^{III} had less of an impact (Figure 3-2b). Subsequently, we detected a small perturbation with added Ir^{III} at $\text{p}[\text{H}^+] = 4.24$ (Figure 3-2c).

Spin Trapping Effect. In order to get better fits to pseudo-first order kinetics and minimize the inhibition by Ir^{III} , the cresol reactions were run in the presence of spin trapping agents. The conventional spin traps illustrated in Scheme 2-1 were investigated for their effects on the kinetics of the cresol/ Ir^{IV} reaction in 0.05 M H^+ . The reaction details are summarized in Table 3-1. The oxidation of 0.02 M cresol by 1×10^{-4} M Ir^{IV} with a 5-fold excess of Ir^{III} in presence of 2 mM DNBBS was found to effectively decrease the half-life of the reaction, whereas the other scavengers have little impact. The reaction between 0.01 M cresol and 1×10^{-4} M Ir^{IV} with 1 mM DNBBS yields an excellent pseudo-first-order fit as shown in Figure 3-3. This demonstrates that DNBBS can act as an efficient phenoxy radical scavenger under these conditions.

2-Methylphenol Dependence. In presence of 1 mM DNBBS, the reactions between various concentrations of cresol (0.001–0.02 M) and 1×10^{-4} M of Ir^{IV} were carried out under acidic conditions (0.05 M HClO_4). The kinetic data are shown in Table A-7. When

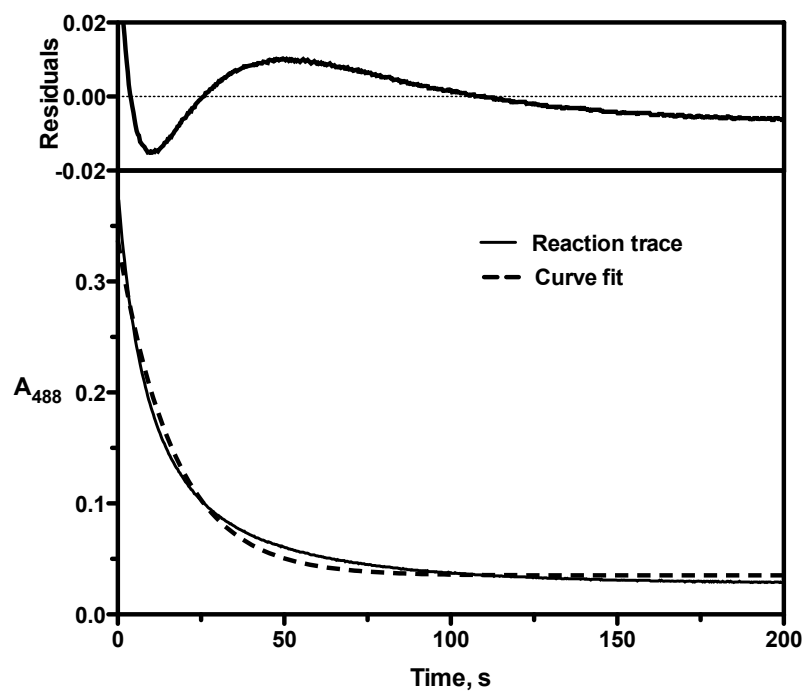


Figure 3-1. Kinetic trace of the Ir^{IV} consumption in the cresol oxidation. Lower box shows the experimental trace (solid line) and the pseudo-first-order fit (dashed line). Upper box shows the residuals in the fit. $[\text{Ir}^{\text{IV}}]_0 = 1 \times 10^{-4} \text{ M}$; $[\text{cresol}]_{\text{tot}} = 0.01 \text{ M}$; $[\text{HClO}_4] = 0.05 \text{ M}$; $\mu = 0.1 \text{ M (LiClO}_4)$; $T = 25 \text{ }^\circ\text{C}$.

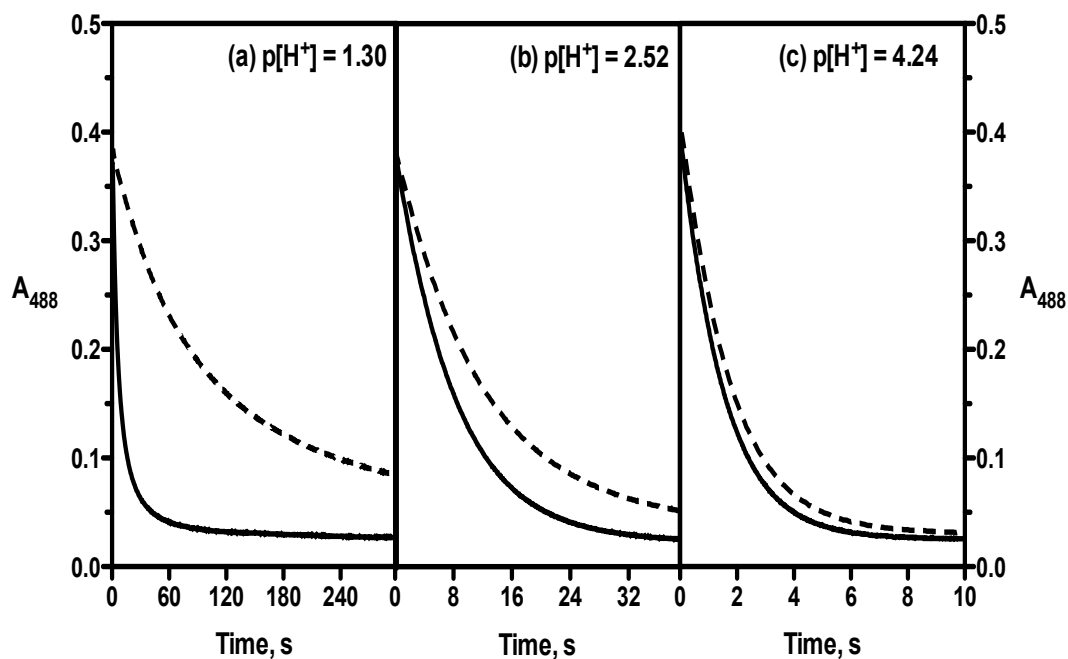


Figure 3-2. Comparative traces of the cresol reaction with Ir^{IV} (solid line) and in the presence of added Ir^{III} (dashed line) in H_2O . $[\text{Ir}^{\text{IV}}]_0 = 1 \times 10^{-4} \text{ M}$; $[\text{Ir}^{\text{III}}]_0 = 5 \times 10^{-4} \text{ M}$; $\mu = 0.1 \text{ M}$ (LiClO_4); $T = 25 \text{ }^\circ\text{C}$. (a) $[\text{Cresol}]_{\text{tot}} = 0.02 \text{ M}$; $[\text{HClO}_4] = 0.05 \text{ M}$. (b) $[\text{Cresol}]_{\text{tot}} = 0.01 \text{ M}$; $\text{p}[\text{H}^+] = 2.52$ (0.02 M monochloroacetate buffer). (c) $[\text{Cresol}]_{\text{tot}} = 0.01 \text{ M}$; $\text{p}[\text{H}^+] = 4.24$ (0.02 M acetate buffer).

Table 3-1. Kinetic Data for the Reaction Between Cresol and Ir^{IV} with Added Ir^{III} in the Presence of Spin Trapping Agents PBN, DMPO, POBN, MNP, DMNBS and DBNBS.^a

Spin Trapping Agent	t _{1/2} , s
No Spin Trapping Agent	61.1
2 mM PBN	59.7
2 mM DMPO	62.6
2 mM POBN	61.5
2 mM MNP	59.4
2 mM DMNBS	55.8
2 mM DBNBS	7.20

^a [Ir^{IV}]₀ = 1 × 10⁻⁴ M; [cresol]_{tot} = 0.02 M; [Ir^{III}]₀ = 5 × 10⁻⁴ M; [HClO₄] = 0.05 M; μ = 0.1 M (LiClO₄); T = 25 °C.

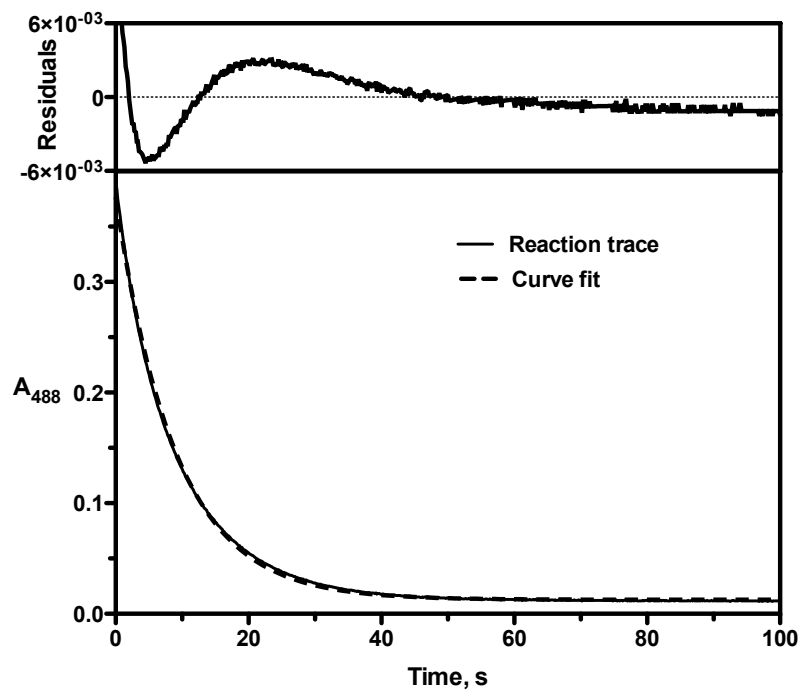


Figure 3-3. Kinetic traces of the cresol reaction with added DNBNS (solid line) and first order fit (dashed line). $[\text{Ir}^{\text{IV}}]_0 = 1 \times 10^{-4} \text{ M}$; $[\text{cresol}]_{\text{tot}} = 0.01 \text{ M}$; $[\text{DNBNS}] = 1 \text{ mM}$; $[\text{HClO}_4] = 0.05 \text{ M}$; $\mu = 0.1 \text{ M (LiClO}_4)$; $T = 25 \text{ }^\circ\text{C}$.

plotting k_{obs} versus [cresol] (Figure 3-4), a good straight line is obtained with a slope equal to $14.06 \pm 0.04 \text{ M}^{-1} \text{ s}^{-1}$ and y-intercept equal to $(1.02 \pm 0.5) \times 10^{-3} \text{ s}^{-1}$, which is equal, within error, to zero. The results indicate that the rate of the reaction exhibits a first order dependence on cresol concentration.

Dependence on $\text{p}[\text{H}^+]$. The influence of $\text{p}[\text{H}^+]$ on the rate of the reaction was examined in the $\text{p}[\text{H}^+]$ range of 1–7 with 1 mM DBNBS. All values of k_{obs} are given in Table A-9. A plot of $k_{\text{obs}}/[\text{cresol}]_{\text{tot}}$ versus $\text{p}[\text{H}^+]$ reveals that the rates increase regularly with increasing $\text{p}[\text{H}^+]$. Generally, the protonated and deprotonated forms of cresol can react with Ir^{IV} through kinetically distinguishable terms, k_{ArOH} and k_{ArO^-} , as shown in the two-term rate law (eq 2-2). A nonlinear least-squares fit of k_{obs} as a function of $\text{p}[\text{H}^+]$ (Figure 3-5) gives $k_{\text{ArOH}} = 16 \pm 1 \text{ M}^{-1} \text{ s}^{-1}$ and $k_{\text{ArO}^-} = (5.2 \pm 0.2) \times 10^7 \text{ M}^{-1} \text{ s}^{-1}$ when holding $\text{p}K_{\text{a}} = 10.09$ at $\mu = 0.1 \text{ M}$ and $25 \text{ }^\circ\text{C}$.⁸¹

A three-term rate law, eq 2-3, was also applied to the data in Table A-9. The values for k_{ArOH} , k_{ArO^-} and k° are: $k_{\text{ArOH}} = 13 \pm 1 \text{ M}^{-1} \text{ s}^{-1}$, $k_{\text{ArO}^-} = (4.5 \pm 0.2) \times 10^7 \text{ M}^{-1}$ and $k^\circ = (0.17 \pm 0.04) \text{ M}^{-1} \text{ s}^{-1}$, respectively, as displayed in Table A-10. The contribution of the additional k° term was calculated over the $\text{p}[\text{H}^+]$ range of 1–7. The maximum value is 28% and occurs at around $\text{p}[\text{H}^+] = 3.6$.

Temperature Dependence. The oxidation of 0.02 M cresol by $2.5 \times 10^{-5} \text{ M}$ of Ir^{IV} in 0.01 M HClO_4 was studied at different temperatures: 8, 15, 25, 35 and $45 \text{ }^\circ\text{C}$. The values of k_{obs} are summarized in Table A-11. Under these conditions, the k_{ArOH} term dominates the reaction kinetics and k_{ArO^-} is negligible. It is reasonable to assume that k_{obs} represents k_{ArOH} . When plotting $\ln(k_{\text{ArOH}}/T)$ versus $1/T$ (Figure 3-6), a linear relationship is obtained with the slope of $-(5.1 \pm 0.1) \times 10^3 \text{ K}$ and intercept equal to 13.6 ± 0.2 .

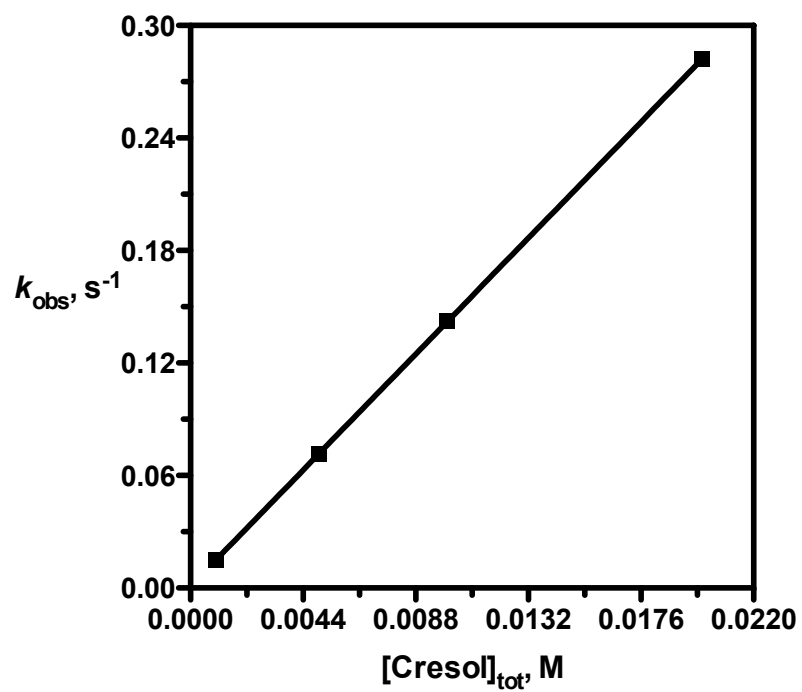


Figure 3-4. Plot of k_{obs} vs $[\text{cresol}]_{\text{tot}}$. $[\text{Ir}^{\text{IV}}]_0 = 1 \times 10^{-4} \text{ M}$; $[\text{cresol}]_{\text{tot}} = (1.0\text{--}20) \times 10^{-3} \text{ M}$; $[\text{DBNBS}] = 1 \text{ mM}$; $[\text{HClO}_4] = 0.05 \text{ M}$; $\mu = 0.1 \text{ M}$ (LiClO_4); $T = 25 \text{ }^\circ\text{C}$. Solid line is linear fit. Data from Table A-7.

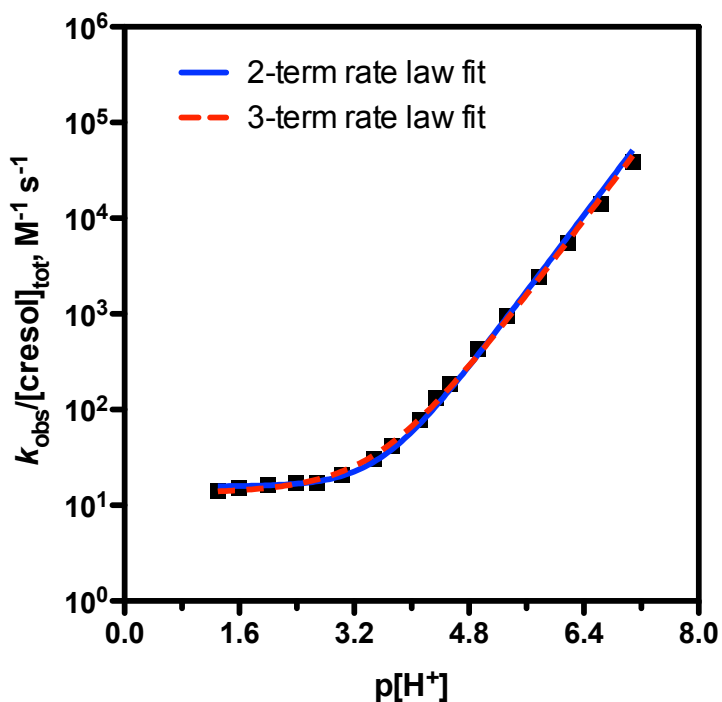


Figure 3-5. Plot of $k_{\text{obs}}/[\text{cresol}]_{\text{tot}}$ vs $\text{p}[\text{H}^+]$ with DBNBS. $[\text{Ir}^{\text{IV}}]_0 = (2.5\text{--}10) \times 10^{-5} \text{ M}$; $[\text{cresol}]_{\text{tot}} = (1.0\text{--}20) \times 10^{-3} \text{ M}$; $[\text{DBNBS}] = 1 \text{ mM}$; $\mu = 0.1 \text{ M}$ (LiClO_4); $T = 25 \text{ }^\circ\text{C}$. $\text{p}[\text{H}^+] = -\log [\text{HClO}_4]$ in the $\text{p}[\text{H}^+]$ range of 1.0–2.2. The following buffers (0.02 M) were employed to maintain constant $\text{p}[\text{H}^+]$ values: monochloroacetate buffer for $2.3 < \text{p}[\text{H}^+] < 3.5$, acetate buffer for $3.7 < \text{p}[\text{H}^+] < 5.4$, and cacodylate buffer for $5.7 < \text{p}[\text{H}^+] < 7.1$. Solid line is the fit to eq 2-2, and the dashed line is the fit to eq 2-3. Data from Table A-9.

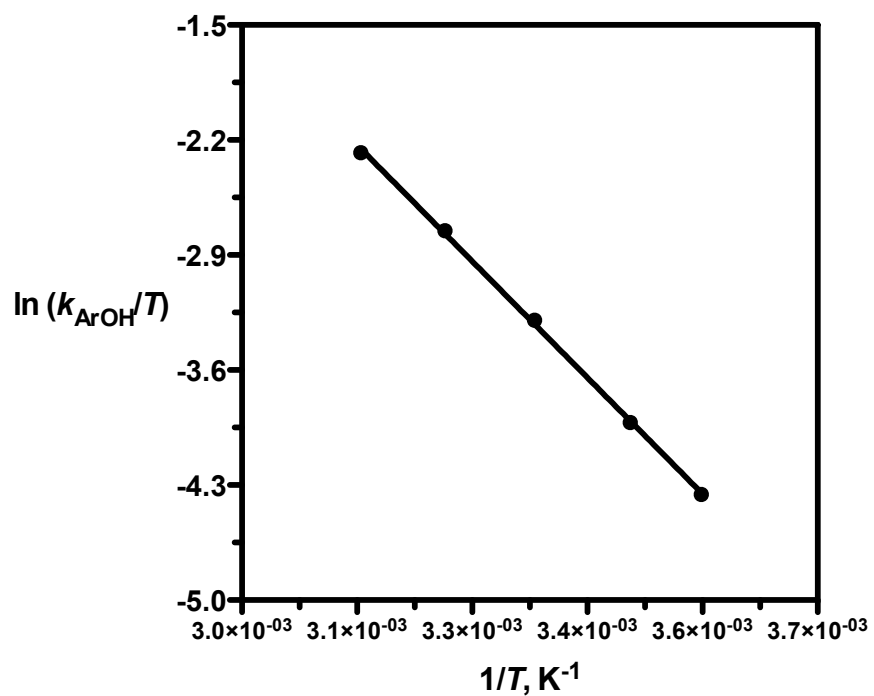


Figure 3-6. Plot of $\log(k_{\text{obs}}/T)$ vs $1/T$. $[\text{Ir}^{\text{IV}}]_0 = 2.5 \times 10^{-5} \text{ M}$; $[\text{cresol}]_{\text{tot}} = 0.02 \text{ M}$; $[\text{HClO}_4] = 0.01 \text{ M}$; $\mu = 0.1 \text{ M}$ (LiClO_4). Solid line is the fit to eq 3-1. Data from Table A-11.

According to Eyring's transition state theory eq 3-1,

$$\ln\left(\frac{k_{ArOH}}{T}\right) = \ln\left(\frac{k_B}{h}\right) + \frac{\Delta S^\ddagger}{R} - \frac{\Delta H^\ddagger}{RT} \quad (3-1)$$

the activation parameters can be calculated as $\Delta H^\ddagger = 42.0 \pm 1 \text{ kJ mol}^{-1}$ and $\Delta S^\ddagger = -84.0 \pm 2 \text{ J mol}^{-1} \text{ K}^{-1}$ after allowance for $\ln(k_B/h) = 23.8$. Here k_B is Boltzmann's constant, h is Planck's constant, and R is the gas constant.

Kinetic Isotope Effect. The deuterium kinetic isotope effect of the reaction between 0.02 M of cresol and 1×10^{-4} M of Ir^{IV} was studied under two conditions, $p[\text{H}^+] = 1.30$ and 2.34. According to the $p[\text{H}^+]$ dependence plot in Figure 3-5, both $p[\text{H}^+]$ s are on the plateau and the equilibrium isotope effects on K_a is not an issue. The observed rate constants measured in presence of 1 mM DBNBS in D_2O and normal H_2O are given in Table A-12. Both results yield the KIE of 2.9 ± 0.2 .

Products. Although no reported λ_{max} values are found for two methyl groups substituted 4,4'-biphenyloquinones, they are expected to appear in the wavelength range of 398 nm (λ_{max} of 4,4'-biphenyloquinone) to 421 nm (λ_{max} of 3,3',5,5'-tetramethyldiphenyloquinone¹⁰⁴). According to our UV-vis spectra, a weak absorption at 412 nm was detected at the end of the cresol and Ir^{IV} reaction, which is indicative of the corresponding biphenyloquinones and overoxidation takes place in cresol reaction.

3.3.2 The Oxidation of 2,6-Dimethylphenol

A kinetic experiment for the reaction of 1×10^{-4} M Ir^{IV} and 0.025 M xylenol was carried out under acidic conditions ($[\text{HClO}_4] = 0.05 \text{ M}$). The trace of Ir^{IV} consumption

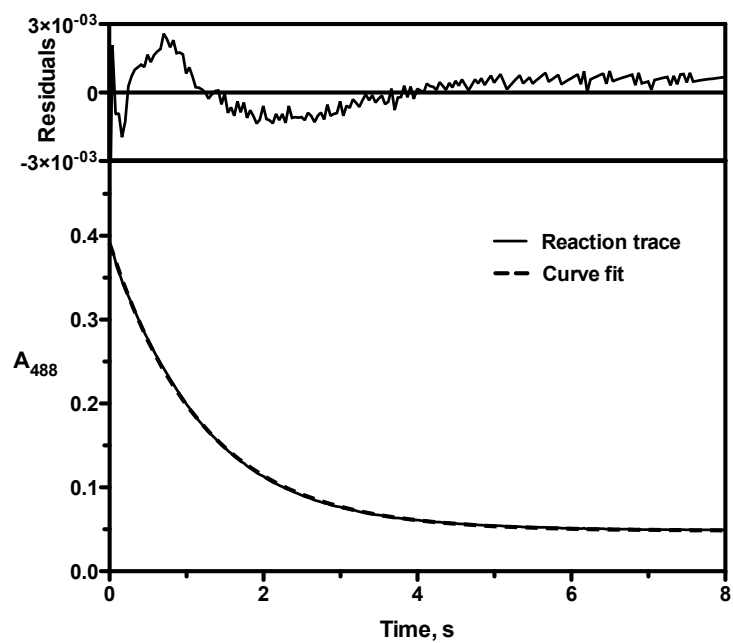


Figure 3-7. Trace of the xylenol reaction (solid line) and first-order fit (dashed line).

$[\text{Ir}^{\text{IV}}]_0 = 1 \times 10^{-4} \text{ M}$; $[\text{xylenol}]_{\text{tot}} = 0.025 \text{ M}$; $[\text{HClO}_4] = 0.05 \text{ M}$; $\mu = 0.1 \text{ M}$ (LiClO_4); $T = 25 \text{ }^\circ\text{C}$.

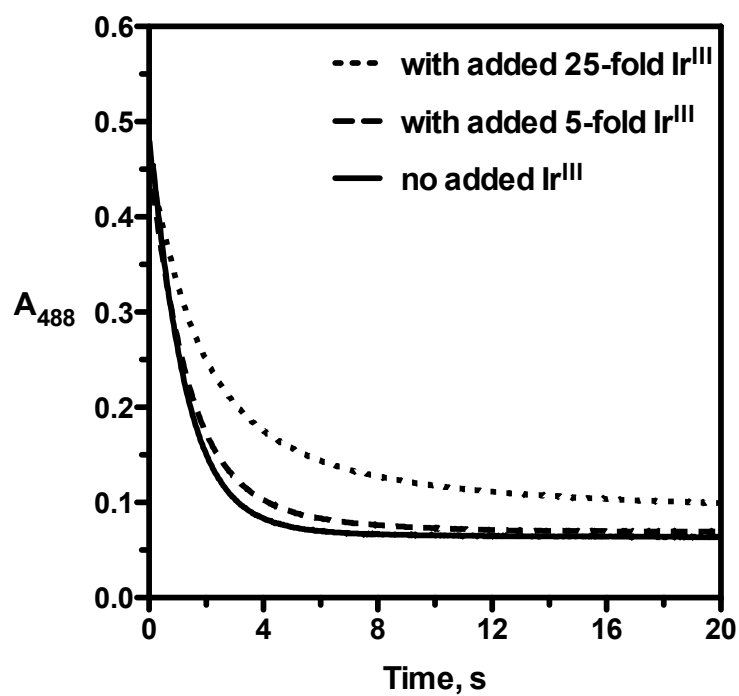


Figure 3-8. Comparative traces of the xylenol reaction (solid line) with added 5×10^{-4} M Ir^{III} (long dashed line) and 2.5×10^{-3} M Ir^{III} (long dashed line). $[\text{Ir}^{\text{IV}}]_0 = 1 \times 10^{-4}$ M; $[\text{xylenol}]_{\text{tot}} = 0.025$ M; $[\text{HClO}_4] = 0.05$ M; $\mu = 0.1$ M (LiClO_4); $T = 25$ °C.

can be well fit to pseudo-first-order kinetics (Figure 3-7) without the need for adding spin trapping agent.

Hexachloroiridate(III) Inhibition. The inhibiting effect of Ir^{III} was examined with 1×10^{-4} M Ir^{IV} and 0.025 M xylenol in 0.05 M HClO₄ in the presence of 5 and 25-fold excess of Ir^{III}. A weak inhibition was observed from Figure 3-8 with 5×10^{-4} M Ir^{III}, which was enhanced by increasing the concentration of the added Ir^{III} to 2.5×10^{-3} M. For our general kinetics studies no additional Ir^{III} is present and the concentration of Ir^{IV} is always below 1×10^{-4} M. Under these conditions Ir^{III} inhibition can be ignored.

Copper Catalysis. Our previous studies on outer-sphere electron-transfer oxidation show that trace copper ions can catalyze the reaction.^{60,73,76,105} The effect of copper catalysis was tested for the oxidation of xylenol in acidic aqueous solution, and the results are shown in Table 3-2.

Table 3-2. Kinetic Effect of Cu²⁺ and Dipic for Xylenol Oxidation.^a

Cu ²⁺ and Dipic	$k_{\text{obs}}/[\text{xylenol}]_{\text{tot}}, \text{M}^{-1} \text{s}^{-1}$
	35.8
5×10^{-6} M Cu ²⁺	35.9
1×10^{-3} M dipic	35.7

^a Cu²⁺ added as Cu(NO₃)₂, [Ir^{IV}]₀ = 1×10^{-4} M; [xylenol]_{tot} = 0.025 M; [HClO₄] = 0.05 M; μ = 0.1 M (LiClO₄); T = 25 °C.

In presence of 5×10^{-6} M Cu(NO₃)₂, the observed rate constant for the oxidation of 0.025 M xylenol by 1×10^{-4} M Ir^{IV} remains the same within error. Moreover, according to our

previous reported results on the oxidation of thioglycolic acid and cysteine,^{77,73} 2,6-pyridinedicarboxylic acid (dipic) effectively inhibits copper catalysis. Consequently, 1×10^{-3} M dipic was added to the reaction between 0.025 M of xylenol and 1×10^{-4} M of Ir^{IV} in 0.05 M HClO₄. No effect observed with the addition of dipic, which confirms that there is no copper catalysis in the oxidation of xylenol.

2,6-Dimethylphenol Dependence. Under pseudo-first-order condition, 1×10^{-4} M Ir^{IV} oxidized various concentration of xylenol (0.0025 – 0.025 M) in 0.05 M HClO₄. The observed rate constants of the reaction are summarized in Table A-13. The plot of k_{obs} versus $[\text{xylenol}]_{\text{tot}}$ shown in Figure 3-9 exhibits a straight line with slope = $35.5 \pm 1.4 \text{ M}^{-1} \text{ s}^{-1}$ and a negligible intercept. The linear relationship indicates that the rate law is first-order with respect to $[\text{xylenol}]_{\text{tot}}$.

Dependence on p[H⁺]. A study of the p[H⁺] dependence of the kinetics was carried out with various xylenol and Ir^{IV} concentrations ($[\text{xylenol}]_{\text{tot}} = (0.25\text{--}5) \times 10^{-3} \text{ M}$; $[\text{Ir}^{\text{IV}}] = (0.25\text{--}1) \times 10^{-4} \text{ M}$) as illustrated in Table A-14 under pseudo-first-order condition over the p[H⁺] range of 1–7. The data set follows eq 2-2, and the nonlinear least-squares fit of $k_{\text{obs}}/[\text{xylenol}]_{\text{tot}}$ versus p[H⁺] plot shown in Figure 3-10 yields $k_{\text{ArOH}} = 47 \pm 2 \text{ M}^{-1} \text{ s}^{-1}$ and $k_{\text{ArO}^-} = (2.0 \pm 0.1) \times 10^8 \text{ M}^{-1} \text{ s}^{-1}$ when holding $\text{p}K_{\text{a}} = 10.38$ at $\mu = 0.1 \text{ M}$ (LiClO₄) and 25 °C. This $\text{p}K_{\text{a}}$ is obtained by using Davies equation ($\log \gamma = -Az_i^2\mu^{1/2}/(1 + \mu^{1/2})$) to convert the reported value, 10.62 at $\mu = 0$ and 25 °C⁸¹, into $\text{p}K_{\text{a}}$ at $\mu = 0.1 \text{ M}$.

Figure 3-10 also displays the nonlinear fit of the data to the 3-term rate law with k_{ArOH} , k_{ArO^-} and k° as $38 \pm 1 \text{ M}^{-1} \text{ s}^{-1}$, $k_{\text{ArO}^-} = (1.71 \pm 0.03) \times 10^8 \text{ M}^{-1}$ and $k^{\circ} = (0.40 \pm 0.04) \text{ M}^{-1} \text{ s}^{-1}$, respectively. These results are summarized in Table A-15. The maximum contribution of the additional k° term is 28% ($\text{p}[\text{H}^+] = 3.7$).

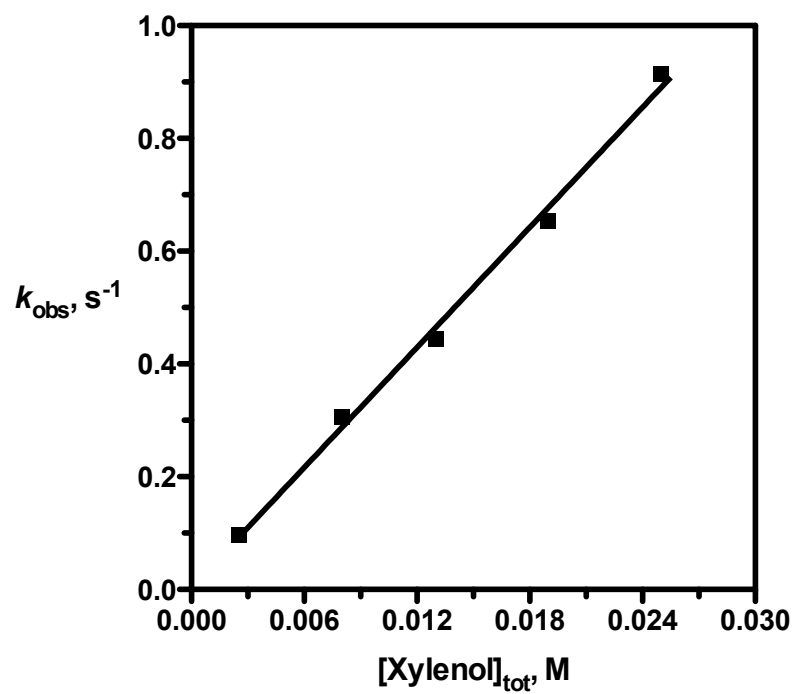


Figure 3-9. Plot of k_{obs} vs $[\text{xylene}]_{\text{tot}}$. $[\text{Ir}^{\text{IV}}]_0 = 1 \times 10^{-4} \text{ M}$; $[\text{xylene}]_{\text{tot}} = (2.5\text{--}25) \times 10^{-3} \text{ M}$; $[\text{HClO}_4] = 0.05 \text{ M}$; $\mu = 0.1 \text{ M}$ (LiClO_4); $T = 25 \text{ }^\circ\text{C}$. Solid line is linear fit. Data from Table A-13.

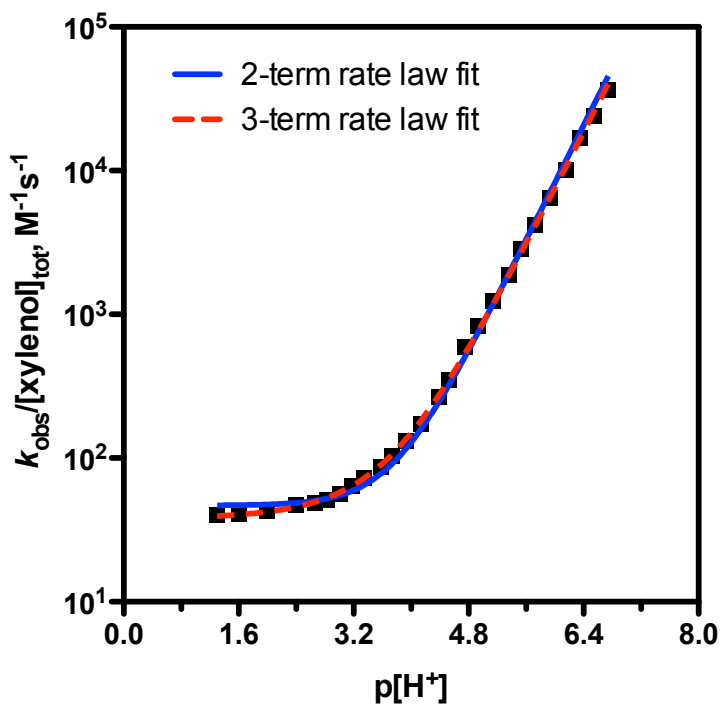


Figure 3-10. Plot of $k_{\text{obs}}/[\text{xylenol}]_{\text{tot}}$ vs $\text{p}[\text{H}^+]$. $[\text{Ir}^{\text{IV}}]_0 = (2.5\text{--}10) \times 10^{-5} \text{ M}$; $[\text{xylenol}]_{\text{tot}} = (2.5\text{--}50) \times 10^{-4} \text{ M}$; $\mu = 0.1 \text{ M (LiClO}_4)$; $T = 25 \text{ }^\circ\text{C}$. $\text{p}[\text{H}^+] = -\log [\text{HClO}_4]$ in the $\text{p}[\text{H}^+]$ range of 1.0–2.2. The following buffers (0.02 M) were employed to maintain constant $\text{p}[\text{H}^+]$ values: monochloroacetate buffer for $2.4 < \text{p}[\text{H}^+] < 3.4$, acetate buffer for $3.5 < \text{p}[\text{H}^+] < 5.4$, and cacodylate buffer for $5.5 < \text{p}[\text{H}^+] < 7.0$. Solid line is the fit to eq 2-2 and the dashed line is the fit to eq 2-3. Data from Table A-14.

Kinetic Isotope Effect. The kinetic isotope effect was measured with 0.025 M xyleneol and 1×10^{-4} M Ir^{IV} at high acidity ($[\text{HClO}_4] = 0.05$ M) where the rate constants are $\text{p}[\text{H}^+]$ independent. The experimental details are shown in Table A-16. The ratio of observed rate constants in H_2O and D_2O are obtained as 2.6 ± 0.1 .

Products. The UV-vis spectrum of the xyleneol and Ir^{IV} mixture at the end of the reaction exhibited an extremely strong absorption at 421 nm which is consistent with the formation of 3,3',5,5'-tetramethyldiphenoquinone as a product according to literature.¹⁰⁴

3.3.3 The Oxidation of 2,4,6-Trimethylphenol (TMP)

A typical kinetic decay of 1×10^{-4} M Ir^{IV} in the reaction of TMP is shown in Figure 3-11. In 0.05 M HClO_4 solution and with only 1.2×10^{-3} M TMP present, the reaction was still fast compared to the oxidation of cresol and xyleneol at the same $\text{p}[\text{H}^+]$ but with higher concentration of reductants. A good-quality pseudo-first order trace was observed and is exhibited in Figure 3-11. Therefore, we expected that Ir^{III} inhibition would not be a problem for the TMP reaction.

Hexachloroiridate(III) Inhibition. In order to check for a possible Ir^{III} effect, the oxidation of 1.2×10^{-3} M TMP by 1×10^{-4} M Ir^{IV} in presence of Ir^{III} was examined under acidic conditions ($[\text{HClO}_4] = 0.05$ M), as shown in Figure 3-12. With high amount of excess Ir^{III} ($= 2.5 \times 10^{-3}$ M) we detected a relatively small inhibition phenomenon. This proved that the degree of kinetic inhibition by Ir^{III} is considerably weak and that the reaction could be studied without a spin trapping agent.

2,4,6-Trimethylphenol Dependence. Under acidic conditions (0.01 M HClO_4), various concentrations of TMP were oxidized by 1×10^{-4} M Ir^{IV} , and the results are presented in Table A-17. A plot of k_{obs} versus $[\text{TMP}]_{\text{tot}}$ in the range of $(0.3-3) \times 10^{-3}$ M

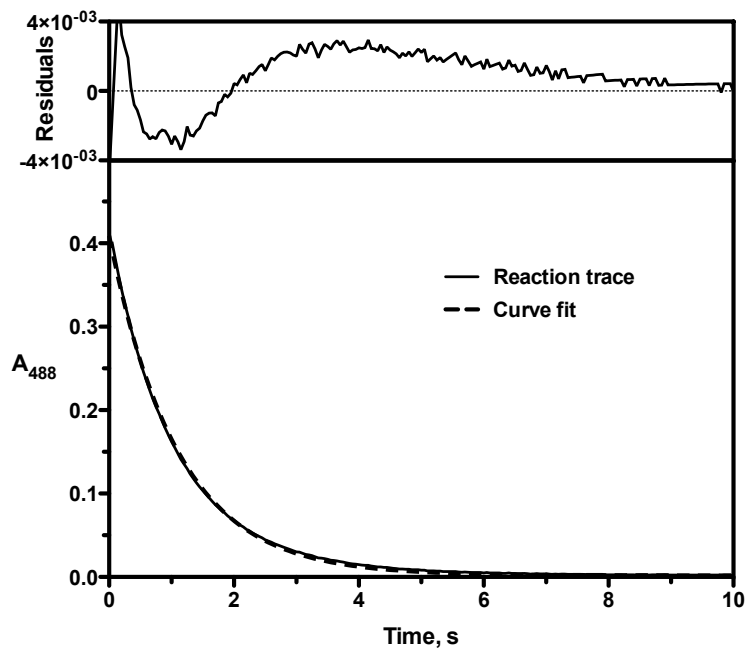


Figure 3-11. Kinetic trace of the Ir^{IV} consumption in the TMP oxidation. Lower box shows the experimental trace (solid line) and the pseudo-first-order fit (dashed line). Upper box shows the residuals in the fit. $[\text{Ir}^{\text{IV}}]_0 = 1 \times 10^{-4} \text{ M}$; $[\text{TMP}]_{\text{tot}} = 1.2 \times 10^{-3} \text{ M}$; $[\text{HClO}_4] = 0.05 \text{ M}$; $\mu = 0.1 \text{ M (LiClO}_4)$; $T = 25 \text{ }^\circ\text{C}$.

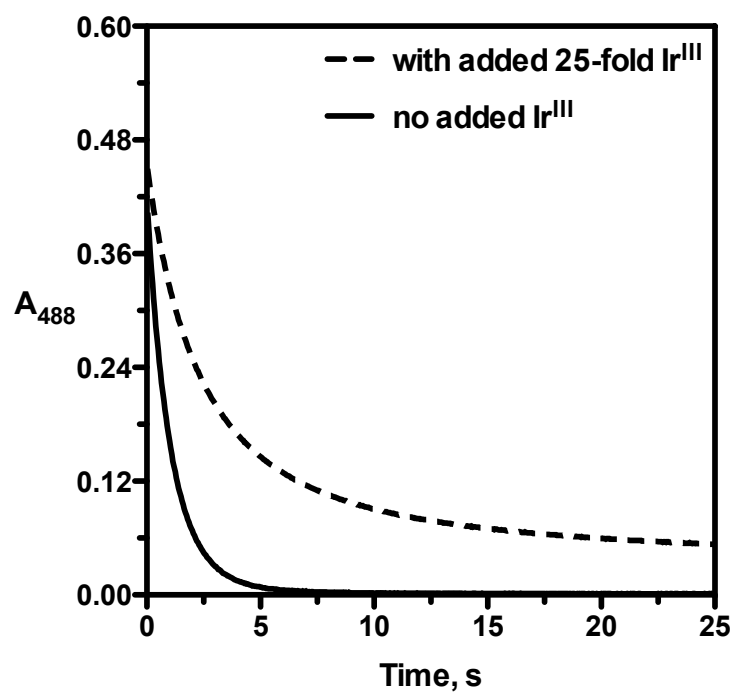


Figure 3-12. Comparative traces of the TMP reaction (solid line) with added Ir^{III} (dashed line). $[\text{Ir}^{\text{IV}}]_0 = 1 \times 10^{-4} \text{ M}$; $[\text{TMP}]_{\text{tot}} = 1.2 \times 10^{-3} \text{ M}$; $[\text{Ir}^{\text{III}}]_0 = 2.5 \times 10^{-3} \text{ M}$; $[\text{HClO}_4] = 0.05 \text{ M}$; $\mu = 0.1 \text{ M}$ (LiClO_4); $T = 25 \text{ }^\circ\text{C}$.

TMP (Figure 3-13) is linear with a slope = $(1.09 \pm 0.02) \times 10^3 \text{ M}^{-1} \text{ s}^{-1}$ and a negligible intercept, indicating a first-order dependence of the rate on the TMP concentration.

Dependence on $p[\text{H}^+]$. The influence of $p[\text{H}^+]$ on the reaction rate was investigated with $2.5 \times 10^{-5} \text{ M}$ of Ir^{IV} and $3 \times 10^{-4} \text{ M}$ of TMP over the $p[\text{H}^+]$ range of 1–7. The experimental data are summarized in Table A-18, and a plot of $k_{\text{obs}}/[\text{TMP}]_{\text{tot}}$ versus $p[\text{H}^+]$ is shown in Figure 3-14. The nonlinear-least-square fit to the rate law eq 2-2 yields $k_{\text{ArOH}} = (1.09 \pm 0.01) \times 10^3 \text{ M}^{-1} \text{ s}^{-1}$ and $k_{\text{ArO}^-} = (2.58 \pm 0.03) \times 10^8 \text{ M}^{-1} \text{ s}^{-1}$ with $pK_{\text{a}} = 10.65$ at $\mu = 0.1 \text{ M}$ and $25 \text{ }^\circ\text{C}$ ($=10.89$ at $\mu = 0$ and $25 \text{ }^\circ\text{C}^{81}$). Since an excellent 2-term rate law fit is obtained for TMP reaction with R square of 0.9998, data need not be fitted to the 3-term rate law.

Kinetic Isotope Effect. The oxidations of $1.5 \times 10^{-3} \text{ M}$ and $3 \times 10^{-3} \text{ M}$ of TMP by $1 \times 10^{-4} \text{ M}$ of Ir^{IV} were detected in H_2O and D_2O at high acidity ($[\text{HClO}_4] = 0.01 \text{ M}$). Under this condition, the reaction is pseudo-first order and $p[\text{H}^+]$ independent. All the data are shown in Table A-19, and the ratio of observed rate constants in H_2O and D_2O is obtained as 2.04 ± 0.01 .

Products Identification. The UV-vis spectrum of TMP and Ir^{IV} mixture at the end of the reaction did not show a detectable absorption around 400 nm, which is quite different from the other phenols. We studied the reaction products by using ^1H NMR spectroscopy. The spectrum of TMP exhibits three distinct peaks as shown in Figure 3-15a: two peaks in the high-field region ($\delta = 2.18$ and 2.19 ppm) correspond to the protons on methyl groups and one peak in the low-field region ($\delta = 6.90 \text{ ppm}$) represents the two equivalent aromatic protons. The ^1H NMR spectrum of the reaction solution was detected by mixing $1 \times 10^{-3} \text{ M}$ of Ir^{IV} and $3 \times 10^{-3} \text{ M}$ of TMP in D_2O , as shown in

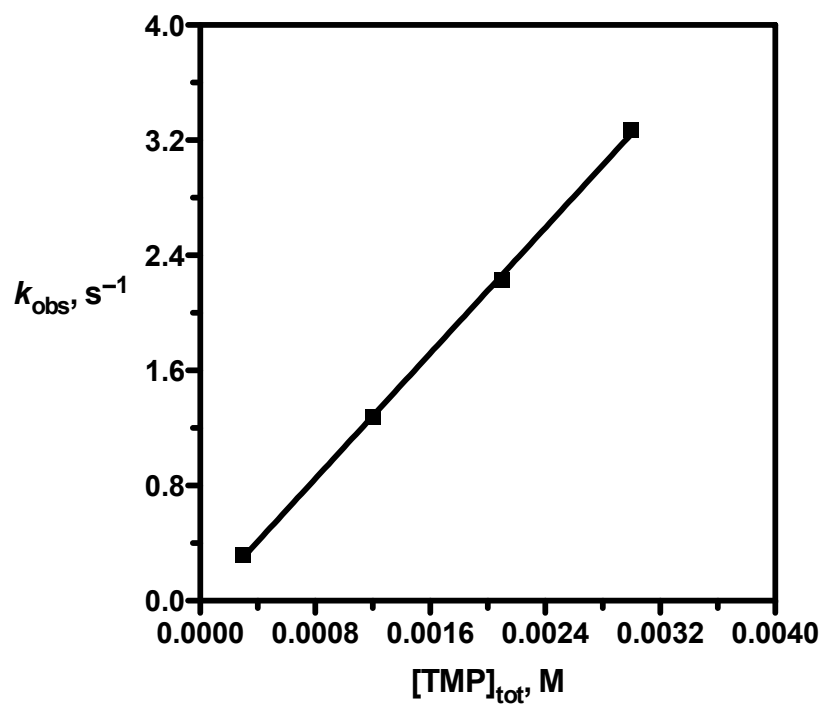


Figure 3-13. Plot of k_{obs} vs $[\text{TMP}]_{\text{tot}}$. $[\text{Ir}^{\text{IV}}]_0 = 2.5 \times 10^{-5} \text{ M}$; $[\text{TMP}]_{\text{tot}} = (0.3\text{--}3.0) \times 10^{-3} \text{ M}$; $[\text{HClO}_4] = 0.01 \text{ M}$; $\mu = 0.1 \text{ M}$ (LiClO_4); $T = 25 \text{ }^\circ\text{C}$. Solid line is linear fit. Data from Table A-17.

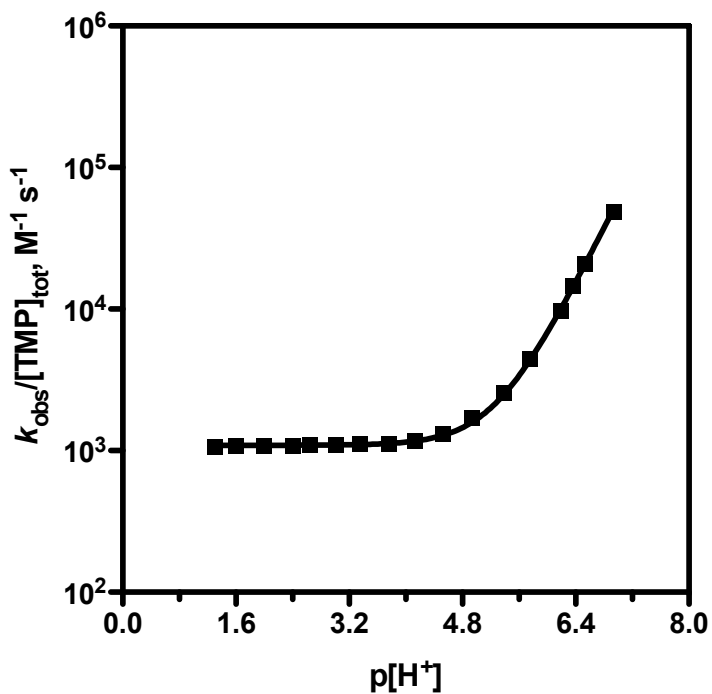


Figure 3-14. Plot of $k_{\text{obs}}/[\text{TMP}]_{\text{tot}}$ vs $\text{p}[\text{H}^+]$. $[\text{Ir}^{\text{IV}}]_0 = 2.5 \times 10^{-5} \text{ M}$; $[\text{TMP}]_{\text{tot}} = 3.0 \times 10^{-4} \text{ M}$; $\mu = 0.1 \text{ M}$ (LiClO_4); $T = 25 \text{ }^\circ\text{C}$. $\text{p}[\text{H}^+] = -\log [\text{HClO}_4]$ in the $\text{p}[\text{H}^+]$ range of 1.0–2.2. The following buffers (0.02 M) were employed to maintain constant $\text{p}[\text{H}^+]$ values: monochloroacetate buffer for $2.4 < \text{p}[\text{H}^+] < 3.5$, acetate buffer for $3.6 < \text{p}[\text{H}^+] < 5.5$, and cacodylate buffer for $5.6 < \text{p}[\text{H}^+] < 7.0$. Solid line is the fit to 2-term rate law eq 2-2. Data from Table A-18.

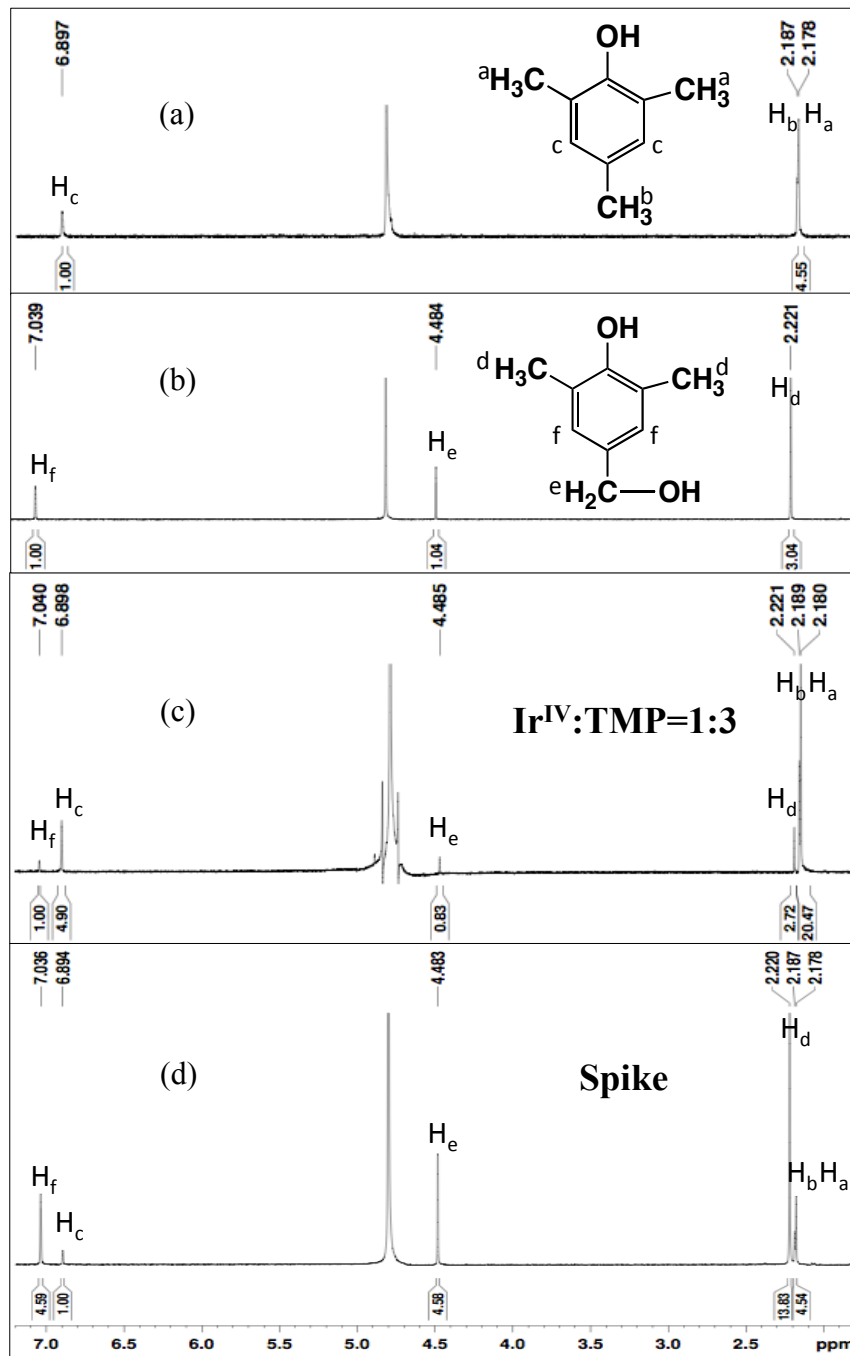


Figure 3-15. ^1H NMR identification of TMP oxidation Products. (a) The ^1H NMR spectrum of TMP in D_2O . (b) The ^1H NMR spectrum of 4-hydroxymethyl-2,6-dimethylphenol in D_2O . (c) A sample of the reaction solution with 3 mM TMP oxidized by 1 mM Ir^{IV} in D_2O . (d) Spiked reaction solution in c with 4-hydroxymethyl-2,6-dimethylphenol.

Figure 3-15c. Comparing to the spectrum of TMP, three additional peaks ($\delta = 2.22, 4.48$ and 7.04 ppm) were observed for the reaction solution, which must be the product of the oxidation of TMP. After analyzing the chemical shifts and integrals, we predicted that the product is 4-hydroxymethyl-2,6-dimethylphenol, which was confirmed via comparison to an independently prepared standard (its ^1H NMR spectrum is shown in Figure 3-15b). Spiking the reaction solution with 4-hydroxymethyl-2,6-dimethylphenol increased the intensity of the three resonances, as shown in Figure 3-15d, further bolstering the identification. Additional information was also obtained from the integrals. The difference in the integrals for the rest of TMP and the product 4-hydroxymethyl-2,6-dimethylphenol (2.22 ppm) reveals that the stoichiometry of Ir^{IV} : TMP is equal to 2:1 if all Ir^{IV} was reduced.

Overoxidation. In order to get insight into the overoxidation of TMP, the oxidation of 4-hydroxymethyl-2,6-dimethylphenol was examined with 1×10^{-4} M Ir^{IV} and 1×10^{-3} M 4-hydroxymethyl-2,6-dimethylphenol at $\text{p}[\text{H}^+] = 1.3$ and 4.4 . The values of $k_{\text{obs}}/[\text{4-hydroxymethyl-2,6-dimethylphenol}]_{\text{tot}}$ are 193 and $505 \text{ M}^{-1} \text{ s}^{-1}$, respectively. In comparison with the values of $k_{\text{obs}}/[\text{TMP}]_{\text{tot}}$, $1.06 \times 10^3 \text{ M}^{-1} \text{ s}^{-1}$ at $\text{p}[\text{H}^+] = 1.3$, and $1.31 \times 10^3 \text{ M}^{-1} \text{ s}^{-1}$ at $\text{p}[\text{H}^+] = 4.5$ (shown in Table A-18), we found that the oxidation of TMP is 2–5 times faster than that of 4-hydroxymethyl-2,6-dimethylphenol in the $\text{p}[\text{H}^+]$ range of 1.3–4.5. Besides, the high concentration of TMP enables it to be more rapidly oxidized by Ir^{IV} than 4-hydroxymethyl-2,6-dimethylphenol, thereby limiting further oxidation.

3.3.4 The Oxidation of 4-Methoxyphenol

A typical kinetic trace of Ir^{IV} reduction in the MOP oxidation is shown in

Figure 3-16. The reaction was carried out with 3×10^{-4} M of MOP and 2.5×10^{-5} M of Ir^{IV} and can be well fitted to a pseudo-first order curve with small deviations, which means that under these systems the Ir^{III} inhibition is negligible and no trapping agent is required for the kinetic studies.

Dependence on $\text{p}[\text{H}^+]$. The $\text{p}[\text{H}^+]$ dependence was studied with 2.5×10^{-5} M of Ir^{IV} and 3×10^{-4} M of MOP over the $\text{p}[\text{H}^+]$ range of 1–7. The experimental data are summarized in Table A-21, and a plot of $k_{\text{obs}}/[\text{MOP}]_{\text{tot}}$ versus $\text{p}[\text{H}^+]$ is shown in Figure 3-17. When fitting the data to the rate law eq 2-2, it yields $k_{\text{ArOH}} = (6.1 \pm 0.1) \times 10^4 \text{ M}^{-1} \text{ s}^{-1}$ and $k_{\text{ArO}^-} = (3.3 \pm 0.1) \times 10^8 \text{ M}^{-1} \text{ s}^{-1}$ with $\text{p}K_{\text{a}} = 9.96$ at $\mu = 0.1 \text{ M}$ and $25 \text{ }^\circ\text{C}$.⁸¹

Kinetic Isotope Effect. The deuterium kinetic isotope effect of reaction between 2.5×10^{-5} M of Ir^{IV} and 3×10^{-4} M of MOP was determined in H_2O and D_2O at high acidity ($[\text{HClO}_4] = 0.05 \text{ M}$). Under this condition, the reaction is pseudo-first order and pH-independent. All the data are shown in Table A-20 and the ratio of observed rate constants in H_2O and D_2O are obtained as 1.9 ± 0.1 .

Temperature Dependence. The reaction between 3×10^{-4} M of MOP and 2.5×10^{-5} M of Ir^{IV} in 0.1 M HClO_4 was carried out at different temperatures: 8, 15, 25, 35 and $45 \text{ }^\circ\text{C}$. The values of k_{obs} are summarized in Table A-22. Under these acidic conditions, it is reasonable to assume that k_{obs} represents k_{ArOH} which dominates the reaction kinetics. A plot of $\ln(k_{\text{ArOH}}/T)$ versus $1/T$ in Figure 3-18 shows a linear relationship with the slope of $-(2.7 \pm 0.2) \times 10^3 \text{ K}$ and intercept equal to 14.4 ± 1 . According to the Eyring equation (3-1), the activation parameters can be calculated as $\Delta H^\ddagger = 22.8 \pm 1 \text{ kJ mol}^{-1}$ and $\Delta S^\ddagger = -78.0 \pm 5 \text{ J mol}^{-1} \text{ K}^{-1}$ using $\ln(k_{\text{B}}/h) = 23.8$.

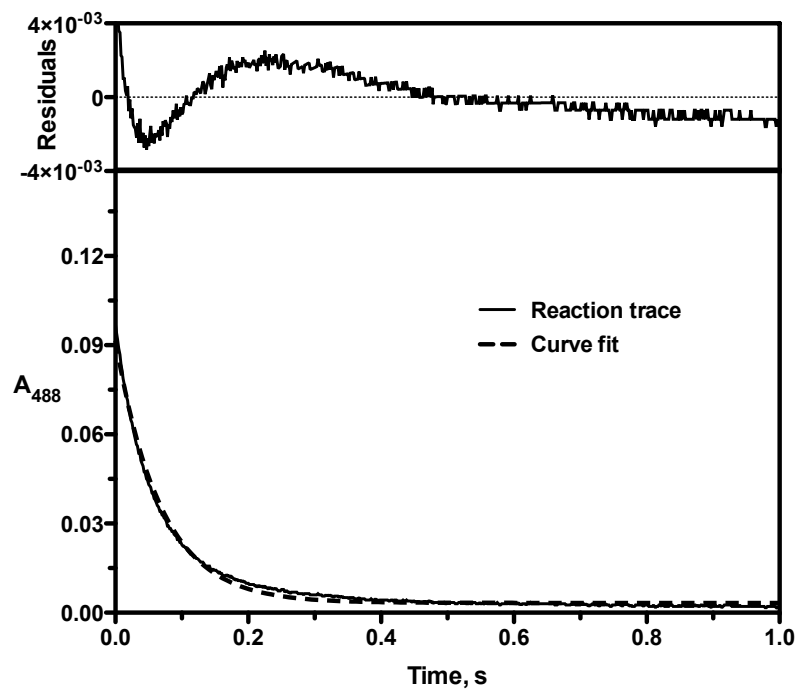


Figure 3-16. Kinetic trace of the Ir^{IV} consumption in the MOP oxidation. Lower box shows the experimental trace (solid line) and the pseudo-first-order fit (dashed line). Upper box shows the residuals in the fit. $[\text{Ir}^{\text{IV}}]_0 = 2.5 \times 10^{-5} \text{ M}$; $[\text{MOP}]_{\text{tot}} = 3 \times 10^{-4} \text{ M}$; $[\text{HClO}_4] = 0.05 \text{ M}$; $\mu = 0.1 \text{ M (LiClO}_4)$; $T = 25 \text{ }^\circ\text{C}$.

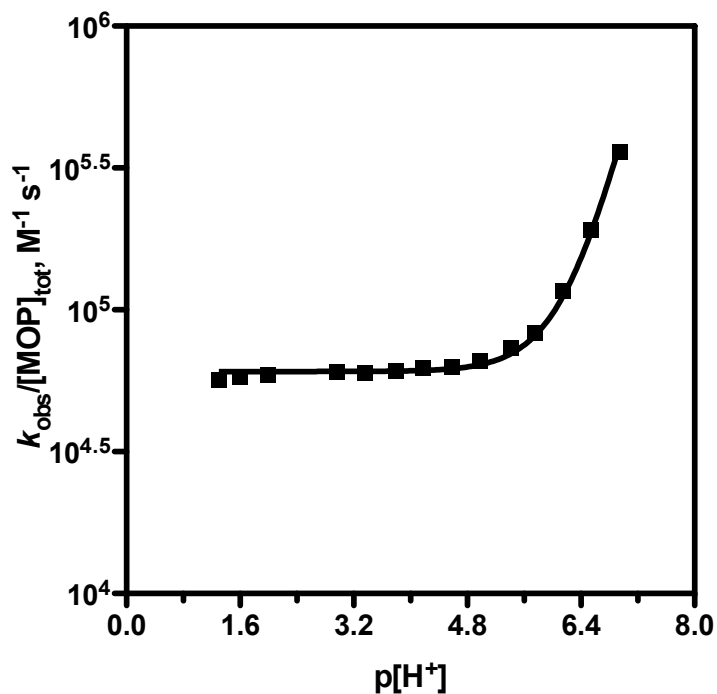


Figure 3-17. Plot of $k_{\text{obs}}/[\text{MOP}]_{\text{tot}}$ vs $\text{p}[\text{H}^+]$. $[\text{Ir}^{\text{IV}}]_0 = 2.5 \times 10^{-5} \text{ M}$; $[\text{MOP}]_{\text{tot}} = 3 \times 10^{-4} \text{ M}$; $\mu = 0.1 \text{ M}$ (LiClO_4); $T = 25 \text{ }^\circ\text{C}$. $\text{p}[\text{H}^+] = -\log [\text{HClO}_4]$ in the $\text{p}[\text{H}^+]$ range of 1.0–2.2. The following buffers (0.02 M) were employed to maintain constant $\text{p}[\text{H}^+]$ values: monochloroacetate buffer for $2.4 < \text{p}[\text{H}^+] < 3.4$, acetate buffer for $3.6 < \text{p}[\text{H}^+] < 5.5$, and cacodylate buffer for $5.6 < \text{p}[\text{H}^+] < 7.0$. Solid line is the fit to 2-term rate law eq 2-2.

Table A-21.

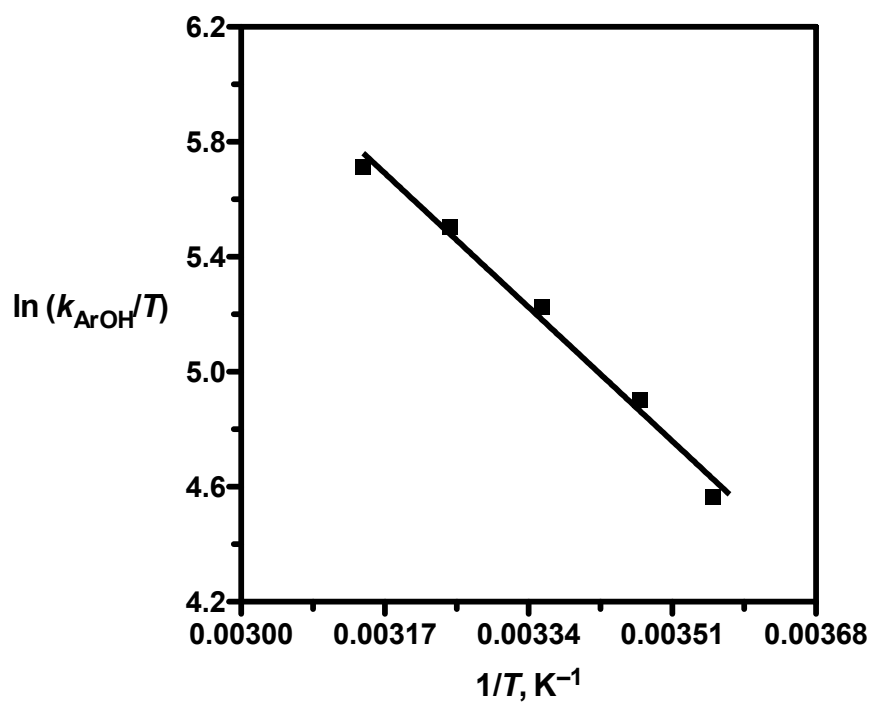


Figure 3-18. Plots of $\ln(k_{\text{obs}}/T)$ vs $1/T$. $[\text{Ir}^{\text{IV}}]_0 = 2.5 \times 10^{-5} \text{ M}$; $[\text{MOP}]_{\text{tot}} = 3 \times 10^{-4} \text{ M}$; $[\text{HClO}_4] = 0.1 \text{ M}$; $T = 25 \text{ }^\circ\text{C}$. Solid line is the fit to eq 3-1. Data from Table A-22.

Control Experiments. In order to gain insight into the reactivity of the methoxy group of MOP, the reactions between 0.01 M of anisole and 1.0×10^{-4} M of Ir^{IV} were tested at 0.1 M ionic strength in 0.05 M HClO_4 and at $\text{p}[\text{H}^+] = 7.0$. No oxidation was observed under both conditions suggesting that the methoxy group is unreactive, which confirms that only the hydroxyl group on MOP participates in the reaction with Ir^{IV} .

3.3.5 The oxidation of 4-*tert*-Butylphenol

The oxidation of 2×10^{-3} M of TBP by 2.5×10^{-5} M of Ir^{IV} was studied in 0.05 M HClO_4 , and the decay of Ir^{IV} at 488 nm is presented in Figure 3-19. When fitting the kinetic trace to a pseudo-first order rate law, we did not obtain a satisfactory result. In order to improve the kinetic behavior, we added 1 mM of DNBNS into the above reaction and obtained a good-quality first-order fit, as shown in Figure 3-20.

Dependence on $\text{p}[\text{H}^+]$. The $\text{p}[\text{H}^+]$ influence on the reaction rate was studied with 2.5×10^{-5} M of Ir^{IV} and $(3.0\text{--}9.0) \times 10^{-4}$ M of TBP over the $\text{p}[\text{H}^+]$ range of 1–7. The experiments are carried out in the presence of 1 mM DNBNS and the data are illustrated in Table A-23. The plot of $k_{\text{obs}}/[\text{TBP}]_{\text{tot}}$ versus $\text{p}[\text{H}^+]$ in Figure 3-21 is fitted to the rate law eq 2-2, and yields $k_{\text{ArOH}} = 29 \pm 3 \text{ M}^{-1} \text{ s}^{-1}$ and $k_{\text{ArO}^-} = (3.6 \pm 0.3) \times 10^7 \text{ M}^{-1} \text{ s}^{-1}$ with $\text{p}K_{\text{a}} = 10.07$ at $\mu = 0.1 \text{ M}$ and $25 \text{ }^\circ\text{C}$ ($\text{p}K_{\text{a}} = 10.31$ at $\mu = 0$ and $25 \text{ }^\circ\text{C}$ ⁸¹).

When fitting the data in Table A-23 to the 3-term rate law eq 2-3, as shown in Figure 3-21, the following values for k_{ArOH} , k_{ArO^-} and k^0 are obtained: $k_{\text{ArOH}} = 18 \pm 1 \text{ M}^{-1} \text{ s}^{-1}$, $k_{\text{ArO}^-} = (2.4 \pm 0.1) \times 10^7 \text{ M}^{-1}$ and $k^0 = (0.48 \pm 0.03) \text{ M}^{-1} \text{ s}^{-1}$, as displayed in Table A-24. The contributions of the additional k^0 term were calculated over the $\text{p}[\text{H}^+]$ range of 1–7. The maximum value is 56% and occurs around $\text{p}[\text{H}^+] = 3.9$.

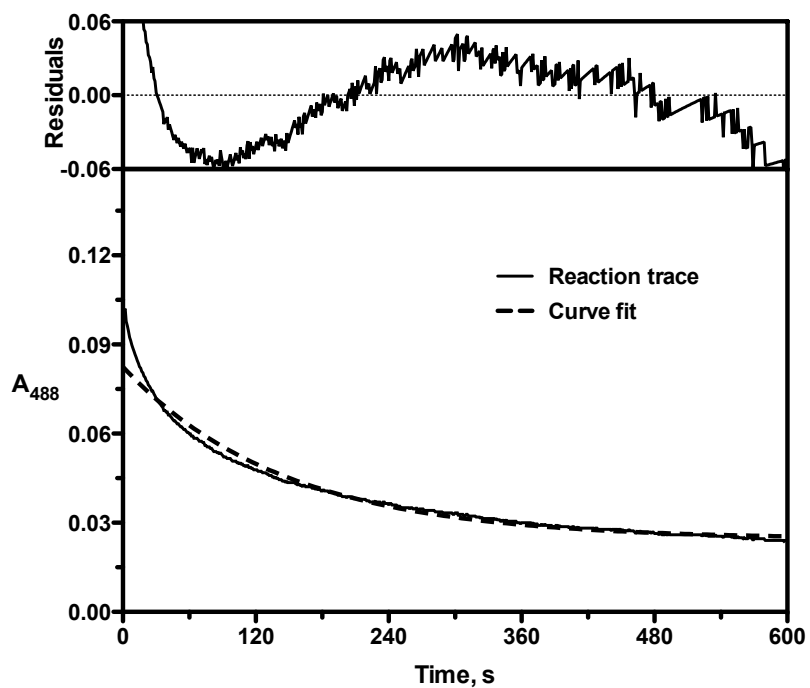


Figure 3-19. Kinetic trace of the Ir^{IV} consumption in the TBP oxidation. Lower box shows the experimental trace (solid line) and the pseudo-first-order fit (dashed line). Upper box shows the residuals in the fit. $[\text{Ir}^{\text{IV}}]_0 = 2.5 \times 10^{-5} \text{ M}$; $[\text{TBP}]_{\text{tot}} = 2 \times 10^{-3} \text{ M}$; $[\text{HClO}_4] = 0.05 \text{ M}$; $\mu = 0.1 \text{ M}$ (LiClO_4); $T = 25 \text{ }^\circ\text{C}$.

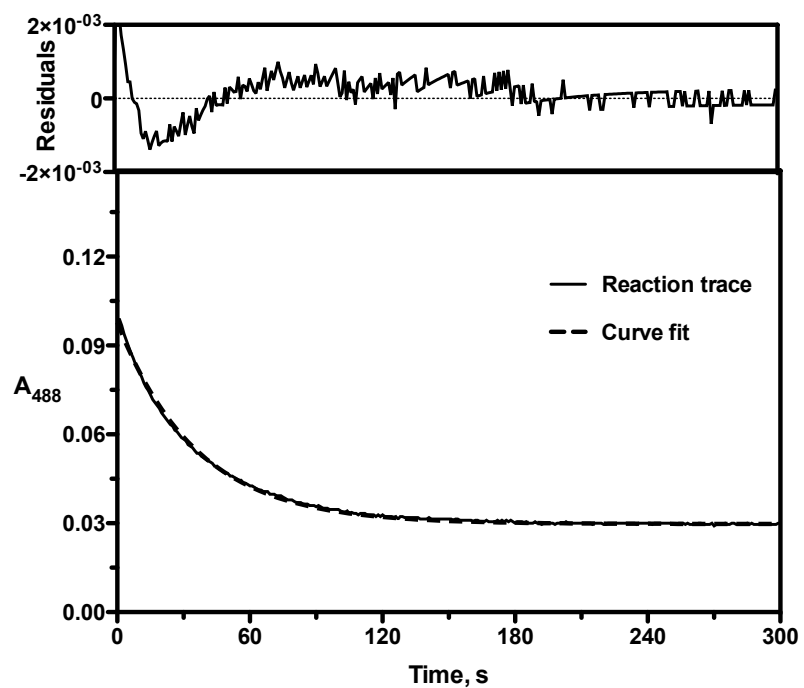


Figure 3-20. Kinetic trace of the Ir^{IV} consumption in the TBP oxidation with DNBNS. Lower box shows the experimental trace (solid line) and the pseudo-first-order fit (dashed line). Upper box shows the residuals in the fit. $[\text{Ir}^{\text{IV}}]_0 = 2.5 \times 10^{-5} \text{ M}$; $[\text{TBP}]_{\text{tot}} = 2 \times 10^{-3} \text{ M}$; $[\text{DNBNS}] = 1 \text{ mM}$; $[\text{HClO}_4] = 0.05 \text{ M}$; $\mu = 0.1 \text{ M (LiClO}_4)$; $T = 25 \text{ }^\circ\text{C}$.

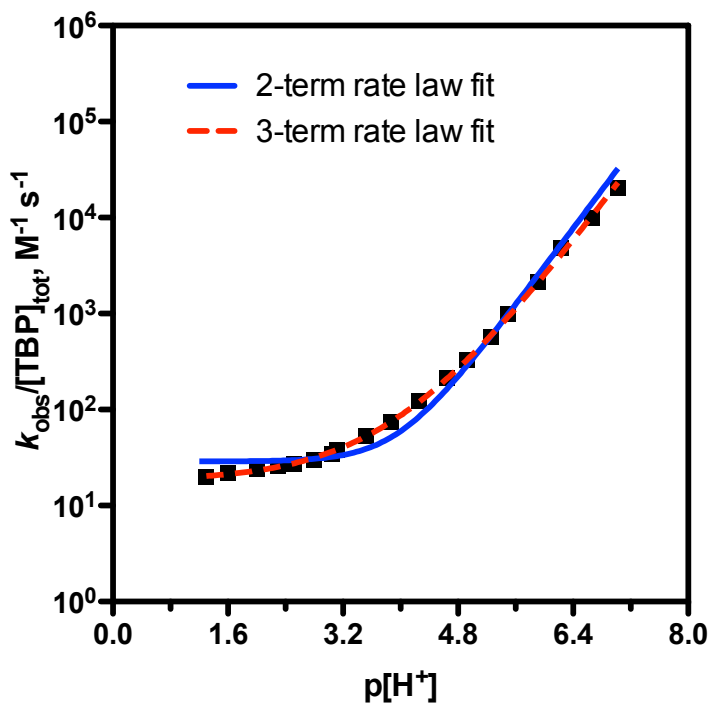


Figure 3-21. Plot of $k_{\text{obs}}/[\text{TBP}]_{\text{tot}}$ vs $\text{p}[\text{H}^+]$. $[\text{Ir}^{\text{IV}}]_0 = 2.5 \times 10^{-5} \text{ M}$; $[\text{DBNBS}] = 1 \text{ mM}$; $\mu = 0.1 \text{ M}$ (LiClO_4); $T = 25 \text{ }^\circ\text{C}$. $\text{p}[\text{H}^+] = -\log [\text{HClO}_4]$ in the $\text{p}[\text{H}^+]$ range of 1.0–2.2. The following buffers (0.02 M) were employed to maintain constant $\text{p}[\text{H}^+]$ values: monochloroacetate buffer for $2.3 < \text{p}[\text{H}^+] < 3.4$, acetate buffer for $3.5 < \text{p}[\text{H}^+] < 5.3$, and cacodylate buffer for $5.5 < \text{p}[\text{H}^+] < 7.1$. Solid line is the fit to eq 2-2 and the dashed line is the fit to eq 2-3. Data from Table A-23.

3.4 Discussion and Conclusion

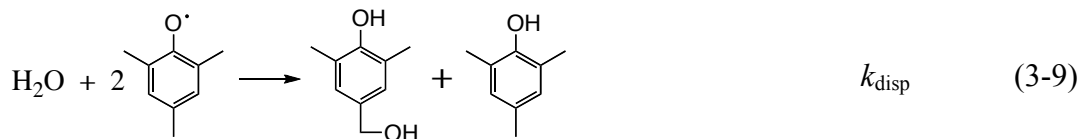
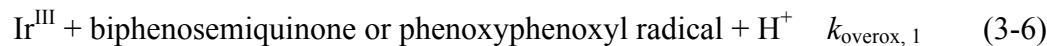
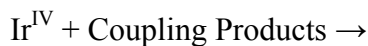
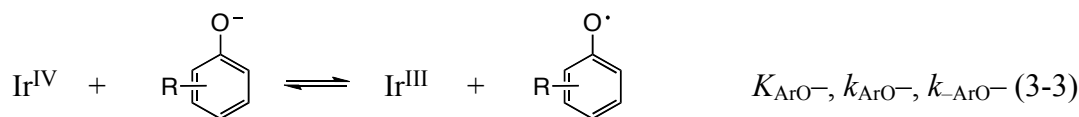
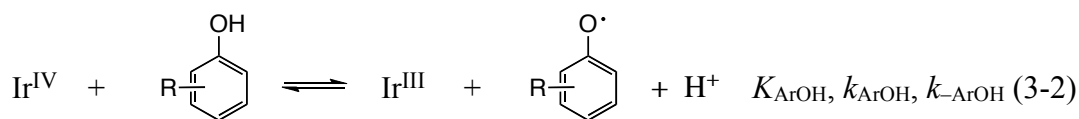
3.4.1 Mechanism

As we reported in the previous work,¹⁰⁶ a similar mechanisms are proposed for *ortho*-substituted phenols, cresol and xylenol: first, the reactions between Ir^{IV} and neutral phenols undergo a concerted proton-coupled electron-transfer oxidation to produce the corresponding phenoxyl radical, Ir^{III} and a proton, as shown in eq 3-2. K_{ArOH} , k_{ArOH} and k_{-ArOH} are the equilibrium constant and rate constants for this step. The oxidation of the conjugate base phenolate anions is a reversible outer-sphere one-electron transfer process (eq 3-3), forming a phenoxyl radical. K_{ArO^-} , k_{ArO^-} and k_{-ArO^-} represent the equilibrium constant and second-order rate constants of this pathway. Second, the phenoxyl radicals undergo bimolecular C–C coupling to produce biphenols and C–O coupling to produce phenoxyphenol (eq 3-5), which is subsequently oxidized by Ir^{IV} to form biphenosemiquinones or phenoxyphenoxyl radicals (eq 3-6). k_{dim} corresponds to the coupling rate constant and $k_{overox,1}$ is the rate constant of further overoxidation. Lastly, biphenosemiquinones are easily oxidized by Ir^{IV} to form biphenoquinones with rate constant of $k_{overox,2}$, as illustrated in eq 3-7. Phenoxyphenoxyl radicals can dimerize with rate constant k_{dec} according to eq 3-8.

Eqs 3-2 to 3-5 are also proposed for the oxidation of *para*-substituted phenol, TBP, which only forms the corresponding 2,2' product. Further oxidations by Ir^{IV} are shown in eqs 3-6 and 3-7. Because no overoxidation was detected from our experiments, the oxidation of another *para*-substituted phenol, MOP, only undergoes steps 3-2 to 3-5.

For the TMP reaction, the *ortho*- and *para*- positions of TMP are all occupied with methyl groups, therefore, dimerizations through C-C and C-O couplings of the

corresponding phenoxyl radical generated from eqs 3-2 and 3-3 are impossible. The disproportionation pathway undergoes, as depicted in eq 3-9, based on the observation of 4-hydroxymethyl-2,6-dimethylphenol as the oxidation product, and k_{disp} is given for the rate constant of this step. Compared with the TMP oxidation, the reaction between Ir^{IV} and 4-hydroxymethyl-2,6-dimethylphenol is 2–5 times slower. Therefore, the overoxidation process does not occur with TMP.



Here, R represents 2-CH₃, 2,6-(CH₃)₂, 4-OCH₃ and 4-C(CH₃)₃. The forward second-order rate constants in eqs 3-2 and 3-3 were obtained experimentally and are summarized in Table 3-3.

3.4.2 Mechanism of k_{ArO^-} Term

Marcus Theory. At high pH, most of the reductants are phenoxide anions instead of phenols and their oxidation by Ir^{IV} occurs through a simple outer-sphere reversible electron transfer mechanism. With the size and unbalanced charge correction term W_{12} , we could use the cross-relationship of the Marcus theory (eqs 1-12 to 1-15) to obtain more accurate self-exchange rate constants for phenoxide anions. The cross electron-transfer rate constant k_{12} , k_{ArO^-} , was obtained experimentally and illustrated in Table 3-3. The radii of phenoxides are estimated using CPK Atomic Models. Other parameters are the same as those described for the phenol oxidation in Chapter 2. The calculated self-exchange rate constants of the phenoxide radical/anion couple, k_{11} , are shown in Table 3-4.

The driving force ($-\Delta G^\circ$) for the electron transfer step between Ir^{IV} and phenoxide anion can be calculated from the difference between the potential for Ir^{IV}/Ir^{III} couple (= 0.893 V vs NHE at $\mu = 0.1 \text{ M}$)⁹³ and that for ArO[•]/ArO⁻ couple shown in Table 3-4. The corrected Gibbs free energy, $\Delta G^{\circ\prime}$, is related to ΔG° through the relation of eq 1-4 where w_{12} (summarized in Table 3-4) is the coulombic work between [IrCl₆]²⁻ and phenoxide anion, and w_{21} is that between [IrCl₆]³⁻ and the phenoxyl radical (equal to zero). From the experimental rate constants, k_{ArO^-} , we can calculate the values for activation barrier (ΔG^\ddagger) according to eq 1-7 using $Z = 10^{11} \text{ M}^{-1} \text{ s}^{-1}$. The reorganization energy (λ) can be estimated using the adiabatic Marcus relationship in which the activation barrier is

Table 3-3. Kinetic Data for the Reaction of Phenols with Ir^{IV}.

substrate	$k_{\text{ArOH}},^a \text{ M}^{-1} \text{ s}^{-1}$	$k_{\text{ArO}^-},^a \text{ M}^{-1} \text{ s}^{-1}$	$\text{p}K_{\text{a}}$	KIE	σ^{+a}
Phenol	0.77 ± 0.03	$(8.0 \pm 0.2) \times 10^6$	9.79^b	3.5 ± 0.3	0
Cresol	16 ± 1	$(5.2 \pm 0.2) \times 10^7$	10.09^b	2.9 ± 0.2	-0.20^c
Xylenol	47 ± 2	$(2.0 \pm 0.1) \times 10^8$	10.38^d	2.6 ± 0.1	-0.40^e
TMP	$(1.09 \pm 0.01) \times 10^3$	$(2.58 \pm 0.03) \times 10^8$	10.65^d	2.04 ± 0.01	-0.71^e
MOP	$(6.1 \pm 0.1) \times 10^4$	$(3.3 \pm 0.10) \times 10^8$	9.96	1.9 ± 0.1	-0.78
TBP	29 ± 3	$(3.6 \pm 0.3) \times 10^7$	10.07^d		-0.26
POP	$(1.2 \pm 0.1) \times 10^3$	$(1.1 \pm 0.2) \times 10^8$	9.90^f		-0.50

^a Brown and Hammett substituent constant. The value for *para*-substituted phenols are from reference 107 except where specifically noted. ^b Obtained from reference 81 at $\mu = 0.1 \text{ M}$ and 25°C . ^c $\sigma^+ = 0.66 \times \sigma^+$ (*para*-cresol) with σ^+ (*para*-cresol) = -0.31 according to reference 107. ^d In reference 81, $\text{p}K_{\text{a}}$ values of xylenol, TMP and TBP are reported at zero ionic strength, 10.62, 10.89 and 10.31, respectively. They are converted in to $\text{p}K_{\text{a}}$ s at $\mu = 0.1 \text{ M}$ by using Davies equation. ^e Sum of each substituent constant. ^f The reported $\text{p}K_{\text{a}1} = 9.81$ at $\mu = 0.25 \text{ M}$ in reference 87 is converted to $\text{p}K_{\text{a}1} = 9.90$ at $\mu = 0.1 \text{ M}$ by using Davies equation.

Table 3-4. Calculated Data for Phenols and the Reactions with Ir^{IV}.

substrate	$r,^a$ Å	$E^\circ(\text{ArO}^\bullet/\text{ArO}^-),^b$ V	$k_{11},^b$ $\text{M}^{-1} \text{s}^{-1}$	f_{12}^c	w_{12}^d	$\Delta G^{0,e}$ $\text{ArO}^- \rightarrow \text{ArO}^\bullet$	$\Delta G^{f,j}$ $\text{ArO}^- \rightarrow \text{ArO}^\bullet$
phenol	2.5	0.80 ^g	2.3×10^6	0.74	3.2	-12.3	23.4
cresol	2.9	0.77 ^h	3.4×10^7	0.61	2.9	-15.0	18.7
xylenol	3.1	0.56 ⁱ	8.2×10^5	0.11	2.8	-34.8	15.4
TMP	3.2	0.50 ^j	2.4×10^5	0.05	2.8	-40.8	14.8
MOP	2.9	0.55 ^g	2.0×10^6	0.08	2.9	-36.2	14.1
TBP	3.5	0.77 ^j	1.4×10^7	0.63	2.6	-14.6	19.6
4,4'-BP	3.8	0.64 ^k	4.0×10^7	0.18	2.5	-26.8	12.5
2,2'-BP	4.4	1.00 ^k	3.0×10^8	0.83	2.2	8.21	25.1

^a Radii are estimated from CPK Atomic Models. ^b Self-exchange rate constant calculated from eqs 1-12 to 1-15 for phenolates/phenoxide radicals couples. ^c Constant in eq 1-12. ^d Coulombic work between $[\text{IrCl}_6]^{2-}$ and phenoxide anion with unit in kJ mol^{-1} . ^e Corrected Gibbs free energy in kJ mol^{-1} and calculated from eqs 1-4 and 1-5, with $w_{21} = 0$. ^f In kJ mol^{-1} and calculated according to eq 1-7 with k_{ArO^-} as k_{et} . ^g Reference 88. ^h Reference 108. ⁱ This work. ^j Reference 109. ^k Reference 85.

dependent of the driving force as shown in eq 1-6. A nonlinear fit of ΔG° and $(\Delta G^{\ddagger} - w_{12})$ for all phenols including unsubstituted phenol, 4,4'-biphenol and 2,2'-biphenol to eq 1-6 gives the solid curve in Figure 3-22 with the reorganization energy $\lambda_{12} = 103 \pm 4 \text{ kJ mol}^{-1}$.

The reorganization energy λ_{12} could also be estimated according to the additivity postulate (eq 1-11), in which assumes that the reorganization energy for the overall reaction, λ_{12} , is the average of the reorganization energies of the two individual self-exchange reactions, λ_{11} and λ_{22} . From the self-exchange rate constant of the $\text{Ir}^{\text{IV}}/\text{Ir}^{\text{III}}$ redox couple ($k_{22} = 2 \times 10^5 \text{ M}^{-1} \text{ s}^{-1}$), λ_{22} is calculated to be 130 kJ mol^{-1} when holding $\Delta G^{\circ} = 0$. $\lambda_{11} = 106 \text{ kJ mol}^{-1}$ for the phenoxide anion/phenoxyl radical couple was calculated from its self-exchange rate constant, $k_{11} = 2.3 \times 10 \text{ M}^{-1} \text{ s}^{-1}$, and the method used to calculate the self-exchange rate constant is described in chapter 2. Therefore, a λ_{12} value of 118 kJ mol^{-1} for phenol reaction is calculated according to eq 1-11. This result is larger than the average λ_{12} value ($103 \pm 4 \text{ kJ mol}^{-1}$) obtained from the above-mentioned $\Delta G^{\circ} - (\Delta G^{\ddagger} - w_{12})$ relation because of the different self-exchange barriers for each substrate.

The Hammett Correlation. Because of the strong resonance interaction between electron donating substituents and the electron-deficient center of phenol, the Brown and Hammett substituent constant σ^{+107} is applied to the Hammett equation 3-10,

$$k = k_0 10^{(\rho\sigma^+)} \quad (3-10)$$

where k are the second-order rate constants for the reaction of Ir^{IV} with the substituted phenoxide anions and k_0 is that for the unsubstituted phenoxide anions. ρ is the reaction constant. The σ^+ values for *para*-substituted phenols are taken from the literature,¹⁰⁷

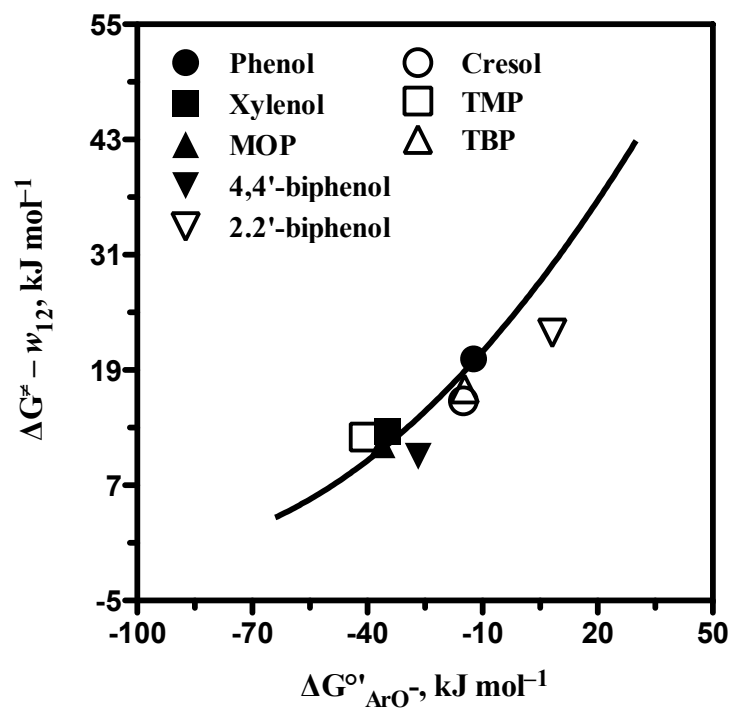


Figure 3-22. Plot of $(\Delta G^{\ddagger} - w_{12})$ versus $\Delta G^{\circ'}$. The solid line is the fit to eq 1-6.

while that for *ortho*-cresol ($\sigma^+ = -0.20$) is calculated according to the relationship provided by Jonsson et al.,¹¹⁰ which is 0.66 times that of the σ^+ for *para*-cresol ($= -0.31$). For the reactions of phenols containing more than one substituent, bi-substituted phenol (xylenol) and tri-substituted phenol (TMP), σ^+ is normally taken as the sum of each substituent constant. All σ^+ are summarized in Table 3-4 including that of 4-phenoxyphenol. When plotting the second-order rate constants of phenoxide anions (k_{ArO^-}) versus σ^+ as shown in Figure 3-23, a correlation is obtained with ρ equal to -2.5 ± 0.3 . The decreasing trend is obeyed by all reactions and implies that the oxidations are aided by electron donating groups. This, in turn, suggests that the reaction center (here, the phenoxyl oxygen) is more positive in the transition state.

Figure 3-24 shows a plot of $\text{p}K_{\text{a}}$ of all phenols at 0.1 M ionic strength versus σ^+ . A linear correlation is achieved with the slope of -1.2 ± 0.1 excluding the reaction of MOP and POP. This result indicates that the oxygen atom attached on the benzene ring affects the correlation between σ^+ and acid-base behavior of phenols.

3.4.3 Mechanism of k_{ArOH} Term

In the two-term rate law, k_{ArOH} refers to the oxidation of phenols in acidic media (in the $\text{p}[\text{H}^+]$ range of 1–3). Under these conditions two possible pathways are considered: a sequential mechanism, including electron transfer prior to the proton transfer (ET/PT), and a concerted PCET (CPET) mechanism. An attempt to distinguish these two processes is performed as described below.

Thermodynamics. The driving force for the concerted proton-coupled electron transfer ($\Delta G^{\circ}_{\text{CPET}}$) and the stepwise ET/PT process ($\Delta G^{\circ}_{\text{ET/PT}}$) can be calculated from the difference between the redox potential of $\text{Ir}^{\text{IV}}/\text{Ir}^{\text{III}}$ couple and that of $\text{ArO}^{\bullet}, \text{H}^+/\text{ArOH}$

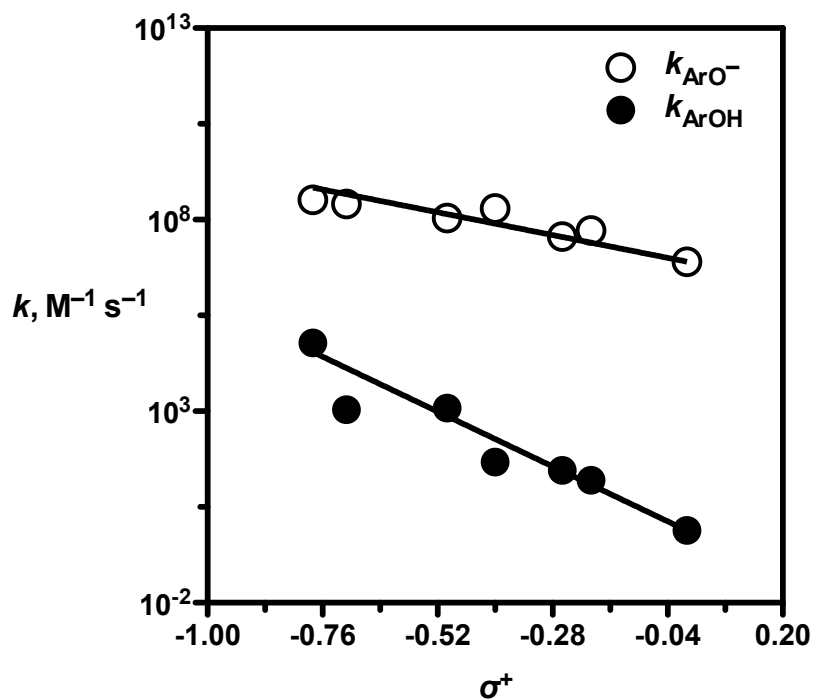


Figure 3-23. Correlations between the second-order rate constants for reaction of phenols (k_{ArOH}) and phenoxide anions (k_{ArO^-}) with Ir^{IV} versus substituent constants σ^+ . Values of k_{ArOH} are labeled with the closed circle and k_{ArO^-} with the open circle. The line is the nonlinear regression to eq 3-10.

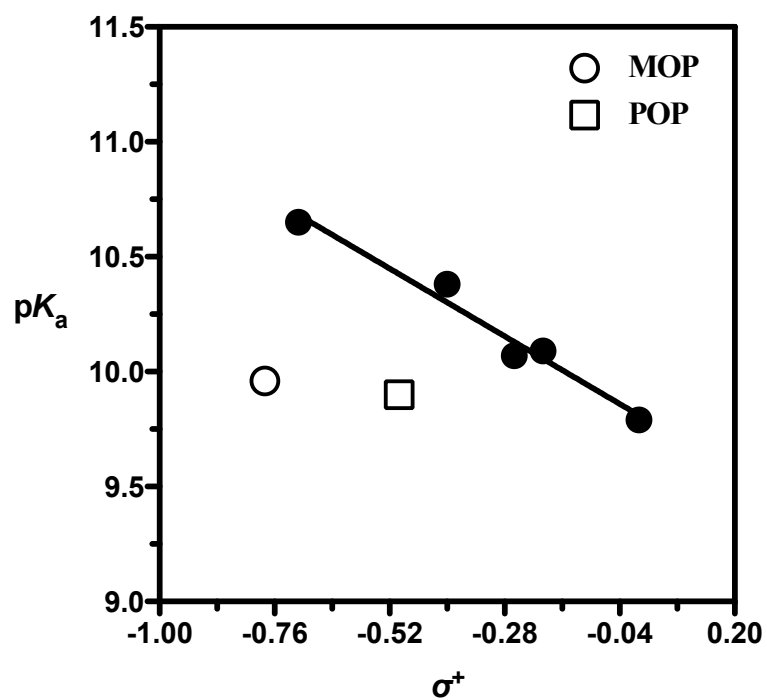


Figure 3-24. Plot of pK_a versus substituent constants σ^+ . The open circle point represents data for the oxidation of MOP and the open square point represents the results for the reaction with 4-phenoxyphenol. The closed circle points resulted from the oxidation of the phenol, cresol, xylenol, TMP, and TBP. Solid line is the linear regression of closed circle points.

couple or $\text{ArOH}^{+}/\text{ArOH}$ couple. Eqs 3-11 and 3-12 show the calculation of $E^\circ(\text{ArO}^\bullet, \text{H}^+/\text{ArOH})$ and $E^\circ(\text{ArOH}^{++}/\text{ArOH})$, respectively.

$$E^\circ(\text{ArO}^\bullet, \text{H}^+/\text{ArOH}) = E^\circ(\text{ArO}^\bullet/\text{ArO}^-) + 0.059 \times \text{p}K_{\text{a, ArOH}} \quad (3-11)$$

$$E^\circ(\text{ArOH}^{++}/\text{ArOH}) = E^\circ(\text{ArO}^\bullet/\text{ArO}^-) + 0.059 \times (\text{p}K_{\text{a, ArOH}} - \text{p}K_{\text{a, ArOH}^{++}}) \quad (3-12)$$

The reported $\text{p}K_{\text{a, ArOH}^{++}}$ values for phenol, cresol and MOP are -2.75^{111} , -1.99^{112} and -1.41^{112} , respectively. No data are available for the other phenols. Table 3-5 lists the reduction potentials and ΔG° . As expected, the driving force for ET/PT pathway in phenol, cresol and MOP oxidation is larger than that for CPET pathway. According to the Marcus theory, in this region where ΔG° is greater than $-\lambda$ the activation barrier ΔG^\ddagger is increased with an increase of ΔG° . Therefore, the ET/PT process has a larger barrier to overcome, which disfavors the stepwise pathway.

The Hammett Correlation. A plot of the second-order rate constants of phenols (k_{ArOH}) versus the Brown and Hammett substituent constant σ^+ is also shown in Figure 3-23 together with the plot of k_{ArO^-} versus σ^+ . A decreasing trend is observed for both k_{ArOH} and k_{ArO^-} , which implies that the oxidations are aided by electron donating groups and the reaction center (here the phenoxyl oxygen) becomes more positive in the transition state. The reaction constant ρ is obtained as -6.0 ± 0.2 when the data are fit to the Hammett equation 3-10 where k refers to k_{ArOH} for substituted phenol and k_0 refers to that for phenol ($= 0.77 \text{ M}^{-1} \text{ s}^{-1}$). Compared to the ρ value for k_{ArO^-} (-2.5 ± 0.3), the more negative value obtained for k_{ArOH} reveals a moderately higher sensitivity to substituent effects for the rates of reaction with phenols than those with phenoxide anions.

Table 3-5. Thermodynamic Parameters for CPET and ET/PT Mechanisms

substrate	CPET			ET/PT		
	$E^\circ(\text{ArO}^\bullet, \text{H}^+ / \text{ArOH}),^a$ V	$\Delta G^\circ_{\text{CPET}},^b$ kJ mol ⁻¹	$\Delta G^\ddagger_{\text{CPET}},^c$ kJ mol ⁻¹	$\text{p}K_{\text{a, ArOH}^{\bullet+}}$	$E^\circ(\text{ArOH}^{\bullet+} / \text{ArOH}),^d$ V	$\Delta G^\circ_{\text{ET/PT}},^e$ kJ mol ⁻¹
phenol	1.38	46.7	46.8	-2.75 ^f	1.54	62.4
cresol	1.36	45.6	45.6	-1.99 ^g	1.48	56.9
xlenol	1.17	27.2	28.7			
TMP	1.13	22.7	25.2			
MOP	1.14	23.6	25.8	-1.41 ^g	1.22	31.6
TBP	1.36	45.4	45.5			
4,4'-BP	1.21	30.8	31.7			
2,2'-BP	1.45	53.8	54.4			

^a Calculated according eq 3-11 with $E^\circ(\text{ArO}^\bullet/\text{ArO}^-)$ listed in Table 3-4 and $\text{p}K_{\text{a,s}}$ in Table 3-3. ^b Equal to $-ZF[E^\circ(\text{Ir}^{\text{IV}}/\text{Ir}^{\text{III}}) - E^\circ(\text{ArO}^\bullet, \text{H}^+/\text{ArOH})]$. ^c Calculated by $\Delta G^\ddagger_{\text{CPET}} = [\lambda (1 + \Delta G^\circ_{\text{CPET}}/\lambda)^2]/4$ with $\lambda = (\lambda_{\text{ox}} + \lambda_{\text{CPET}})/2$ ($\lambda_{\text{CPET}} = 43.4$ kJ mol⁻¹ and $\lambda_{\text{ox, IrIV}} = 130$ kJ mol⁻¹).

^d Calculated according eq 3-12. ^e Equal to $-ZF[E^\circ(\text{Ir}^{\text{IV}}/\text{Ir}^{\text{III}}) - E^\circ(\text{ArOH}^{\bullet+}/\text{ArOH})]$. ^f

Reference 111. ^g Reference 112.

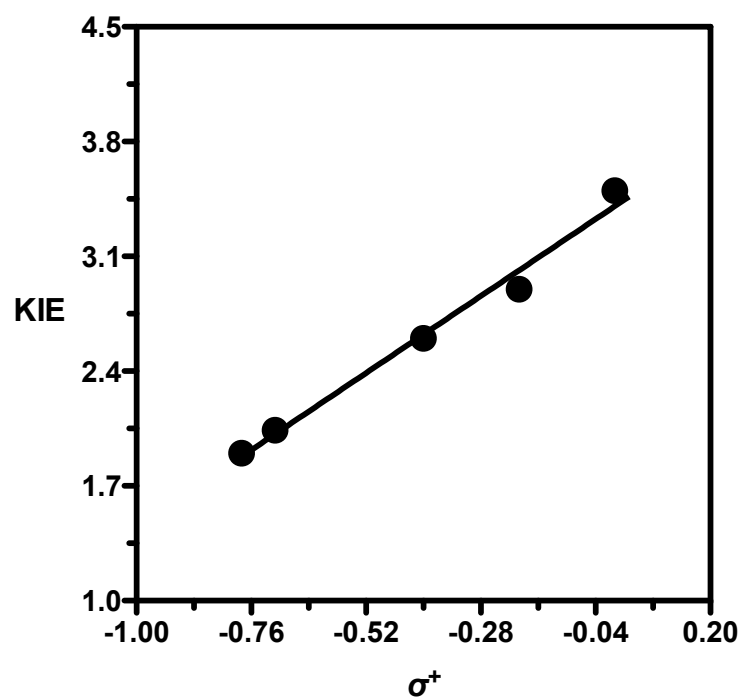


Figure 3-25. Plot of kinetic isotopic effect versus substituent constants σ^+ . The closed circle points are the oxidation of the phenol, cresol, xylene, TMP and TBP and solid line is the linear regression. Data from Table 3-3.

KIE–Hammett Relationship. The deuterium kinetic isotope effects of the reactions between Ir^{IV} and all phenols, except for TBP and POP, versus the Hammett substituent constant σ^+ are plotted in Figure 3-25. A good linear relationship is observed with the slope of 2.0 ± 0.1 .

Comparison with Phenols Oxidation by ClO₂. The oxidations of phenol, cresol, TMP, MOP and TBP by ClO₂ were studied by Hoigne and Bader.¹¹³ They used a two-term rate law to obtain the values for k_{ArOH} and k_{ArO^-} , as shown in Table 3-6.

Table 3-6. Kinetic data for Phenols Oxidation by ClO₂.^a

Reductant	$k_{ArOH}, M^{-1} s^{-1}$	$k_{ArO^-}, M^{-1} s^{-1}$
phenol	0.4 ± 0.1	$(4.9 \pm 0.5) \times 10^7$
cresol	16 ± 4	$(4.4 \pm 0.4) \times 10^8$
TMP	$(3.9 \pm 0.2) \times 10^3$	$(4.0 \pm 1.0) \times 10^9$
MOP	$(2.5 \pm 0.2) \times 10^4$	$(1.7 \pm 0.6) \times 10^9$
TBP	11 ± 3	$(1.5 \pm 0.1) \times 10^8$

^a Reference 114.

When plotting $\ln k$ of phenol oxidation by ClO₂ versus $\ln k$ of Ir^{IV} reactions, a linear relationship, as shown in Figure 3-26, is obtained both for k_{ArOH} and k_{ArO^-} with slopes of 1.0 ± 0.1 and 1.1 ± 0.2 , respectively. This result suggests that the oxidation of phenols by Ir^{IV} is a series of common phenol reactions and that the mechanism of the Ir^{IV} reactions is similar to those of other oxidants, like ClO₂.

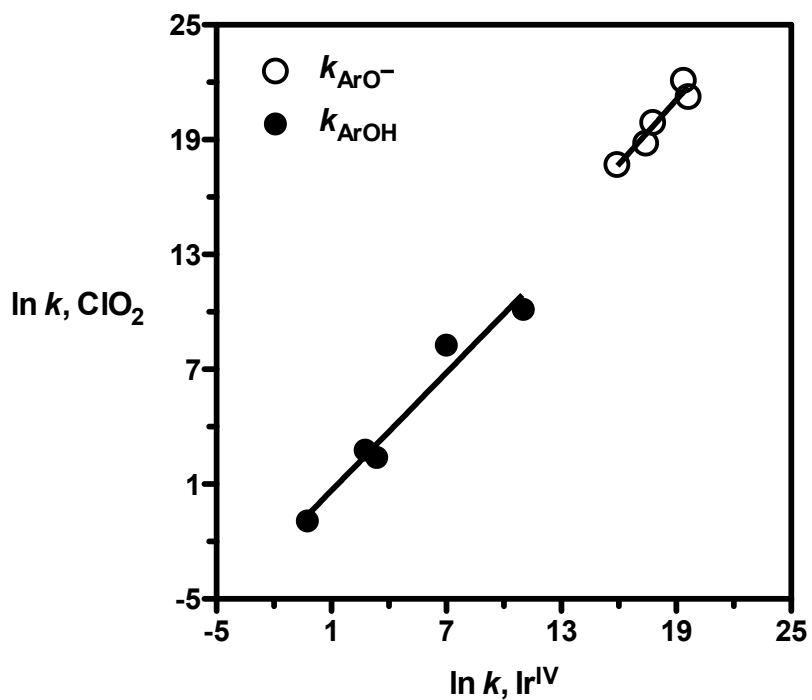


Figure 3-26. Plot of $\ln k(\text{ClO}_2)$ versus $\ln k(\text{Ir}^{\text{IV}})$. The closed circle points are the oxidation of the phenol, cresol, TMP, MOP and TBP by ClO_2 and the open circle points represent these oxidation by Ir^{IV} . Solid lines are the linear regression.

Marcus Theory. According to Bonin,¹¹⁵ the reorganization energy (λ) of a concerted proton-coupled electron-transfer reaction with water acting as the proton acceptor could be estimated according to eq 3-13.

$$\lambda = \frac{\lambda_{\text{ox}} + \lambda_{\text{CPET}}}{2} \quad (3-13)$$

λ_{CPET} is the self-exchange reorganization energy of the reaction described by eq 3-14.



Here, “ \cdots ” represents hydrogen bonds between phenols and H_2O . λ_{CPET} is mainly attributed to solvent organization. The value for phenol reaction was reported as 43.4 kJ mol⁻¹²⁵ and derived from the oxidations by three different oxidants including $[\text{IrCl}_6]^{2-}$. The extension of their results to the ClO_2 oxidation is discussed here by considering the difference of total reorganization energy caused by the different oxidants.

As mentioned in Chapter 2, the self-exchange rate constant of the $\text{Ir}^{\text{IV}}/\text{Ir}^{\text{III}}$ redox couple is equal to $2 \times 10^5 \text{ M}^{-1} \text{ s}^{-1}$, therefore, λ_{ox} is calculated to be 130 kJ mol⁻¹. The self-exchange rate constant for the $\text{ClO}_2/\text{ClO}_2$ redox couple is reported as $160 \text{ M}^{-1} \text{ s}^{-1}$,⁵⁴ which means that λ_{ox} is equal to 201 kJ mol⁻¹. A kinetic study of phenol oxidations by $[\text{Ru}(\text{bpy})_3]^{3+}$, $[\text{Ru}(\text{methyl-bpy})_3]^{3+}$ and $[\text{Ru}(\text{bpy})(\text{ester-bpy})_2]^{3+}$ is reported by Bonin,²⁵ and the data are shown in Table 3-7. λ_{ox} for the $[\text{Ru}(\text{bpy})_3]^{3+}/[\text{Ru}(\text{bpy})_3]^{2+}$ couple is 45.6 kJ mol⁻¹,¹¹⁶ and all three $\text{Ru}^{\text{III}}/\text{Ru}^{\text{II}}$ couples have the same λ_{ox} value.¹¹⁵ With all these λ_{ox} values, the total reorganization energy λ could be calculated according to eq 3-13 with

Table 3-7. Thermodynamic and Kinetic Parameters for Phenol Oxidation by Different Oxidants.

Oxidant	k_{ArOH} , $\text{M}^{-1} \text{s}^{-1}$	λ_{ox} , kJ mol^{-1}	$E^\circ(\text{Ox})$, V	$\Delta G^\circ_{\text{CPET}}$, ^a kJ mol^{-1}	$\Delta G^\ddagger_{\text{CPET}}$, ^b kJ mol^{-1}
$[\text{Ru}(\text{bpy})_3]^{3+c}$	3.0×10^5	45.6^d	1.27	10.3	16.9
$[\text{Ru}(\text{methyl-bpy})_3]^{3+c}$	4.0×10^3	45.6	1.09	27.6	29.2
$[\text{Ru}(\text{bpy})(\text{ester-bpy})_2]^{3+c}$	1.0×10^8	45.6	1.47	-9.03	7.07
ClO_2^e	0.4	201^f	0.95	40.8	54.3
$[\text{IrCl}_6]^{2-}$	0.77	130	0.89	46.7	51.3

^a Equal to $-ZF[E^\circ(\text{ox}) - E^\circ(\text{ArO}^\bullet, \text{H}^+/\text{ArOH})]$. ^b Calculated from $\Delta G^\ddagger_{\text{CPET}} = [\lambda (1 + \Delta G^\circ_{\text{CPET}}/\lambda)^2]/4$ with $\lambda = (\lambda_{\text{ox}} + \lambda_{\text{CPET}})/2$ and $\lambda_{\text{CPET}} = 43.4 \text{ kJ mol}^{-1}$. ^c Reference 25. ^d Reference 116. ^e Reference 114. ^f Reference 54.

$\lambda_{\text{CPET}} = 43.4 \text{ kJ mol}^{-1}$. The different reduction potentials of these oxidants correspond to different driving forces ($\Delta G^{\circ}_{\text{CPET}}$). According to the Marcus theory, the activation barrier ($\Delta G^{\ddagger}_{\text{CPET}}$) could be calculated with the known λ and $\Delta G^{\circ}_{\text{CPET}}$ values by holding the coulombic work terms w_{12} and w_{21} to be zero. A plot of $\ln k_{\text{ArOH}}$ versus $\Delta G^{\ddagger}_{\text{CPET}}$, shown in Figure 3-27, yielded a good linear relationship with slope of -0.40 ± 0.02 and an intercept of 20.3 ± 0.7 . This slope confirms the theoretical value $0.40 (=1000/RT)$ which suggests that Marcus theory can be applied to H₂O-CPET reaction. The intercept value gives the collision frequency, Z , equal to $6.6 \times 10^8 \text{ M}^{-1} \text{ s}^{-1}$ which is smaller than the value in the simple electron transfer process ($= 10 \times 10^{11} \text{ M}^{-1} \text{ s}^{-1}$).

A test about the validity of λ_{CPET} is performed using a two-fold increase ($\lambda_{\text{CPET}} = 86.8 \text{ kJ mol}^{-1}$). The same calculation was made for $\Delta G^{\ddagger}_{\text{CPET}}$, and the plot of $\ln k_{\text{ArOH}}$ versus $\Delta G^{\ddagger}_{\text{CPET}}$ still yielded a good straight line and reproduced the theoretical slope. However, the value of Z increased by almost ten times to $5.3 \times 10^9 \text{ M}^{-1} \text{ s}^{-1}$ compared to that derived with $\lambda_{\text{CPET}} = 43.4 \text{ kJ mol}^{-1}$. Although the accurate λ_{CPET} value cannot be obtained, the results demonstrate that Marcus theory could be successfully applied for H₂O-CPET phenol oxidation and the λ_{CPET} values are the same for all above-mentioned reactions with different oxidants.

The $\Delta G^{\ddagger}_{\text{CPET}}$ values for the oxidation of the phenols by Ir^{IV} are calculated according to Marcus theory (eqs 1-4 and 1-6) and summarized in Table 3-5. The reorganization energy (λ) for each reaction was obtained from eq 3-13 with $\lambda_{\text{CPET}} = 43.4 \text{ kJ mol}^{-1}$ and $\lambda_{\text{ox}} = 130 \text{ kJ mol}^{-1}$. $\Delta G^{\circ}_{\text{CPET}}$ values are also listed in Table 3-5 and the employed coulombic work terms w_{12} and w_{21} were equal to zero. A plot of $\ln k_{\text{ArOH}}$ versus $\Delta G^{\ddagger}_{\text{CPET}}$ is shown in Figure 3-28 and no specific correlation is observed. This result reveals that the λ_{CPET}

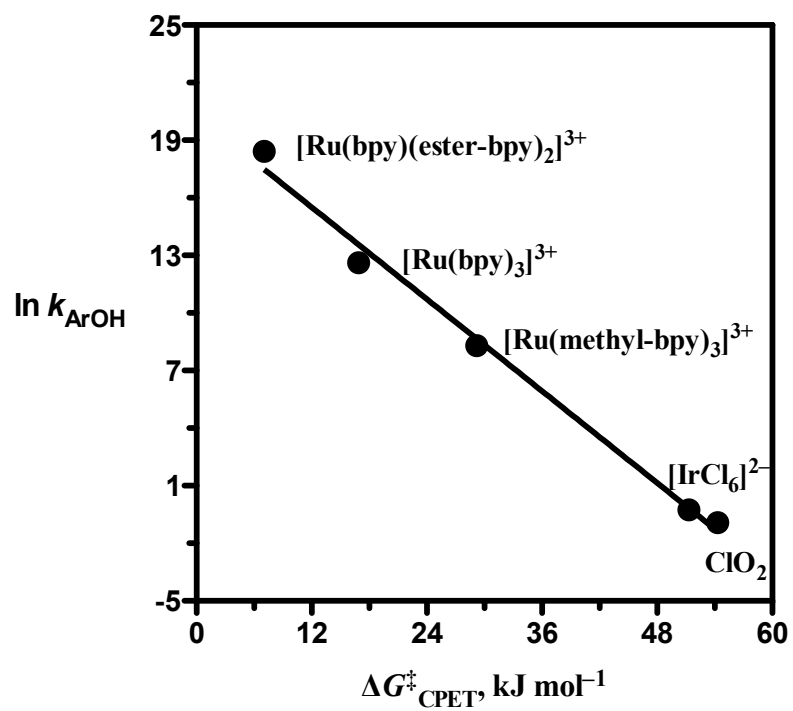


Figure 3-27. Plot of $\ln k_{\text{ArOH}}$ versus $\Delta G_{\text{CPET}}^{\ddagger}$ for phenol oxidation by different oxidants.

Solid line is the linear regression. Data from Table 3-7.

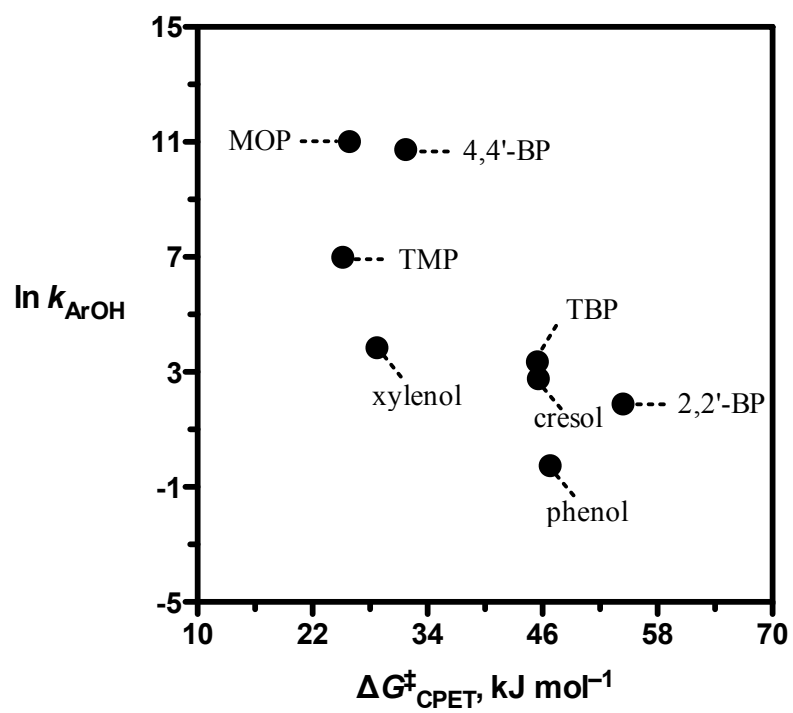


Figure 3-28. Plot of $\ln k_{\text{ArOH}}$ versus $\Delta G^{\ddagger}_{\text{CPET}}$ for the Ir^{IV} reduction by different phenols.

values are influenced by the substituents of phenol, which alter the physical properties of phenol and the hydrogen bonding between phenols and H₂O is expected to change.

Temperature Dependence. The temperature dependence of cresol and MOP are summarized in Table 3-8.

Table 3-8. Activation Parameters for Cresol and MOP Oxidation by Ir^{IV}.^a

substrate	$\Delta G^\ddagger,^b$ kJ mol ⁻¹	$\Delta H^\ddagger,$ kJ mol ⁻¹	$\Delta S^\ddagger,$ J mol ⁻¹ K ⁻¹	$E_a,$ kJ mol ⁻¹	$\Delta G^\ddagger_{\text{CPET}},^c$ kJ mol ⁻¹
Cresol	67.1	42.0	-84.1	44.5	45.6
MOP	46.0	22.8	-78.0	25.3	25.8

^a At 298 K. ^b $\Delta G^\ddagger = \Delta H^\ddagger - 298 \times \Delta S^\ddagger$. ^c Obtained with $\lambda_{\text{CPET}} = 43.4$ kJ mol⁻¹ (derived from phenol reaction).

These reactions were performed at near room temperature, where the Arrhenius activation energy E_a is roughly equal to ΔH^\ddagger plus 2.5 kJ mol⁻¹. The E_a values are consistent with the activation barrier $\Delta G^\ddagger_{\text{CPET}}$ obtained with $\lambda_{\text{CPET}} = 43.4$ kJ mol⁻¹, which is derived from phenol reaction. However, the $\Delta G^\ddagger_{\text{CPET}}$ values derived from Marcus theory are less than the ΔG^\ddagger values by ≈ 20 kJ mol⁻¹, obtained from the temperature dependence experiments for k_{ArOH} .

Chapter 4

OXIDATION OF Ac-Y-NH₂ BY HEXACHLOROIRIDATE(IV)

4.1 Introduction

As one of the most important alpha-amino acids in biological chemistry, tyrosine is of interest to many researchers. The phenol functional group facilitates the electron transfer between tyrosine and other cofactors in photosystem II^{40,41} and RNR.^{18,117} The *C*- and *N*-termini provide tyrosine three p*K*_a's and redox-activity which complicates kinetic studies.

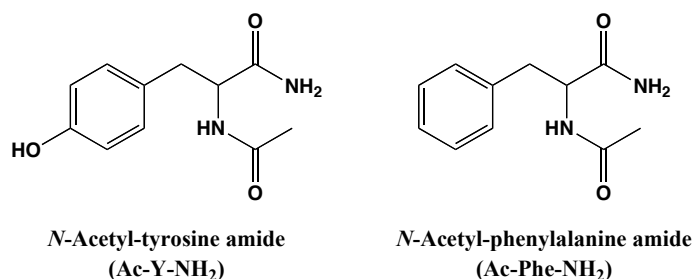
In this chapter, a *N*-acetyl and *C*-amide protected tyrosine, *N*-acetyl-tyrosine amide, is used as a reductant for Ir^{IV}. The kinetic study of this reaction will provide insight into the mechanisms of biological electron transfer reactions. Overoxidation is observed, and two-term and three-term rate laws are applied to obtain the rate constants: k_{ArOH} , k_{ArO^-} and k^o .

4.2 Experimental Section

4.2.1 Reagents and Solutions

All commercial chemical reagents were used as received except as noted. Ammonium hexachloroiridate(III) monohydrate (abbreviated as Ir^{III}), deuterium oxide,

sodium acetate anhydrous, cacodylic acid and sodium hydroxide were purchased from Sigma–Aldrich Chemicals Company. Perchloric acid, acetic acid, monochloroacetic acid were obtained from Fisher Scientific Co. Ammonium hexachloroiridate(IV) (abbreviated as Ir^{IV}) was purchased from Alfa. The spin-trapping agent DBNBS was synthesized as described in Chapter 2. *N*-Acetyl-tyrosine amide (Ac-Y-NH₂) and *N*-acetyl-phenylalanine amide (Ac-Phe-NH₂) were purchased from Bachem, and their structures are shown in Scheme 4-1.



Scheme 4-1. The structures of Ac-Y-NH₂ and Ac-Phe-NH₂.

All solutions were freshly prepared with deionized water provided by a Barnstead NANO Pure Infinity ultrapure water system, and purged with argon gas prior to the reactions to prevent potential complications caused by O₂. The ionic strength was adjusted with lithium perchlorate trihydrate (GFS) and is approximately equal in both oxidants and reductants solutions to prevent Schlieren effects (or refractive index effect⁶³). Selected buffer solutions (acetate, monochloroacetate, and cacodylate buffers) were applied to control the pH if necessary.

4.2.2 Methods

A Corning 450 pH/ion meter was used with a Mettler Toledo InLab 421 or InLab

Semi-Micro-L combination pH electrode. The reference electrode electrolyte was replaced with 3 M NaCl to prevent the formation of KClO₄ precipitate. With the known H⁺ concentration and pH reading, the activity coefficient γ ($= 0.839 \pm 0.04$) was obtained from equation $p[\text{H}^+] = \text{pH} + \log \gamma$, where $p[\text{H}^+]$ is equal to $-\log [\text{H}^+]$.

All measurements were performed at 25.0 ± 0.1 °C. The kinetics experiments were carried out on a Hi-Tech SF-51 stopped-flow spectrophotometer with OLIS 4300 data acquisition and analysis software. UV-vis spectra were monitored on a HP-8453 diode array spectrophotometer equipped with a Brinkman Lauda RM6 thermostated water bath to maintain the temperature at 25 °C. All kinetics data were obtained by monitoring the absorbance of Ir^{IV} at 488 nm. The observed pseudo-first-order rate constants were obtained from fitting kinetic traces over five half lives to first-order exponential functions and each reported observed rate constant is the average of at least 5 shots. The Specfit/32 version 3.0.15 global analysis system was applied to simulate the reaction traces, and the GraphPad Prism 4 or 5 software was used to analyze the rate law with $1/Y^2$ weighting.

4.3 Results

The kinetic trace of a typical reaction between Ac-Y-NH₂ and Ir^{IV} is shown in Figure 4-1. 0.004 M of Ac-Y-NH₂ is oxidized by 2.5×10^{-5} M of Ir^{IV} in 0.05 M HClO₄ at 0.1 M ionic strength. Although we attempted to use a small amount of Ir^{IV} to obtain an improved first-order kinetics, the consumption curve of Ir^{IV} does not fit a first-order exponential function well.

4.3.1 Hexachloroiridate(III) Inhibition

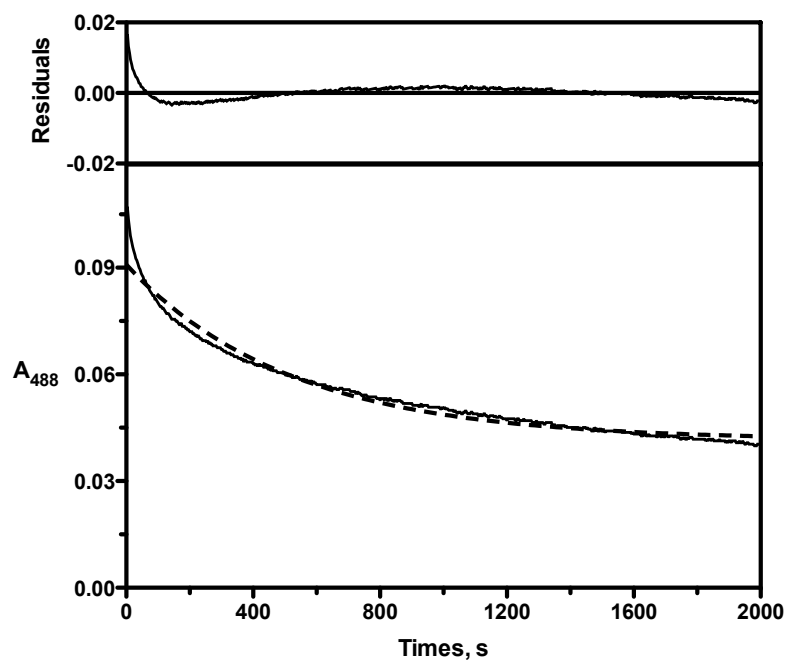


Figure 4-1. Trace of the Ac-Y-NH₂ reaction (solid line) and first-order fit (dashed line).

[Ac-Y-NH₂]_{tot} = 0.004 M; [Ir^{IV}]₀ = 2.5 × 10⁻⁵ M, [HClO₄] = 0.05 M; μ = 0.1 M (LiClO₄);

T = 25 °C.

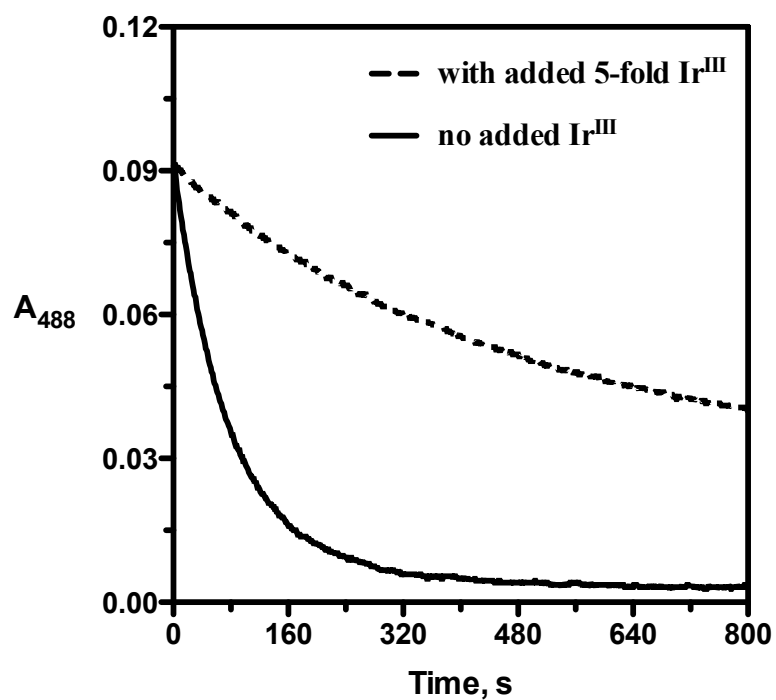


Figure 4-2. Comparative traces of the Ac-Y-NH₂ reaction (solid line) with added Ir^{III} (dashed line). [Ac-Y-NH₂]_{tot} = 8.0 × 10⁻⁴ M; [Ir^{IV}]₀ = 2.5 × 10⁻⁵ M; [Ir^{III}] = 12.5 × 10⁻⁵ M; p[H⁺] = 3.5 (0.02 M acetate buffer); μ = 0.1 M (LiClO₄); T = 25 °C.

The solid line in Figure 4-2 displays the reaction traces of 8.0×10^{-4} M Ac-Y-NH₂ and 2.5×10^{-5} M Ir^{IV} at p[H⁺] = 3.5, while the dashed line shows the kinetic trace of the same reaction with the addition of a 5-fold excess of Ir^{III}. A significant difference is observed when comparing these two reactions, which implies that the oxidation of Ac-Y-NH₂ by Ir^{IV} is affected by Ir^{III}.

4.3.2 Spin Trapping Effect

In order to remove the Ir^{III} inhibition, the phenoxy radical spin trapping agent, DBNBS, was applied to the Ir^{IV} reaction. Various concentrations of DBNBS (0.1–10 mM) were added into the solutions containing 0.004 M of Ac-Y-NH₂ and 2.5×10^{-5} M of Ir^{IV} in 0.05 M HClO₄. The first half-lives of all these reactions are summarized in Table 4-1.

Table 4-1. Kinetic Data for the Reaction of Ac-Y-NH₂ with Ir^{IV} in the Presence of DBNBS.^a

[DBNBS], mM	t _{1/2} , s
0	165
0.1	133
0.5	74.7
1.0	58.3
2.0	50.0
5.0	36.7
10	36.7

^a [Ac-Y-NH₂]_{tot} = 0.004 M; [Ir^{IV}]₀ = 2.5×10^{-5} M; [HClO₄] = 0.05 M; μ = 0.1 M

(LiClO₄); T = 25 °C.

The reaction rate increases with increasing concentrations of DNBNS and approaches a maximum value when 5 mM DNBNS were added. Subsequently, the rate does not change even after adding more DNBNS. In the presence of 5 mM DNBNS, a good first-order fit was obtained as shown in Figure 4-3 at 488 nm. This result suggests that 5 mM DNBNS is sufficient to prevent Ir^{III} inhibition.

4.3.3 Ac-Y-NH₂ Dependence

At p[H⁺] = 2.8, the oxidations of $(8.0\text{--}72) \times 10^{-4}$ M of Ac-Y-NH₂ by 2.5×10^{-5} M of Ir^{IV} were examined in presence of 5 mM DNBNS under pseudo-first-order conditions. All kinetic data are collected in Table A-25. When plotting the observed rate constants versus the total concentrations of Ac-Y-NH₂, a linear relationship is obtained as shown in Figure 4-4 with the slope of $13.0 \pm 0.1 \text{ M}^{-1} \text{ s}^{-1}$. This result indicates that the rate law is first-order with respect to Ac-Y-NH₂ as shown in eq 4-1:

$$k_{\text{obs}} = k [\text{Ac-Y-NH}_2]_{\text{tot}} \quad (4-1)$$

4.3.4 Dependence on p[H⁺]

The p[H⁺] dependence was studied using 2.5×10^{-5} M of Ir^{IV} and $(3.0\text{--}64) \times 10^{-4}$ M of Ac-Y-NH₂ over the p[H⁺] range of 1–7 in the presence of 5 mM DNBNS. The experimental data are summarized in Table A-26, and a plot of $k_{\text{obs}}/[\text{Ac-Y-NH}_2]_{\text{tot}}$ versus p[H⁺] is shown in Figure 4-5. The simple two-term rate law, eq 2-2, is applied to analyze the data. K_a is the acid dissociation constant of Ac-Y-NH₂, $\text{p}K_a = 9.90$.⁴⁵ k_{ArOH} and k_{ArO^-} represent the reactivity of Ac-Y-NH₂ and the corresponding phenolate species. A

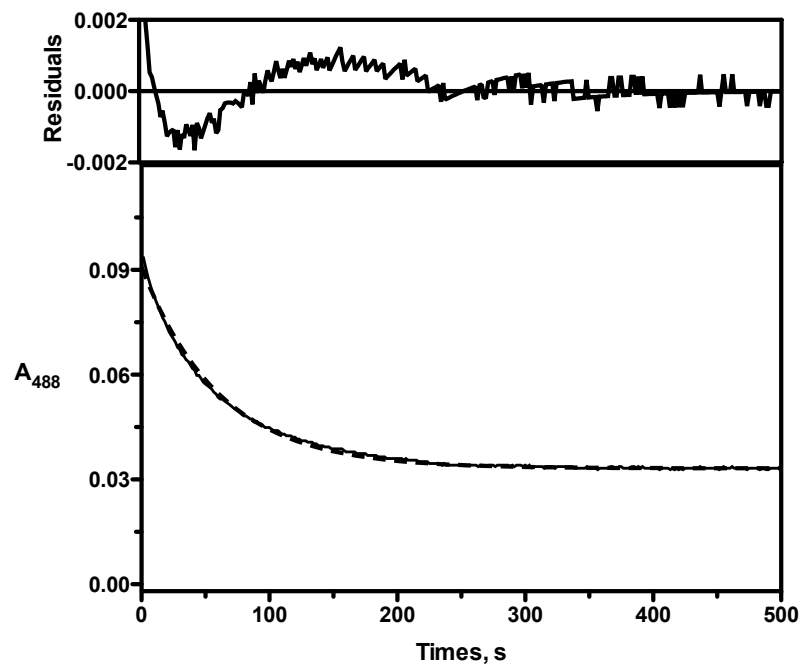


Figure 4-3. Trace of the Ac-Y-NH₂ reaction in the presence of DBNBS (solid line) and first-order fit (dashed line). [Ac-Y-NH₂]_{tot} = 0.004 M; [Ir^{IV}]₀ = 2.5 × 10⁻⁵ M, [DBNBS] = 5 mM; [HClO₄] = 0.05 M; μ = 0.1 M (LiClO₄); T = 25 °C.

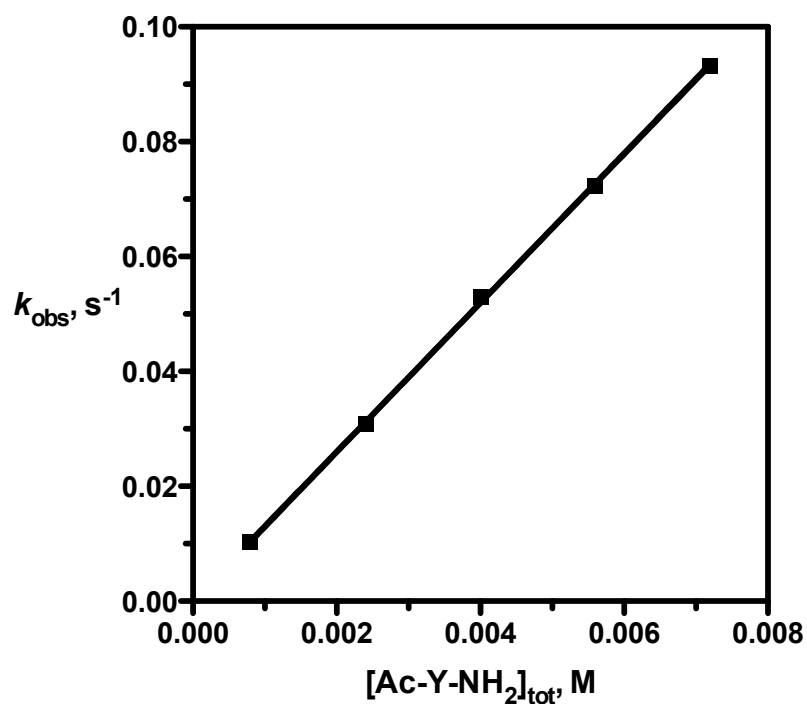


Figure 4-4. Plot of k_{obs} vs $[\text{Ac-Y-NH}_2]_{\text{tot}}$. $[\text{Ac-Y-NH}_2]_{\text{tot}} = (8.0\text{--}72) \times 10^{-4}$ M; $[\text{Ir}^{\text{IV}}]_0 = 2.5 \times 10^{-5}$ M; $[\text{DBNBS}] = 5$ mM; $\text{p}[\text{H}^+] = 2.8$ (0.02 M monochloroacetate buffer); $\mu = 0.1$ M (LiClO_4); $T = 25$ °C. Solid line is linear fit. Data from Table A-25.

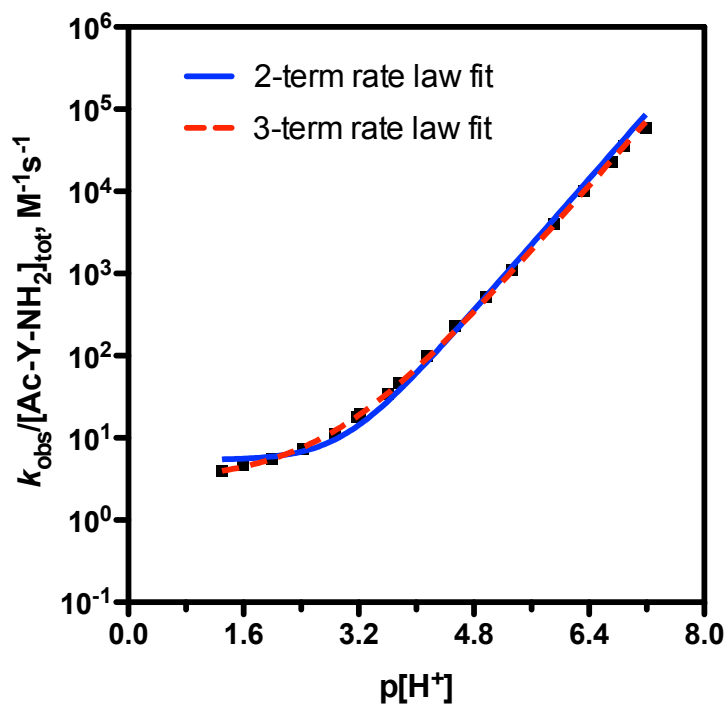


Figure 4-5. Plot of $k_{\text{obs}}/[\text{Ac-Y-NH}_2]_{\text{tot}}$ vs $\text{p}[\text{H}^+]$. $[\text{Ac-Y-NH}_2]_{\text{tot}} = (3.0\text{--}64) \times 10^{-4}$ M; $[\text{Ir}^{\text{IV}}]_0 = 2.5 \times 10^{-5}$ M; $[\text{DBNBS}] = 5$ mM; $\mu = 0.1$ M (LiClO_4); $T = 25$ °C. $\text{p}[\text{H}^+] = -\log [\text{HClO}_4]$ in the $\text{p}[\text{H}^+]$ range of 1.0–2.2. The following buffers (0.02 M) were employed to maintain constant $\text{p}[\text{H}^+]$ values: monochloroacetate buffer for $2.4 < \text{p}[\text{H}^+] < 3.4$, acetate buffer for $3.6 < \text{p}[\text{H}^+] < 5.4$, and cacodylate buffer for $5.4 < \text{p}[\text{H}^+] < 7.4$. Solid line is the fit to eq 2-2 and the dashed line is the fit to eq 2-3. Data from Table A-26.

nonlinear least-squares fit of the data to eq 2-2 yielded $k_{\text{ArOH}} = 5.4 \pm 0.6 \text{ M}^{-1} \text{ s}^{-1}$ and $k_{\text{ArO}^-} = (4.5 \pm 0.3) \times 10^7 \text{ M}^{-1} \text{ s}^{-1}$.

Figure 4-5 shows a fit of the data in Table A-26 to the 3-term rate law (eq 2-3), values for k_{ArOH} , k_{ArO^-} and k° are obtained, with $k_{\text{ArOH}} = 2.9 \pm 0.2 \text{ M}^{-1} \text{ s}^{-1}$, $k_{\text{ArO}^-} = (3.6 \pm 0.1) \times 10^7 \text{ M}^{-1} \text{ s}^{-1}$ and $k^{\circ} = 0.22 \pm 0.02 \text{ M}^{-1} \text{ s}^{-1}$, as displayed in Table A-27. The contributions of the additional k° term were calculated over the $\text{p}[\text{H}^+]$ range of 1–7. The maximum value is 49% and occurs around $\text{p}[\text{H}^+] = 2.8$.

4.3.5 Stoichiometry and Overoxidation

A spectrophotometric titration of Ac-Y-NH₂ with Ir^{IV} was performed to determine the consumption ratio. The experiments were investigated in 0.02 M acetate buffer at $\text{p}[\text{H}^+] = 5.5$. Figure 4-6a shows the absorption spectra changes resulting from titrating 2.4 mL of $1.0 \times 10^{-4} \text{ M}$ Ac-Y-NH₂ with $2.3 \times 10^{-3} \text{ M}$ of Ir^{IV} solution. All spectra were obtained after the completion of oxidation. The absorption spectrum after adding $2.3 \times 10^{-7} \text{ mol}$ of Ir^{IV} is displayed in Figure 4-6b. Under this condition, the peak at 275 nm (maximum absorbance of Ac-Y-NH₂ with $\epsilon_{275} = 1.5 \times 10^3 \text{ M}^{-1} \text{ cm}^{-1}$) reveals that some Ac-Y-NH₂ is still present in the solution and all added Ir^{IV} is consumed, therefore, the absorption of Ir^{IV} is not an issue. A new peak at 416 nm and a shoulder around 340 nm are observed, which indicates the absorption of products. Same maximum absorption (275 nm) has been found for Ac-Y-NH₂ and its analogous species *N*-acetyltyrosine,¹¹⁸ so the coupling product of Ac-Y-NH₂ oxidation is expected to have maximum absorption at around 286 nm in analogy to the *N*-acetyltyrosine dimer. However, no peak is observed at this wavelength. The peak at 416 nm may originate from the overoxidation product quinone species. The titration curves at 340 nm (Figure 4-7a) and 488 nm (Figure 4-7b)

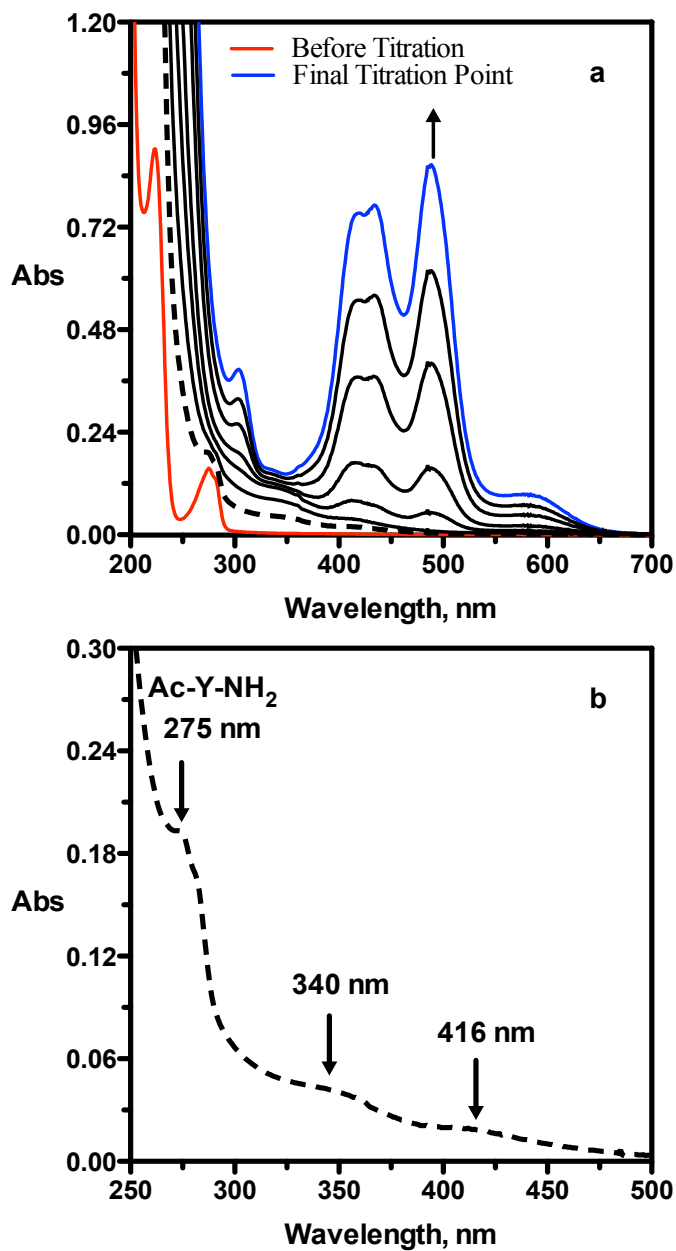


Figure 4-6. Titration of Ac-Y-NH₂ (2.4 mL, 1.0×10^{-4} M) with 2.3×10^{-3} M of Ir^{IV} at $p[H^+] = 5.5$ (0.02 M acetate buffer) and 25 °C. All spectra were obtained after the completion of the oxidation. Dashed lines in (a) and (b) are the spectra obtained after adding 2.3×10^{-7} mol of Ir^{IV}.

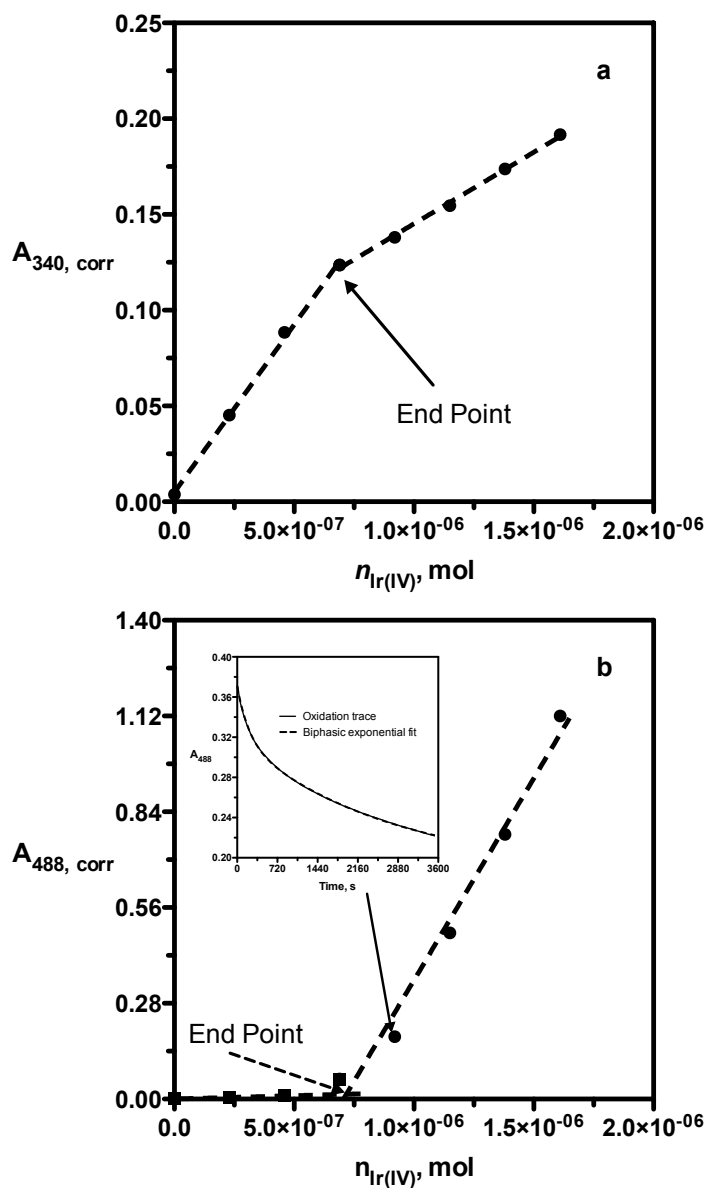


Figure 4-7. The titration curve of Ac-Y-NH₂ (2.4 mL, 0.1 mmol) solution by 2.5×10^{-5} M of Ir^{IV} solution at $p[H^+] = 5.5$ (0.02 M acetate buffer) and 25 °C. Closed circles represent the data corrected for volume changes. Dashed lines are the linear regression fit. (a) 340 nm. (b) 488 nm. The insert shows an oxidation trace (solid line) and a bi-phase exponential fit (dashed line) after titrating with 9.2×10^{-7} mol of Ir^{IV}.

are corrected for volume changes using $A_{\text{corr}} = A_{\text{obs}} * V_{\text{total}}/V_{\text{initial}}$. The increase of absorption after the end point at 340 nm in Figure 4-7a is due to the absorption of Ir^{IV}. The consumption ratio of $n_{\text{IrIV}}/n_{\text{Ac-Y-NH}_2}$ amounted to 2.9, which indicates that overoxidation occurs under these conditions. Significant oxidation is detected even after the end point as shown in the insert in Figure 4-7b when titrating with 9.2×10^{-7} mol of Ir^{IV}. The kinetic decay trace fits a biphasic exponential curve well with a fast rate constant of $(4.7 \pm 0.1) \times 10^{-3} \text{ s}^{-1}$ and a slow rate constant of $(3.7 \pm 0.1) \times 10^{-4} \text{ s}^{-1}$. All titration curves in Figure 4-6a were collected at the end of the show rate. The biphasic phenomenon may be attributed to the further oxidation of the decomposition products of the Ac-Y-NH₂ overoxidation, and the addition of Ir^{IV} could accelerate this process. No oxidation is observed after adding 1.38×10^{-6} mol of Ir^{IV}.

4.3.6 Control Experiments

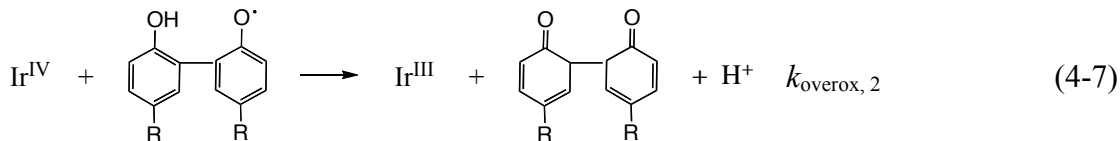
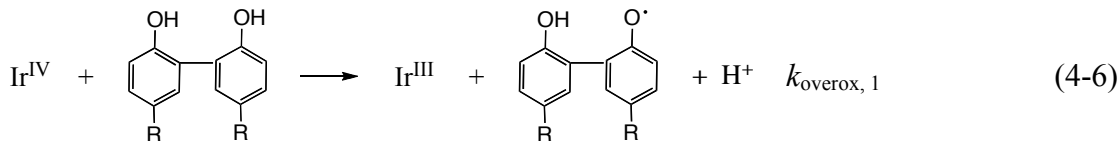
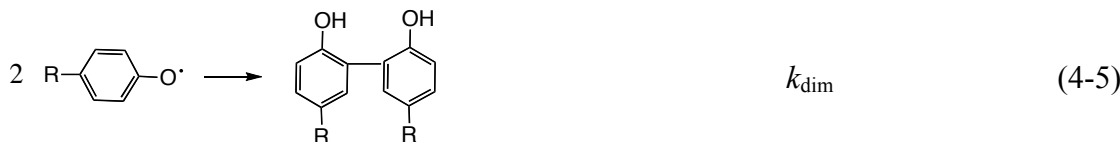
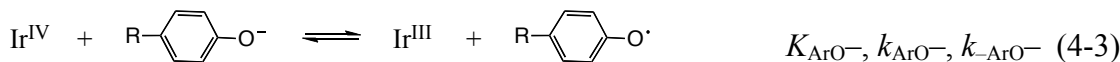
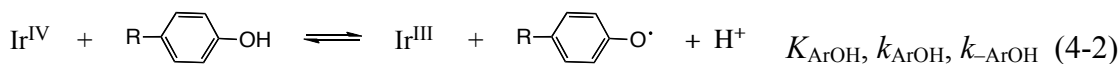
In order to gain insight about the reactivity of the caboxamide groups of Ac-Y-NH₂, the reactions between 3.0×10^{-3} M of Ac-Phe-NH₂ and 1.0×10^{-4} M of Ir^{IV} were tested at 0.1 M ionic strength in 0.05 M HClO₄ and at $\text{p}[\text{H}^+] = 7.0$. No oxidation was observed under both conditions, which confirms that only the hydroxyl group of Ac-Y-NH₂ participates in the reaction with Ir^{IV}.

4.4 Discussion and Conclusion

A mechanism similar to the one established for phenols in chapter 2 and 3 is proposed for the reaction between Ir^{IV} and Ac-Y-NH₂. Concerted proton-coupled electron-transfer takes place when the reductant is Ac-Y-NH₂ according to eq 4-2. K_{ArOH} ,

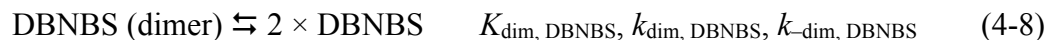
k_{ArOH} and k_{-ArOH} are the equilibrium constant and rate constants for this reaction.

Reversible outer-sphere one-electron transfer occurs when the conjugate base, the phenolate anion, of Ac-Y-NH₂ is the major reactant (eq 4-3). K_{ArO^-} , k_{ArO^-} and k_{-ArO^-} represent the equilibrium constant and second-order rate constants of this pathway. The relevant acid/base equilibrium between Ac-Y-NH₂ and its phenolate anion is described by eq 4-4 with K_a as the acid dissociation constant. The phenoxy radicals formed in processes 4-2 and 4-3 undergo bimolecular C–C coupling to produce 2,2'-biphenol derivative (eq 4-5), which undergoes further oxidation by Ir^{IV} to form the corresponding biphenosemiquinone (eq 4-6). k_{dim} represents the coupling rate constant and $k_{overox, 1}$ is the rate constant of further overoxidation. As we mentioned before, biphenosemiquinone is readily oxidized by Ir^{IV} with formation of biphenoquinone (rate constant = $k_{overox, 2}$) is described in reaction 4-7.



Here, R represent $-\text{CH}_2\text{CH}(\text{CONH}_2)(\text{NHCOCH}_3)$.

In the presence of the spin trap DBNBS, the dimerization step (eq 4-8) of DBNBS with an equilibrium constant $K_{\text{dim, DBNBS}}$, of 1.3×10^{-3} M is included in the mechanism. The Ac-Y-NH₂ phenoxy radical is scavenged by DBNBS to form an adduct which undergoes a rapid oxidation by Ir^{IV} as described in eqs 4-9 and 4-10.



Marcus Theory. The electron-transfer rate constant, k_{ArO^-} , is analyzed using the Marcus theory equations 1-12 to 1-15 where k_{12} is the cross electron-transfer rate constant ($k_{\text{ArO}^-} = 4.5 \times 10^7 \text{ M}^{-1} \text{ s}^{-1}$), k_{11} and k_{22} are the self-exchange rate constants of the Ac-Y-NH₂•/Ac-Y-NH₂⁻ and Ir^{IV}/Ir^{III} redox couples. A value for k_{22} of $2 \times 10^5 \text{ M}^{-1} \text{ s}^{-198}$ is used in the calculation, $1 \times 10^{11} \text{ M}^{-1} \text{ s}^{-1}$ is used for Z , the collision frequency.⁹⁹ Z_i, Z_j are the ionic charges of the reactants, R is the ideal gas constant, and r is the center to center distance between two reactants when they are approaching each other. The radii of $[\text{IrCl}_6]^{2-}$ and Ac-Y-NH₂⁻ are 4.1 \AA^{58} and 4.2 \AA , respectively, estimated from CPK Atomic Models. μ is the ionic strength. The value of K_{12} was calculated to be 1.8×10^4 from the redox potential of the Ac-Y-NH₂•/Ac-Y-NH₂⁻ couple (= 0.64 V vs NHE⁴⁵) and the Ir^{IV}/Ir^{III} couple (= 0.893 V vs NHE at $\mu = 0.1 \text{ M}^{93}$). With all these parameters and the experimental value of k_{12} and K_{12} , k_{11} is calculated from above equations as $2.9 \times 10^5 \text{ M}^{-1} \text{ s}^{-1}$.

The rate constant of the H₂O-CPET process, k_{ArOH} , is also analyzed with the Marcus theory, setting λ_{CPET} equal to 43.4 kJ mol⁻¹. The driving force, $\Delta G^{\circ}_{\text{CPET}}$, is calculated to be 32.8 kJ mol⁻¹ with the reduction potential of the Ac-Y-NH₂[•]/Ac-Y-NH₂ couple as 1.23 V vs NHE. With the known λ_{CPET} and $\Delta G^{\circ}_{\text{CPET}}$ values, the activation barrier, $\Delta G^{\ddagger}_{\text{CPET}}$, is estimated to be 33.4 kJ mol⁻¹ from equation 1-6, where the coulombic work term w_{12} is equal to zero.

Overoxidation. The large stoichiometric ratio (= 2.9) of $n_{\text{IrIV}}/n_{\text{Ac-Y-NH}_2}$ suggests that the oxidation of Ac-Y-NH₂ by Ir^{IV} is highly affected by extensive overoxidation. Although in the presence of DBNBS, the reaction may also be influenced by overoxidation, which results in a large maximum contribution of the additional k° term (49%) in a three-term rate law over the p[H⁺] range of 1–7. A significant maximum contribution of the additional k° (56%) is also found in the oxidation of TBP where a large substituted group is located on the *para* position. This result indicates that the large substituent on *para* position may enhance the overoxidation effect, which leads to a significant pH-dependent rate constant.

Chapter 5
OXIDATION OF PHENOL BY
TRIS-(1,10-PHENANTHROLINE)OSMIUM(III)

5.1 Introduction

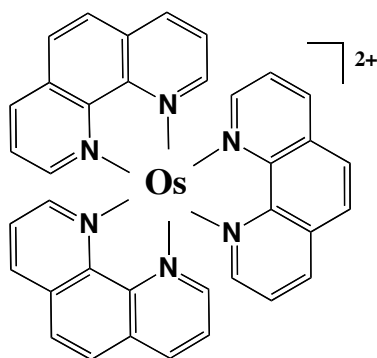
Tris-(1,10-phenanthroline)osmium(III) is another substitution-inert oxidant which has a reduction potential close to that of $[\text{IrCl}_6]^{2-}$, but differs in that it is a cation. As shown in Marcus theory, the electrostatic energy is dependent on the charges of the oxidant, which influences the activation barrier (ΔG^\ddagger) and thereby the rate of electron transfer.

The oxidation of phenol by tris-(1,10-phenanthroline)osmium(III) is reported in this chapter. The Os^{III} complex was obtained by conversion of the corresponding Os^{II} complex with bromine. All kinetic data were obtained in the presence of Os^{II} in order to avoid complications arising from excess bromine. A second order rate law on $[\text{Os}^{\text{III}}]$ and $[\text{phenol}]_{\text{tot}}$ is established, and a mechanism is proposed.

5.2 Experimental Section

5.2.1 Reagents and Solutions

All commercial chemical reagents were used as received except as noted. Sodium acetate anhydrous, cacodylic acid and sodium hydroxide were purchased from Sigma–Aldrich Chemicals Company. Perchloric acid, sodium chloride, ammonium chloride, acetic acid, monochloroacetic acid, ethanol, diethyl ether, 1,4-dioxane, petroleum ether, ethyl acetate, bromine, acetonitrile, hydrochloric acid and hydrogen peroxide were from Fisher Scientific Co. Phenol (Fluka) was recrystallized from a 75% w/w water solution as described in the literature.⁶² Pure [Os(phen)₃]Cl₂ (Os^{II}) was prepared following a procedure of a prior study⁵⁹ and its structure is shown in Scheme 5-1.



Scheme 5-1. Structure of [Os(phen)₃]²⁺.

All aqueous solutions were freshly prepared with deionized water provided by a Barnstead NANO Pure Infinity ultrapure water system, and purged with argon gas prior to the reactions to prevent potential complications caused by O₂. A solution of ≈ 0.1 M bromine in acetonitrile was prepared under argon gas and kept in the dark. The bromine stock solution was then diluted and the concentration was quantified spectrally according to the absorbance of bromine at λ_{max} (392 nm) with $\epsilon_{392} = 183 \pm 4 \text{ M}^{-1} \text{ cm}^{-1}$.¹¹⁹ The ionic strength was adjusted by NaCl and was approximately equal in both oxidants and

reductants solutions to prevent Schlieren effects (or refractive index effect⁶³). Selected buffer solutions (acetate, monochloroacetate, and cacodylate buffers) were applied to control the pH if necessary.

Preparation of [Os(phen)₃]³⁺ Solutions. The Os^{III} aqueous solution (concentration of CH₃CN is less than 1% v/v) was prepared in situ under argon gas by adding a 0.01 M bromine-acetonitrile solution (saturated with Ar) into the Os^{II} solution in 0.01 M HCl right before the reaction.⁵⁶ In order to prevent complications caused by bromine, an excess of Os^{II} was maintained. The solutions were protected from light at all times.

5.2.2 Methods

A Corning 450 pH/ion meter was used with a Mettler Toledo InLab Semi-Micro-L combination pH electrode. Electrode calibrations at $\mu = 0.1$ M (LiClO₄) were carried out with 0.01–0.1 M perchloric acid. With the known H⁺ concentration and pH reading, the activity coefficient γ ($= 0.839 \pm 0.04$) was obtained from equation $p[\text{H}^+] = \text{pH} + \log \gamma$, where $p[\text{H}^+]$ is equal to $-\log [\text{H}^+]$.

All measurements were performed at 25.0 ± 0.1 °C. The kinetics experiments were carried out on a Hi-Tech SF-51 stopped-flow spectrophotometer with OLIS 4300 data acquisition and analysis software. UV-vis spectra were monitored on a HP-8453 diode array spectrophotometer equipped with a Brinkman Lauda RM6 thermostated water bath to maintain the temperature at 25 °C. All kinetics data were obtained by monitoring the absorbance of at 480 nm or 550 nm with a 375-nm optical UV cut-off filter to prevent photoreactions. k_{obs} is the observed second-order rate constant based on concentration according to eq 5-1.

$$\frac{1}{[\text{Os}^{\text{III}}]} - \frac{1}{[\text{Os}^{\text{III}}]_0} = k_{\text{obs}} t \quad (5-1)$$

The observed second-order rate constant based on absorbance, k_{obs}' , was obtained from fitting kinetic traces over 4 half-lives to the second-order function according to eq 5-2.

Each reported experimental rate constant is the average of at least 4 shots.

$$\frac{1}{A_{\infty} - A} - \frac{1}{A_{\infty} - A_0} = k_{\text{obs}}' t \quad (5-2)$$

k_{obs} is calculated from k_{obs}' by multiplying of the molar absorptivity differences of Os^{II} and Os^{III} ($\epsilon_{\text{OsII}} - \epsilon_{\text{OsIII}}$) at the particular wavelength, as shown in eq 5-3.

$$k_{\text{obs}} = k_{\text{obs}}' (\epsilon_{\text{OsII}} - \epsilon_{\text{OsIII}}) \quad (5-3)$$

The Specfit/32 version 3.0.15 global analysis system was applied to simulate the reaction traces, and the GraphPad Prism 5 software was used to analyze the rate law with $1/Y^2$ weighting. ^1H NMR spectra were acquired on a Bruker AV 400 MHz spectrometer; chemical shifts in D_2O are relative to DSS.

5.3 Results

5.3.1 Characterization of the Osmium Complexes

Figure 5-1 shows the ^1H NMR spectrum of $[\text{Os}(\text{phen})_3]\text{Cl}_2$ in the low-field region. There are four signals at chemical shifts of 7.58, 8.08, 8.29 and 8.42 ppm, which are assigned to the four non-equivalent protons in the phenanthroline rings. The UV-vis spectrum of $[\text{Os}(\text{phen})_3]\text{Cl}_2$ in acidic aqueous solution, as shown in Figure 5-2, displays a maximum absorption peak at 430 nm with $\epsilon_{430} = (1.80 \pm 0.15) \times 10^4 \text{ M}^{-1} \text{ cm}^{-1}$, which is consistent with the reported value $1.85 \times 10^4 \text{ M}^{-1} \text{ cm}^{-1}$.⁵⁹ In order to avoid complications arising from the potential biphenoquinone products which exhibit an absorption at around 400 nm, we performed our kinetic measurements at 480 nm where $\epsilon_{480} = (1.67 \pm 0.13) \times 10^4 \text{ M}^{-1} \text{ cm}^{-1}$. Under pseudo-second-order conditions, high amounts of Os^{II} were required to be present in the solution, which produced an extremely strong absorbance at 480 nm that exceeded the detection limit. Therefore, we followed the reactions at 550 nm, where Os^{II} absorbs relatively weakly with $\epsilon_{550} = (5.15 \pm 0.34) \times 10^3 \text{ M}^{-1} \text{ cm}^{-1}$.

We obtained the UV-vis spectrum of $[\text{Os}(\text{phen})_3]\text{Cl}_3$ (Figure 5-2) via bromine oxidation of Os^{II} in 0.01 M HCl. The maximum absorption difference between Os^{III} and Os^{II} appears around 480 nm. All molar absorptivities of both Os^{III} and Os^{II} at 430, 480 and 550 nm are summarized in Table 5-1. The molar absorptivity differences of Os^{II} and Os^{III} ($\epsilon_{\text{Os}^{\text{II}}} - \epsilon_{\text{Os}^{\text{III}}}$) at particular wavelengths are also displayed in Table 5-1.

5.3.2 Kinetics

The oxidation of 0.02 M phenol by $0.67 \times 10^{-5} \text{ M Os}^{\text{III}}$ was carried out in 0.02 M acetate buffer at $\text{p}[\text{H}^+] = 4.1$ in the presence of $1.56 \times 10^{-5} \text{ M Os}^{\text{II}}$. The reaction trace at 480 nm is shown in Figure 5-3a and can be fit to a pseudo-second-order model. The kinetic trace of the reaction between $0.73 \times 10^{-5} \text{ M}$ of Os^{III} and 0.002 M phenol with 1.28

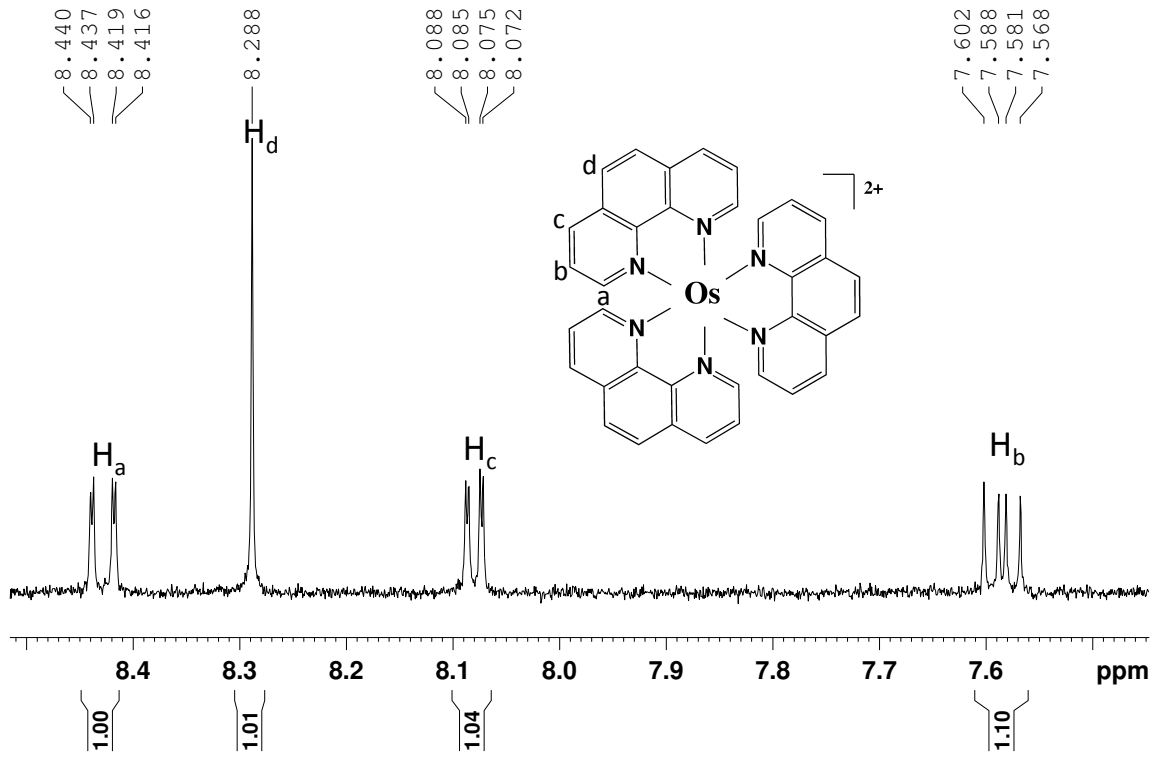


Figure 5-1. ¹H NMR spectrum of [Os(phen)₃]²⁺ in D₂O (aromatic region).

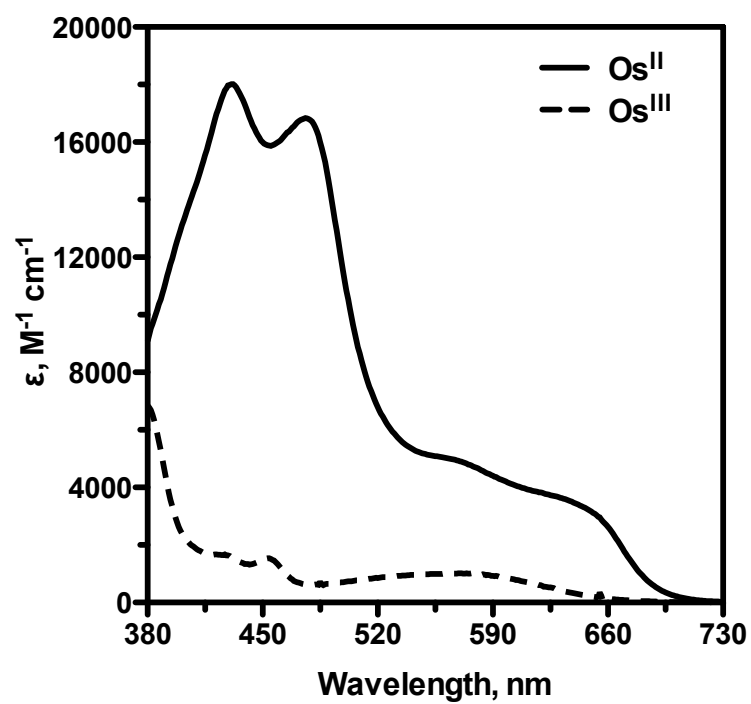


Figure 5-2. UV-vis Spectra of $[\text{Os}(\text{phen})_3]\text{Cl}_2$ (solid line) and $[\text{Os}(\text{phen})_3]\text{Cl}_3$ (dashed line) in 0.01 M HCl solution.

Table 5-1. UV-Visible Absorbance of Os Complexes in 0.01 M HCl Solution.

	$\epsilon_{430}, \text{M}^{-1} \text{cm}^{-1}$	$\epsilon_{480}, \text{M}^{-1} \text{cm}^{-1}$	$\epsilon_{550}, \text{M}^{-1} \text{cm}^{-1}$
Os ^{II}	$(1.80 \pm 0.1) \times 10^4$	1.67×10^4	5.15×10^3
Os ^{III}	1.61×10^3	6.30×10^2	9.83×10^2
	$(\epsilon_{\text{OsII}} - \epsilon_{\text{OsIII}})_{430},$	$(\epsilon_{\text{OsII}} - \epsilon_{\text{OsIII}})_{480},$	$(\epsilon_{\text{OsII}} - \epsilon_{\text{OsIII}})_{550},$
	$\text{M}^{-1} \text{cm}^{-1}$	$\text{M}^{-1} \text{cm}^{-1}$	$\text{M}^{-1} \text{cm}^{-1}$
	1.64×10^4	1.61×10^4	4.16×10^3

$\times 10^{-5}$ M of Os^{II} at 550 nm at $\text{p}[\text{H}^+] = 5.1$ is shown in Figure 5-3b. A good-quality pseudo-second-order fit was also obtained.

Os^{III} Dependence. In the presence of more than 10-fold excess of Os^{II} over Os^{III}, the oxidations of 0.002 M phenol by various concentrations of Os^{III} were studied at $\text{p}[\text{H}^+] = 5.1$. Kinetic traces of reactions were acquired at 550 nm. The observed first half-lives are summarized in Table A-28. A plot of half-life versus $1/[\text{Os}^{\text{III}}]_0$ yielded a straight line, as shown in Figure 5-4, with a slope of $(1.56 \pm 0.03) \times 10^{-5}$ M s. This result implies that the rate law is second-order with respect to the initial concentration of Os^{III} according to eq 5-4.

$$-\frac{d[\text{Os}^{\text{III}}]}{dt} = k_{\text{obs}} [\text{Os}^{\text{III}}]^2 \quad (5-4)$$

Phenol Dependence. Under pseudo-second-order conditions, a series of reactions

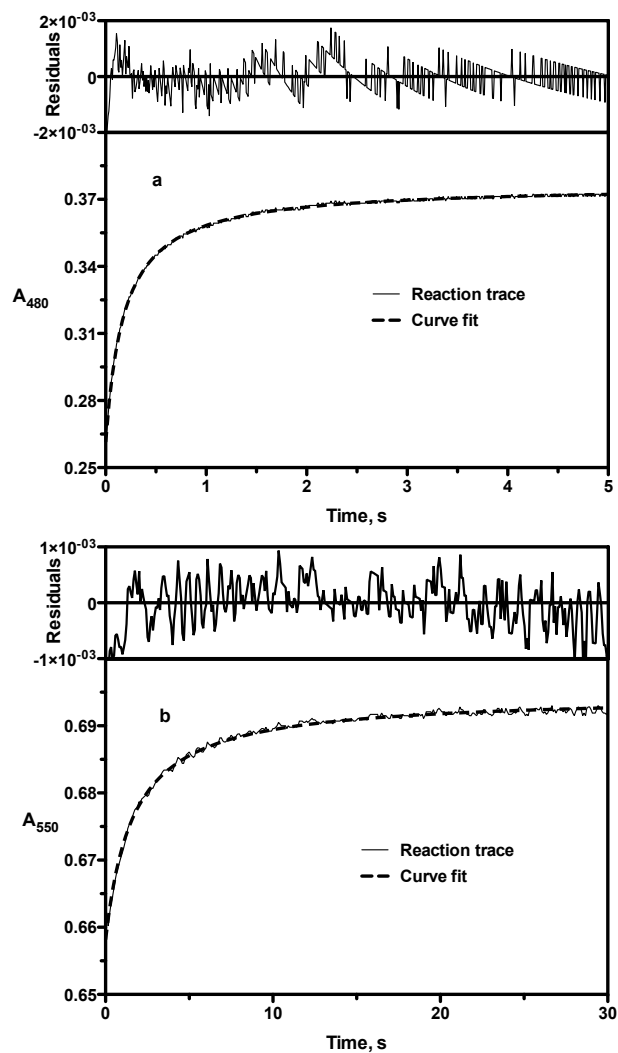


Figure 5-3. Kinetic traces of the phenol oxidation by Os^{III} . $\mu = 0.1 \text{ M}$ (NaCl); $T = 25^\circ\text{C}$. Lower box shows the experimental trace (solid line) and the pseudo-second-order fit (dashed line). Upper box shows the residuals of the fit. (a) Monitored at 480 nm; $[\text{Os}^{\text{III}}]_0 = 0.67 \times 10^{-5} \text{ M}$; $[\text{Os}^{\text{II}}]_0 = 1.56 \times 10^{-5} \text{ M}$; $[\text{phenol}] = 0.02 \text{ M}$; $\text{p}[\text{H}^+] = 4.1$ (0.02 M acetate buffer). (b) Monitored at 550 nm; $[\text{Os}^{\text{III}}]_0 = 0.79 \times 10^{-5} \text{ M}$; $[\text{Os}^{\text{II}}]_0 = 1.27 \times 10^{-4} \text{ M}$; $[\text{phenol}] = 0.002 \text{ M}$; $\text{p}[\text{H}^+] = 5.1$ (0.02 M acetate buffer).

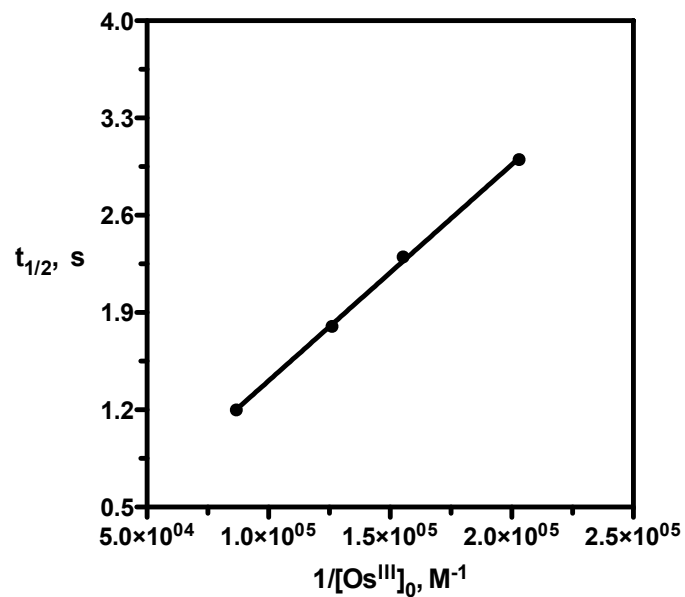


Figure 5-4. Plot of $t_{1/2}$ vs $1/[\text{Os}^{\text{III}}]_0$. All the reactions were run under pseudo-second-order conditions at 550 nm. $[\text{Os}^{\text{III}}]_0 = (0.49\text{--}1.15) \times 10^{-5}$ M; $[\text{Os}^{\text{II}}]_0 = (12.2\text{--}12.7) \times 10^{-5}$ M; $[\text{phenol}] = 0.002$ M; $\mu = 0.1$ M (NaCl); $T = 25^\circ\text{C}$; $\text{p}[\text{H}^+] = 5.1$ (0.02 M acetate buffer). Solid line is the linear fit. Data from Table A-28.

between 1.21×10^{-5} M of Os^{III} and various concentrations of phenol (0.002–0.02 M) were followed at 550 nm at a $\text{p}[\text{H}^+]$ of around 5.5 (acetate buffer) in the presence of 12.4×10^{-5} M Os^{II} . Figure 5-5 shows the kinetic trace of a reaction with 0.002 M phenol and its pseudo-second-order fit. Kinetic data of all the four reactions are summarized in Table A-29. The linear plot of the observed second-order rate constant versus $[\text{phenol}]_{\text{tot}}^2$, shown in Figure 5-6, yielded a slope of $(9.20 \pm 0.13) \times 10^9 \text{ M}^{-3} \text{ s}^{-1}$. Thus, the rate law is second-order with respect to the total concentration of phenol as described in eq 5-5.

$$k_{\text{obs}} = k [\text{phenol}]_{\text{tot}}^2 \quad (5-5)$$

Os^{II} Dependence. The oxidations of 0.0025 or 0.005 M phenol by $(0.47\text{--}1.38) \times 10^{-5}$ M of Os^{III} in the presence of $(0.68\text{--}1.51) \times 10^{-5}$ M of Os^{II} were studied in the presence of 0.02 M acetate buffer at $\text{p}[\text{H}^+] = 4.7$ and were followed at 480 nm. The first half-life and observed second-order rate constants are summarized in Table A-30. A linear relationship between $k_{\text{obs}}/[\text{phenol}]_{\text{tot}}^2$ and $1/[\text{Os}^{\text{II}}]_0^2$ was observed and is shown in Figure 5-7 with a slope of $(3.39 \pm 0.11) \text{ M}^{-1} \text{ s}^{-1}$ and an intercept of $(2.58 \pm 0.16) \times 10^{10} \text{ M}^{-3} \text{ s}^{-1}$. It should be noted that under those conditions, for example, the oxidation by 1.38×10^{-5} M of Os^{III} in presence of 0.68×10^{-5} M of Os^{II} , the concentration of Os^{II} during the reaction can not be treated as a constant value. And the rate constants obtained from pseudo-second-order kinetics are much slower than those without the influence of Os^{II} . This would increase the slope and decrease the intercept in Figure 5-7. However, the observed linear relationship suggests that the rate law follows an inverse second-order dependence on the initial concentration of Os^{II} according to eq 5-6.

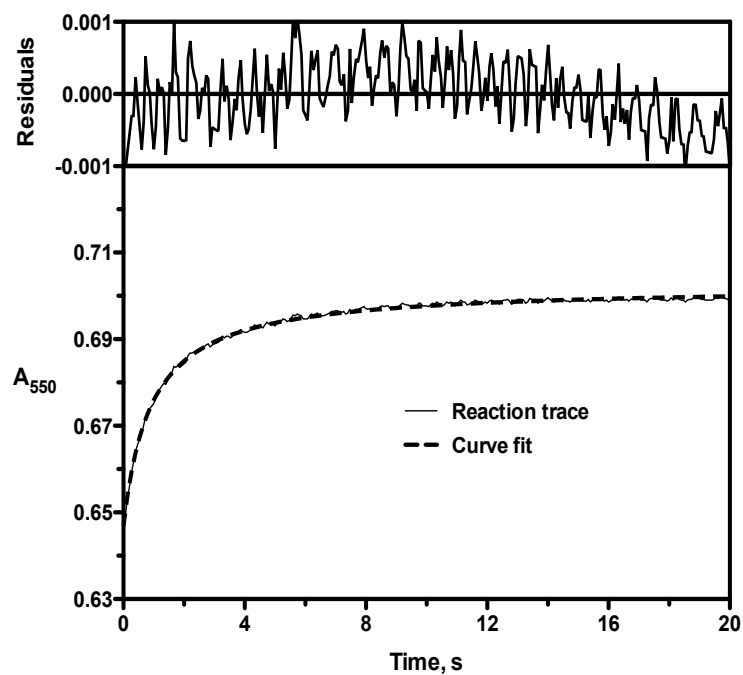


Figure 5-5. Kinetic trace of phenol oxidation by Os^{III} at 550 nm. $\mu = 0.1 \text{ M}$ (NaCl); $T = 25^\circ\text{C}$. Lower box shows the experimental trace (solid line) and the pseudo-second-order fit (dashed line). Upper box shows the residuals in the fit. $[\text{Os}^{\text{III}}]_0 = 1.21 \times 10^{-5} \text{ M}$; $[\text{Os}^{\text{II}}]_0 = 12.4 \times 10^{-5} \text{ M}$; $[\text{phenol}] = 0.002 \text{ M}$; $\mu = 0.1 \text{ M}$ (NaCl); $T = 25^\circ\text{C}$; $\text{p}[\text{H}^+] = 5.4$ (0.02 M acetate buffer).

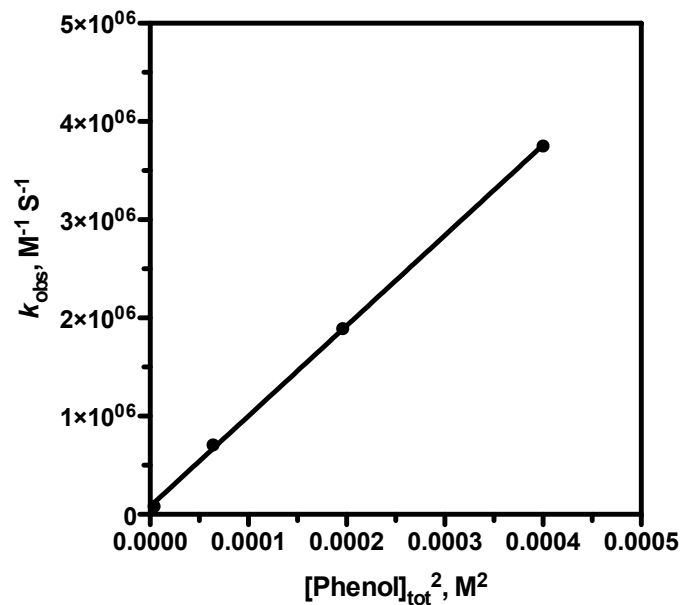


Figure 5-6. Plot of k_{obs} vs $[\text{phenol}]_{\text{tot}}^2$. All the reactions were studied at 550 nm using pseudo-second-order conditions. $[\text{Os}^{\text{III}}]_0 = 1.21 \times 10^{-5} \text{ M}$; $[\text{Os}^{\text{II}}]_0 = 12.4 \times 10^{-5} \text{ M}$; $[\text{phenol}] = (0.002\text{--}0.02) \text{ M}$; $\mu = 0.1 \text{ M (NaCl)}$; $T = 25^\circ\text{C}$; $\text{p}[\text{H}^+]$ values of 5.44–5.68 were maintained using a 0.02 M acetate buffer. Solid line is the linear fit. Data from Table A-29.

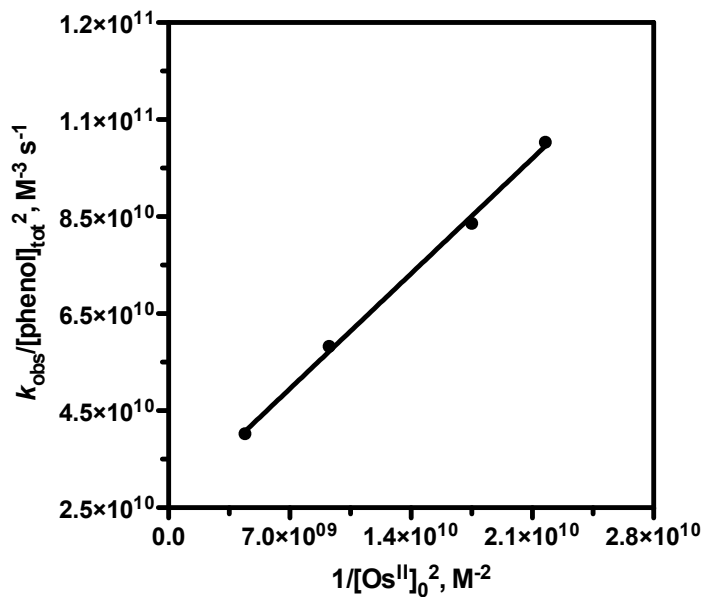


Figure 5-7. Plot of $k_{\text{obs}}/[\text{phenol}]_{\text{tot}}^2$ vs $1/[\text{Os}^{\text{II}}]_0^2$. All the reactions were run under “pseudo-second-order” conditions at 480 nm. $[\text{Os}^{\text{III}}]_0 = (0.47\text{--}1.38) \times 10^{-5}$ M; $[\text{Os}^{\text{II}}]_0 = (0.68\text{--}1.51) \times 10^{-5}$ M; $[\text{phenol}]_{\text{tot}} = (2.5\text{--}5.0) \times 10^{-3}$ M; $\mu = 0.1$ M (NaCl); $T = 25^\circ\text{C}$; $\text{p}[\text{H}^+] = 4.7$ (0.02 M acetate buffer). Solid line is the linear fit. Data from Table A-30.

$$k_{\text{obs}} = k' \frac{1}{[\text{Os}^{\text{II}}]_0^2} \quad (5-6)$$

p[H⁺] Dependence. The phenol oxidations by $(0.39\text{--}0.67) \times 10^{-5}$ M of Os^{III} were studied over the p[H⁺] range of 4.0–6.4 at 480 nm. The detailed reaction conditions and kinetic data are collected in Table A-31. According to the pre-equilibrium approximation and the mechanism proposed in the next section, a rearrangement of the k_{obs} expression (eq 5-18) as shown below yields

$$\frac{[\text{Os}^{\text{II}}]_0^2 k_{\text{obs}}}{[\text{ArOH}]_{\text{tot}}^2} = 2k_{\text{dim}} \left(\frac{K_{\text{ArOH}}}{K_{\text{a}} + 10^{-\text{p}[\text{H}^+]}} \right)^2 \quad (5-7)$$

Here, K_{a} is the acid dissociation constant of phenol, $\text{p}K_{\text{a, ArOH}} = 9.79$ at $\mu = 0.1$ M⁸¹. k_{dim} represents the dimerization rate constant of phenoxy radicals. The value of K_{ArOH} ($= 1.1 \times 10^{-9}$ M) was calculated from the redox potential of the $\text{C}_6\text{H}_5\text{O}^\bullet$, $\text{H}^+/\text{C}_6\text{H}_5\text{OH}$ and Os^{III}/Os^{II} couples. $E_{\text{f}}(\text{C}_6\text{H}_5\text{O}^\bullet/\text{C}_6\text{H}_5\text{O}^-) = 0.797$ V is corrected from 0.79 V at $\mu = 0.0$ M⁸⁸ by means of the equation $\log \gamma = -Az_i^2 \mu^{1/2}/(1 + \mu^{1/2})$ and $E_{\text{f}}(\text{C}_6\text{H}_5\text{O}^\bullet, \text{H}^+/\text{C}_6\text{H}_5\text{OH}) = 1.376$ V is calculated from $E_{\text{f}}(\text{ArO}^\bullet, \text{H}^+/\text{ArOH}) = E_{\text{f}}(\text{ArO}^\bullet/\text{ArO}^-) + 0.0592\text{p}K_{\text{a}}$. The redox potential of the Os^{III}/Os^{II} couple was obtained from the supporting data of reference⁵⁶ as 0.846 V vs NHE at $\mu = 0.1$ M. When plotting $[\text{Os}^{\text{II}}]_0^2 k_{\text{obs}}/[\text{phenol}]_{\text{tot}}^2$ versus p[H⁺] and fitting the data to eq 5-7, a good quality fit was achieved with $\log 2k_{\text{dim}}$ of 9.49, as shown in Figure 5-8. This value is close to the reported $\log 2k_{\text{dim}}$ value of 9.36.⁹⁵ If we consider a 5 mV uncertainty in the redox potential for each couple the resulting uncertainty of \log

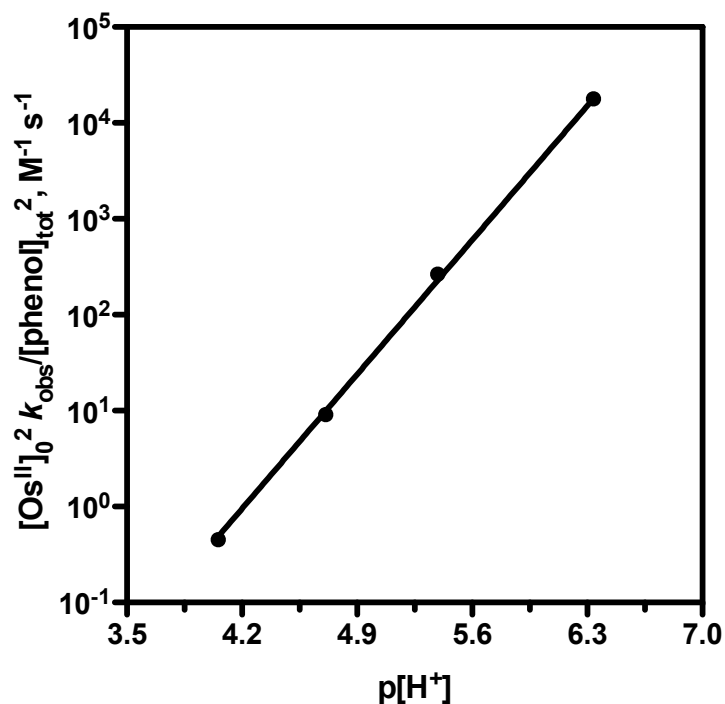


Figure 5-8. Plot of $[\text{Os}^{\text{II}}]_0^2 k_{\text{obs}}/[\text{phenol}]_{\text{tot}}^2$ versus $\text{p}[\text{H}^+]$. All the reactions were run under “pseudo-second-order” conditions at 480 nm. $[\text{Os}^{\text{III}}]_0 = (0.39\text{--}0.67) \times 10^{-5}$ M; $[\text{Os}^{\text{II}}]_0 = (1.51\text{--}1.81) \times 10^{-5}$ M; $[\text{phenol}]_{\text{tot}} = (0.2\text{--}20) \times 10^{-3}$ M; $\mu = 0.1$ M (NaCl); $T = 25$ °C. The following buffers (0.02 M) were employed to maintain constant $\text{p}[\text{H}^+]$ values: acetate buffer for $4.0 < \text{p}[\text{H}^+] < 5.4$, and cacodylate buffer for $\text{p}[\text{H}^+] = 6.34$. Solid line is fit to eq 5-7. Data from Table A-31.

$2k_{\text{dim}}$ is 0.30.

Spin Trapping Effect. The influence of spin trapping agent DBNBS was tested for the phenol oxidation by Os^{III} . 1 or 10 mM of DBNBS was added into the reaction mixture containing 1.26×10^{-5} M of Os^{III} and 0.0025 M of phenol in the presence of 0.75×10^{-5} M of Os^{II} at $\text{p}[\text{H}^+] = 4.71$. All data are summarized in Table 5-2.

Table 5-2. Kinetic Data for the Reaction of Phenol with Os^{III} in the Presence of Dipic or DBNBS.^a

[DBNBS], mM ^b	$t_{1/2}$, s
0	0.11
1.0	0.08
10	0.03
[Dipic], mM ^c	$t_{1/2}$, s
0	0.18
1.0	0.18

^a All the reactions were monitored at 480 nm. $\mu = 0.1$ M (NaCl); $T = 25^\circ\text{C}$. ^b $[\text{Os}^{\text{III}}]_0 = (1.23\text{--}1.38) \times 10^{-5}$ M; $[\text{Os}^{\text{II}}]_0 = (0.68\text{--}0.79) \times 10^{-5}$ M; $[\text{phenol}]_{\text{tot}} = 0.0025$ M; $\text{p}[\text{H}^+] = 4.71$ (0.02 M acetate buffer). ^c $[\text{Os}^{\text{III}}]_0 = 0.67 \times 10^{-5}$ M; $[\text{Os}^{\text{II}}]_0 = 1.56 \times 10^{-5}$ M; $[\text{phenol}]_{\text{tot}} = 0.02$ M; $\text{p}[\text{H}^+] = 4.05$ (0.02 M acetate buffer).

A decrease of the first half-life is observed with increasing DBNBS concentration. A kinetic trace of the reaction with 10 mM DBNBS is shown in Figure 5-9. A good quality pseudo first-order fit was obtained at 480 nm, which implies that the phenoxyl radical is

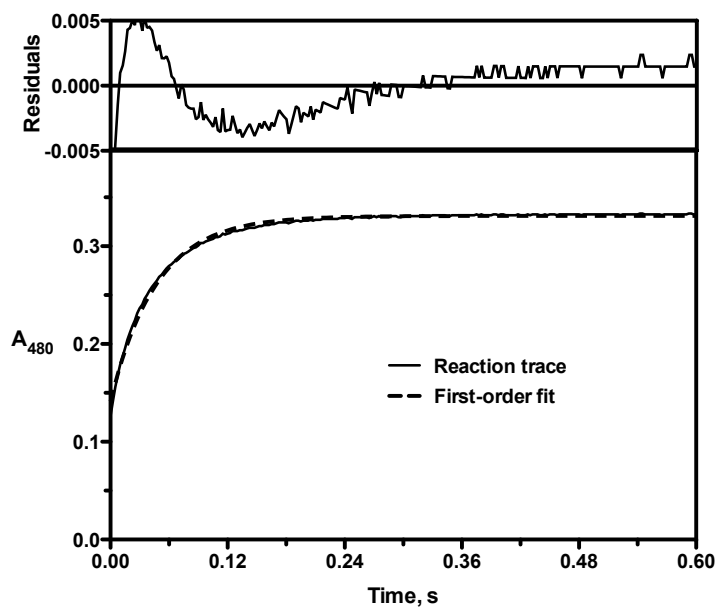


Figure 5-9. Kinetic trace of phenol oxidation by Os^{III} with DNBBS at 480 nm. $\mu = 0.1$ M (NaCl); $T = 25^\circ\text{C}$. Lower box shows the experimental trace (solid line) and the pseudo-first-order fit (dashed line). Upper box shows the residuals in the fit. $[\text{Os}^{\text{III}}]_0 = 1.29 \times 10^{-5}$ M; $[\text{Os}^{\text{II}}]_0 = 0.71 \times 10^{-5}$ M; $[\text{phenol}] = 0.0025$ M; $[\text{DNBBS}] = 10$ mM; $\mu = 0.1$ M (NaCl); $T = 25^\circ\text{C}$; $\text{p}[\text{H}^+] = 4.71$ (0.02 M acetate buffer).

scavenged by the spin tapping agent DNBNS.

Metal Catalysis. According to previous reported results on the oxidation of thioglycolic acid and cysteine,^{73, 77} 2,6-pyridinedicarboxylic acid (dipic) is an effective inhibitor of the copper catalysis. 1×10^{-3} M of dipic was added to the reaction between 0.02 M of phenol and 0.67×10^{-5} M of Os^{III} at $\text{p}[\text{H}^+] = 4.05$ with 15.6×10^{-5} M of Os^{II} . The experiments were monitored at 480 nm and the data are collected in Table 5-2. No effect was observed, which suggests that no copper catalysis is involved in the oxidation of phenol by Os^{III} , and that catalytic effects of other metals could also be excluded.

5.4 Discussion and Conclusion

According to the above results, the following mechanism, eqs 5-8 to 5-11, is proposed to account for the oxidation of phenol by Os^{III} in the absence of spin traps:



This mechanism looks identical to the outer-sphere proton-coupled electron-transfer oxidation of phenol by Ir^{IV} as we described in Chapter 2. However, the kinetics is quite different: the first two steps (eqs 5-8 and 5-9) rapidly approach equilibrium instead of being the rate-limiting steps as shown in Ir^{IV} reaction. Therefore, we propose a second-order rate law and this rate law can be derived as follows:

$$-\frac{d[\text{Os}^{\text{III}}]}{dt} = 2k_{\text{dim}} [\text{ArO}^\bullet]^2 \quad (5-12)$$

According to the pre-equilibrium approximation, the expression of concentration of the phenoxyl radical (eq 5-16) is obtained from eqs 5-13 to 5-15.

$$K_{\text{ArOH}} = \frac{[\text{Os}^{\text{II}}][\text{ArO}^\bullet][\text{H}^+]}{[\text{Os}^{\text{III}}][\text{ArOH}]} \quad (5-13)$$

$$K_{\text{ArO}^-} = \frac{[\text{Os}^{\text{II}}][\text{ArO}^\bullet]}{[\text{Os}^{\text{III}}][\text{ArO}^-]} \quad (5-14)$$

$$[\text{ArOH}]_{\text{tot}} = [\text{ArOH}] + [\text{ArO}^-] \quad (5-15)$$

$$[\text{ArO}^\bullet] = \frac{[\text{Os}^{\text{III}}][\text{ArOH}]_{\text{tot}}}{[\text{Os}^{\text{II}}]} \left(\frac{K_{\text{ArOH}}}{K_a + [\text{H}^+]} \right) \quad (5-16)$$

Substitution of eq 5-16 into eq 5-12 gives the rate law (eq 5-17) and the observed rate constant can be expressed by eq 5-18.

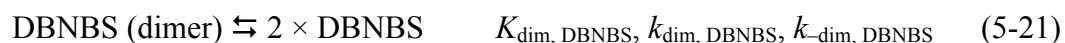
$$-\frac{d[\text{Os}^{\text{III}}]}{dt} = 2k_{\text{dim}} \frac{[\text{Os}^{\text{III}}]^2 [\text{ArOH}]_{\text{tot}}^2}{[\text{Os}^{\text{II}}]^2} \left(\frac{K_{\text{ArOH}}}{K_a + [\text{H}^+]} \right)^2 \quad (5-17)$$

$$k_{\text{obs}} = 2k_{\text{dim}} \frac{[\text{ArOH}]_{\text{tot}}^2}{[\text{Os}^{\text{II}}]_0^2} \left(\frac{K_{\text{ArOH}}}{K_a + [\text{H}^+]} \right)^2 \quad (5-18)$$

Thus, the rate law obtained for phenol oxidation by Os^{III} follows an inverse second-order with respect to $[\text{Os}^{\text{II}}]$ and $[\text{H}^+]$, and second-order with respect to $[\text{Os}^{\text{III}}]$ and $[\text{phenol}]_{\text{tot}}$.

Kinetic simulations based on the above mechanism were performed with the model listed in Table 5-3. The experimental half-lives obtained in the absence of DBNBS at different $p[H^+]$ values are consistent with those from simulations (Table 5-4).

In the presence of spin trap agent DBNBS, three more steps were added to the mechanism:



As discussed previously, only the monomer of DBNBS can scavenge the phenoxy radical, and the equilibrium constant, $K_{\text{dim, DBNBS}}$, of the dimerization of DBNBS is 1.3×10^{-3} M. A first-order rate law of phenol oxidation by Os^{III} with DBNBS is proposed:

$$-\frac{d[Os^{III}]}{dt} = k_{DBNBS} [DBNBS][ArO^\bullet] \quad (5-22)$$

$$-\frac{d[Os^{III}]}{dt} = k_{DBNBS}[DBNBS] \frac{[Os^{III}][ArOH]_{\text{tot}}}{[Os^{II}]} \left(\frac{K_{ArOH}}{K_a + [H^+]} \right) \quad (5-23)$$

The simulation results of scavenging of the phenoxy radical by DBNBS with a k_{DBNBS} value ($= 2.0 \times 10^5 \text{ M}^{-1} \text{ s}^{-1}$) together with those obtained from the phenol oxidation by Ir^{IV} are shown in Table 5-5. Good agreements are obtained from the comparisons of the simulation results and the experimental data. The simulations are influenced by the removal of dimerization step in the presence of 1 mM DBNBS, whereas, no change is

Table 5-3. The Mechanism of Phenol Reaction and the Simulation Model.

Equations	Kinetic Parameter ^a	Reactions in the model ^b	Species
eq 5-8	$k_{ArOH} = 5.7$	$A + B \rightarrow C + D + E$	k_1 A = Os ^{III}
	$k_{-ArOH} = 5.2 \times 10^9$	$C + D + E \rightarrow A + B$	k_{-1} B = C ₆ H ₅ OH
eq 5-9	$k_{ArO^-} = 2.0 \times 10^9$	$A + F \rightarrow C + D$	k_2 C = Os ^{II}
	$k_{-ArO^-} = 3.0 \times 10^8$	$C + D \rightarrow A + F$	k_{-2} D = C ₆ H ₅ O [•]
eq 5-10	$K_a = 1.6 \times 10^{-10}$	$B \rightarrow E + F$	k_3 E = H ⁺
		$E + F \rightarrow B$	k_{-3} F = C ₆ H ₅ O ⁻
	$K = K_a/K_w$	$B + G \rightarrow F + H$	k_4 G = OH ⁻
		$F + H \rightarrow B + G$	k_{-4} H = H ₂ O
Buffer	$K_{a, \text{buffer}}$	$I \rightarrow J + E$	k_5 I = Buffer
		$J + E \rightarrow I$	k_{-5} J = Conjugate Base
	$K = K_{a, \text{buffer}}/K_w$	$I + G \rightarrow J + H$	k_6
		$J + H \rightarrow I + G$	k_{-6}
eq 5-11	$k_{\text{dim}} = 2.3 \times 10^9$	$2 * D \rightarrow K$	k_7 K = Coupling Products
eq 5-19	$k_{\text{DBNBS}} = 2.0 \times 10^5$	$D + L \rightarrow M$	k_{19} L = DBNBS
eq 5-20	$k_{\text{adduct}} = 1.0 \times 10^7$	$A + M \rightarrow C + N$	k_{20} M = Adduct [•]
eq 5-21	$k_{\text{dim, DBS}} = 1.3 \times 10^6$	$O \rightarrow 2 * L$	k_{21} N = Adduct ⁺
	$k_{-\text{dim, DBS}} = 1.0 \times 10^9$	$2 * L \rightarrow O$	k_{-21} O = DBNBS dimer

^a Rate constants k (M⁻¹ s⁻¹), acid dissociation constant K_a and water dissociation constant

$K_w = 1.0 \times 10^{-14}$. ^b $k_3, k_{-3}, k_4, k_{-4}, k_5, k_{-5}, k_6$ and k_{-6} are the diffusion-controlled forward and reverse rate constants obtained according to the equilibriums.

Table 5-4. Comparison of the Experimental Data with the Simulation Results at different $p[H^+]$.^a

$p[H^+]^b$	$[phenol]_{tot} \times 10^3, M$	$t_{1/2, exp}, S$	$t_{1/2, sim}, S$
4.05	20	0.18	0.19
4.71	5.0	0.18	0.18
5.39	1.0	0.27	0.28
6.34	0.2	0.11	0.09

^a $[Os^{III}]_0 = (0.39-0.67) \times 10^{-5} M$; $[Os^{II}]_0 = (1.51-1.81) \times 10^{-5} M$; The following buffers (0.02 M) were employed to maintain constant $p[H^+]$ values: acetate buffer for $4.0 < p[H^+] < 5.4$, and cacodylate buffer for $p[H^+] = 6.34$.

Table 5-5. Comparison of the Experimental Data to the Simulation Results in the Presence of Various Concentration of DBNBS.^a

[DBNBS], mM	$t_{1/2, exp}, S$	$t_{1/2, sim}, S$
1.0	0.08	0.11
10	0.03	0.05

^a $[Os^{III}]_0 = (1.23-1.29) \times 10^{-5} M$; $[Os^{II}]_0 = (0.71-0.79) \times 10^{-5} M$; $[phenol]_{tot} = 0.0025 M$; $p[H^+] = 4.71$ (0.02 M acetate buffer).

observed with 10 mM DNBNS. These results confirm the competition between scavenging the phenoxy radical by DNBNS and their dimerization.

Marcus Theory. In equations 1-12 to 1-15, k_{12} is the cross electron-transfer rate constants, k_{11} and k_{22} are the self-exchange rate constants of $C_6H_5O^*/C_6H_5O$ and Os^{III}/Os^{II} redox couples. k_{11} is $1.9 \times 10^8 M^{-1} s^{-1}$ according to literature¹⁰¹ and a value for k_{22} of $3 \times 10^8 M^{-1} s^{-1}$ is used in the calculation. $1 \times 10^{11} M^{-1} s^{-1}$ is used for Z , the collision frequency.⁹⁹ Z_i, Z_j are the ionic charges of the reactants, R is the ideal gas constant, and r is the center to center distance between two reactants when they are approaching to each other. The radii of Os^{III} and $C_6H_5O^-$ are 6.7^{56} \AA and 2.5 \AA , respectively, estimated from CPK Atomic Models. μ is the ionic strength. w_{ij} is the electrostatic energy between reactants i and j . If the distance r is in angstroms and μ in molar, then w_{12} can be calculated according to eq 1-15 in kilojoules per mole. K_{12} ($K_{ArO^-} = 7.0$) was calculated from $K_{ArO^-} = K_{ArOH}/K_a$ with $K_{ArOH} = 1.1 \times 10^{-9} M$ and $pK_a = 9.79$. With all these parameters k_{12} ($= k_{ArO^-}$) is calculated to be $2.1 \times 10^9 M^{-1} s^{-1}$ and k_{-ArO^-} is equal to $3.0 \times 10^8 M^{-1} s^{-1}$.

References

- (1) Chance, B.; Nishimura, M. *P. Natl. Acad. Sci. USA* **1960**, *46*, 19.
- (2) Marcus, R. A.; Sutin, N. *Biochim. Biophys. Acta* **1985**, *811*, 265.
- (3) Stanbury, D. M. *Adv. Inorg. Chem.* **2003**, *54*, 351.
- (4) Kozik, M.; Baker, L. C. W. *J. Am. Chem. Soc.* **1990**, *112*, 7604.
- (5) Marcus, R. A. *J. Phys. Chem.* **1968**, *72*, 891.
- (6) Fukuzumi, S.; Wong, C. L.; Kochi, J. K. *J. Am. Chem. Soc.* **1980**, *102*, 2928.
- (7) Hwang, J. K.; Warshel, A. *J. Am. Chem. Soc.* **1987**, *109*, 715.
- (8) Arnaut, L. G.; Formosinho, S. J. *J. Photochem. Photobiol. A: Chem.* **1993**, *75*, 1.
- (9) Weinstock, I. A. *Chem. Rev.* **1998**, *98*, 113.
- (10) Roth, J. P.; Yoder, J. C.; Won, T. J.; Mayer, J. M. *Science* **2001**, *294*, 2524.
- (11) Barzykin, A. V.; Frantsuzov, P. A.; Seki, K.; Tachiya, M. *Adv. Chem. Phys.* **2002**, *123*, 511.
- (12) Marcus, R. A. *J. Chem. Phys.* **1965**, *43*, 679.
- (13) Taylor, S. M.; Halpern, J. *J. Am. Chem. Soc.* **1959**, *81*, 2933.
- (14) Mitchell, P. *Nature* **1961**, *191*, 144.
- (15) Binstead, R. A.; Moyer, B. A.; Samuels, G. J.; Meyer, T. J. *J. Am. Chem. Soc.* **1981**, *103*, 2897.
- (16) Fang, J. Y.; Hammes-Schiffer, S. *J. Chem. Phys.* **1997**, *106*, 8442.
- (17) Cukier, R. I.; Nocera, D. G. *Annu. Rev. Phys. Chem.* **1998**, *49*, 337.

- (18) Stubbe, J.; Nocera, D. G.; Yee, C. S.; Chang, M. C. Y. *Chem. Rev.* **2003**, *103*, 2167.
- (19) Mayer, J. M.; Hrovat, D. A.; Thomas, J. L.; Borden, W. T. *J. Am. Chem. Soc.* **2002**, *124*, 11142.
- (20) Costentin, C.; Evans, D. H.; Robert, M.; Saveant, J. M.; Singh, P. S. *J. Am. Chem. Soc.* **2005**, *127*, 12490.
- (21) Siegbahn, P. E. M.; Blomberg, M. R. A. *Chem. Rev.* **2010**, *110*, 7040.
- (22) Mayer, J. M. *Annu. Rev. Phys. Chem.* **2004**, *55*, 363.
- (23) Huynh, M. H. V.; Meyer, T. J. *Chem. Rev.* **2007**, *107*, 5004.
- (24) Hammes-Schiffer, S.; Stuchebrukhov, A. A. *Chem. Rev.* **2010**, *110*, 6939.
- (25) Bonin, J.; Costentin, C.; Louault, C.; Robert, M.; Routier, M.; Saveant, J. M. *P. Natl. Acad. Sci. USA* **2010**, *107*, 3367.
- (26) Bonin, J.; Costentin, C.; Louault, C.; Robert, M.; Saveant, J. M. *J. Am. Chem. Soc.* **2011**, *133*, 6668.
- (27) Song, N.; Stanbury, D. M. *Inorg. Chem.* **2008**, *47*, 11458.
- (28) Abraham, M. H.; Abraham, R. J.; Byrne, J.; Griffiths, L. *J. Org. Chem.* **2006**, *71*, 3389.
- (29) Tyman, J. H. P. *Synthetic and natural phenols*; Elsevier: Amsterdam [The Netherlands]; New York, 1996.
- (30) Ellestad, G. A.; Kunstmann, M. P.; Whaley, H. A.; Patterson, E. L. *J. Am. Chem. Soc.* **1968**, *90*, 1325.
- (31) Marrian, G. F.; Haslewood, G. A. D. *Biochem. J.* **1932**, *26*, 1227.
- (32) Robertson, A.; Robinson, R. *J. Chem. Soc.* **1928**, 1460.
- (33) Fomum, Z. T.; Ayafor, J. F.; Wandji, J. *J. Nat. Prod.* **1987**, *50*, 921.
- (34) Feldberg, W.; Toh, C. C. *J. Physiol-London* **1953**, *119*, 352.
- (35) Titeler, M.; Lyon, R. A.; Glennon, R. A. *Psychopharmacology* **1988**, *94*, 213.
- (36) Johnson, M. P.; Hoffman, A. J.; Nichols, D. E. *Eur. J. Pharmacol.* **1986**, *132*, 269.

- (37) Guitton, J.; Favetta, P.; Degoute, C. S.; Perdrix, J. P.; Dufresne, C.; Boulieu, R. *Brit. J. Anaesth.* **2002**, *88*, 653.
- (38) Higashiyama, S.; Iwabuki, H.; Morimoto, C.; Hieda, M.; Inoue, H.; Matsushita, N. *Cancer Sci.* **2008**, *99*, 214.
- (39) Bettelheim, F. R. *J. Am. Chem. Soc.* **1954**, *76*, 2838.
- (40) Blomberg, M. R. A.; Siegbahn, P. E. M. *BBA-Bioenergetics* **2004**, *1655*, 45.
- (41) Babcock, G. T.; Tommos, C. *BBA-Bioenergetics* **2000**, *1458*, 199.
- (42) Rappaport, F.; Guergova-Kuras, M.; Nixon, P. J.; Diner, B. A.; Lavergne, J. *Biochemistry* **2002**, *41*, 8518.
- (43) Haumann, M.; Mulkidjanian, A.; Junge, W. *Biochemistry* **1999**, *38*, 1258.
- (44) Yokoyama, K.; Uhlin, U.; Stubbe, J. *J. Am. Chem. Soc.* **2010**, *132*, 8385.
- (45) Seyedsayamdost, M. R.; Yee, C. S.; Reece, S. Y.; Nocera, D. G.; Stubbe, J. *J. Am. Chem. Soc.* **2006**, *128*, 1562.
- (46) Reece, S. Y.; Stubbe, J.; Nocera, D. G. *BBA-Bioenergetics* **2005**, *1706*, 232.
- (47) Fecenko, C. J.; Thorp, H. H.; Meyer, T. J. *J. Am. Chem. Soc.* **2007**, *129*, 15098.
- (48) Irebo, T.; Reece, S. Y.; Sjodin, M.; Nocera, D. G.; Hammarstrom, L. *J. Am. Chem. Soc.* **2007**, *129*, 15462.
- (49) Reece, S. Y.; Nocera, D. G. *J. Am. Chem. Soc.* **2005**, *127*, 9448.
- (50) Sjodin, M.; Irebo, T.; Utas, J. E.; Lind, J.; Merenyi, G.; Akermark, B.; Hammarstrom, L. *J. Am. Chem. Soc.* **2006**, *128*, 13076.
- (51) Cecil, R.; Littler, J. S. *J. Chem. Soc. B* **1968**, 1420.
- (52) Costentin, C.; Robert, M.; Saveant, J. M. *J. Am. Chem. Soc.* **2007**, *129*, 5870.
- (53) Stanbury, D. M.; Wilmarth, W. K.; Khalaf, S.; Po, H. N.; Byrd, J. E. *Inorg. Chem.* **1980**, *19*, 2715.
- (54) Stanbury, D. M.; Lednicky, L. A. *J. Am. Chem. Soc.* **1984**, *106*, 2847.
- (55) Sarala, R.; Stanbury, D. M. *Inorg. Chem.* **1990**, *29*, 3456.
- (56) Sarala, R.; Rabin, S. B.; Stanbury, D. M. *Inorg. Chem.* **1991**, *30*, 3999.

- (57) Hung, M. L.; Mckee, M. L.; Stanbury, D. M. *Inorg. Chem.* **1994**, *33*, 5108.
- (58) Sun, J. F.; Stanbury, D. M. *J. Chem. Soc., Dalton Trans.* **2002**, 785.
- (59) Hung, M. L.; Stanbury, D. M. *Inorg. Chem.* **2005**, *44*, 9952.
- (60) Makarycheva-Mikhailova, A. V.; Stanbury, D. M.; Mckee, M. L. *J. Phys. Chem. B* **2007**, *111*, 6942.
- (61) Kauffman, G. B.; Teter, L. A. *Inorg. Synth.* **1966**, *8*, 223.
- (62) Perrin, D. D.; Armarego, W. L. F. *Purification of Laboratory Chemicals, 3rd Edition*; Pergamon Press, 1988.
- (63) Braithwaite, A.; Henthorn, K.; Elliott, G. E. P.; Marshall, B. W.; Smith, A. C.; Emslie, J. J.; Kaseke, C. T.; Tyson, J. F.; Ham, G.; Griffiths, P. D. *Anal. Proc.* **1981**, *18*, 60.
- (64) Kaur, H.; Leung, K. H. W.; Perkins, M. J. *J. Chem. Soc., Chem. Commun.* **1981**, 142.
- (65) Hamilton, L.; Nielsen, B. R.; Davies, C. A.; Symons, M. C. R.; Winyard, P. G. *Free Rad. Res.* **2003**, *37*, 41.
- (66) Kanetani, F.; Yamaguchi, H. *B. Chem. Soc. Jpn.* **1981**, *54*, 3048.
- (67) Konaka, R.; Sakata, S. *Chem. Lett.* **1982**, 411.
- (68) Amblard, F.; Govindarajan, B.; Lefkove, B.; Rapp, K. L.; Detorio, M.; Arbiser, J. L.; Schinazi, R. F. *Bioorg. Med. Chem. Lett.* **2007**, *17*, 4428.
- (69) Padwa, A.; Wisnieff, T. J.; Walsh, E. J. *J. Org. Chem.* **1989**, *54*, 299.
- (70) *Spartan '08*; Wavefunction, Inc: Irvine, CA.
- (71) Bruhn, H.; Nigam, S.; Holzwarth, J. F. *Faraday Discuss.* **1982**, *74*, 129.
- (72) Bonin, J.; Costentin, C.; Robert, M.; Saveant, J. M. *Org. Biomol. Chem.* **2011**, *9*, 4064.
- (73) Hung, M. L.; Stanbury, D. M. *Inorg. Chem.* **2005**, *44*, 3541.
- (74) Ram, M. S.; Stanbury, D. M. *Inorg. Chem.* **1985**, *24*, 4233.
- (75) Huang, H.; Sommerfeld, D.; Dunn, B. C.; Eyring, E. M.; Lloyd, C. R. *J. Phys. Chem. A* **2001**, *105*, 3536.

- (76) Wang, X. G.; Stanbury, D. M. *Inorg. Chem.* **2008**, *47*, 1224.
- (77) Saha, B.; Hung, M. L.; Stanbury, D. M. *Inorg. Chem.* **2002**, *41*, 5538.
- (78) O'Brien, P.; Salacinski, H. J. *Arch. Toxicol.* **1996**, *70*, 787.
- (79) Zalomaeva, O. V.; Trukhan, N. N.; Ivanchikova, I. D.; Panchenko, A. A.; Roduner, E.; Talsi, E. P.; Sorokin, A. B.; Rogov, V. A.; Kholdeeva, O. A. *J. Mol. Catal. A: Chem.* **2007**, *277*, 185.
- (80) Ide, H.; Hagi, A.; Ohsumi, S.; Murakami, A.; Makino, K. *Biochem. Int.* **1992**, *27*, 367.
- (81) Martell, A. E.; Smith, R. M.; Motekaitis, R. J. *NIST Critically Selected Stability Constants of Metal Complexes Database, 7.0* U. S. Department of Commerce: Gaithersburg, MD, 2003.
- (82) Fine, D. A. *Inorg. Chem.* **1969**, *8*, 1014.
- (83) Ye, M.; Schuler, R. H. *J. Phys. Chem.* **1989**, *93*, 1898.
- (84) Das, T. N. *J. Phys. Chem. A* **2001**, *105*, 5954.
- (85) Jonsson, M.; Lind, J.; Merenyi, G. *J. Phys. Chem. A* **2002**, *106*, 4758.
- (86) Jonsson, M.; Lind, J.; Merenyi, G. *J. Phys. Chem. A* **2003**, *107*, 5878.
- (87) Stradins, J.; Hasanli, B. *J. Electroanal. Chem.* **1993**, *353*, 57.
- (88) Lind, J.; Shen, X.; Eriksen, T. E.; Merenyi, G. *J. Am. Chem. Soc.* **1990**, *112*, 479.
- (89) Papina, A. A.; Koppenol, W. H. *Chem. Res. Toxicol.* **2007**, *20*, 2021.
- (90) Al-Ajlouni, A.; Bakac, A.; Espenson, J. H. *Inorg. Chem.* **1993**, *32*, 5792.
- (91) Al-Ajlouni, A. M.; Shawakfeh, K. Q.; Rajal, R. *Kinet. Catal.* **2009**, *50*, 88.
- (92) Pelizzetti, E.; Mentasti, E. *J. Inorg. Nucl. Chem.* **1977**, *39*, 2227.
- (93) Margerum, D. W.; Chellappa, K. L.; Bossu, F. P.; Burce, G. L. *J. Am. Chem. Soc.* **1975**, *97*, 6894.
- (94) Neta, P.; Grodkowski, J. *J. Phys. Chem. Ref. Data* **2005**, *34*, 109.
- (95) Tripathi, G. N. R.; Schuler, R. H. *Chem. Phys. Lett.* **1982**, *88*, 253.

- (96) Binstead, R. A.; Jung, B.; Zuberbuhler, A. D. *Specfit/32 Global Analysis System, version 3.0*; Spectrum Software Associates: Marlborough, MA USA, 2000.
- (97) Zuckerman, J. J. *Inorganic Reactions and Methods*; VCH: Deerfield Beach, FL, 1986; Vol. 15.
- (98) Hurwitz, P.; Kustin, K. *Trans. Faraday Soc.* **1966**, *62*, 427.
- (99) Ram, M. S.; Stanbury, D. M. *J. Phys. Chem.* **1986**, *90*, 3691.
- (100) McDonald, W. J.; Einarsdottir, O. *J. Phys. Chem. A* **2008**, *112*, 11400.
- (101) Schuler, R. H.; Neta, P.; Zemel, H.; Fessenden, R. W. *J. Am. Chem. Soc.* **1976**, *98*, 3825.
- (102) Hansch, C.; Leo, A.; Taft, R. W. *Chem. Rev.* **1991**, *91*, 165.
- (103) Kaji, M.; Ogami, K.; Endo, T. *J. Appl. Polym. Sci.* **1999**, *72*, 953.
- (104) Saito, K.; Tago, T.; Masuyama, T.; Nishide, H. *Angew. Chem. Int. Ed.* **2004**, *43*, 730.
- (105) Wang, X. G.; Stanbury, D. M. *J. Phys. Chem. A* **2004**, *108*, 7637.
- (106) Song, N.; Stanbury, D. M. *Inorg. Chem.*, Accepted.
- (107) Brown, H. C.; Okamoto, Y. *J. Am. Chem. Soc.* **1958**, *80*, 4979.
- (108) Roder, M.; Foldiak, G.; Wojnarovits, L. *Radiat. Phys. Chem.* **1999**, *55*, 515.
- (109) Jonsson, M.; Lind, J.; Reitberger, T.; Eriksen, T. E.; Merenyi, G. *J. Phys. Chem.* **1993**, *97*, 8229.
- (110) Jonsson, M.; Lind, J.; Eriksen, T. E.; Merenyi, G. *J. Chem. Soc. Perk. T. 2* **1993**, 1567.
- (111) Das, T. N. *J. Phys. Chem. A* **2005**, *109*, 3344.
- (112) Dixon, W. T.; Murphy, D. *J. Chem. Soc. Farad. T. 2* **1978**, *74*, 432.
- (113) Hoigne, J.; Bader, H. *Water Res.* **1994**, *28*, 45.
- (114) Tratnyek, P. G.; Hoigne, J. *Water Res.* **1994**, *28*, 57.
- (115) Saveant, J. M.; Bonin, J.; Costentin, C.; Louault, C.; Robert, M. *J. Am. Chem. Soc.* **2011**, *133*, 6668.

- (116) Young, R. C.; Keene, F. R.; Meyer, T. J. *J. Am. Chem. Soc.* **1977**, *99*, 2468.
- (117) Stubbe, J.; Riggs-Gelasco, P. *Trends Biochem. Sci.* **1998**, *23*, 438.
- (118) Michon, T.; Chenu, M.; Kellershon, N.; Desmadril, M.; Gueguen, J. *Biochemistry* **1997**, *36*, 8504.
- (119) Callahan, R. W.; Brown, G. M.; Meyer, T. J. *Inorg. Chem.* **1975**, *14*, 1443.

Appendix A

EXPERIMENTAL DETAILS IN CHAPTERS 2–5

Table A-1. Kinetic Dependence of Phenol Oxidation on $[\text{Phenol}]_{\text{tot}}$.^a

p[H ⁺] = 1.3 ^b , with DBNBS		p[H ⁺] = 5.1 ^c , no DBNBS	
[phenol] _{tot} × 10 ³ , M	<i>k</i> _{obs} × 10 ³ , s ⁻¹	[phenol] _{tot} × 10 ³ , M	<i>k</i> _{obs} , s ⁻¹
22.2	14.4	1.77	0.270
44.3	27.8	8.86	1.13
266	163	22.2	2.64
443	272	44.3	4.78

^a All the reactions were run under pseudo-first-order conditions. $[\text{Ir}^{\text{IV}}]_0 = 1 \times 10^{-4}$ M; $\mu = 0.1$ M (LiClO₄); $T = 25$ °C. ^b $[\text{HClO}_4] = 0.05$ M; $[\text{phenol}]_{\text{tot}} = (22.2\text{--}443) \times 10^{-3}$ M; $[\text{DBNBS}] = 10$ mM. ^c p[H⁺] = 5.1 (0.02 M acetate buffer); $[\text{phenol}]_{\text{tot}} = (1.77\text{--}44.3) \times 10^{-3}$ M.

Table A-2. Kinetic Dependence of Phenol Oxidation on p[H⁺] Without DBNBS.^a

p[H ⁺] ^b	[phenol] _{tot} × 10 ³ , M	k _{obs} /[phenol] _{tot} , M ⁻¹ s ⁻¹
2.46	44.3	7.26 × 10 ⁻¹
2.57	44.3	8.16 × 10 ⁻¹
2.71	44.3	9.58 × 10 ⁻¹
2.86	44.3	1.15
2.97	44.3	1.30
3.01	44.3	1.43
3.16	44.3	1.80
3.39	44.3	2.71
3.62	44.3	4.46
3.80	44.3	6.12
3.99	44.3	8.87
4.19	44.3	13.1
4.37	44.3	19.8
4.59	44.3	30.4
4.78	44.3	47.9
4.98	44.3	70.7
5.18	44.3	108
5.36	44.3	170
5.64	4.43	353
5.76	4.43	498
5.96	4.43	771
6.18	4.43	1.24 × 10 ³
6.35	4.43	1.84 × 10 ³
6.57	4.43	3.12 × 10 ³
6.74	4.43	4.67 × 10 ³

^a All the reactions were run under pseudo-first-order conditions. [Ir^{IV}]₀ = 1 × 10⁻⁴ M; μ = 0.1 M (LiClO₄); T = 25 °C. ^b The following buffers (0.02 M) were employed to maintain constant p[H⁺] values: monochloroacetate buffer for 2.4 < p[H⁺] < 3.4, acetate buffer for 3.6 < p[H⁺] < 5.4, and cacodylate buffer for 5.6 < p[H⁺] < 7.0.

Table A-3. Kinetic Dependence of Phenol Oxidation on p[H⁺] with DBNBS.^a

p[H ⁺] ^b	[phenol] _{tot} × 10 ³ , M	k _{obs} /[phenol] _{tot} , M ⁻¹ s ⁻¹
1.00	44.3	6.80 × 10 ⁻¹
1.20	44.3	6.71 × 10 ⁻¹
1.40	44.3	7.51 × 10 ⁻¹
1.60	44.3	7.55 × 10 ⁻¹
1.80	44.3	8.45 × 10 ⁻¹
2.00	44.3	9.50 × 10 ⁻¹
2.20	44.3	1.10
2.61	44.3	1.39
2.68	44.3	1.49
2.74	44.3	1.60
2.96	44.3	2.18
3.26	44.3	3.72
3.38	44.3	4.00
3.65	44.3	7.53
3.80	44.3	10.4
3.92	44.3	13.3
4.09	44.3	19.5
4.36	44.3	31.3
4.49	44.3	41.8
4.67	44.3	61.9
4.83	44.3	85.9
4.99	44.3	121
5.16	44.3	161
5.41	4.43	352
5.63	4.43	574
5.85	4.43	922
6.08	4.43	1.40 × 10 ³
6.24	4.43	2.04 × 10 ³
6.41	4.43	2.97 × 10 ³
6.60	4.43	4.18 × 10 ³
6.73	4.43	5.66 × 10 ³
6.94	1.77	9.75 × 10 ³

^a [Ir^{IV}]₀ = 1 × 10⁻⁴ M; [DBNBS] = 10 mM; μ = 0.1 M (LiClO₄); T = 25 °C. ^b p[H⁺] = -log

[HClO₄] in the p[H⁺] range of 1.0–2.2. The following buffers (0.02 M) were employed to

maintain constant p[H⁺] values: monochloroacetate buffer for 2.4 < p[H⁺] < 3.4, acetate

buffer for 3.6 < p[H⁺] < 5.4, and cacodylate buffer for 5.4 < p[H⁺] < 7.0.

Table A-4. Nonlinear-Least-Squares Regression Results of the $k_{\text{obs}}/[\text{phenol}]_{\text{tot}}$ vs $\text{p}[\text{H}^+]$ Plot with 2-Term and 3-Term Rate Law Models in the Absence of DBNBS.

		2-term rate law (eq 2-2)	3-term rate law (eq 2-3)
Best-fit values	$k_{\text{ArOH}}, \text{M}^{-1} \text{s}^{-1}$	0.540	0.395
	$k_{\text{ArO}^-}, \text{M}^{-1} \text{s}^{-1}$	5.05×10^6	4.90×10^6
	$k^0, \text{M}^{-1} \text{s}^{-1}$		6.54×10^{-3}
Std. Error	$k_{\text{ArOH}}, \text{M}^{-1} \text{s}^{-1}$	2.59×10^{-2}	6.36×10^{-2}
	$k_{\text{ArO}^-}, \text{M}^{-1} \text{s}^{-1}$	7.80×10^4	9.51×10^4
	$k^0, \text{M}^{-1} \text{s}^{-1}$		2.74×10^{-3}
95 % Confidence Intervals	$k_{\text{ArOH}}, \text{M}^{-1} \text{s}^{-1}$	0.486 to 0.594	0.264 to 0.527
	$k_{\text{ArO}^-}, \text{M}^{-1} \text{s}^{-1}$	4.89×10^6 to 5.21×10^6	4.70×10^6 to 5.09×10^6
	$k^0, \text{M}^{-1} \text{s}^{-1}$		8.68×10^{-4} to 1.22×10^{-2}
Degrees of Freedom		23	22
Goodness of Fit	R squared	0.9992	0.9994
	Weighted Sum of Squares (1/(Y*Y))	8.93×10^{-2}	7.02×10^{-2}
	Sy.x	6.23×10^{-2}	5.65×10^{-2}

Table A-5. Nonlinear-Least-Squares Regression Results of the $k_{\text{obs}}/[\text{phenol}]_{\text{tot}}$ vs $\text{p}[\text{H}^+]$ Plot with 2-Term and 3-Term Rate Law Models in the Presence of DBNBS.

		2-term rate law (eq 2-2)	3-term rate law (eq 2-3)
Best-fit values	$k_{\text{ArOH}}, \text{M}^{-1} \text{s}^{-1}$	0.769	0.594
	$k_{\text{ArO}^-}, \text{M}^{-1} \text{s}^{-1}$	8.02×10^6	7.32×10^6
	$k^{\circ}, \text{M}^{-1} \text{s}^{-1}$		2.01×10^{-2}
Std. Error	$k_{\text{ArOH}}, \text{M}^{-1} \text{s}^{-1}$	3.316×10^{-2}	2.93×10^{-2}
	$k_{\text{ArO}^-}, \text{M}^{-1} \text{s}^{-1}$	2.03×10^5	1.47×10^5
	$k^{\circ}, \text{M}^{-1} \text{s}^{-1}$		2.80×10^{-3}
95 % Confidence Intervals	$k_{\text{ArOH}}, \text{M}^{-1} \text{s}^{-1}$	0.701 to 0.836	0.534 to 0.654
	$k_{\text{ArO}^-}, \text{M}^{-1} \text{s}^{-1}$	7.60×10^6 to 8.44×10^6	7.01×10^6 to 7.61×10^6
	$k^{\circ}, \text{M}^{-1} \text{s}^{-1}$		1.44×10^{-2} to 2.59×10^{-2}
Goodness of Fit	Degrees of Freedom	30	29
	R squared	0.9978	0.9992
	Weighted Sum of Squares (1/(Y*Y))	0.382	0.138
	Sy.x	0.113	6.90×10^{-2}

Table A-6. Comparison of k_{obs} in H₂O and in D₂O.^a

$[\text{phenol}]_{\text{tot}} \times 10^3, \text{ M}$	$k_{\text{obs}} \times 10^3, \text{ s}^{-1}, \text{ D}_2\text{O}$	$k_{\text{obs}} \times 10^3, \text{ s}^{-1}, \text{ H}_2\text{O}$	$\text{KIE} = k_{\text{H}}/k_{\text{D}}$
44.3	8.35	27.9	3.34
133	24.8	96.1	3.87
222	43.9	142	3.22

^a $[\text{Ir}^{\text{IV}}]_0 = 1 \times 10^{-4} \text{ M}$; $[\text{HClO}_4] = 0.09 \text{ M}$; $\mu = 0.1 \text{ M}$; $[\text{DBNBS}] = 10 \text{ mM}$; $T = 25 \text{ }^\circ\text{C}$.

Table A-7. Kinetic Dependence on $[\text{Cresol}]_{\text{tot}}$.^a

$[\text{cresol}]_{\text{tot}} \times 10^3, \text{ M}$	$k_{\text{obs}} \times 10^2, \text{ s}^{-1}$
1.0	1.48
5.0	7.12
10	14.2
20	28.2

^a $[\text{Ir}^{\text{IV}}]_0 = 1 \times 10^{-4} \text{ M}$; $[\text{DBNBS}] = 1 \text{ mM}$; $[\text{HClO}_4] = 0.05 \text{ M}$; $\mu = 0.1 \text{ M (LiClO}_4)$; $T = 25 \text{ }^\circ\text{C}$.

Table A-8. Kinetic Dependence of Biphenols and 4-Phenoxyphenol Oxidation on p[H⁺].^a

Substrate	p[H ⁺] ^b	[Substrate] _{tot} × 10 ⁴ , M	<i>k</i> _{obs} /[Substrate] _{tot} , M ⁻¹ s ⁻¹	<i>k</i> _{obs,2} , ^c s ⁻¹
4,4'-biphenol	1.30	1.0	4.06 × 10 ⁴	
	4.37	1.0	5.54 × 10 ⁴	
	5.94	1.0	1.74 × 10 ⁵	
	6.91	0.50	1.16 × 10 ⁶	
2,2'-biphenol	1.30	14	8.57	
	3.81	10	8.81 × 10 ²	
	5.34	10	2.05 × 10 ⁴	
	6.72	3.0	3.47 × 10 ⁵	
2,4'-biphenol ^d	1.30	2.0	3.54 × 10 ³	3.51 × 10 ⁻²
	2.48	2.5	3.22 × 10 ³	5.57 × 10 ⁻²
	3.83	1.0	5.63 × 10 ³	2.52 × 10 ⁻²
	5.29	1.0	8.69 × 10 ³	3.89 × 10 ⁻²
	6.85	2.0	2.02 × 10 ⁵	1.20
4-phenoxy phenol	1.30	3.0	7.43 × 10 ²	
	2.46	3.0	1.31 × 10 ³	
	3.59	3.0	1.43 × 10 ³	
	4.44	3.0	1.90 × 10 ³	
	4.95	3.0	2.62 × 10 ³	
	6.41	3.0	3.45 × 10 ⁴	
	7.06	3.0	1.45 × 10 ⁵	

^a [Ir^{IV}]₀ = 2.5 × 10⁻⁵ M; μ = 0.1 M (LiClO₄); T = 25 °C; ^b p[H⁺] = -log [HClO₄] in the p[H⁺] range of 1.0–2.2. The following buffers (0.02 M) were employed to maintain constant p[H⁺] values: monochloroacetate buffer for 2.4 < p[H⁺] < 3.6, acetate buffer for 3.7 < p[H⁺] < 5.4, and cacodylate buffer for 5.5 < p[H⁺] < 7.1. ^c Slow observed first-order rate constant from two-exponential fit. ^d Two-exponential fit was applied to biphasic trace.

Table A-9. Kinetic Dependence of Cresol Oxidation on $p[H^+]$ with DNBNS.^a

$p[H^+]$	$[cresol]_{tot} \times 10^3, M$	$[Ir^{IV}]_0 \times 10^5, M$	$k_{obs}/[cresol]_{tot}, M^{-1} s^{-1}$
1.30	20	2.5	14.2
1.60	20	2.5	15.1
2.00	20	2.5	16.3
2.39	20	2.5	17.1
2.68	10	10	17.0
3.04	10	10	20.8
3.47	10	10	30.9
3.73	10	5.0	41.4
4.12	10	5.0	79.0
4.33	1.0	5.0	134
4.53	1.0	2.5	186
4.93	1.0	5.0	432
5.33	1.0	5.0	965
5.78	1.0	5.0	2.42×10^3
6.18	1.0	5.0	5.55×10^3
6.63	1.0	5.0	1.42×10^4
7.08	1.0	5.0	3.88×10^4

^a $[DNBNS] = 1 \text{ mM}$; $\mu = 0.1 \text{ M (LiClO}_4)$; $T = 25 \text{ }^\circ\text{C}$. ^b $p[H^+] = -\log [HClO_4]$ in the $p[H^+]$

range of 1.0–2.2. The following buffers (0.02 M) were employed to maintain constant $p[H^+]$ values: monochloroacetate buffer for $2.3 < p[H^+] < 3.5$, acetate buffer for $3.7 < p[H^+] < 5.4$, and cacodylate buffer for $5.7 < p[H^+] < 7.1$.

Table A-10. Nonlinear-Least-Squares Regression Results of the $k_{\text{obs}}/[\text{cresol}]_{\text{tot}}$ vs $\text{p}[\text{H}^+]$ Plot with 2-Term and 3-Term Rate Law Models in the Presence of DBNBS.

		2-term rate law (eq 2-2)	3-term rate law (eq 2-3)
Best-fit values	$k_{\text{ArOH}}, \text{M}^{-1} \text{s}^{-1}$	15.8	13.2
	$k_{\text{ArO}^-}, \text{M}^{-1} \text{s}^{-1}$	5.24×10^7	4.54×10^7
	$k^0, \text{M}^{-1} \text{s}^{-1}$		0.168
Std. Error	$k_{\text{ArOH}}, \text{M}^{-1} \text{s}^{-1}$	0.915	0.864
	$k_{\text{ArO}^-}, \text{M}^{-1} \text{s}^{-1}$	2.48×10^6	2.16×10^6
	$k^0, \text{M}^{-1} \text{s}^{-1}$		4.02×10^{-2}
95 % Confidence Intervals	$k_{\text{ArOH}}, \text{M}^{-1} \text{s}^{-1}$	13.8 to 17.7	11.3 to 15.0
	$k_{\text{ArO}^-}, \text{M}^{-1} \text{s}^{-1}$	4.72×10^7 to 5.77×10^7	4.07×10^7 to 5.00×10^7
	$k^0, \text{M}^{-1} \text{s}^{-1}$		8.14×10^{-2} to 0.254
Degrees of Freedom		15	14
Goodness of Fit	R squared	0.9975	0.9988
	Weighted Sum of Squares (1/(Y*Y))	0.280	0.132
	Sy.x	0.137	9.71×10^{-2}

Table A-11. Kinetic Dependence of Cresol Oxidation on Temperature.^a

T, °C	$k_{\text{obs}}, \text{s}^{-1}$
8.0	0.072
15	0.114
25	0.221
35	0.393
45	0.653

^a $[\text{Ir}^{\text{IV}}]_0 = 2.5 \times 10^{-5} \text{ M}$; $[\text{cresol}]_{\text{tot}} = 0.02 \text{ M}$; $[\text{HClO}_4] = 0.01 \text{ M}$; $\mu = 0.1 \text{ M}$ (LiClO_4).

Table A-12. Kinetic Isotope Effect for Oxidation of Cresol.^a

Expt. No.	$k_{\text{obs}}, \text{s}^{-1}, \text{D}_2\text{O}$	$k_{\text{obs}} \times 10^3, \text{s}^{-1}, \text{H}_2\text{O}$	KIE = $k_{\text{H}}/k_{\text{D}}$
1 ^b	0.077	0.240	3.12
2 ^b	0.077	0.239	3.10
3 ^c	0.087	0.238	2.74
4 ^c	0.086	0.239	2.78

^a $[\text{Ir}^{\text{IV}}]_0 = 1 \times 10^{-4} \text{ M}$; $[\text{cresol}] = 0.02 \text{ M}$; $\mu = 0.1 \text{ M}$ (LiClO_4); $T = 25 \text{ }^\circ\text{C}$. ^b $[\text{HClO}_4] = 0.05$

M ; $[\text{DBNBS}] = 1 \text{ mM}$. ^c $\text{p}[\text{H}^+] = 2.34$ (0.02 M monochloroacetate buffer).

Table A-13. Kinetic Dependence on $[\text{Xylenol}]_{\text{tot}}$.^a

$[\text{xylenol}]_{\text{tot}} \times 10^3, \text{ M}$	$k_{\text{obs}}, \text{ s}^{-1}$
2.50	0.096
8.00	0.305
13.0	0.444
19.0	0.653
25.0	0.914

^a $[\text{Ir}^{\text{IV}}]_0 = 1 \times 10^{-4} \text{ M}$; $[\text{HClO}_4] = 0.05 \text{ M}$; $\mu = 0.1 \text{ M (LiClO}_4)$; $T = 25 \text{ }^\circ\text{C}$.

Table A-14. Kinetic Dependence of Xylenol Oxidation on p[H⁺].^a

p[H ⁺]	[Ir ^{IV}] ₀ × 10 ⁵ , M	[Xylenol] _{tot} × 10 ⁴ , M	k _{obs} /[xylenol] _{tot} , M ⁻¹ ·s ⁻¹
1.30	10	50	40.1
1.60	10	50	40.7
2.00	10	50	43.0
2.40	10	50	47.4
2.67	10	50	48.6
2.83	10	50	51.3
3.00	10	50	56.4
3.18	10	50	63.7
3.34	10	50	73.3
3.58	10	50	86.7
3.73	10	50	104
3.93	10	50	132
4.13	10	50	174
4.39	10	50	264
4.53	10	50	350
4.75	10	25	590
4.93	10	25	828
5.14	10	25	1.24 × 10 ³
5.36	10	25	1.86 × 10 ³
5.53	2.5	5.0	2.85 × 10 ³
5.73	2.5	5.0	4.17 × 10 ³
5.94	2.5	5.0	6.48 × 10 ³
6.16	2.5	5.0	1.01 × 10 ⁴
6.35	2.5	2.5	1.69 × 10 ⁴
6.54	2.5	2.5	2.41 × 10 ⁴
6.74	2.5	2.5	3.65 × 10 ⁴

^a μ = 0.1 M (LiClO₄); T = 25 °C. ^b p[H⁺] = -log [HClO₄] in the p[H⁺] range of 1.0–2.2.

The following buffers (0.02 M) were employed to maintain constant p[H⁺] values:

monochloroacetate buffer for 2.4 < p[H⁺] < 3.4, acetate buffer for 3.5 < p[H⁺] < 5.4, and

cacodylate buffer for 5.5 < p[H⁺] < 7.0.

Table A-15. Nonlinear-Least-Squares Regression Results of the $k_{\text{obs}}/[\text{xylenol}]_{\text{tot}}$ vs $\text{p}[\text{H}^+]$ Plot with 2-Term and 3-Term Rate Law Models.

		2-term rate law (eq 2-2)	3-term rate law (eq 2-3)
Best-fit values	$k_{\text{ArOH}}, \text{M}^{-1} \text{s}^{-1}$	46.7	37.6
	$k_{\text{ArO}^-}, \text{M}^{-1} \text{s}^{-1}$	1.97×10^8	1.71×10^8
	$k^0, \text{M}^{-1} \text{s}^{-1}$		0.403
Std. Error	$k_{\text{ArOH}}, \text{M}^{-1} \text{s}^{-1}$	1.83	1.06
	$k_{\text{ArO}^-}, \text{M}^{-1} \text{s}^{-1}$	6.09×10^6	3.25×10^6
	$k^0, \text{M}^{-1} \text{s}^{-1}$		3.76×10^{-2}
95 % Confidence Intervals	$k_{\text{ArOH}}, \text{M}^{-1} \text{s}^{-1}$	43.0 to 50.5	35.4 to 39.8
	$k_{\text{ArO}^-}, \text{M}^{-1} \text{s}^{-1}$	1.84×10^8 to 2.09×10^8	1.64×10^8 to 1.77×10^8
	$k^0, \text{M}^{-1} \text{s}^{-1}$		0.325 to 0.481
Goodness of Fit	Degrees of Freedom	24	23
	R squared	0.9974	0.9996
	Weighted Sum of Squares (1/(Y*Y))	0.293	5.00×10^{-2}
	Sy.x	0.110	4.66×10^{-2}

Table A-16. Kinetic Isotope Effect for Oxidation of Xylenol.^a

$k_{\text{obs}}, \text{s}^{-1}, \text{D}_2\text{O}$	$k_{\text{obs}} \times 10^3, \text{s}^{-1}, \text{H}_2\text{O}$	$\text{KIE} = k_{\text{H}}/k_{\text{D}}$
0.337	0.884	2.62
0.354	0.913	2.58
0.359	0.926	2.58
0.347	0.912	2.62

^a $[\text{Ir}^{\text{IV}}]_0 = 1 \times 10^{-4} \text{ M}$; $[\text{xylenol}] = 0.025 \text{ M}$; $[\text{HClO}_4] = 0.05 \text{ M}$; $\mu = 0.1 \text{ M}$ (LiClO_4); $T = 25 \text{ }^\circ\text{C}$.

Table A-17. Kinetic Dependence on $[\text{TMP}]_{\text{tot}}$.^a

$[\text{TMP}]_{\text{tot}}, \times 10^3 \text{ M}$	$k_{\text{obs}}, \text{s}^{-1}$
0.3	0.32
1.2	1.27
2.1	2.23
3.0	3.27

^a $[\text{Ir}^{\text{IV}}]_0 = 2.5 \times 10^{-5} \text{ M}$; $[\text{HClO}_4] = 0.01 \text{ M}$; $\mu = 0.1 \text{ M}$ (LiClO_4); $T = 25 \text{ }^\circ\text{C}$.

Table A-18. $p[\text{H}^+]$ Dependence of TMP Oxidation.^a

$p[\text{H}^+]^b$	$k_{\text{obs}}/[\text{TMP}]_{\text{tot}}, \text{M}^{-1} \text{s}^{-1}$
1.30	1.06×10^3
1.60	1.07×10^3
2.00	1.07×10^3
2.41	1.08×10^3
2.64	1.09×10^3
3.01	1.10×10^3
3.36	1.11×10^3
3.76	1.11×10^3
4.13	1.17×10^3
4.53	1.31×10^3
4.94	1.69×10^3
5.38	2.55×10^3
5.75	4.42×10^3
6.18	9.64×10^3
6.35	1.45×10^4
6.93	4.88×10^4

^a $[\text{Ir}^{\text{IV}}]_0 = 2.5 \times 10^{-5} \text{ M}$; $[\text{TMP}]_{\text{tot}} = 3.0 \times 10^{-4} \text{ M}$; $\mu = 0.1 \text{ M (LiClO}_4)$; $T = 25 \text{ }^\circ\text{C}$. ^b $p[\text{H}^+]$

$= -\log [\text{HClO}_4]$ in the $p[\text{H}^+]$ range of 1.0–2.2. The following buffers (0.02 M) were employed to maintain constant $p[\text{H}^+]$ values: monochloroacetate buffer for $2.4 < p[\text{H}^+] < 3.5$, acetate buffer for $3.6 < p[\text{H}^+] < 5.5$, and cacodylate buffer for $5.6 < p[\text{H}^+] < 7.0$.

Table A-19. Kinetic Isotope Effect for Oxidation of TMP.^a

$[\text{TMP}]_{\text{tot}} \times 10^3, \text{ M}$	$k_{\text{obs}}, \text{ s}^{-1} \text{ D}_2\text{O}$	$k_{\text{obs}}, \text{ s}^{-1} \text{ H}_2\text{O}$	$\text{KIE} = k_{\text{H}}/k_{\text{D}}$
3.0	1.74	3.55	2.05
3.0	1.73	3.56	2.06
1.5	0.82	1.67	2.02

^a $[\text{Ir}^{\text{IV}}]_0 = 1 \times 10^{-4} \text{ M}$; $[\text{HClO}_4] = 0.01 \text{ M}$; $\mu = 0.1 \text{ M}$ (LiClO_4); $T = 25 \text{ }^\circ\text{C}$.

Table A-20. Kinetic Isotope Effect for Oxidation of MOP.^a

$k_{\text{obs}}, \text{ s}^{-1}, \text{ D}_2\text{O}$	$k_{\text{obs}}, \text{ s}^{-1}, \text{ H}_2\text{O}$	$\text{KIE} = k_{\text{H}}/k_{\text{D}}$
7.44	15.1	2.03
7.63	14.7	1.93
7.71	14.4	1.87

^a $[\text{Ir}^{\text{IV}}]_0 = 2.5 \times 10^{-5} \text{ M}$; $[\text{MOP}]_{\text{tot}} = 3 \times 10^{-4} \text{ M}$; $[\text{HClO}_4] = 0.05 \text{ M}$; $\mu = 0.1 \text{ M}$ (LiClO_4); $T = 25 \text{ }^\circ\text{C}$.

Table A-21. Kinetic Dependence of MOP Oxidation on $p[H^+]$.^a

$p[H^+]^b$	$k_{\text{obs}}/[MOP]_{\text{tot}}, M^{-1}\cdot s^{-1}$
1.30	5.68×10^4
1.60	5.80×10^4
2.00	5.88×10^4
2.97	6.05×10^4
3.36	6.01×10^4
3.79	6.09×10^4
4.18	6.25×10^4
4.58	6.31×10^4
4.98	6.62×10^4
5.41	7.34×10^4
5.75	8.26×10^4
6.15	1.17×10^5
6.54	1.91×10^5
6.94	3.61×10^5

^a $[Ir^{IV}]_0 = 2.5 \times 10^{-5} M$; $[MOP]_{\text{tot}} = 3 \times 10^{-4} M$; $\mu = 0.1 M$ (LiClO₄); $T = 25 \text{ }^\circ\text{C}$; ^b $p[H^+] = -\log [HClO_4]$ in the $p[H^+]$ range of 1.0–2.2. The following buffers (0.02 M) were employed to maintain constant $p[H^+]$ values: monochloroacetate buffer for $2.4 < p[H^+] < 3.4$, acetate buffer for $3.6 < p[H^+] < 5.5$, and cacodylate buffer for $5.6 < p[H^+] < 7.0$.

Table A-22. Kinetic Dependence of MOP Oxidation on Temperature.^a

T, °C	k_{obs} , s ⁻¹
8.0	8.11
15	11.6
25	16.6
35	22.7
45	28.9

^a $[\text{Ir}^{\text{IV}}]_0 = 2.5 \times 10^{-5} \text{ M}$; $[\text{MOP}]_{\text{tot}} = 3 \times 10^{-4} \text{ M}$; $[\text{HClO}_4] = 0.1 \text{ M}$; $T = 25 \text{ }^\circ\text{C}$.

Table A-23. Kinetic Dependence of TBP Oxidation on $p[H^+]$.^a

$p[H^+]$	$[TBP]_{tot} \times 10^3, M$	$k_{obs}/[TBP]_{tot}, M^{-1} s^{-1}$
1.30	0.9	19.7
1.60	0.9	22.0
2.00	0.9	24.1
2.30	0.7	26.0
2.52	0.7	27.5
2.80	0.7	30.0
3.05	0.7	34.9
3.12	0.5	37.7
3.52	0.5	53.1
3.87	0.5	75.0
4.26	0.5	123
4.65	0.5	213
4.93	0.5	331
5.26	0.5	572
5.50	0.3	987
5.91	0.3	2.12×10^3
6.23	0.3	4.80×10^3
6.66	0.3	9.99×10^3
7.02	0.3	2.04×10^4

^a $[Ir^{IV}]_0 = 2.5 \times 10^{-5} M$; $[DBNBS] = 1 \text{ mM}$; $\mu = 0.1 M$ ($LiClO_4$); $T = 25 \text{ }^\circ\text{C}$. ^b $p[H^+] = -\log [HClO_4]$ in the $p[H^+]$ range of 1.0–2.2. The following buffers (0.02 M) were employed to maintain constant $p[H^+]$ values: monochloroacetate buffer for $2.4 < p[H^+] < 3.4$, acetate buffer for $3.5 < p[H^+] < 5.3$, and cacodylate buffer for $5.5 < p[H^+] < 7.1$.

Table A-24. Nonlinear-Least-Squares Regression Results of the $k_{\text{obs}}/[\text{TBP}]_{\text{tot}}$ vs $\text{p}[\text{H}^+]$ Plot with 2-Term and 3-Term Rate Law Models in the Presence of DBNBS.

		2-term rate law (eq 2-2)	3-term rate law (eq 2-3)
Best-fit values	$k_{\text{ArOH}}, \text{M}^{-1} \text{s}^{-1}$	28.8	18.2
	$k_{\text{ArO}^-}, \text{M}^{-1} \text{s}^{-1}$	3.61×10^7	2.40×10^7
	$k^0, \text{M}^{-1} \text{s}^{-1}$		0.483
Std. Error	$k_{\text{ArOH}}, \text{M}^{-1} \text{s}^{-1}$	2.62	0.744
	$k_{\text{ArO}^-}, \text{M}^{-1} \text{s}^{-1}$	3.34×10^6	8.71×10^5
	$k^0, \text{M}^{-1} \text{s}^{-1}$		3.05×10^{-2}
95 % Confidence Intervals	$k_{\text{ArOH}}, \text{M}^{-1} \text{s}^{-1}$	23.3 to 34.3	16.6 to 19.7
	$k_{\text{ArO}^-}, \text{M}^{-1} \text{s}^{-1}$	2.91×10^7 to 4.32×10^7	2.21×10^7 to 2.58×10^7
	$k^0, \text{M}^{-1} \text{s}^{-1}$		0.418 to 0.548
Goodness of Fit	Degrees of Freedom	17	16
	R squared	0.9892	0.9994
	Weighted Sum of Squares (1/(Y*Y))	1.14	5.98×10^{-2}
	Sy.x	0.258	6.11×10^{-2}

Table A-25. Kinetic Dependence on $[\text{Ac-Y-NH}_2]_{\text{tot}}$.^a

$[\text{Ac-Y-NH}_2]_{\text{tot}} \times 10^3, \text{ M}$	$k_{\text{obs}}, \text{ s}^{-1}$
0.8	0.010
2.4	0.031
4.0	0.053
5.6	0.072
7.2	0.093

^a All the reactions were run under pseudo-first-order conditions. $[\text{Ac-Y-NH}_2]_{\text{tot}} = (8.0\text{--}72) \times 10^{-4} \text{ M}$; $[\text{Ir}^{\text{IV}}]_0 = 2.5 \times 10^{-5} \text{ M}$; $[\text{DBNBS}] = 5 \text{ mM}$; $\text{p}[\text{H}^+] = 2.8$ (0.02 M monochloroacetate buffer); $\mu = 0.1 \text{ M}$ (LiClO_4); $T = 25 \text{ }^\circ\text{C}$.

Table A-26. Kinetic Dependence of Ac-Y-NH₂ Oxidation on p[H⁺].^a

p[H ⁺]	[Ac-Y-NH ₂] _{tot} × 10 ³ , M	<i>k</i> _{obs} /[Ac-Y-NH ₂] _{tot} , M ⁻¹ s ⁻¹
1.30	6.40	3.98
1.60	6.40	4.72
2.00	6.40	5.47
2.42	2.25	7.44
2.87	4.80	11.3
3.17	4.80	18.0
3.22	2.10	19.7
3.61	2.10	34.0
3.77	2.10	46.5
4.15	2.10	99.4
4.54	1.20	230
4.96	1.20	518
5.33	1.20	1.10×10 ³
5.92	0.3	3.97×10 ³
6.33	0.3	1.01×10 ⁴
6.71	0.3	2.26×10 ⁴
6.89	0.3	3.56×10 ⁴
7.19	0.3	5.99×10 ⁴

^a [Ac-Y-NH₂]_{tot} = (3.0–64) × 10⁻⁴ M; [Ir^{IV}]₀ = 2.5 × 10⁻⁵ M; [DBNBS] = 5 mM; μ = 0.1

M (LiClO₄); *T* = 25 °C. ^b p[H⁺] = -log [HClO₄] in the p[H⁺] range of 1.0–2.2. The

following buffers (0.02 M) were employed to maintain constant p[H⁺] values:

monochloroacetate buffer for 2.4 < p[H⁺] < 3.4, acetate buffer for 3.6 < p[H⁺] < 5.4, and

cacodylate buffer for 5.4 < p[H⁺] < 7.4.

Table A-27. Nonlinear-Least-Squares Regression Results of the $k_{\text{obs}}/[\text{Ac-Y-NH}_2]_{\text{tot}}$ vs $\text{p}[\text{H}^+]$ Plot with 2-Term and 3-Term Rate Law Models in the Presence of DBNBS.

		2-term rate law (eq 2-2)	3-term rate law (eq 2-3)
Best-fit values	$k_{\text{ArOH}}, \text{M}^{-1} \text{s}^{-1}$	5.380	2.885
	$k_{\text{ArO}^-}, \text{M}^{-1} \text{s}^{-1}$	4.47×10^7	3.59×10^7
	$k^0, \text{M}^{-1} \text{s}^{-1}$		0.222
Std. Error	$k_{\text{ArOH}}, \text{M}^{-1} \text{s}^{-1}$	0.590	0.235
	$k_{\text{ArO}^-}, \text{M}^{-1} \text{s}^{-1}$	2.92×10^6	9.89×10^5
	$k^0, \text{M}^{-1} \text{s}^{-1}$		1.90×10^{-2}
95 % Confidence Intervals	$k_{\text{ArOH}}, \text{M}^{-1} \text{s}^{-1}$	4.129 to 6.632	2.384 to 3.386
	$k_{\text{ArO}^-}, \text{M}^{-1} \text{s}^{-1}$	3.85×10^7 to 5.09×10^7	3.38×10^7 to 3.80×10^7
	$k^0, \text{M}^{-1} \text{s}^{-1}$		0.182 to 0.263
Goodness of Fit	Degrees of Freedom	16	15
	R squared	0.9909	0.9992
	Weighted Sum of Squares (1/(Y*Y))	0.732	0.068
	Sy.x	0.214	6.72×10^{-2}

Table A-28. Kinetic Dependence on $[\text{Os}^{\text{III}}]_0$.^a

$[\text{Os}^{\text{III}}]_0 \times 10^5, \text{ M}$	$t_{1/2}, \text{ s}$	$k_{\text{obs}}, \text{ M}^{-1} \text{ s}^{-1}$
0.49	3.0	7.14×10^4
0.64	2.3	5.95×10^4
0.79	1.8	6.84×10^4
1.15	1.2	7.11×10^4

^a All the reactions were run under pseudo-second-order conditions at 550 nm. $[\text{Os}^{\text{II}}]_0 = (12.2\text{--}12.7) \times 10^{-5} \text{ M}$; $[\text{phenol}] = 0.002 \text{ M}$; $\mu = 0.1 \text{ M (NaCl)}$; $T = 25^\circ\text{C}$; $\text{p}[\text{H}^+] = 5.1$ (0.02 M acetate buffer).

Table A-29. Kinetic data for the oxidation with various $[\text{phenol}]_{\text{tot}}$.^a

$[\text{phenol}]_{\text{tot}}, \text{ M}$	$\text{p}[\text{H}^+]^b$	$k_{\text{obs}}, \text{ M}^{-1} \text{ s}^{-1}$
0.002	5.44	8.12×10^4
0.008	5.63	7.08×10^5
0.014	5.67	1.89×10^6
0.020	5.68	3.75×10^6

^a All the reactions were run under pseudo-second-order conditions at 550 nm. $[\text{Os}^{\text{III}}]_0 = 1.21 \times 10^{-5} \text{ M}$; $[\text{Os}^{\text{II}}]_0 = 12.4 \times 10^{-5} \text{ M}$; $\mu = 0.1 \text{ M (NaCl)}$; $T = 25^\circ\text{C}$. ^b The $\text{p}[\text{H}^+]$ values were maintained using 0.02 M acetate buffers.

Table A-30. Kinetic Dependence on $[\text{Os}^{\text{II}}]_0$.^a

$[\text{Os}^{\text{II}}]_0 \times 10^5, \text{ M}$	$[\text{Os}^{\text{III}}]_0 \times 10^5, \text{ M}$	$[\text{phenol}]_{\text{tot}} \times 10^3, \text{ M}$	$t_{1/2}, \text{ s}$	$k_{\text{obs}}, \text{ M}^{-1} \text{ s}^{-1}$
0.68	1.38	2.5	0.11	6.27×10^5
0.76	1.23	5.0	0.04	2.09×10^6
1.04	0.92	5.0	0.08	1.46×10^6
1.51	0.47	5.0	0.18	1.01×10^6

^a All the reactions were run under “pseudo-second-order” conditions at 480 nm. $[\text{Os}^{\text{III}}]_0 = (0.47\text{--}1.38) \times 10^{-5} \text{ M}$; $[\text{Os}^{\text{II}}]_0 = (0.68\text{--}1.51) \times 10^{-5} \text{ M}$; $[\text{phenol}]_{\text{tot}} = (2.5\text{--}5.0) \times 10^{-3} \text{ M}$; $\mu = 0.1 \text{ M}$ (NaCl); $T = 25^\circ\text{C}$; $\text{p}[\text{H}^+] = 4.7$ (0.02 M acetate buffer).

Table A-31. Kinetic Dependence on $\text{p}[\text{H}^+]$.^a

$\text{p}[\text{H}^+]^b$	$[\text{phenol}]_{\text{tot}} \times 10^3, \text{ M}$	$[\text{Os}^{\text{II}}]_0 \times 10^5, \text{ M}$	$k_{\text{obs}}, \text{ M}^{-1} \text{ s}^{-1}$
4.05	20	1.56	7.46×10^5
4.71	5.0	1.51	1.01×10^6
5.39	1.0	1.71	9.07×10^5
6.34	0.2	1.81	2.19×10^6

^a All the reactions were run under “pseudo-second-order” conditions at 480 nm. $[\text{Os}^{\text{III}}]_0 = (0.39\text{--}0.67) \times 10^{-5} \text{ M}$; $\mu = 0.1 \text{ M}$ (NaCl); $T = 25^\circ\text{C}$. ^b The following buffers (0.02 M) were employed to maintain constant $\text{p}[\text{H}^+]$ values: acetate buffer for $4.0 < \text{p}[\text{H}^+] < 5.4$, and cacodylate buffer for $\text{p}[\text{H}^+] = 6.34$